ABSTRACT

(PhD)

ELECTROMAGNETIC SCATTERING FROM INHOMOGENEOUS OBJECTS OF ARBITRARY SHAPE EMBEDDED IN A LAYERED MEDIUM

by

Ergün Şimşek

Department of Electrical Engineering
Duke University

Date: ______________________________

Approved:

____
Qing Huo Liu, Supervisor

____
William T. Joines

____
David R. Smith

____
Thomas P. Witelski

____
Tomoyuki Yoshie

An abstract of a dissertation submitted in partial fulfillment of the
requirements for the degree of Doctor of Philosophy
in the Department of Electrical Engineering
in the Graduate School of
Duke University

2006

ABSTRACT

(PhD)

ELECTROMAGNETIC SCATTERING FROM INHOMOGENEOUS OBJECTS OF ARBITRARY SHAPE EMBEDDED IN A LAYERED MEDIUM

by

Ergün Şimşek

Department of Electrical Engineering
Duke University

Date: Nov. 7, 2006

Approved:

Qing Huo Liu, Supervisor

William T. Joines

David R. Smith

Thomas P. Witelski

Tomoyuki Yoshie

An abstract of a dissertation submitted in partial fulfillment of the requirements for the degree of Doctor of Philosophy in the Department of Electrical Engineering in the Graduate School of Duke University

2006

Abstract

In this thesis, novel surface and hybrid integral equation solvers have been developed for the electromagnetic scattering from inhomogeneous objects in a layered medium. To evaluate the layered medium Green's functions (LMGFs) efficiently, a new extraction procedure is developed which is valid for any kind of source-field point combination. The extraction procedure is implemented appropriately for each individual term of the integrand and the contribution of the each term is calculated analytically. To calculate the scattered electric and magnetic fields from homogeneous objects of arbitrary shape embedded in a layered medium, the surface integral equation is solved by using the Method of Moments (MoM). Then, its exterior part is utilized as a radiation boundary condition for the finite-element method (FEM) which allows the objects inside the surface to be arbitrarily inhomogeneous. For the sake of computational efficiency, the sparse and symmetric FEM matrix is stored by using a row-indexed scheme to reach its the non-zero elements quickly. The coupled FEM/MoM matrix solved by using the biconjugate-gradient (BCG) method which requires $O(KN^2)$ CPU time and $O(N^2)$ memory, where N is the number of unknowns and K is the number of iterations. The CPU time for the evaluation of LMGFs is reduced by a simple interpolation technique. The overall accuracy and efficiency of the developed method are supported with several examples including two and three-dimensional inhomogeneous and composite structures. For the 2D case, it is shown that a spectral accuracy in the integral can be achieved by using the fast Fourier transform (FFT) algorithm and the subtraction of singularities in Green's functions. The number of points on the radiation boundary is only around 5 points per wavelength, that gives substantial saving in memory and CPU time requirements.

To my father Münür Şimşek...

Contents

List of Tables

List of Figures

Acknowledgements

I would like to express my deep and sincere gratitude to my supervisor, Professor Qing Huo Liu for believing in me and giving this opportunity to work with him. From first day to the last, he has been a great advisor and a role-model. I know of no advisor as dedicated and committed to his students as Prof. Liu. I hope, I will be able to follow the way he has gone through.

I would like to thank to my colleagues Dr. Lin-Ping Song, Dr. Boujun Wei, Dr. Chun Yu, and Jianguo Liu for their collaborations.

I would like to thank to my teachers Hayriye Sakarya, Ahmet Küçükerdönmez, and Mehmet Ünver because of their enormous efforts on me. They were not only my teachers but also my heroes, and they still are.

Most of all, I would like to thank my beloved family: my father Münür Şimşek, my mother Gülbeden Şimşek, and my brother Engin Şimşek. I am grateful for their continuing support and encouragement. I wish my father could see my dissertation and graduation from Duke. This dissertation is dedicated to him.

Last but not least, I would like to thank to *Aşkimu* Selin for her love and care. In every sentence of this thesis, in every figure, there is something from her. She was my lucky *seven* and I hope this will never change.

Contribution of the Author

The aim of this work is to develop novel spectral and hybrid integral methods for electromagnetic scattering from arbitrarily-shaped inhomogeneous objects embedded in a layered medium. The author has been involved with the development of the theory and formulations, their numerical implementations, and testing and verifying of these developed methods.

The author's list of publications in given in the Biography section at the end of the thesis. The articles, [P1] through [P6] are all written by the author under the supervision of Prof. Qing H. Liu.

The article [P1] is a novel singularity subtraction technique for the layered medium Green's functions developed by the author. The results presented in [P1] are compared with the third author's own program. The preliminary results of this work are given in [C1] and [C2].

The article [P2] is a novel 2D surface integral equation solver for layered media developed by the author in collaboration with the second author. The preliminary results of this work are presented in [C3].

The article [P3] is a novel 2D hybrid integral equation solver for layered media developed by the author in collaboration with the second author. The preliminary results of this work are given in [C4].

The author has developed a 3D surface integral equation solver in collaboration with Dr. Chun Yu and the author has utilized this solver as a novel radiation boundary condition for finite-element method in 3D. The related paper is in preparation. The preliminary results of this work are presented in [C5] and [C6].

The articles [P5]-[P7] are not included in this thesis.

Chapter 1

Introduction

Electromagnetic and acoustic scattering from inhomogeneous objects of arbitrary shape embedded in a layered medium has been an important research topic because of its wide application in areas such as geophysical exploration, remote sensing, land-mine detection, biomedical imaging, underwater acoustics, interconnect simulations, microstrip antennas, and monolithic microwave integrated circuits. The complex background and the large number of unknowns associated with realistic targets make the problem more challenging.

In order to solve a layered medium scattering problem, there are two main ingredients: the layered medium Green's functions (LMGF) and an integral equation solver. To many researchers, the first ingredient, the LMGF, is an obstacle due to their complicated formulation. In addition to their complexity, the straightforward numerical integration methods are not efficient for these integrals because of the slowly decaying and highly oscillating behavior of the Sommerfeld integrands [1]-[4], [46]. Extensive research has been done to accelerate this process through methods such as the fast Hankel transform (FHT) approach [5]-[6], the window function approach [7], the steepest descent path (SDP) approach [82], and the discrete complex image method (DCIM) [8]-[21], [28], and [47].

All of these methods have some advantages and disadvantages. This work describes a new extraction procedure that can be incorporated in these methods to improve the efficiency. This procedure is an improved version of the extraction procedure implemented in DCIM, and is valid for any kind of source-field point combination. The extraction procedure is implemented appropriately for each individual term of the integrand and the contribution of the extracted terms is calculated analytically. However, for the sake of robustness, instead of approximating the remaining integral with complex images, the remaining integral is calculated numerically by using Gaussian quadratures. Results of this method have been validated by comparison with many examples in the literature, and the high efficiency has been verified.

Once we are capable of calculating the LMGFs efficiently, we can solve the scattering problem by utilizing the appropriate integral equation. For a homogeneous scatter with an arbitrary geometry in a layered medium, the surface integral equation (SIE) method is a powerful tool to calculate the scattered electromagnetic fields, because in this case, only the surface of the scatterer needs to be discretized. The classical methods for solving such integral equations are the method of moments (MOM) [27]-[30], fast multipole method (FMM) [31]-[35], and adaptive integral method [36]-[41]. However, for inhomogeneous objects, the SIE must be combined with other methods such as the finite element method (FEM) in order to account for the inhomogeneity. In this approach, the computational domain can be truncated by using a radiation boundary condition (RBC). In the last three decades, several RBCs have been developed [53]-[77]. One of them is the hybrid finite element/boundary element method (FEM/BEM), which uses SIE as an RBC on the boundary surrounding the scatterer(s), and the FEM in the bounded region [54]-[58], [63], [65]-[69]. In this method, the number of the required samples taken on the boundary can be decreased depending on the accuracy of SIE, hence the matrix size of the FEM problem can be reduced. Because of this lower memory requirement and geometrical and material adaptability, the FEM/BEM is a very useful and powerful method for the analysis of scattering by inhomogeneous objects in layered media. Because of these advantages, we proceed to develop a complete set of numerical methods to solve layered medium scattering problems efficiently both for the two-dimensional (2D) and three-dimensional (3D) homogeneous and inhomogeneous scatterers either by using a surface integral equation or a hybrid finite element/boundary element method.

For the 2D case, we extend the spectral integral method (SIM), which was proposed as an alternative way of solving the surface integral equation efficiently for a homogeneous scatter in free space and for periodic structures by Liu *et. al*. [42], to arbitrarily-shaped smooth dielectric and PEC cylinders embedded in layered media. This algorithm is related to the fast method originally developed by Bojarski [43] for sound-soft circular cylinders, and extended by Schuster [44] to multi-layer circular cylinders, and by Hu [45] to sound-soft or sound-hard smooth cylinders. Liu *et. al*. [42] further extended the SIM to arbitrarily-shaped smooth dielectric cylinders, and to periodic structures such as photonic crystals. The idea behind this method is the use of a fast Fourier transform (FFT) algorithm and the subtraction of singularities in Green's functions to achieve a spectral accuracy in the integral. Here, we extend this method to arbitrarily-shaped smooth dielectric and PEC cylinders embedded in layered media by using 2D layered-medium Green's functions. To avoid the discontinuous behaviors of the fields and Green's function (i.e., the functions or their derivatives being discontinuous) across the layer interfaces in the problems where the scatterer resides in several layers, first we assume that the object is located completely within one single layer in the multilayered medium. We have demonstrated high accuracy and efficiency of the method. 1% accuracy can be obtained with about three points per wavelength sampling. Numerical results also confirm that the SIM is applicable to concave objects.

Next, we improve SIM to handle the discontinuous behavior of the fields and Green's function across the layer interfaces so that SIM can be now applied to a scatterer straddling several layers. This step is a crucial improvement over [79], and makes SIM applicable for a large number of layered medium problems. After this improvement, we utilize the SIM as an RBC for layered medium problems in 2D. For the implementation of radiation boundary condition, an artificial boundary $\partial\Gamma$ is applied to truncate the arbitrarily shaped inhomogenous scatterer(s) from the layered medium. The finite element method is applied in the interior region to calculate the field, while the spectral integral method is applied on the outer boundary $\partial\Gamma$ to relate the field and induced current. The field and current on the boundary for the FEM are obtained from the SIM results via a highly accurate trigonometric interpolation through FFT. The singular terms in the Green's functions and the non-smooth terms in their derivatives are handled appropriately. High-order accuracy of SIM provides the capability of low sampling density on the outer boundary $\partial\Gamma$, which significantly reduces the number of unknowns on $\partial\Gamma$. Combining SIM with FEM has many advantages for both homogeneous and layered media problems beside reducing the matrix size. First, scattering problems can be solved for arbitrarily shaped inhomogeneous scatterers. Second, the number of the scatterers can be as many as needed. Third, the scatterers can reside in several layers. Finally, the freedom of using any type of smooth element, e.g. an ellipse, as an outher boundary helps to reduce the size of truncated domain. The efficiency of the developed algorithm has been supported with several examples including inhomogeneous and composite structures. The number of points on the radiation boundary is only around 5 points per wavelength, thus giving substantial saving in memory and CPU time requirements. Applications are also demonstrated for inhomogeneous and composite structures.

The success of the developed 2D SIM and hybrid SIM/FEM methods leads us to develop their 3D versions. Moving from 2D to 3D brings a lot of difficulties with it. The form of the integral equations, the type of the basis functions, and the meshing elements are all more complicated. Now, we have to use the dyadic LMGFs, which are 3×3 tensors and hence 9 times longer CPU time and larger memory are required for the evaluation and storage. Furthermore, the singularity of the each dyadic LMGF component must be handled appropriately. The singularities in the surface and volume integrals are more difficult than the ones in 2D case. Moreover, we have another serious issue to resolve: the implemention of the FFT algorithm to the 3D layered medium problems. For a free space, the Green's function has R dependency, where R is the distance from the source point (x', y', z') to the field point (x, y, z). However, for the multilayered background, the LMGF has $(\rho, z|z')$ dependency, where $\rho = \sqrt{(x - x')^2 + (y - y')^2}$, assuming planar layers are all parallel to the xy plane. For this case, the solution of the matrix equation can be accelerated by using the FFT algorithm for the objects having a surface partially parallel to xy plane. On top of that, due to the LMGFs' $(\rho, z|z')$ dependency, we can utilize a very simple interpolation technique to evaluate the LMGFs very rapidly. Because of these reasons, we decide to use a cuboid-shaped radiation boundary for our 3D implementation. To achieve our target, we first develop a 3D layered medium surface integral equation (SIE) solver based on the Method of Moments [96] by using RWG basis functions [97]. The Gaussian quadrature rules [70, 71] are followed for the numerical evaluation of the surface integrals, where the surface of the scatterer can be discretized with either rectangular or triangular patches. The formulation and implementation can handle 3D dielectric and PEC objects. For the singular terms, the Duffy transformation [89] is utilized. A simple interpolation technique has been used to accelerate the layered medium Green's function calculation [49, 50]. The influence of this step is shown to be less than 1% in terms of the accuracy, whereas in terms of the computation time there is a significant improvement. The accuracy of the overall method is validated with several examples. As long as the sampling density is bigger than 10 PPW, the implemented MoM can produce very accurate results.

Then in the final step of this work, we utilize the exterior part of our layered medium surface integral equation solver as a 3D radiation boundary condition. Similar to the 2D case, an artificial boundary is applied to truncate the arbitrarily 3D shaped inhomogenous scatterer(s) from the layered medium. The finite-element method is applied in the interior region to calculate the field, while the method of moments is applied on the outer boundary to relate the field and induced current. Due to the form of the chosen basis functions and meshing, the fields and currents on the boundary for the FEM are obtained from the solution of the final matrix equation without using any additional interpolation. For the FEM part, we adopt the code EMAP (ElectroMagnetic Analysis Program), a three-dimensional finite-element modeling code developed by several researchers at the University of Missouri [99], in this work. The inhomogeneous interior problem is discretized with tetrahedrons. To increase the efficiency of the overall method, the symmetric and sparse FEM matrix is stored with a row-indexed scheme, and the bi-conjugate gradient solver is used. The validity of the hybrid method is supported with several examples by using homogeneous and inhomogeneous scatterers.

The organization of this thesis is as follows.

Chapter 2 is a brief review of the Green's function methods for solving integral equations. We describe derivations of free space scalar and dyadic Green's functions,

Table 1.1: Organization of Chapters

Chapter 1	Introduction
Chapter 2	Preliminaries
Chapter 3	Layered Medium Green's Functions
Chapter 4	2D Layered Medium Surface Integral Equation Solver: SIM
Chapter 5	2D Layered Medium Hybrid Integral Equation Solver: SIM/FEM
Chapter 6	3D Layered Medium Surface Integral Equation Solver: MoM
Chapter 7	3D Layered Medium Hybrid Integral Equation Solver: MoM/FEM

and layered medium Green's functions.

Chapter 3 presents an efficient method to evaluate the 2D and 3D multilayered medium Green's functions for general electric and magnetic sources. Without finding any surface poles or steepest descent path, a special extraction procedure is applied to each term of the Sommerfeld integrands to make them rapidly decreasing functions of k_ρ. The contributions of the extracted terms are calculated analytically. The remaining integrals are computed adaptively by using Gaussian quadratures. The accuracy of the method has been confirmed by comparing with many examples in literature, and the high efficiency has been demonstrated.

Chapter 4 introduces a 2D spectral integral method for electromagnetic scattering from dielectric and perfectly electric conducting (PEC) objects with a closed boundary embedded in a layered medium. Two-dimensional (2D) layered medium Green's functions are computed adaptively by using Gaussian quadratures. The singular terms in the Green's functions and the non-smooth terms in their derivatives are handled appropriately to achieve exponential convergence. Numerical results, compared with the ones obtained by using other methods, demonstrate the spectral accuracy and high efficiency of the proposed method. They also confirm that the SIM is applicable to concave objects.

Chapter 5 presents a 2D spectral integral method (SIM) for electromagnetic scattering from dielectric and perfectly electric conducting (PEC) objects with a closed boundary residing in several layers of a multilayered medium and its usage as a radiation boundary condition to truncate the computational domain in the finite element method (FEM). Because of the high accuracy of the SIM, the sampling density on the radiation boundary requires less than five points per wavelength to achieve 1% accuracy. We also demostrate applications of this method to inhomogeneous and composite structures.

In Chapter 6, we describe the surface equivalence principle. Based on this principle, the surface integral equations for both homogeneous and multilayered background are given. Next, some implementation details for the MoM solution, such as singularity treatment, meshing, and interpolation are discussed. Finally, the validity of the developed layered medium MoM implementation is supported with numerical examples.

In Chapter 7, we present a 3D FEM formulation. Next, we provide some details about the evaluation of FEM matrices and the coupling of FEM and MoM matrices. Finally, the validity of the developed hybrid FEM/MoM method is demonstrated with numerical examples.

Chapter 8 includes some potential future projects. In Appendix A, a detailed formulation of the developed singularity treatment for the layered medium Green's functions is given. In Appendix B, a brief biography of George Green is provided.

Chapter 2

Green's Functions

The Green's function method is a very powerful and efficient technique to solve boundary-value problems. To illustrate the efficiency of this method, a review article by Jin and Chew [24] is followed.

When there are N point charges (q_i, for $i = 1, 2, \cdots, N$) located at $\mathbf{r}_i$ in a free space, the total potential at $\mathbf{r}$ can be obtained by using the principle of linear superposition as follows

$$\phi(\mathbf{r}) = \sum_{i=1}^{N} \phi_i(\mathbf{r}) = \sum_{i=1}^{N} \frac{q_i}{4\pi\epsilon|\mathbf{r} - \mathbf{r_i}|}, \tag{2.1}$$

where ϕ_i denotes the potential due to i^{th} point charge located at $\mathbf{r}_i$. When we have a volume electric charge, we can divide the volume into many small cubes which behave like point charges as

$$q_i \approx \rho(\mathbf{r}_i)\Delta V_i, \tag{2.2}$$

where $\mathbf{r}_i$ denotes the center of the i^{th} cube having volume ΔV_i and charge density $\rho(\mathbf{r}_i)$. Then, again by using the principle of linear superposition, the total potential can be approximated as

$$\phi(\mathbf{r}) = \sum_{i=1}^{N} \phi_i(\mathbf{r}) \approx \sum_{i=1}^{N} \frac{\rho(\mathbf{r}_i)\Delta V_i}{4\pi\epsilon|\mathbf{r} - \mathbf{r_i}|}. \tag{2.3}$$

When we take the limit, Eq. (2.3) becomes

$$\phi(\mathbf{r}) = \lim_{\Delta V_i \to 0} \sum_{i=1}^{\infty} \frac{\rho(\mathbf{r}_i)\Delta V_i}{4\pi\epsilon|\mathbf{r} - \mathbf{r_i}|}. \tag{2.4}$$

which can be written in the integral form as

$$\phi(\mathbf{r}) = \int_V \frac{\rho(\mathbf{r}')}{4\pi\epsilon|\mathbf{r}-\mathbf{r}'|} dV', \tag{2.5}$$

where V denotes the volume of the electric charge. Equation (2.6) can be written as

$$\phi(\mathbf{r}) = \int_V \rho(\mathbf{r}')G(\mathbf{r},\mathbf{r}')dV' \tag{2.6}$$

where

$$G(\mathbf{r},\mathbf{r}') = \frac{1}{4\pi\epsilon|\mathbf{r}-\mathbf{r}'|}. \tag{2.7}$$

Here, $G(\mathbf{r},\mathbf{r}')$ is called the Green's function, which helps us to find the potential as the corresponding linear superposition of the potentials produced by the point sources.

From the general point of view, Green's function is an impulse response of a linear circuit system. The convolution of the impulse response with any input function gives the system response to that input. Similarly, the potential produced by an arbitrary distribution of sources can be obtained easily, once the Green's function corresponding to the potential due to a point source in found. As a result, instead of solving Poisson's equation for each new source repeatedly, we can use linear superposition to obtain solutions to any sources, once we have the Green's function for that specific problem. Moreover, finding the Green's function is much easier than finding the solution to an arbitrary source.

2.1 Free-Space Green's Functions

The inhomogeneous Helmholtz equation is given by

$$\nabla^2\phi(\mathbf{r}) + k^2\phi(\mathbf{r}) = -f(\mathbf{r}), \tag{2.8}$$

where ϕ is a wave function in our case, k is the wave number. We assume that, there is no reflection in infinite free space, so $\phi(\mathbf{r})$ satisfies the radiation condition given by

$$r\left(\frac{\partial\phi}{\partial r}+jk\phi\right)=0 \qquad \text{as r} \rightarrow \infty \tag{2.9}$$

We can solve Eq. (2.8) for each f, or we can use Green's function method as follows: first, we can find Helmholtz equation's Green's function by

$$\nabla^2 G_0(\mathbf{r},\mathbf{r}')+k^2 G_0(\mathbf{r},\mathbf{r}')=-\delta(\mathbf{r}-\mathbf{r}') \tag{2.10}$$

where $\delta(\mathbf{r}-\mathbf{r}')$ is the delta function which is given by $\delta(\mathbf{r}-\mathbf{r}')=\delta(x-x')\delta(y-y')\delta(z-z')$ in rectangular coordinates. If we can find G_0, then we can obtain ϕ using the principle of linear superposition as

$$\phi(\mathbf{r})=\int_V G_0(\mathbf{r},\mathbf{r}')f(\mathbf{r}')dV' \tag{2.11}$$

where V is the support of $f(\mathbf{r})$, which is the volume having nonzero $f(\mathbf{r})$. Let us assume that $\mathbf{r}'$ is located at the origin of spherical coordinates. By using spherical symmetry

$$\frac{1}{r_1^2}\frac{d}{dr_1}\left[r_1^2\frac{dG_0(\mathbf{r}_1,0)}{dr_1}\right]+k^2 G_0(\mathbf{r}_1,0)=-\delta(\mathbf{r}_1,0) \tag{2.12}$$

where $\mathbf{r}_1=\mathbf{r}-\mathbf{r}'$. When $r_1\neq 0$, Eq. (2.12) can be written as

$$\frac{d^2}{dr_1^2}\left[r_1^2 G_0(\mathbf{r}_1,0)\right]+k^2 r_1 G_0(\mathbf{r}_1,0)=0 \tag{2.13}$$

which has a solution

$$r_1 G_0(\mathbf{r}_1,0)=Ae^{-jkr_1} \qquad \text{or} \qquad G_0(\mathbf{r}_1,0)=Ae^{-jkr_1}/r_1 \tag{2.14}$$

The unknown coefficient A can be found by plugging (2.14) into (2.12) and integrating it over a small sphere centered at the origin which gives us $A = (4\pi)^{-1}$. As a result,

$$G_0(\mathbf{r}_1, 0) = \frac{e^{-jkr_1}}{4\pi r_1} \tag{2.15}$$

and in the original coordinates

$$G_0(\mathbf{r}, \mathbf{r}') = \frac{e^{-jk|\mathbf{r}-\mathbf{r}'|}}{4\pi|\mathbf{r}-\mathbf{r}'|}. \tag{2.16}$$

When we follow the same procedure for two-dimensional case, we obtain

$$G_0(\rho, \rho') = \frac{H_0^{(2)}(k|\boldsymbol{\rho}-\boldsymbol{\rho}'|)}{4j}, \tag{2.17}$$

where $\boldsymbol{\rho} = \hat{x}x + \hat{y}y$ and $H_0^{(2)}(k|\boldsymbol{\rho}-\boldsymbol{\rho}'|)$ is the zeroth-order Hankel function of the second kind.

2.2 Dyadic Green's Functions

For vectorial functions, the Green's function is a dyad. In electrodynamics, both source and fields are vectors with three components. Each component of the source can produce all three components of the fields, so this dyadic Green's function has to have 9 components, which can be expressed as a 3×3 matrix.

Free Space Dyadic Green's Functions

The electric field produced by an electric current source $\mathbf{J}(\mathbf{r})$ in a free space satisfies

$$\nabla \times \nabla \times \mathbf{E}(\mathbf{r}) - k^2\mathbf{E}(\mathbf{r}) = -j\omega\mu\mathbf{J}(\mathbf{r}). \tag{2.18}$$

We need to find a dyadic Green's function $\bar{\mathbf{G}}_0$ which relates $\mathbf{E}(\mathbf{r})$ and $\mathbf{J}(\mathbf{r})$ with

$$\mathbf{E}(\mathbf{r}) = -j\omega\mu \int_V \bar{\mathbf{G}}_0(\mathbf{r},\mathbf{r}') \cdot \mathbf{J}(\mathbf{r}') dV' \tag{2.19}$$

where V is the support of the current. By plugging (2.19) into (2.18)

$$\begin{aligned} \int_V \nabla \times \nabla \times \bar{\mathbf{G}}_0(\mathbf{r},\mathbf{r}') \cdot \mathbf{J}(\mathbf{r}') dV' - k^2 \int_V \bar{\mathbf{G}}_0(\mathbf{r},\mathbf{r}') \cdot \mathbf{J}(\mathbf{r}') dV' \\ = \int_V \bar{\mathbf{I}}\delta(\mathbf{r}-\mathbf{r}') \cdot \mathbf{J}(\mathbf{r}') dV' \end{aligned} \tag{2.20}$$

where $\bar{\mathbf{I}}$ is the unit dyad ($\bar{\mathbf{I}} = \hat{x}\hat{x}+\hat{y}\hat{y}+\hat{z}\hat{z}$). Eq. (2.20) could be satisfied for arbitrary $\mathbf{J}(\mathbf{r})$ if

$$\nabla \times \nabla \times \bar{\mathbf{G}}_0(\mathbf{r},\mathbf{r}') - k^2 \bar{\mathbf{G}}_0(\mathbf{r},\mathbf{r}') = \bar{\mathbf{I}}\delta(\mathbf{r}-\mathbf{r}'). \tag{2.21}$$

$\bar{\mathbf{G}}_0(\mathbf{r},\mathbf{r}')$ is called the dyadic Green's function of the electric type relating $\mathbf{E}$ to $\mathbf{J}$.

To find the dyadic Green's functions, first let us take the scalar product of (2.21) with an arbitrary vector $\mathbf{a}$.

$$\nabla \times \nabla \times \bar{\mathbf{G}}_0(\mathbf{r},\mathbf{r}') \cdot \mathbf{a} - k^2 \bar{\mathbf{G}}_0(\mathbf{r},\mathbf{r}') \cdot \mathbf{a} = \mathbf{a}\delta(\mathbf{r}-\mathbf{r}'). \tag{2.22}$$

If we use $\nabla \times \nabla \times \mathbf{A} = \nabla(\nabla \cdot \mathbf{A}) - \nabla^2 \mathbf{A}$, (2.22) becomes

$$\nabla^2 \bar{\mathbf{G}}_0(\mathbf{r},\mathbf{r}') \cdot \mathbf{a} + k^2 \bar{\mathbf{G}}_0(\mathbf{r},\mathbf{r}') \cdot \mathbf{a} = \nabla \left(\nabla \cdot \bar{\mathbf{G}}_0(\mathbf{r},\mathbf{r}') \cdot \mathbf{a} \right) - \mathbf{a}\delta(\mathbf{r}-\mathbf{r}'). \tag{2.23}$$

If we take the divergence of both sides, (2.22) becomes

$$\nabla \cdot \bar{\mathbf{G}}_0(\mathbf{r},\mathbf{r}') \cdot \mathbf{a} = -\frac{1}{k^2} \nabla \cdot [\mathbf{a}\delta(\mathbf{r}-\mathbf{r}')]. \tag{2.24}$$

So, Eq. (2.22) can be written as

$$\nabla^2 \bar{\mathbf{G}}_0(\mathbf{r},\mathbf{r}') \cdot \mathbf{a} + k^2 \bar{\mathbf{G}}_0(\mathbf{r},\mathbf{r}') \cdot \mathbf{a} = -\left(1 + \frac{\nabla\nabla\cdot}{k^2}\right) [\mathbf{a}\delta(\mathbf{r}-\mathbf{r}')] . \tag{2.25}$$

From the scalar case, we know that

$$\nabla^2 G_0(\mathbf{r},\mathbf{r}') + k^2 G_0(\mathbf{r},\mathbf{r}') = -\delta(\mathbf{r}-\mathbf{r}'). \tag{2.26}$$

Moreover, $1 + \nabla\nabla\cdot/k^2$ is a linear operator which commutes with ∇^2

$$\bar{\mathbf{G}}_0(\mathbf{r},\mathbf{r}')\cdot\mathbf{a} = \left(1+\frac{\nabla\nabla\cdot}{k^2}\right)[\mathbf{a}G_0(\mathbf{r},\mathbf{r}')] = \left(1+\frac{\nabla\nabla}{k^2}\right)[G_0(\mathbf{r},\mathbf{r}')\cdot\mathbf{a}]\,. \tag{2.27}$$

Since $\mathbf{a}$ is an arbitrary vector, we can conclude that

$$\bar{\mathbf{G}}_0(\mathbf{r},\mathbf{r}') = \left(1+\frac{\nabla\nabla}{k^2}\right)G_0(\mathbf{r},\mathbf{r}'). \tag{2.28}$$

Eq. (2.28) is the explicit representation of the dyadic Green's function in terms of the scalar Green's functions which is only valid for homogeneous unbounded space. The evaluation of dyadic Green's function for layered media has different procedure which is described next.

2.3 Scalar Form of Maxwell′s Equations and Transmission Line Green′s Functions

Electric and magnetic fields are governed by the Maxwell's Equations due to arbitrary electric and magnetic currents ($\mathbf{J}$ and $\mathbf{M}$, respectively) as follows

$$\nabla\times\mathbf{E} = -j\omega\mu_0\mu_r\mathbf{H} - \mathbf{M} \tag{2.29}$$

$$\nabla\times\mathbf{H} = j\omega\epsilon_0\epsilon_r\mathbf{E} + \mathbf{J} \tag{2.30}$$

By decomposing the fields into transverse and longitudinal components Maxwell's equations can be written as

$$\frac{d}{dz}\tilde{\mathbf{E}}_\rho = \frac{1}{j\omega\epsilon_0\epsilon_r}(k^2 - \mathbf{k}_\rho\mathbf{k}_\rho.)(\tilde{\mathbf{H}}_\rho\times\hat{z}) + \frac{\tilde{J}_z}{\omega\epsilon_0\epsilon_r}\mathbf{k}_\rho - \tilde{\mathbf{M}}_\rho\times\hat{z} \tag{2.31}$$

$$\frac{d}{dz}\tilde{\mathbf{H}}_\rho = \frac{1}{j\omega\mu_0\mu_r}(k^2 - \mathbf{k}_\rho\mathbf{k}_\rho.)(\hat{z} \times \tilde{\mathbf{E}}_\rho) + \frac{\tilde{M}_z}{\omega\mu_0\mu_r}\mathbf{k}_\rho - \hat{z} \times \tilde{\mathbf{M}}_\rho \tag{2.32}$$

$$-j\omega\epsilon_0\epsilon_r\tilde{E}_z = j\mathbf{k}_\rho.(\tilde{\mathbf{H}}_\rho \times \hat{z}) + \tilde{J}_z \tag{2.33}$$

$$j\omega\mu_0\mu_r\tilde{H}_z = j\mathbf{k}_\rho.(\hat{z} \times \tilde{\mathbf{H}}_\rho) + \tilde{M}_z \tag{2.34}$$

Note that the transverse coordinate $\boldsymbol{\rho} = \hat{x}x + \hat{y}y$ is replaced by the spectral counterpart $\mathbf{k}_\rho = \hat{x}k_x + \hat{y}k_y$ according to Fourier Transformation

$$\tilde{g}(\mathbf{k}_\rho, z) = \int_{-\infty}^{\infty}\int_{-\infty}^{\infty} g(\boldsymbol{\rho}, z)e^{\mathbf{k}_\rho \cdot \boldsymbol{\rho}}dxdy \tag{2.35}$$

$$g(\boldsymbol{\rho}, z) = \frac{1}{(2\pi)^2}\int_{-\infty}^{\infty}\int_{-\infty}^{\infty} \tilde{g}(\mathbf{k}_\rho, z)e^{-\mathbf{k}_\rho \cdot \boldsymbol{\rho}}dxdy \tag{2.36}$$

By introducing Fourier-Bessel transform pair, Eq-2.35 and Eq-2.36 can be written as

$$\tilde{g}(\mathbf{k}_\rho, z) = \frac{1}{2\pi}\int_0^{\infty} g(\rho, z)J_0(k_\rho\rho)\rho d\rho \tag{2.37}$$

$$g(\rho, z) = \frac{1}{2\pi}\int_0^{\infty} \tilde{g}(\mathbf{k}_\rho, z)J_0(k_\rho\rho)k_\rho dk_\rho \tag{2.38}$$

where

$$J_0(k_\rho\rho) = \frac{1}{2\pi}\int_0^{2\pi} e^{-\mathbf{k}_\rho \cdot \boldsymbol{\rho}}d\phi \tag{2.39}$$

$$\mathbf{k}_\rho = \hat{x}k_\rho cos\phi + \hat{y}k_\rho sin\phi \tag{2.40}$$

$$\phi = tan^{-1}\frac{y - y'}{x - x'} \tag{2.41}$$

It is useful to use a new coordinate system, which is depicted in Figure 2.1 . The relationship between the two coordinate systems can be given by

$$\begin{bmatrix} \hat{u} \\ \hat{v} \end{bmatrix} = \begin{bmatrix} cos\phi & sin\phi \\ -sin\phi & cos\phi \end{bmatrix} \begin{bmatrix} \hat{x} \\ \hat{y} \end{bmatrix} \tag{2.42}$$

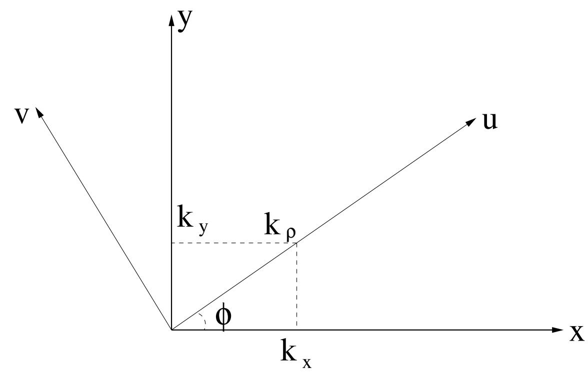

Figure 2.1: Coordinate rotation from (x,y) to (u,v)

After this transformation, two decoupled sets of transmission line equations are obtained. For TM waves,

$$\frac{d}{dz}\tilde{E}_u = -jk_z Z^{TM}\tilde{H}_v + \frac{k_\rho}{\omega\epsilon_0\epsilon_r}\tilde{J}_z - \tilde{M}_v \tag{2.43}$$

$$\frac{d}{dz}\tilde{H}_v = -jk_z Y^{TM}\tilde{E}_u + \frac{k_\rho}{\omega\mu_0\mu_r}\tilde{M}_z - \tilde{J}_u \tag{2.44}$$

$$\tilde{E}_z = -\frac{1}{j\omega\epsilon_0\epsilon_r}(jk_\rho\tilde{H}_v + \tilde{J}_z) \tag{2.45}$$

where

$$Z^{TM} = \frac{1}{Y^{TM}} = \frac{k_z}{\omega\epsilon_0\epsilon_r} \quad and \quad k_z = \sqrt{k_0^2\epsilon_r\mu_r - k_\rho^2} \tag{2.46}$$

For TE waves,

$$\frac{d}{dz}\tilde{E}_v = -jk_z Z^{TE}\tilde{H}_u + \frac{k_\rho}{\omega\epsilon_0\epsilon_r}\tilde{J}_z - \tilde{M}_u \tag{2.47}$$

$$\frac{d}{dz}\tilde{H}_u = -jk_z Y^{TE}\tilde{E}_v + \frac{k_\rho}{\omega\mu_0\mu_r}\tilde{M}_z - \tilde{J}_v \tag{2.48}$$

$$\tilde{H}_z = -\frac{1}{j\omega\mu_0\mu_r}(jk_\rho\tilde{E}_v + \tilde{M}_z) \tag{2.49}$$

where

$$Z^{TE} = \frac{1}{Y^{TE}} = \frac{\omega\mu_0\mu_r}{k_z} \quad and \quad k_z = \sqrt{k_0^2\epsilon_r\mu_r - k_\rho^2} \tag{2.50}$$

($\tilde{E}_u$, $\tilde{H}_v$) can be interpreted as voltage and current on a transverse magnetic (TM) transmission line. ($\tilde{E}_v$, $\tilde{H}_u$) can be interpreted as voltage and current on a transverse electric (TE) transmission line. ($\tilde{J}_z$,$\tilde{M}_u$,$\tilde{M}_v$) are associated with series voltage sources on the transmission line. ($\tilde{M}_z$,$\tilde{J}_u$,$\tilde{J}_v$) are associated with shunt current sources on the transmission line. As a result, (V_v^p, I_v^p) represent the voltage and current due to a series voltage source and (V_i^p, I_i^p) represent the voltage and current due to a shunt current source where p is either TM or TE. Each layer has a characteristic wave impedance,wave number, and width; hence each layer can be represented by a transmission line which has the same impedance, wave number, and height. At

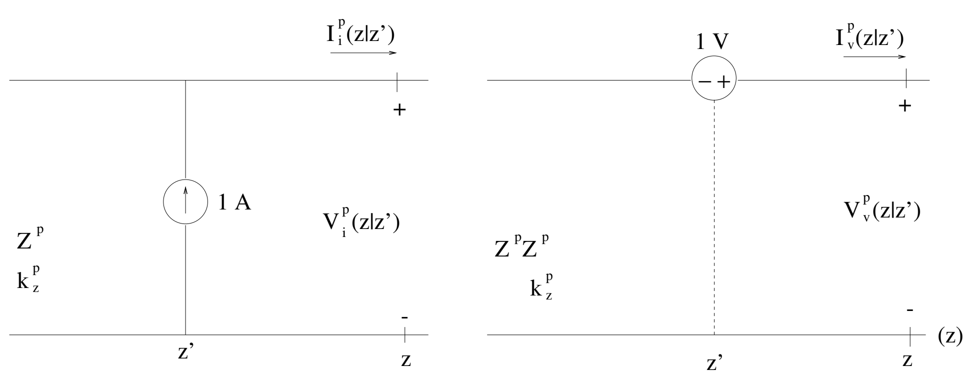

Figure 2.2: Transmission line representation with (a) shunt current source (b) series voltage source

Figure 2.2, $V_i^p(z|z')$ and $I_i^p(z|z')$ denote the voltage and current at z, respectively, due to a 1-A shunt current source at z', while $V_v^p(z|z')$ and $I_v^p(z|z')$ denote the voltage and current at z, respectively, due to a 1-V series voltage source at z'. They satisfy the following equations

$$\frac{dV_i^p}{dz} = -jk_zZ^pI_i^p \tag{2.51}$$

$$\frac{I_i^p}{dz} = -jk_z Y^p V_i^p + \delta(z - z') \tag{2.52}$$

$$\frac{V_v^p}{dz} = -jk_z Z^p I_v^p + \delta(z - z') \tag{2.53}$$

$$\frac{I_v^p}{dz} = -jk_z Y^p V_v^p \tag{2.54}$$

To find the Transmission Line Green's Functions (TLGF), the transmission line excited by a unit strength voltage or current source at z' in section m. Chew derived the generalize reflection coefficient at the interface between the two adjacent layers as follows [23]:

$$\tilde{\Gamma}_{i,i+1}^p = \frac{R_{i,i+1}^p + \tilde{\Gamma}_{i+1,i+2}^p e^{-j2k_{z,i+1}d_{i+1}}}{1 + R_{i,i+1}^p \tilde{\Gamma}_{i+1,i+2}^p e^{-j2k_{z,i+1}d_{i+1}}} \tag{2.55}$$

where $\tilde{\Gamma}_{i,i+1}^p$ represents the generalized reflection coefficient between layer i and layer i+1 and d_i is the height of the i^{th} layer. $R_{i,i+1}^p$ denotes the p type Fresnel reflection coefficient given by

$$R_{i,i+1}^{TM} = \frac{\epsilon_{r,i+1}k_{z,i} - \epsilon_{r,i}k_{z,i+1}}{\epsilon_{r,i+1}k_{z,i} + \epsilon_{r,i}k_{z,i+1}} \tag{2.56}$$

$$R_{i,i+1}^{TE} = \frac{\mu_{r,i+1}k_{z,i} - \mu_{r,i}k_{z,i+1}}{\mu_{r,i+1}k_{z,i} + \mu_{r,i}k_{z,i+1}} \tag{2.57}$$

Since all the Fresnel reflection coefficients are known, generalized reflection coefficients can be calculated recursively by using boundary conditions. When the top (bottom) layer is not PEC, then $\tilde{\Gamma}_{1,0}^p = 0$ ($\tilde{\Gamma}_{N,N+1}^p = 0$). When the top (bottom) layer is PEC, then $\tilde{\Gamma}_{2,1}^p = -1$ ($\tilde{\Gamma}_{N-1,N}^p = -1$). By using calculated generalized reflection coefficients voltage and currents at z due a source at z' can be calculated as follows. Note that, ($\tilde{G}^{p,VI}, \tilde{G}^{p,VV}, \tilde{G}^{p,II}, \tilde{G}^{p,IV}$ are equal to $(V_i^p, V_v^p, I_i^p, I_v^p)$, respectively. To remind that $(V_i^p, V_v^p, I_i^p, I_v^p)$ are actually spectral domain layered media Green's functions, $(\tilde{G}^{p,VI}, \tilde{G}^{p,VV}, \tilde{G}^{p,II}, \tilde{G}^{p,IV})$ is used in the next part and in the following chapters.

TLGF: $m = n$ case

When source and field points belong to the same layer

$$\tilde{G}_{nn}^{p,VI}(z|z') = \frac{Z_n^p}{2}\{A_0^p + A_{1,2,3,4}^p\} \tag{2.58}$$

$$\tilde{G}_{nn}^{p,II}(z|z') = \frac{1}{2}\{\pm A_0^p - A_{1,4}^p + A_{2,3}^p\} \tag{2.59}$$

$$\tilde{G}_{nn}^{p,VV}(z|z') = \frac{1}{2}\{\pm A_0^p + A_{1,3}^p - A_{2,4}^p\} \tag{2.60}$$

$$\tilde{G}_{nn}^{p,IV}(z|z') = \frac{1}{2Z_n^p}\{A_0^p - A_{1,2}^p + A_{3,4}^p\} \tag{2.61}$$

where p is either TE or TM, and the sign of the primary field term is positive when $z > z'$, otherwise it is negative. In the above, $A_{i,\cdots,k} = A_i + \cdots + A_k$

$$A_i^p = a_i^p e^{-jkz_{z,n}\alpha_i}, \quad i = 0, 1, 2, 3, 4 \tag{2.62}$$

$$Z_i^{TE} = \frac{1}{Y_i^{TE}} = \frac{\omega\mu_i}{k_{z,i}}, \quad Z_i^{TM} = \frac{1}{Y_i^{TM}} = \frac{k_{z,i}}{\omega\epsilon_i} \tag{2.63}$$

$$\begin{array}{ll} r_i = \sqrt{\rho^2 + \alpha_i^2} & \\ \alpha_0 = |z - z'| & a_0^p = 1 \\ \alpha_1 = 2z_n - (z + z') & a_1^p = \Gamma_{n,n+1}^p \\ \alpha_2 = (z + z') - 2z_{n-1} & a_2^p = \Gamma_{n,n-1}^p \\ \alpha_3 = 2d_n - \alpha_0 & a_3^p = a_1^p a_2^p \\ \alpha_4 = 2d_n + \alpha_0 & a_4^p = a_3^p \end{array} \tag{2.64}$$

Figure 2.3 shows where these primary field and reflection terms come from.

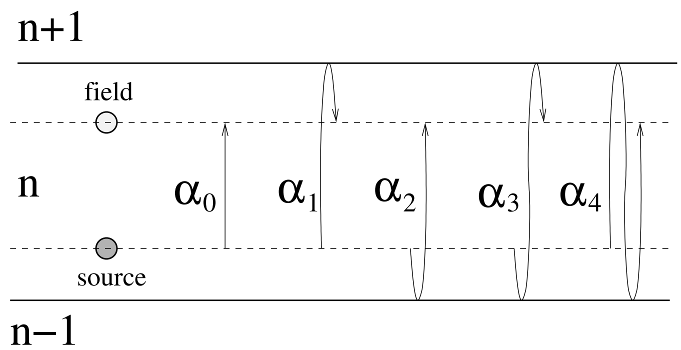

Figure 2.3: Physical demonstration of primary and quasi static field terms.

TLGF: $m > n$ **case**

When source and field points are in different layers, spectral domain Green's function can be computed by using voltage/current transfer functions as follows,

$$\begin{aligned}
\tilde{G}_{mn}^{p,VI}(z|z') &= T_{V,mm}^{p} T_{V,mn}^{p} \tilde{G}_{nn}^{p,VI}(z_n|z') \\
\tilde{G}_{mn}^{p,II}(z|z') &= T_{I,mm}^{p} T_{V,mn}^{p} \tilde{G}_{nn}^{p,VI}(z_n|z') \\
\tilde{G}_{mn}^{p,VV}(z|z') &= T_{V,mm}^{p} T_{V,mn}^{p} \tilde{G}_{nn}^{p,VV}(z_n|z') \\
\tilde{G}_{mn}^{p,IV}(z|z') &= T_{I,mm}^{p} T_{V,mn}^{p} \tilde{G}_{nn}^{p,VV}(z_n|z')
\end{aligned} \tag{2.65}$$

where $T_{P,mm}$ denotes the P type (either voltage or current) transfer function between a point z in layer-m and the lower boundary of that layer, z_{m-1}; and $T_{V,mn}$ denotes the voltage transfer function between z_{m-1} and the upper boundary of the n^{th} layer, z_n. Multiplication of these two terms with $\tilde{G}_{nn}^{p}(z_n|z')$ gives $\tilde{G}_{nn}^{p}(z|z')$.

$$\begin{aligned}
T_{V,mm}^{p} &= \frac{\left[1 + \Gamma_{m,m+1}^{p} e^{-j2k_{zm}(z_m - z)}\right] e^{-jk_{zm}(z - z_{m-1})}}{1 + \Gamma_{m,m+1}^{p} e^{-j2k_{zm}d_m}} \\
T_{I,mm}^{p} &= Y_m^p \frac{\left[1 - \Gamma_{m,m+1}^{p} e^{-j2k_{zm}(z_m - z)}\right] e^{-jk_{zm}(z - z_{m-1})}}{1 + \Gamma_{m,m+1}^{p} e^{-j2k_{zm}d_m}}
\end{aligned} \tag{2.66}$$

$$T_{V,mn}^{p} = \prod_{t=n+1}^{m-1} \frac{(1 + \Gamma_{t,t+1}^{p}) e^{-jk_{zt}d_t}}{1 + \Gamma_{t,t+1}^{p} e^{-j2k_{zt}d_t}} \tag{2.67}$$

Note that $T^p_{V,mn} = 1$ when $m = n + 1$.

TLGF: $m < n$ case

Similarly, for $m < n$ case

$$\begin{aligned}
\tilde{G}^{p,VI}_{mn}(z|z') &= T^p_{V,mm} T^p_{V,mn} \tilde{G}^{p,VI}_{nn}(z_{n-1}|z') \\
\tilde{G}^{p,II}_{mn}(z|z') &= T^p_{I,mm} T^p_{V,mn} \tilde{G}^{p,VI}_{nn}(z_{n-1}|z') \\
\tilde{G}^{p,VV}_{mn}(z|z') &= T^p_{V,mm} T^p_{V,mn} \tilde{G}^{p,VV}_{nn}(z_{n-1}|z') \\
\tilde{G}^{p,IV}_{mn}(z|z') &= T^p_{I,mm} T^p_{V,mn} \tilde{G}^{p,VV}_{nn}(z_{n-1}|z')
\end{aligned} \tag{2.68}$$

$$\begin{aligned}
T^p_{V,mm} &= \frac{\left[1 + \Gamma^p_{m,m-1} e^{-j2k_{zm}(z - z_{m-1})}\right] e^{-jk_{zm}(z_m - z)}}{1 + \Gamma^p_{m,m-1} e^{-j2k_{zm} d_m}} \\
T^p_{I,mm} &= -Y^p_m \frac{\left[1 - \Gamma^p_{m,m-1} e^{-j2k_{zm}(z - z_{m-1})}\right] e^{-jk_{zm}(z_m - z)}}{1 + \Gamma^p_{m,m-1} e^{-j2k_{zm} d_m}}
\end{aligned} \tag{2.69}$$

$$T^p_{V,mn} = \prod_{t=m+1}^{n-1} \frac{(1 + \Gamma^p_{t,t-1}) e^{-jk_{zt} d_t}}{1 + \Gamma^p_{t,t-1} e^{-j2k_{zt} d_t}} \tag{2.70}$$

Note that $T^p_{V,mn} = 1$ when $m = n + 1$.

Layered Media, Integral Equations, and Green's Functions

Consider a general multilayer media, as shown in Figure 2.4 . Layer i exists between z_{i-1} and z_i (note that $z_0 = \infty$, $z_{n-1} = 0$ and, $z_n = -\infty$) is characterized by relative permittivity ϵ_{ri}, relative permeability μ_{ri}, and conductivity σ_i. In linear media, electric and magnetic fields due to arbitrary electric and magnetic currents ($\mathbf{J}$ and $\mathbf{M}$, respectively) can be expressed as

$$\mathbf{E} = \langle \tilde{\overline{\overline{\mathbf{G}}}}^{EJ}; \mathbf{J} \rangle + \langle \tilde{\overline{\overline{\mathbf{G}}}}^{EM}; \mathbf{M} \rangle \tag{2.71}$$

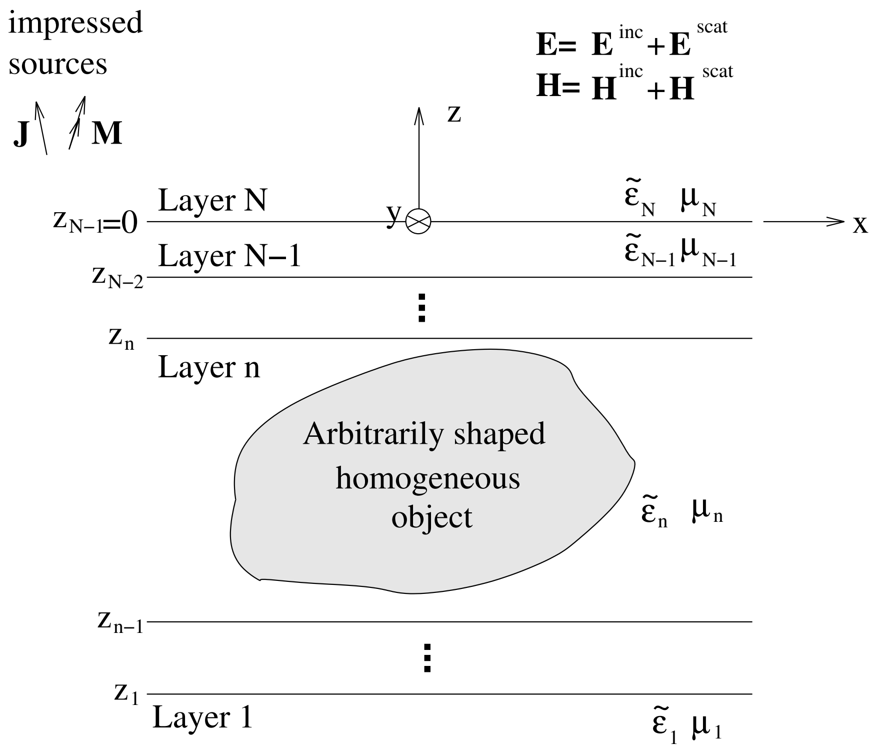

Figure 2.4: Arbitrarily shaped object in a multilayer media

$$\mathbf{H} = \langle \tilde{\bar{\mathbf{G}}}^{HJ}; \mathbf{J} \rangle + \langle \tilde{\bar{\mathbf{G}}}^{HM}; \mathbf{M} \rangle \tag{2.72}$$

where $\tilde{\bar{G}}^{PQ}(\mathbf{r}, \mathbf{r}')$ is the Dyadic Green's Function (DGF) relating P-type fields at $\mathbf{r}$ due to Q-type currents at $\mathbf{r}'$ [26]. External equivalent of this structure is depicted in Figure 2.5 . $(\mathbf{J}^i, \mathbf{M}^i)$ are impressed currents which create impressed fields $(\mathbf{E}^i, \mathbf{H}^i)$ and $(\mathbf{J}^s, \mathbf{M}^s)$ surface currents which create scattered fields $(\mathbf{E}^s, \mathbf{H}^s)$. Note that $(\mathbf{E}, \mathbf{H}) = (\mathbf{E}^i + \mathbf{E}^s, \mathbf{H}^i + \mathbf{H}^s)$. The boundary condition at S+ (exterior surface) can be written as

$$\mathbf{J}^s = \hat{n} \times (\mathbf{H}^i + \mathbf{H}^s[\mathbf{J}^s, \mathbf{M}^s])_{S+} \tag{2.73}$$

$$\mathbf{M}^s = -\hat{n} \times (\mathbf{E}^i + \mathbf{E}^s[\mathbf{J}^s, \mathbf{M}^s])_{S+} \tag{2.74}$$

where $\hat{n}$ is the outward unit vector normal to S. Note that $\langle , \rangle$ shows the integral of products of two functions, however, $\langle ; \rangle$ shows the integral of dot products of two functions. Once DGF's are derived, (3.1) and (3.2) can be used to evaluate the impressed fields first and then scattered can be expressed in terms of the unknown surface currents.

Consider no magnetic current case first, the fields can be expressed in terms of vector and scalar potentials through the equations

$$\mathbf{E} = -j\omega\mathbf{A} - \nabla\Phi \tag{2.75}$$

$$\mathbf{H} = \frac{1}{\mu_0\mu_r}\nabla \times \mathbf{A} \tag{2.76}$$

$$\Phi = -\frac{1}{j\omega\epsilon_0\epsilon_r\mu_0\mu_r}\nabla.\mathbf{A} \tag{2.77}$$

One can use the linearity of the problem and writes

$$\mathbf{H} = \langle \tilde{\bar{\bar{G}}}^{HJ}; \mathbf{J} \rangle \tag{2.78}$$

$$\mathbf{A} = \mu_0 \langle \tilde{\bar{\bar{G}}}^{A}; \mathbf{J} \rangle \tag{2.79}$$

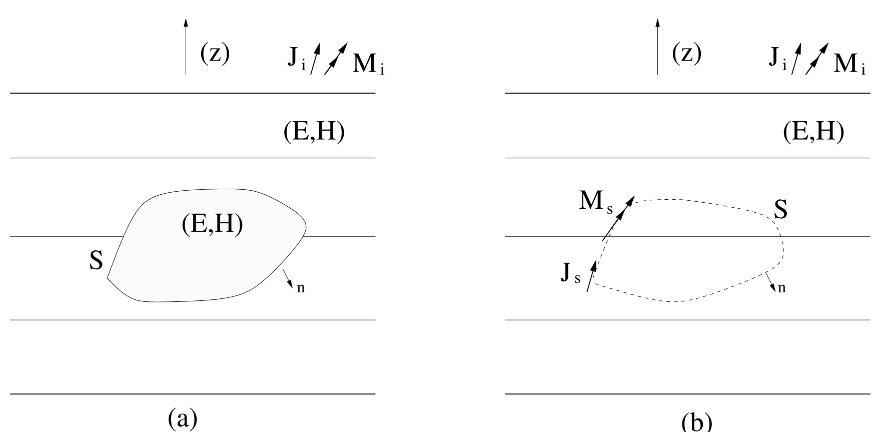

Figure 2.5: (a) Original problem. (b) Equivalent Problem

where $\tilde{\bar{\bar{G}}}^{A}$ is the vector potential DGF. Clearly, the Green's function for vector potential is associated with the magnetic field by

$$\tilde{\bar{\bar{G}}}^{HJ} = \frac{1}{\mu_r}\nabla \times \tilde{\bar{\bar{G}}}^{A} \tag{2.80}$$

There are several forms of $\tilde{\bar{\bar{G}}}^{A}$. The traditional form is given by

$$\tilde{\bar{\bar{G}}}^{A} = \begin{bmatrix} \tilde{G}_{xx} & 0 & 0 \\ 0 & \tilde{G}_{xx} & 0 \\ \tilde{G}_{zx} & \tilde{G}_{zy} & \tilde{G}_{zz} \end{bmatrix} \tag{2.81}$$

where

$$\tilde{G}^{A}_{xx} = \frac{1}{j\omega\mu_0}V_i^{TE} \tag{2.82}$$

$$\tilde{G}^{A}_{zz} = \frac{\mu_{r,n}}{j\omega\epsilon_0\epsilon_{r,m}}I_v^{TM} \tag{2.83}$$

$$\tilde{G}^{A}_{zx} = \frac{\mu_r k_x}{jk_\rho^2}(I_i^{TE} - I_i^{TM}) \tag{2.84}$$

Electric field can be calculated by using equations 2.75 and 2.79. Note that this field involves only the vector potential. Since nabla operator is a difficult task to implement in an MoM implementation, the scalar potential can be chosen specifically to transfer the nabla operator to the current [26] according to following equation

$$\frac{1}{\epsilon_r\mu_r}\nabla.\tilde{G}^{A} = -\nabla G^{\Phi} + C^{\Phi}\hat{z} \tag{2.85}$$

where G^{Φ} is scalar potential Green's functions and C^{Φ} is the correction function given by

$$\tilde{G}^{\Phi} = \frac{j\omega\epsilon_0}{k_\rho^2}(V_i^{TM} - V_i^{TE}) \tag{2.86}$$

$$\tilde{C}^{\Phi} = \frac{k_0^2 \mu_r'}{k_\rho^2}(V_v^{TM} - V_v^{TE}) \tag{2.87}$$

Then electric field can be written as

$$\mathbf{E} = -j\omega\mu_0 \langle \bar{\mathbf{G}}^{\,A}; \mathbf{J}\rangle - \frac{1}{j\omega\epsilon_0}\nabla\Big(\langle G^{\Phi}, \nabla'.\mathbf{J}\rangle + \langle C^{\Phi}\hat{z}; \mathbf{J}\rangle\Big) \tag{2.88}$$

Combination of the first and third term gives the mixed-potential representation of **E**:

$$\mathbf{E} = -j\omega\mu_0 \langle \bar{\mathbf{K}}^{\,A}; \mathbf{J}\rangle - \frac{1}{j\omega\epsilon_0}\nabla\Big(\langle G^{\Phi}, \nabla'.\mathbf{J}\rangle\Big) \tag{2.89}$$

where

$$\tilde{\bar{\bar{K}}}^{\,A} = \begin{bmatrix} \tilde{G}_{xx} & 0 & \tilde{G}_{xz} \\ 0 & \tilde{G}_{xx} & \tilde{G}_{yz} \\ \tilde{G}_{zx} & \tilde{G}_{zy} & \tilde{G}_{zz} \end{bmatrix} \tag{2.90}$$

$$\tilde{G}_{xx}^{A} = \frac{1}{j\omega\mu_0}V_i^{TE} \tag{2.91}$$

$$\tilde{G}_{zx}^{A} = \frac{\mu_r k_x}{jk_\rho^2}(I_i^{TE} - I_i^{TM}) \tag{2.92}$$

$$\tilde{G}_{yz}^{A} = \frac{\mu_r' k_y}{jk_\rho^2}(V_v^{TE} - V_v^{TM}) \tag{2.93}$$

$$\tilde{G}^{\Phi} = \frac{j\omega\epsilon_0}{k_\rho^2}(V_i^{TM} - V_i^{TE}) \tag{2.94}$$

$$\tilde{G}_{zz}^{A} = \frac{1}{j\omega\epsilon_0}\Big[\Big(\frac{\mu_{r,n}}{\epsilon_{r,m}} - \frac{\mu_{r,m}k_{z,m}^2}{\epsilon_{r,n}k_\rho^2}\Big)I_v^{TM} + \frac{k_0^2\mu_{r,n}\mu_{r,m}}{k_\rho^2}I_v^{TE}\Big] \tag{2.95}$$

Since $\tilde{G}_{zx}^{A}$ and $\tilde{G}_{zy}^{A}$ has the same kernel and there is a direct relationship between the unsymmetrical components given by Eq-2.96 and Eq-2.97, only four components have to be calculated in aggregate: $\tilde{G}^A_{xx}$,$\tilde{G}^A_{zx}$, $\tilde{G}^A_{zz}$, and $\tilde{G}^\Phi$

$$\tilde{G}^A_{xz} = -\frac{\mu_r'}{\mu_r}\tilde{G}^A_{zx} \tag{2.96}$$

$$\tilde{G}^A_{yz} = -\frac{\mu_r'}{\mu_r}\tilde{G}^A_{zy} \tag{2.97}$$

The transformation from spectral domain to spatial domain can be written as

$$G(\rho, z|z') = \frac{1}{2\pi}\int_0^\infty \tilde{G}(\mathbf{k}_\rho, z|z')J_0 k_\rho \rho k_\rho dk_\rho \tag{2.98}$$

The fast and accurate evaluation of this Sommerfeld type integral is described in the next chapter.

Chapter 3

Singularity Subtraction for Evaluation of Green's Functions for Multilayer Media

In order to solve layered-medium problems in application areas such as geophysical prospecting and remote sensing [28, 29, 82], interconnect simulations, microstrip antennas and monolithic microwave integrated circuits [83]-[85], vector and scalar Green's functions must be computed. Straightforward numerical integration methods are not efficient for these integrals because of the slowly decaying and highly oscillating behavior of the Sommerfeld integrands [1]-[4], [46]. Extensive research has been done to accelerate this process through methods such as the fast Hankel transform (FHT) approach [5]-[6], the window function approach [7], the steepest descent path (SDP) approach [82], and the discrete complex image method (DCIM) [8]-[21], [28], and [47].

It is shown that the efficiency of the numerical integration can be improved by deforming the integration path in the complex k_ρ plane and using the Hankel functions pair instead of Bessel functions [46]. Deforming the integration path according to Cauchy's theorem avoids the singularities; it has been used in most recent methods. The usage of the Hankel functions pair helps for the faster convergence, especially when the source and field points are close to each other. In terms of the computation time, the numerical integration method is the slowest one with respect to other methods. In the SDP approach, the integration path is also deformed [82]. In addition to path deformation, leading order approximation has been used to increase the speed of integration. The difficulty related to the implementation of this method is the determination of the steepest path for the media having many layers.

The window function approach utilizes a window function as a convolution kernel to the time domain Green's function [7]. Similar to the effect of low pass filtering used in signal processing, convolution with a window function in the spatial domain accelerates the decay of integrand in the Sommerfeld integration.

The DCIM, which can be described as the approximation of the spectral domain Green's function in terms of complex exponentials whose Hankel transform can be obtained analytically, is one of the most popular methods developed to approximate the Green's functions efficiently. It has been improved by the help of several researchers in the last two decades. In the very beginning, the primary and quasi-static field terms are subtracted from the integrand and the remaining integrand is approximated with the complex images via Sommerfeld identity. However, since the method was constructed on the Sommerfeld identity, it is not applicable to problems having source and field points in different layers because of the $k_{z,n}$ dependence in the Sommerfeld identity. Furthermore, the method was valid only for the symmetrical (i.e., diagonal) components of the dyadic Green's functions. Hojjat *et al.* extended the method to the non-symmetrical (i.e., off-diagonal) components by using a semi-infinite integral of Bessel functions [17]. More recently, Ge and Eselle [21] proposed a new closed-form formulation based on a class of semi-infinite integrals of Bessel functions and applied the generalized pencil of function (GPOF) method to approximate the remaining integrand with another set of complex images (having only k_ρ dependence), making the method valid for any kind of source-field point combination. Aksun has shown that by using a multilevel DCIM it is possible to obtain very accurate results for printed structures without subtraction of the primary and quasi-static field terms [47]. However, the lack of surface-wave extraction often results in errors in the far-field region because the surface waves behave in the manner of cylindrical waves and thus it is inappropriate to approximate them by spherical waves. In other words, DCIM without any extraction might work efficiently for printed-circuit structures but cannot handle the problems such as aerospace applications where the object size is comparable to or much larger than the wavelength. Ling *et al*. proposed a new method to achieve the surface-wave extraction by evaluating a contour integral recursively in the complex k_ρ plane [18]. Moreover, some researchers developed new formulations to increase the efficiency of the method for the Method of Moment (MOM) implementation. For example, Liu *et al*. [20] reformulated the Formulation-C Green's functions for multilayered media to extract z-dependent part when the source and observation points are in different layers.

All of these methods have some advantages and disadvantages. In this work, a new extraction procedure is presented which can be incorporated in these methods to improve the efficiency. This procedure can be described as the improved version of the extraction procedure implemented in DCIM, and is valid for any kind of source-field point combination. The subtraction procedure is implemented appropriately for each individual term of the integrand and the contribution of the subtracted terms is calculated analytically. However, for the sake of robustness, instead of approximating the remaining integral with complex images, the remaining integral is calculated numerically by using Gaussian quadratures. The results of this method have been validated by comparison with many examples in literature, and the high efficiency has been verified.

3.1 The Theory

Consider a general multilayer medium consisting of N layers separated by $N-1$ planar interfaces parallel to the xy plane, as shown in Figure 3.1. Layer i exists between z_i and z_{i-1} and is characterized by relative permittivity $\epsilon_{r,i}$ and relative permeability $\mu_{r,i}$. In a linear medium, electric and magnetic fields due to arbitrary

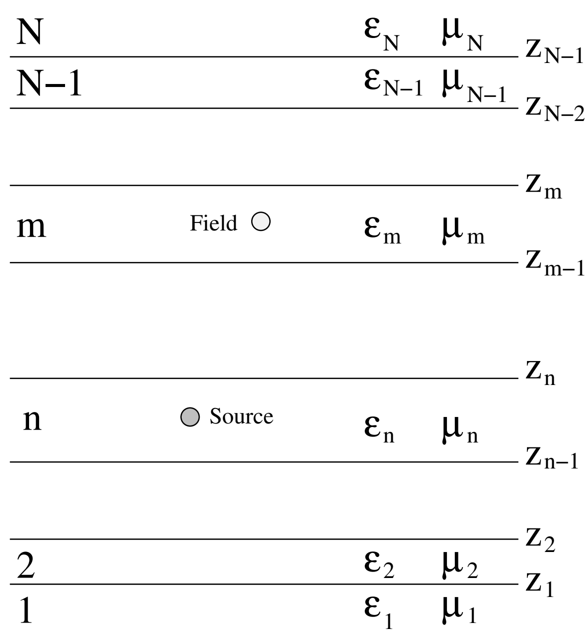

Figure 3.1: (a) An N-layer medium with source and field points in layer n and layer m,respectively.

electric and magnetic currents (**J** and **M**, respectively) can be expressed as

$$\mathbf{E} = \langle \tilde{\bar{\bar{\mathbf{G}}}}^{EJ}; \mathbf{J} \rangle + \langle \tilde{\bar{\bar{\mathbf{G}}}}^{EM}; \mathbf{M} \rangle \tag{3.1}$$

$$\mathbf{H} = \langle \tilde{\bar{\bar{\mathbf{G}}}}^{HJ}; \mathbf{J} \rangle + \langle \tilde{\bar{\bar{\mathbf{G}}}}^{HM}; \mathbf{M} \rangle \tag{3.2}$$

where $\tilde{\bar{\bar{\mathbf{G}}}}^{PQ}(\mathbf{r}, \mathbf{r}')$ is the Dyadic Green's Function (DGF) relating P-type fields at $\mathbf{r}$ due to Q-type currents at $\mathbf{r}'$ [26]. Once the DGF's have been calculated for the layered medium, the electric and magnetic fields at any point can be obtained with the superposition principle. For the details of the derivation procedure of the multilayer media Green's functions, the reader may refer to [26] and [23]. Basically, by transforming the problem from spatial domain to spectral domain, each layer can be represented by a uniform transmission line having the same physical properties; hence the electric and magnetic fields can be interpreted as voltage and current, respectively, on a transmission line. By using this transmission line analogy, Green's functions in spectral domain, called transmission line Green's functions (TLGF), can be calculated easily. The spatial domain DGF is the inverse transformation from spectral domain to spatial domain and is known as a Sommerfeld Integral given by

$$G_{\zeta,\eta}(\rho, z|z') = \frac{1}{2\pi} \int_0^{\infty} \tilde{G}_{\zeta,\eta}(\mathbf{k}_\rho, z|z') J_\nu(k_\rho \rho) k_\rho^{\nu+1} dk_\rho \tag{3.3}$$

where $\nu = 0, 1$, J_ν is ν^{th} order Bessel function, $\rho = \sqrt{(x - x')^2 + (y - y')^2}$, $G_{\zeta,\eta}(\rho, z|z')$ is the spatial domain Green's Function relating the field at (x, y, z) in layer m due to a point source at (x', y', z') in layer n; $\tilde{G}_{\zeta,\eta}(\mathbf{k}_\rho, z|z')$ is the spectral domain counterpart.

3.2 Spatial Domain Green's Functions and Subtraction Procedure

There are several types of dyadic Green's functions [26]. In this work, the traditional form of dyadic Green's functions for vector potential $\mathbf{A}$ is chosen as an example and the formulation of the spectral domain Green's functions is presented in the Appendix. The spatial domain Green's functions are obtained by taking the Sommerfeld integral given in (3.3). In general, we have two typical integrals for the spatial domain Green's functions associated with the vector and scalar potentials

$$I_1 = \int_0^\infty \xi_1(k_\rho, k_{z,m}) \frac{e^{-jk_{z,n}\alpha}}{k_{z,n}} J_0(k_\rho \rho) k_\rho dk_\rho \tag{3.4}$$

for symmetrical components of the Green's function, and

$$I_2 = \int_0^\infty \xi_2(k_\rho, k_{z,m}) e^{-jk_{z,n}\alpha} J_1(k_\rho \rho) dk_\rho \tag{3.5}$$

for non-symmetrical components of the Green's function, where $\xi_i(k_\rho, k_{z,m})$ contains the generalized reflection coefficients and some constants depending on the type of the Green's functions involved. Below we describe the singularity subtraction for different scenarios depending on where the relative locations of the source and field points.

3.2.1 Source and Field Points in the Same Layer

When the source and field points are located in the same layer ($n = m$), the Green's function can be separated into the primary field and reflected field. The singularity subtraction is only needed for the reflected field as the primary field terms are obtained directly from the expressions for a homogeneous medium. In this case, for the primary field term, $\xi_i(k_\rho, k_{z,m})$ is constant and equal to $1/2\pi$; and as in DCIM, the contribution of this component can be calculated analytically by using Sommerfeld identity as follows

$$\int_0^\infty \frac{e^{-jk_{z,n}\alpha}}{k_{z,n}} J_0(k_\rho \rho) k_\rho dk_\rho = \frac{e^{-jk_n r}}{r} \tag{3.6}$$

where $r = \sqrt{\rho^2 + \alpha^2}$ and α is some distance.

For the reflection terms, $\xi_i(k_\rho, k_{z,m})$ is not a constant, but its asymptotic expression can be obtained by

$$\lim_{k_\rho \to \infty} \begin{cases} k_{z,i} = k_{z,j} = -jk_\rho \\ \Gamma_{i,j} = R_{i,j} \\ \xi_i(k_\rho, k_{z,m}) = \tilde{\xi}_i \end{cases} \tag{3.7}$$

where $\tilde{\xi}_i$ is a finite constant, $\Gamma_{i,j}$ and $R_{i,j}$ are the generalized and Fresnel reflection coefficients, respectively, between layer-i and layer-j.

Using (4.6) in (3.4) yields

$$\begin{aligned} I_1 &= \int_0^\infty \left[\xi_1(k_\rho, k_{z,m})e^{-jk_{z,n}\alpha} - \tilde{\xi}_1 e^{-jk_{z,n}\alpha} + \tilde{\xi}_1 e^{-jk_{z,n}\alpha}\right] \frac{k_\rho}{k_{z,n}} J_0(k_\rho \rho) dk_\rho \\ &= \int_0^\infty \left[\xi_1(k_\rho, k_{z,m})e^{-jk_{z,n}\alpha} - \tilde{\xi}_1 e^{-jk_{z,n}\alpha}\right] \frac{k_\rho}{k_{z,n}} J_0(k_\rho \rho) dk_\rho + \frac{\tilde{\xi}_1 e^{-jk_n r}}{r} \end{aligned} \tag{3.8}$$

where $\tilde{\xi}_1 = \lim_{k_\rho \to \infty} \xi_1(k_\rho, k_{z,m})$. This subtraction process is valid for the symmetrical components of the dyadic Green's function, but not directly applicable to the non-symmetrical components because of lack of closed-form expression for the subtracted part. However, for the non-symmetrical components, the following equation can be used [16, 86]

$$\int_0^\infty e^{-k_\rho \alpha} J_1(k_\rho \rho) dk_\rho = \frac{1}{\rho}\left(1 - \frac{\alpha}{\sqrt{\alpha^2 + \rho^2}}\right) \tag{3.9}$$

Then, (3.5) can be written as

$$\begin{aligned} I_2 &= \int_0^\infty \left[\xi_2(k_\rho, k_{z,m})e^{-jk_{z,n}\alpha} - \tilde{\xi}_2 e^{-k_\rho \alpha} + \tilde{\xi}_2 e^{-k_\rho \alpha}\right] J_1(k_\rho \rho) dk_\rho \\ &= \int_0^\infty \left[\xi_2(k_\rho, k_{z,m})e^{-jk_{z,n}\alpha} - \tilde{\xi}_2 e^{-k_\rho \alpha}\right] J_1(k_\rho \rho) dk_\rho + \frac{\tilde{\xi}_2}{\rho}\left(1 - \frac{\alpha}{\sqrt{\alpha^2 + \rho^2}}\right) \end{aligned} \tag{3.10}$$

where $\tilde{\xi}_2 = \lim_{k_\rho \to \infty} \xi_2(k_\rho)$.

As a result, for the case where the source and field points are in the same layer (i.e., $m = n$), the subtraction procedure for the dyadic Green's function can be formulated as follows

$$\begin{aligned}
G_{xx}^{A} &= \frac{1}{2\pi}\int_{0}^{\infty}\left[\tilde{G}_{xx}^{A} - \tilde{G}_{xx,subt}^{A}\right] J_0(k_\rho \rho) k_\rho \; dk_\rho + G_{xx,add}^{A} \\
G_{zz}^{A} &= \frac{1}{2\pi}\int_{0}^{\infty}\left[\tilde{G}_{zz}^{A} - \tilde{G}_{zz,subt}^{A}\right] J_0(k_\rho \rho) k_\rho \; dk_\rho + G_{zz,add}^{A} \\
G_{zx}^{A} &= \frac{1}{2\pi}\int_{0}^{\infty}\left[\tilde{G}_{zx}^{A} - \tilde{G}_{zx,subt}^{A}\right] J_1(k_\rho \rho) \; dk_\rho + G_{zx,add}^{A}
\end{aligned} \tag{3.11}$$

where the subtracted integrands are

$$\begin{aligned}
\tilde{G}_{xx,subt}^{A} &= \frac{1}{2jk_{z,n}} \tilde{A}_{0,1,2,3,4}^{TE,1} \\
\tilde{G}_{zz,subt}^{A} &= \frac{1}{2jk_{z,n}} \left(\tilde{A}_{0,3,4}^{TM,1} - \tilde{A}_{1,2}^{TM,1}\right) \\
\tilde{G}_{zx,subt}^{A} &= \frac{1}{2j} \left(\tilde{A}_{1,4}^{TE,2} - \tilde{A}_{2,3}^{TE,2} - \tilde{A}_{1,4}^{TM,2} + \tilde{A}_{2,3}^{TM,2}\right)
\end{aligned} \tag{3.12}$$

while the closed-form expressions for the subtracted terms are

$$\begin{aligned}
G_{xx,add}^{A} =& \bar{A}_{0,1,2,3,4}^{TE,1} \\
G_{zz,add}^{A} =& \bar{A}_{0,3,4}^{TM,1} - \bar{A}_{1,2}^{TM,1} \\
G_{zx,add}^{A} =& \bar{A}_{1,4}^{TE,2} - \bar{A}_{2,3}^{TE,2} - \bar{A}_{1,4}^{TM,2} + \bar{A}_{2,3}^{TM,2}
\end{aligned} \tag{3.13}$$

In the above,

$$\tilde{A}_{i}^{p,1} = \tilde{a}_{i}^{p} e^{-jk_{z,n}\alpha_i}, \quad \tilde{A}_{i}^{p,2} = \tilde{a}_{i}^{p} e^{-k_\rho \alpha_i} \tag{3.14}$$

$$\bar{A}_{i}^{p,1} = \tilde{a}_{i}^{p} \frac{e^{-jk_{z,n}r_i}}{4\pi r_i}, \quad \bar{A}_{i}^{p,2} = \frac{\tilde{a}_{i}^{p}}{4\pi\rho}\left(1 - \frac{\alpha_i}{r_i}\right) \tag{3.15}$$

where $A_{i,\cdots,k} = A_i + \cdots + A_k$, and

$$\tilde{a}_{0}^{p} = 1, \quad \tilde{a}_{1}^{p} = R_{n,n+1}^{p}, \quad \tilde{a}_{2}^{p} = R_{n,n-1}^{p}, \quad \tilde{a}_{3}^{p} = \tilde{a}_{4}^{p} = \tilde{a}_{1}^{p}\tilde{a}_{2}^{p} \tag{3.16}$$

$$r_i = \sqrt{\rho^2 + \alpha_i^2} \tag{3.17}$$

The above subtraction procedure is very crucial when α_i is small as the exponential term $e^{-jk_{z,n}\alpha_i}$ approaches one and does not decay with k_ρ when $\alpha_i \to 0$. In other words, when the source and field points are close to each other and close to an interface between two adjacent layers, the integrand decays slowly without subtraction. This situation is shown in Figure 3.2 as case 1.

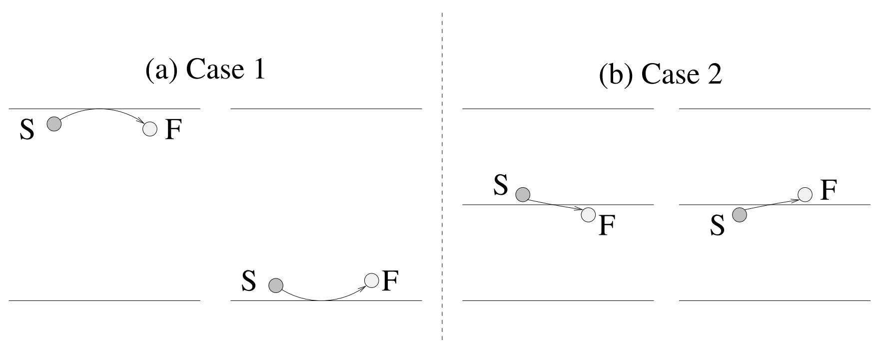

Figure 3.2: (a) Case 1: Source and field points are in the same layer, and (b) Case 2: Source and field points are in adjacent layers.

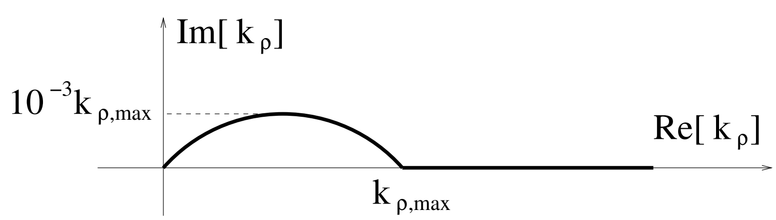

Figure 3.3: Integration path in the complex k_ρ plane, $k_{\rho,max} = 1.2\max\{k_1, k_2, \cdots, k_N\}$.

To demonstrate the importance of this subtraction, a 6-layer geometry used in [85] is chosen as an example (Figure 3.4). The integrand is calculated for some k_ρ values along the integration path illustrated in Figure 4.1 [46]. The frequency is 30 GHz, $\rho = \lambda_0$ and $z = z' = 0.3 + \delta z$ mm where $\delta z = \lambda_0/1000$. Figure 3.5 depicts the integrand of the corresponding integral, i.e., $\tilde{G}^A_{zx} J_1(k_\rho \rho)$, the zx component of the dyadic Green's function for vector potential $\mathbf{A}$, with and without subtraction. As can be seen from the figure, after subtraction the integrand becomes a rapidly decreasing function of k_ρ. In fact, the decaying is exponential, and is six orders of magnitude smaller than the original integrand at $k_\rho = 10^6$.

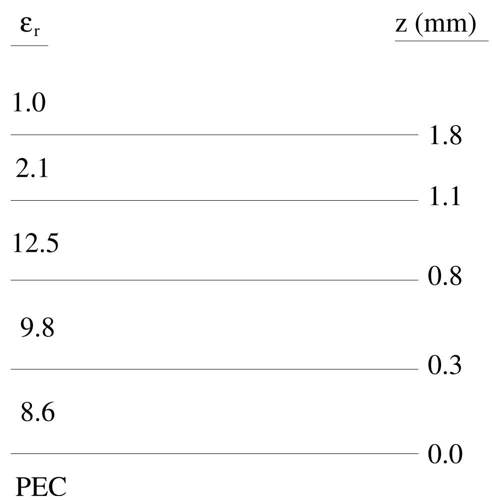

Figure 3.4: A 6 layer medium.

The efficiency of this subtraction procedure becomes even more obvious as the source and field points get closer to the interface. Figure 3.6 shows the number of segments used in the adaptive integration with and without subtraction for the same geometry with different δz values. Clearly, after the subtraction, the integrand decays rapidly no matter how small δz is, and the Green's functions are computed accurately by using only a few hundred integration segments or less.

To summarize the procedure for $m = n$ case, the primary field term's contributions are calculated via the closed-form expressions for a homogeneous medium (also obtainable by using Sommerfeld identity), and for each reflection term the above subtraction procedure must be performed individually. Once the subtraction has been

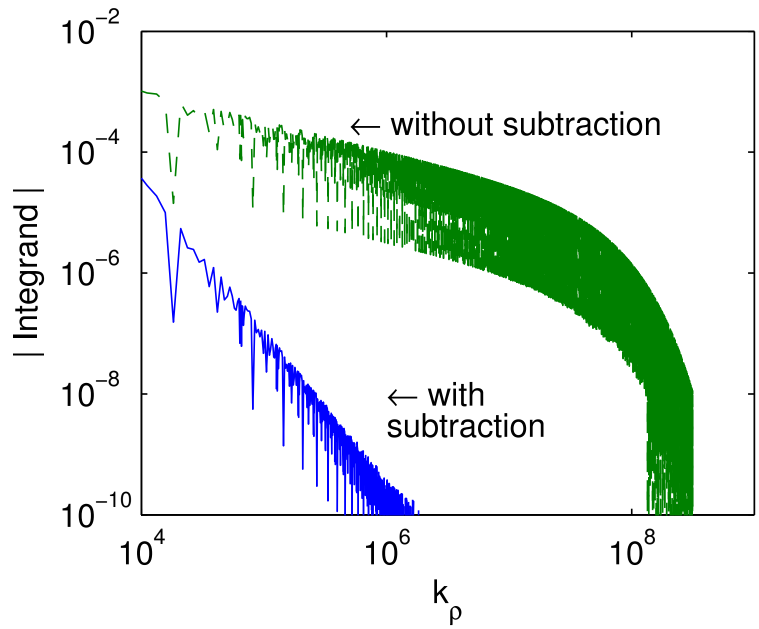

Figure 3.5: The magnitude of the integrand $\tilde{G}^A_{zx} J_1(k_\rho \rho)$ sampled along the integration path for $z = z' = 0.3 + \lambda_0/1000$ mm ($m = n$ case) for the 6-layer medium depicted in Fig. 3.4.

done, the integration of the remaining integrand can be calculated adaptively. In other words, the integral can be calculated segment by segment on the Sommerfeld integration path until the desired accuracy is obtained.

3.2.2 Source and Field Points in Different Layers

The above subtraction procedure is very efficient but is restricted to $m = n$ case. When source and field points are close to each other but belonging to two different adjacent layers, shown in Case 2 in Figure 3.2, some of the exponential terms' magnitudes are close to one, making the integrand an extremely slowly decaying function of k_ρ. Because of the different $k_{z,i}$ dependence, Sommerfeld identity does not apply here. However, singularity subtraction is still possible by using the only common

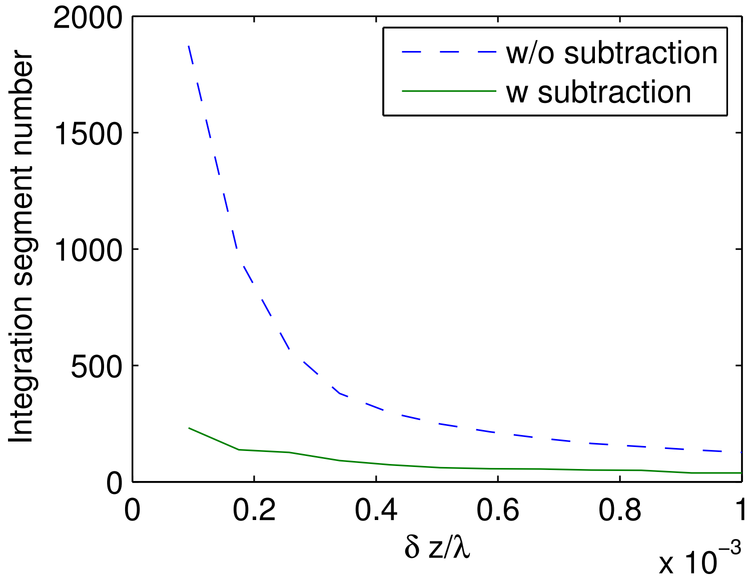

Figure 3.6: The effect of subtraction on the convergence: The number of the segments used in adaptive integration with and without subtraction, $m = n$ case

parameter: k_ρ. It is known that [21, 86]

$$\int_0^\infty e^{-k_\rho \alpha} J_0(k_\rho \rho) dk_\rho = \frac{1}{\sqrt{\alpha^2 + \rho^2}} \tag{3.18}$$

Similar to the subtraction procedure described for non-symmetrical components, using (4.6) and (A.11) in (3.4) yields

$$\begin{aligned} I_1 = \int_0^\infty & \left[\xi_1(k_\rho, k_{z,m}) e^{-jk_{z,n}\alpha} \frac{k_\rho}{k_{z,n}} \right. \\ & \left. -j\tilde{\xi}_1 e^{-k_\rho \alpha} + j\tilde{\xi}_1 e^{-k_\rho \alpha} \right] J_0(k_\rho \rho) dk_\rho \\ = \int_0^\infty & \left[\xi_1(k_\rho, k_{z,m}) e^{-jk_{z,n}\alpha} \frac{k_\rho}{k_{z,n}} - j\tilde{\xi}_1 e^{-k_\rho \alpha} \right] J_0(k_\rho \rho) dk_\rho \\ & + \frac{j\tilde{\xi}_1}{\sqrt{\alpha^2 + \rho^2}} \end{aligned} \tag{3.19}$$

Since (A.12) and (A.11) have k_ρ dependence only, (3.10) and (3.19) are valid for any source-field layer combination. Note that for $m = n$ case, there are 5 terms associated with TLGF and this number becomes 10 when $m = n \pm 1$. The subtraction procedure must be performed appropriately for all those 10 terms. For $m = n - 1$ case, the subtracted integrands in (3.11) can be written as

$$\begin{aligned}
\tilde{G}^{A}_{xx,subt} &= \sum_{v=1}^{2} \frac{1}{2k_\rho} \tilde{B}^{TE,1}_{v0,1,2,3,4} \\
\tilde{G}^{A}_{zz,subt} &= \sum_{v=1}^{2} \frac{1}{2k_\rho} \tilde{B}^{TM,1}_{v0,3,4} - \tilde{B}^{TM,1}_{v1,2} \\
\tilde{G}^{A}_{zx,subt} &= \sum_{v=1}^{2} \frac{1}{2j} \left(\tilde{B}^{TE,2}_{v1,4} - \tilde{B}^{TE,2}_{v0,2,3} - \tilde{B}^{TM,2}_{v1,4} + \tilde{B}^{TM,2}_{v0,2,3} \right)
\end{aligned} \tag{3.20}$$

The closed-form expressions for the subtracted integrals are

$$\begin{aligned}
G^{A}_{xx,add} =& \frac{\mu_n}{\mu_m} \sum_{v=1}^{2} \bar{B}^{TE,1}_{v0,1,2,3,4} \\
G^{A}_{zz,add} =& \frac{\epsilon_m}{\epsilon_n} \sum_{v=1}^{2} \bar{B}^{TM,1}_{v0,3,4} - \bar{B}^{TM,1}_{v1,2} \\
G^{A}_{zx,add} =& \sum_{v=1}^{2} \bar{B}^{TE,2}_{v1,4} - \bar{B}^{TE,2}_{v0,2,3} - \bar{B}^{TM,2}_{v1,4} + \bar{B}^{TM,2}_{v0,2,3}
\end{aligned} \tag{3.21}$$

In the above,

$$\begin{aligned}
\tilde{B}^{p,1}_{1i} &= \tilde{a}^{p}_{i} e^{-jk_\rho(\beta_1+\alpha_i)} \qquad \tilde{B}^{p,2}_{1i} = \tilde{a}^{p}_{i} e^{-k_\rho(\beta_1+\alpha_i)} \\
\tilde{B}^{p,1}_{2i} &= R_{m,m-1} \tilde{a}^{p}_{i} e^{-jk_\rho(\beta_2+\alpha_i)} \\
\tilde{B}^{p,2}_{2i} &= R_{m,m-1} \tilde{a}^{p}_{i} e^{-k_\rho(\beta_2+\alpha_i)}
\end{aligned} \tag{3.22}$$

$$\begin{aligned}
\bar{B}^{p,1}_{1i} &= \tfrac{\tilde{a}^{p}_{i}}{4\pi r_{1i}} & \bar{B}^{p,2}_{1i} &= \tfrac{\tilde{a}^{p}_{i}}{4\pi\rho} \left(1 - \tfrac{\alpha_i+\beta_1}{r_{1i}}\right) \\
\bar{B}^{p,1}_{2i} &= R_{m,m-1} \tfrac{\tilde{a}^{p}_{i}}{4\pi r_{2i}} & \bar{B}^{p,2}_{2i} &= R_{m,m-1} \tfrac{\tilde{a}^{p}_{i}}{4\pi\rho} \left(1 - \tfrac{\alpha_i+\beta_2}{r_{2i}}\right)
\end{aligned} \tag{3.23}$$

where $r_{vi} = \sqrt{\rho^2 + (\beta_v + \alpha_i)^2}$ and $v = 1, 2$

$$\beta_1 = z_m - z, \qquad \beta_2 = z_m + z - 2z_{m-1} \tag{3.24}$$

and $R_{m,m-1}$ is the Fresnel reflection coefficient and is independent of k_ρ.

This described procedure is as successful as $m = n$ case. Figure 3.7 depicts the integrand $\tilde{G}^A_{zx} J_1(k_\rho \rho)$ with and without subtraction when $z = (0.3 - \delta z)$ mm and $z' = (0.3 + \delta z)$ mm where, $z = 0.3$ mm is the layer interface and $\delta z = \lambda_0/1000$. Again, after subtraction the integrand becomes a rapidly decreasing function of k_ρ. Similar to the experiment done for $m = n$ case (Figure 3.6), the efficiency of this

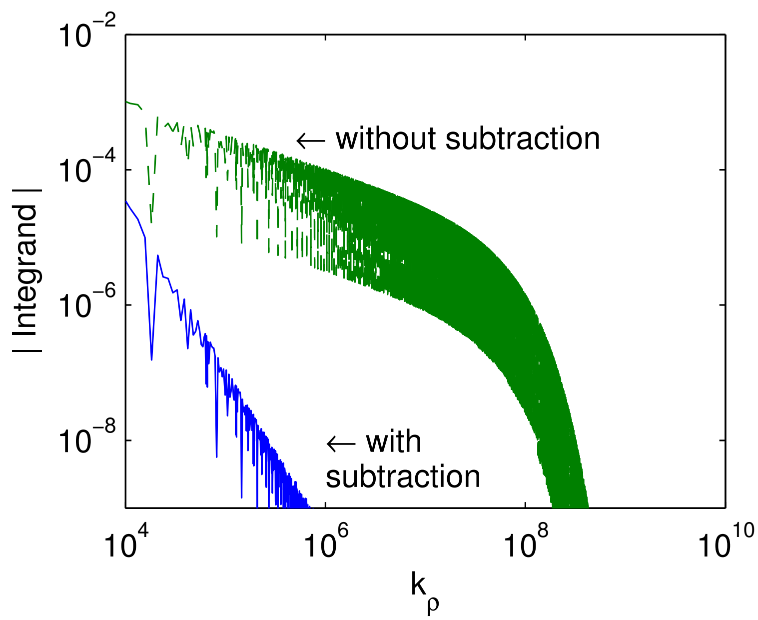

Figure 3.7: The magnitude of the integrand $\tilde{G}^A_{\mathbf{zx}} J_1(k_\rho \rho)$ sampled along the integration path for $z = (0.3 - \lambda_0/1000)$ mm, $z' = (0.3 + \lambda_0/1000)$ ($m = n - 1$ case) for the 6-layer medium depicted in Fig. 3.4

subtraction procedure becomes even more significant as the source and field points get closer to the interface. Figure 3.8 shows the number of the segments used in the adaptive integration with and without subtraction for the same geometry with different δz values for $\rho = \lambda_0$, $z' = 0.3 + \delta z$ mm and $z = 0.3 - \delta z$ mm where $z = 0.3$ mm is an interface of two adjacent layers shown in Figure 3.4. Again, after the subtraction, the integrand decays rapidly (in fact, exponential) no matter how small δz is.

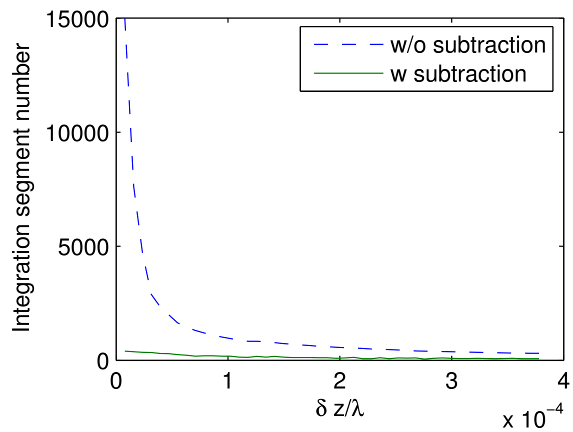

Figure 3.8: The effect of subtraction on the convergence: The number of the segments used in adaptive integration with and without subtraction, $m = n - 1$ case.

In the above, the formulation is presented for $m = n$ and $m = n - 1$ cases. The formulation for $m = n + 1$ case is very similar to $m = n - 1$ case. This procedure can be extended to $|m - n| > 1$ case easily by using asymptotic relations given by (4.6) with the help of semi-infinite integral equations (A.12) and (A.11). For example, for $m > n$ case, the terms to be subtracted can be formulated as

$$\begin{aligned}
\tilde{G}^{p,VI}_{mn,subt}(z|z') &= \tilde{T}^{p}_{V,mm}\tilde{T}^{p}_{V,mn}\tilde{G}^{p,VI}_{nn,subt}(z_n|z') \\
\tilde{G}^{p,II}_{mn,subt}(z|z') &= \tilde{T}^{p}_{I,mm}\tilde{T}^{p}_{V,mn}\tilde{G}^{p,VI}_{nn,subt}(z_n|z') \\
\tilde{G}^{p,VV}_{mn,subt}(z|z') &= \tilde{T}^{p}_{V,mm}\tilde{T}^{p}_{V,mn}\tilde{G}^{p,VV}_{nn,subt}(z_n|z') \\
\tilde{G}^{p,IV}_{mn,subt}(z|z') &= \tilde{T}^{p}_{I,mm}\tilde{T}^{p}_{V,mn}\tilde{G}^{p,VV}_{nn,subt}(z_n|z')
\end{aligned} \tag{3.25}$$

where

$$\tilde{G}^{p,VI}_{nn,subt}(z|z') = \frac{\tilde{Z}^p_n}{2}\{\tilde{A}^{p,v}_0 + \tilde{A}^{p,v}_{1,2,3,4}\} \tag{3.26}$$

$$\tilde{G}^{p,II}_{nn,subt}(z|z') = \frac{1}{2}\{\pm\tilde{A}^{p,v}_0 - \tilde{A}^{p,v}_{1,4} + \tilde{A}^{p,v}_{2,3}\} \tag{3.27}$$

$$\tilde{G}^{p,VV}_{nn,subt}(z|z') = \frac{1}{2}\{\pm\tilde{A}^{p,v}_0 + \tilde{A}^{p,v}_{1,3} - \tilde{A}^{p,v}_{2,4}\} \tag{3.28}$$

$$\tilde{G}^{p,IV}_{nn,subt}(z|z') = \frac{1}{2\tilde{Z}^p_n}\{\tilde{A}^{p,v}_0 - \tilde{A}^{p,v}_{1,2} + \tilde{A}^{p,v}_{3,4}\} \tag{3.29}$$

$\tilde{A}^{p,v}_i$ is either $\tilde{A}^{p,1}_i$ or $\tilde{A}^{p,2}_i$ given by (3.14) depending on the order of the Bessel function and

$$\begin{aligned}\tilde{T}^p_{V,mm} &= (1 + R^p_{m,m+1}e^{-j2k_\rho(z_m - z)})e^{-jk_\rho(z - z_{m-1})}\\ \tilde{T}^p_{I,mm} &= \tilde{Y}^p_m(1 - R^p_{m,m+1}e^{-j2k_\rho(z_m - z)})e^{-jk_\rho(z - z_{m-1})}\end{aligned} \tag{3.30}$$

$$\tilde{T}^p_{V,mn} = \prod_{t=n+1}^{m-1}(1 + R^p_{t,t+1})e^{-k_\rho d_t} \tag{3.31}$$

$$\tilde{Z}^{TE}_i = \frac{1}{\tilde{Y}^{TE}_i} = \frac{\omega\mu_i}{k_\rho}, \quad \tilde{Z}^{TM}_i = \frac{1}{\tilde{Y}^{TM}_i} = \frac{k_\rho}{\omega\epsilon_i} \tag{3.32}$$

The number of the terms needs to be subtracted is given by $5 \times 2^{|m-n|}$. The effect of the subtraction may not be obvious for the problems having many thick layers and when the source and field points are very far away from each other. Under such circumstances, the integrand decays rapidly by itself and the subtraction procedure does not further improve the convergence; however, it does not degrade the convergence either, since the subtracted terms also decay exponentially. For example, Figure 3.9 shows the integrand $\tilde{G}^A_{zx}J_1(k_\rho\rho)$ with and without subtraction for $\rho = \lambda_0$, $z' = 0.2$

mm and $z = 0.9$ mm ($m = n+2$) for the 6-layer medium. Obviously, the subtraction procedure does not affect the decaying speed in a negative way. Usually, if the total thickness of the layers between the source and field points exceeds 10% of the local wavelength, such singularity subtraction does not have to be utilized. However, for the problems with thin layers, for very large values of ρ, the integral does not converge rapidly without singularity subtraction. As an example of the case $m = n + 2$, we study a 7-layer medium obtained by adding a very thin layer (thickness=$\lambda_0/10$, $\epsilon_r = 24$) between $z = 0.3$ mm and $z = 0.301$ mm on the 6-layer medium in the previous example. Figure 3.10 shows the integrand $\tilde{G}^A_{zx} J_1(k_\rho \rho)$ with and without subtraction when $\rho = 100\lambda_0$, $z' = (0.3 - \lambda_0/1000)$ mm and $z' = (0.301 + \lambda_0/1000)$ mm, for this 7-layer medium. Clearly, after subtraction, the integrand decays much more rapidly, making the method useful also for $|m - n| > 1$ when layers are thin.

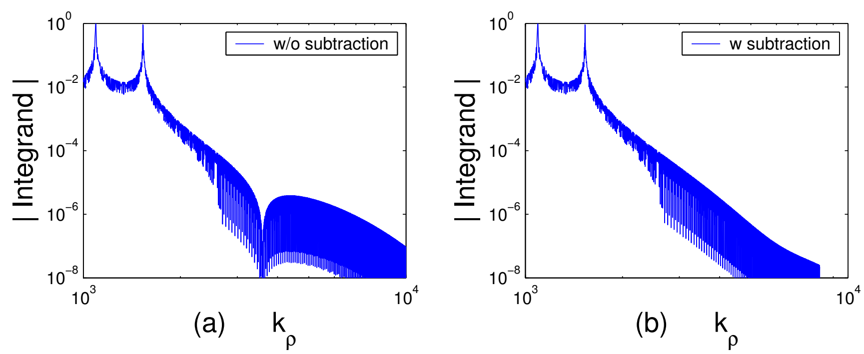

Figure 3.9: The magnitude of the integrand $\tilde{G}^A_{zx} J_1(k_\rho \rho)$ sampled along the integration path for $z = 0.9$ mm, $z' = 0.2$ ($m = n + 2$ case) for the 6-layer medium depicted in Fig. 3.4.

The above singularity subtraction is presented for $\mathbf{G}^{AJ}$. However, this method is valid for all types of Green's functions such as $\mathbf{G}^{EJ}$,$\mathbf{G}^{HJ}$, traditional or alternative form $\mathbf{G}^A$ and 2D Green's functions [52]. The asymptotic formulas required for these

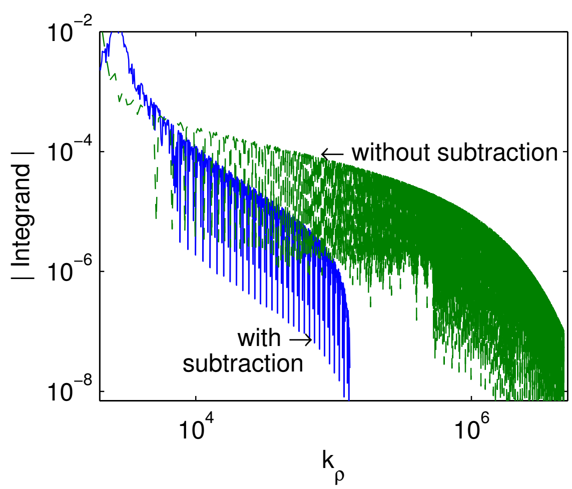

Figure 3.10: The magnitude of the integrand $\tilde{G}_{zx}^{A} J_1(k_\rho \rho)$ sampled along the integration path for the 7-layer medium.

Green's functions are (A.12), (A.11) and following formulas and their derivatives

$$\int_0^\infty e^{-k_\rho \gamma} k_\rho J_0(k_\rho \rho) dk_\rho = \frac{\gamma}{(\gamma^2 + \rho^2)^{3/2}} \tag{3.33}$$

$$\int_0^\infty e^{-k_\rho \gamma} k_\rho^2 J_0(k_\rho \rho) dk_\rho = \frac{2\gamma^2 - \rho^2}{(\gamma^2 + \rho^2)^{5/2}} \tag{3.34}$$

$$\int_0^\infty e^{-k_\rho \gamma} k_\rho J_1(k_\rho \rho) dk_\rho = \frac{\rho}{(\gamma^2 + \rho^2)^{3/2}} \tag{3.35}$$

$$\int_0^\infty e^{-k_\rho \gamma} k_\rho^2 J_1(k_\rho \rho) dk_\rho = \frac{3\gamma\rho}{(\gamma^2 + \rho^2)^{5/2}} \tag{3.36}$$

3.3 Numerical Results

The described technique has been implemented for several types of spatial domain Green's function both in 2D and 3D. Since 2D results have been presented in [52], here only 3D examples are presented. The first two examples are chosen to demonstrate the accuracy of the method. The first example, Figure 3.11, shows the magnitude of the traditional form Green's functions associated with the magnetic vector potential. The geometry is the 6 layer medium shown in Figure 3.4. The frequency is 30 GHz and $z = z' = 0.4$ mm. Figure 3.12 is obtained by using the same geometry parameters, except that $z = 1.4$ mm.

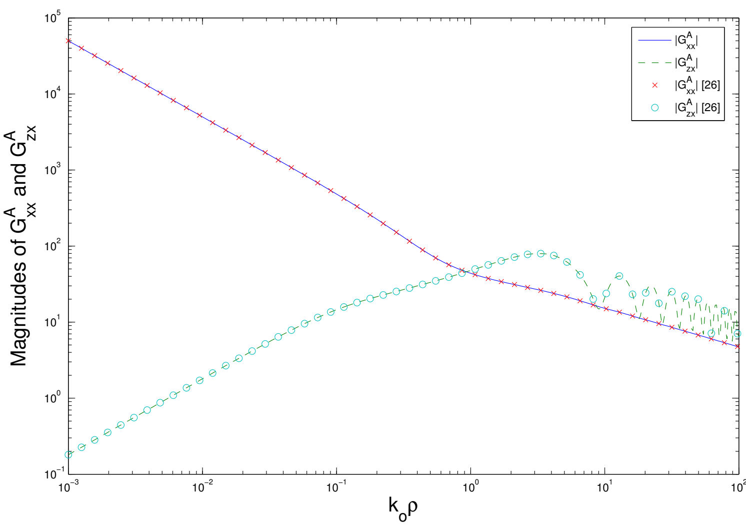

Figure 3.11: The magnitudes of G^A_{xx} and G^A_{zx} compared with [18] for the 6 layer medium with $z = z' = 0.4$ mm.

Figure 3.14 shows the magnitude of the different type of Green's functions ($\mathbf{G}^{EJ}$) for a 4-layer medium shown in Figure 3.13. The wavelength in the free space is 633 nm and the source is located at $z' = 750$ nm. The field points are chosen from $z = -1000$ nm to $z = 1000$ nm.

In all figures, the results are calculated using with described procedure and compared with those obtained by direct numerical integration along the Sommerfeld integration path (SIP). In all cases the excellent agreement has been verified.

Another issue is the efficiency. To demonstrate the efficiency of the method, a

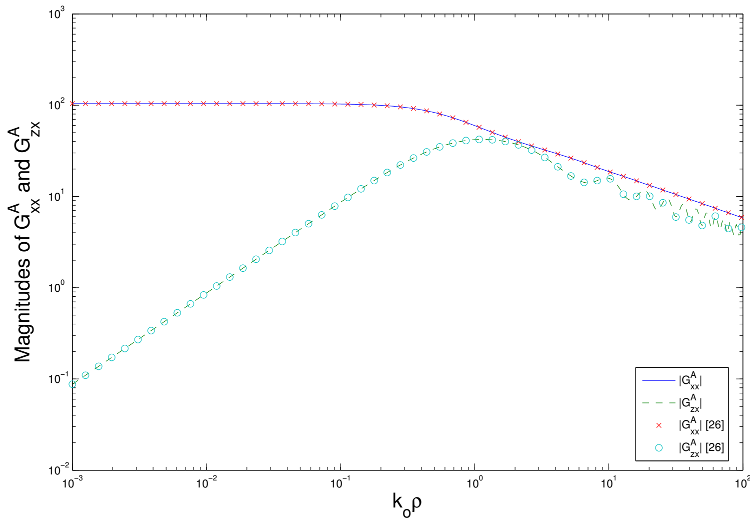

Figure 3.12: The magnitudes of G^A_{xx} and G^A_{zx} compared with [18] for the 6 layer medium with $z' = 0.4$ mm, $z = 1.4$ mm.

5-layer geometry is chosen as Figure 3.15. The Green's function $\mathbf{G^A}$ is calculated with and without subtraction for different z, z' and ρ values. Both programs were compiled with Fortran77 UNIX compiler on a Dell Optiplex GX260 desktop with Intel P4 2.4 GHz processor and 1024M RAM. The last two columns of Table I show the CPU times with and without subtraction for the same accuracy level (10^{-9}). With the classical numerical integration, depending on z, z' and ρ, the execution

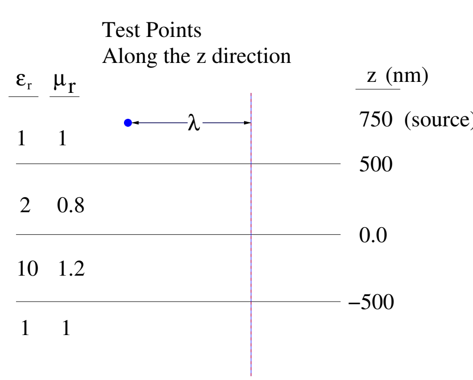

Figure 3.13: A 4-layer medium.

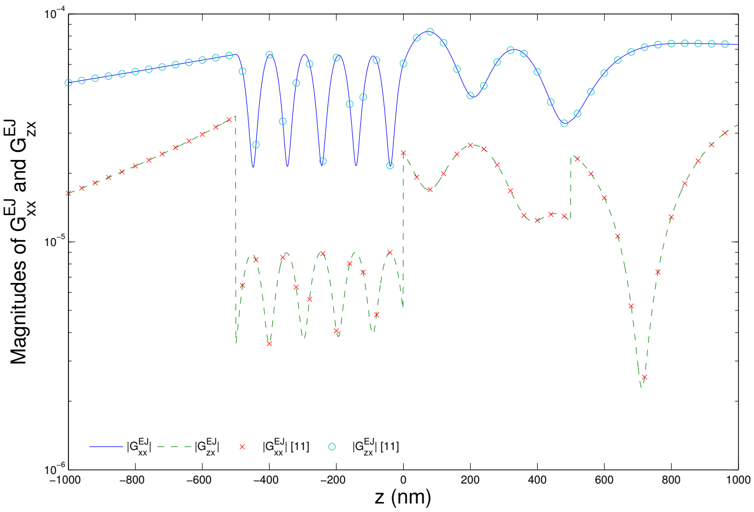

Figure 3.14: The magnitudes of G_{xx}^{EJ} and G_{zx}^{EJ} compared with [46] for the 4 layer medium with $z' = 750$ nm, $z = [-1000, 1000]$ nm.

time changes dramatically. For large ρ values, it may take more than 2 minutes just for one sample, whereas it takes less a second with this described method even for $\rho = 10\lambda$.

Figure 3.15: A 5-layer medium.

The efficient computation of the dyadic Green's functions for layered media is an important part of fast forward and inverse scattering problems for 3-D targets buried in such environments (see for examples, [49, 87]).

Table 3.1: Experiment Results

z' (mm)	z (mm)	ρ/λ_0	CPU (s) W/O	CPU (s) W/
0.7622	0.7618	0.1	1.63	0.31
0.7622	0.7618	1	147	0.98
0.508	0.507	1	49	0.47
0.508	0.507	10	131	0.98

3.4 Conclusion

In this work, a numerically efficient way of evaluating the multilayer medium Green's functions has been presented. The singularity terms that cause slow convergence have been subtracted analytically. No matter how close the source and field points are to an interface or no matter how large ρ is, the described subtraction procedure makes the integrand a rapidly decreasing function of k_ρ. Since the remaining integral is calculated numerically as accurate as desired, the complete procedure is error controllable and a robust method. The accuracy and the efficiency of the method have been verified via representative numerical examples.

Chapter 4

A 2D Spectral Integral Method (SIM) for Layered Media

For a homogeneous scatter with an arbitrary geometry in a layered medium, the surface integral equation method is a powerful tool to calculate the scattered electromagnetic fields. The classical methods for solving such integral equations are the method of moments (MOM) [27]-[30], fast multipole method (FMM) [31]-[35], and adaptive integral method [36]-[41].

Recently, Liu *et. al*. [42] proposed a spectral integral method as an alternative way of solving the surface integral equation efficiently for a homogeneous scatter in free space and for periodic structures. This algorithm is related to the fast method originally developed by Bojarski [43] for sound-soft circular cylinders, and extended by Schuster [44] to multi-layer circular cylinders, and by Hu [45] to sound-soft or sound-hard smooth cylinders. Liu *et. al*. [42] further extended the SIM to arbitrarily-shaped smooth dielectric cylinders, and to periodic structures such as photonic crystals. The idea behind this method is the use of fast Fourier transform (FFT) algorithm and the subtraction of singularities in Green's functions to achieve a spectral accuracy in the integral. Here, we extend this method to arbitrarily-shaped smooth dielectric and PEC cylinders embedded in layered media by using 2D layered-medium Green's functions. To avoid the discontinuous behaviors of the fields and Green's function (i.e., the functions or their derivatives being discontinuous) across the layer interfaces in the problems where the scatterer resides in several layers, in this chapter the object must locate completely within one single layer in the multilayered medium. Next chapter investigates objects traversing several layers.

The outline of this chapter is as follows: first the brief formulation of 2D layered-medium Green's function is presented. Next, the implementation of SIM for layered media is described. Finally, the accuracy and the efficiency of the method are verified with several numerical examples.

4.1 2D Green's Functions

Consider a general multilayer medium consisting of N layers separated by $N-1$ interfaces parallel to the x axis. Layer i ($i = 1, \cdots, N$) exists between $y = y_i$ and y_{i-1} ($y_0 \to -\infty$ and $y_N \to \infty$) and is characterized by relative complex permittivity $\tilde{\epsilon}_{r,i}$ and relative permeability $\mu_{r,i}$; the wavenumber inside the layer is given by $k_i = \omega\sqrt{\tilde{\epsilon}_i \mu_i}$. The time dependency of e^{jwt} is implied.

In the absence of a scatterer, the electric or magnetic field at (x, y) due to a unit line source at (x', y') can be calculated by using layered-medium Green's functions. The formulation of the Green's function for 2D is very similar to the 3D case, and the reader may refer to [27], [23], [26], and [25] for the details of derivation. Essentially, by transforming the problem from the spatial domain to spectral domain, each layer can be represented by a uniform transmission line having the same physical properties; hence the electric and magnetic fields can be interpreted as voltage and current, respectively, on a transmission line. By using this transmission line analogy, Green's functions in the spectral domain, called transmission line Green's functions (TLGF), can be derived easily. The spatial domain Green's function is the inverse transformation from spectral domain to spatial domain and is known as a Sommerfeld integral given by

$$G^p(x-x',y|y') = \frac{1}{2\pi}\int_{-\infty}^{\infty} \tilde{\tilde{G}}^p_{mn}(k_x,y|y')e^{jk_x(x-x')}dk_x$$
$$= \frac{1}{\pi}\int_{0}^{\infty} \tilde{\tilde{G}}^p_{mn}(k_x,y|y')\cos k_x(x-x')dk_x \tag{4.1}$$

where $G^p(x-x',y|y')$ is the p type (p is either TE_z or TM_z) Green's function relating the field at (x,y) in layer m due to a unit source at (x',y') in layer n; $\tilde{\tilde{G}}^p_{mn}$ is its spectral domain counterpart (TLGF) which has a closed form expression depending on the locations of the source and field points:

$$\tilde{\tilde{G}}^p = \frac{\tilde{G}^p_{mn}}{j\omega\varsigma^p_m} \tag{4.2}$$

the subscripts mn refer to the source layer (n) and field layer (m), and ς^p_n is either μ_m or $\tilde{\epsilon}_m$ for TE_z or TM_z cases, respectively.

4.1.1 $m = n$

When the source and field points belong to the same layer,

$$\tilde{G}^p_{nn}(y|y') = \frac{\omega\varsigma^p_n}{2k_{y,n}}A^p_{0,1,2,3,4} \tag{4.3}$$

In the above, $A_{i,\cdots,k} = A_i + \cdots + A_k$,

$$A^p_i = a^p_i e^{-jk_{y,n}\alpha_i}, \quad i = 0,1,2,3,4 \tag{4.4}$$

$$\begin{array}{ll} \alpha_0 = |y-y'| & a^p_0 = 1 \\ \alpha_1 = 2y_n - (y+y') & a^p_1 = \Gamma^p_{n,n+1} \\ \alpha_2 = (y+y') - 2y_{n-1} & a^p_2 = \Gamma^p_{n,n-1} \\ \alpha_3 = 2d_n + (y-y') & a^p_3 = a^p_1 a^p_2 \\ \alpha_4 = 2d_n - (y-y') & a^p_4 = a^p_3 \end{array} \tag{4.5}$$

where $\Gamma^p_{i,j}$ is the p type generalized reflection coefficient which can be calculated recursively as explained in Chapter 1. Note that,

$$\lim_{k_x \to \infty} \left\{ \begin{array}{c} k_{y,i} = k_{y,j} = -jk_x \\ \Gamma^p_{i,j} = R^p_{i,j} \end{array} \right. \tag{4.6}$$

This means that A^p_i terms may converge to a number which is different than 0. The subtraction of integrand's asymptote increases its decaying speed. $\tilde{G}^{p,(0)}_{nn}(y|y')$, the asymptote of $\tilde{G}^p_{nn}(y|y')$, can be given as

$$\tilde{G}^{p,(0)}_{nn}(y|y') = \frac{\omega \varsigma^p_n}{2k_{y,n}} B^p_{0,1,2,3,4} \tag{4.7}$$

$$B^p_i = b^p_i e^{-jk_{y,n}\alpha_i}, \quad i = 0, 1, 2, 3, 4 \tag{4.8}$$

$$b^p_0 = 1, \quad b^p_1 = R^p_{n,n+1}, \quad b^p_2 = R^p_{n,n-1}, \quad b^p_3 = b^p_4 = b^p_1 b^p_2 \tag{4.9}$$

The subtracted terms' contribution in spatial domain can be written as

$$G^{p,(0)}(x - x', y|y') = \frac{1}{4j} \sum_{i=0}^{4} b^p_i H^{(2)}_0 (k_m \rho_i) \tag{4.10}$$

where $\rho_i = \sqrt{(x - x')^2 + \alpha_i^2}$.

4.1.2 $m \neq n$

When the source and field points are in different layers and $m > n$, the spectral domain Green's function can be computed by using voltage/current transfer functions as follows,

$$\tilde{G}^p_{mn}(y|y') = T^p_{mm} T^p_{mn} \tilde{G}^p_{nn}(y_n|y') \tag{4.11}$$

where T^p_{mm} denotes the p type transfer function between a point y in layer m and the lower boundary of that layer, y_{m-1}; and T_{mn} denotes the p type transfer function between y_{m-1} and the upper boundary of the n^{th} layer, y_n:

$$T^p_{mm} = \frac{\left[1 + \Gamma^p_{m,m+1} e^{-j2k_{y,m}(y_m - y)}\right] e^{-jk_{y,m}(y - y_{m-1})}}{1 + \Gamma^p_{m,m+1} e^{-j2k_{y,m} d_m}} \tag{4.12}$$

$$T^p_{mn} = \prod_{t=n+1}^{m-1} \frac{(1 + \Gamma^p_{t,t+1}) e^{-jk_{y,t} d_t}}{1 + \Gamma^p_{t,t+1} e^{-j2k_{y,t} d_t}} \tag{4.13}$$

Multiplication of these two terms with $\tilde{G}^p_{nn}(y_n|y')$ gives $\tilde{G}^p_{mn}(y|y')$. Note that $T^p_{mn} = 1$ when $m = n + 1$.

The formulation for $m < n$ is very similar to the case where $m > n$ and can be obtained easily by using symmetry.

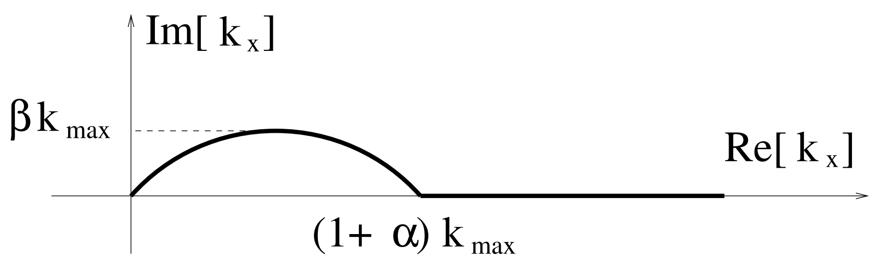

Figure 4.1: The Sommerfeld integration path in the complex k_x plane, where $k_{max} = \max\{Re(k_1, k_2, \cdots, k_N)\}$, $\alpha > 0$, and $\beta > 0$. In the numerical examples, $\alpha = 0.2$ and $\beta = 0.001$ are used.

For the 3D case, it is shown that the efficiency of the numerical integration can be improved by deforming the integration path in the complex k_ρ plane [23, 46]. As shown in Fig. 4.1, the maximum displacement from the real axis is set to βk_{max}. Since the first integration segment requires little computation time compared to the whole Sommerfeld integral, we have not optimized the choice of β. In the following numerical examples, we chose $\alpha = 0.2$ and $\beta = 0.001$. The reader is referred to [47] for more discussions on the integration path. By using the deformed Sommerfeld integration path depicted in Figure 4.1, the spatial domain Green's functions can be calculated numerically. In this work, to speed up the numerical evaluation of the Sommerfeld integrals, we subtract the direct field term between the source and field points and the so-called "quasi-dynamic" term in the reflection (i.e., the term at the limit when $k_x \to \infty$) when $m = n$, and the "quasi-dynamic" transmission term when $m \neq n$. (One 3D version of such subtraction is described in Chapter 3.) We found that this special subtraction procedure is especially effective for source and field points in two adjacent layers and very close to the layer interface.

4.2 Spectral Integration Method for Layered Media

For the TM$_z$ case, the 2D Helmholtz equation for the scalar field E_z is

$$\nabla^2 E_z + k_\gamma^2 E_z = -f_\gamma \tag{4.14}$$

where subscript γ indicates the region outside ($\gamma = l$) or inside ($\gamma = d$) the object, f_γ is the source excitation, $k_l = \omega\sqrt{\mu_l \tilde{\epsilon}_l}$ for the l^{th} layer ($l = 1, 2, \cdots, N$) and $k_d = \omega\sqrt{\mu_d \tilde{\epsilon}_d}$ for the dielectric object. Since the formulation and all the examples are presented here for the TM$_z$ case, the superscript p is omitted for the rest of the formulation. In this work, we assume the scatterer is entirely within one layer.

For a smooth dielectric object embedded in a layered medium, the boundary integral equations on the surface of the scatterer D are

$$E_z^{inc}(\mathbf{r}) + \oint_D \left[\frac{\partial E_z(\mathbf{r}')}{\partial n'} G_l(\mathbf{r}, \mathbf{r}') - E_z(\mathbf{r}') \frac{\partial G_l(\mathbf{r}, \mathbf{r}')}{\partial n'} \right] ds' = \frac{E_z(\mathbf{r})}{2} \tag{4.15}$$

$$-\oint_D \left[\frac{\partial E_z(\mathbf{r}')}{\partial n'}G_d(\mathbf{r},\mathbf{r}') - E_z(\mathbf{r}')\frac{\partial G_d(\mathbf{r},\mathbf{r}')}{\partial n'}\right] ds' = \frac{E_z(\mathbf{r})}{2} \tag{4.16}$$

for $\mathbf{r} \in D$, where f_d is assumed zero, E_z^{inc} is the incident wave from outside the object (i.e., $f_l \neq 0$, $f_d = 0$). $\hat{\mathbf{n}}$ is the outward unit normal, and $R = |\mathbf{r} - \mathbf{r}'|$. Inside the dielectric object, the homogeneous space Green's function and its normal derivative can be written as

$$G_d(\mathbf{r},\mathbf{r}') = -\frac{j}{4}H_0^{(2)}(k_d R) \tag{4.17}$$

$$\frac{\partial G_d(\mathbf{r},\mathbf{r}')}{\partial n'} = \frac{jk_d}{4}H_1^{(2)}(k_d R)\frac{\mathbf{R}\cdot\hat{\mathbf{n}}'}{R} \tag{4.18}$$

Outside the object, the layered-medium Green's function is required and it can be written as a summation of two separate terms: the primary field term (G_{pri}) and the remaining reflection term (G_{refl}):

$$G(x - x', y|y') = G_{pri} + G_{refl} \tag{4.19}$$

Then its normal derivative can be written as

$$\begin{aligned}\frac{\partial G_l}{\partial n'} &= \frac{\partial G_{pri}}{\partial n'} + \frac{\partial G_{refl}}{\partial n'} = \frac{\partial G_{pri}}{\partial n'} + \hat{\mathbf{n}}'\cdot\nabla G_{refl} \\ &= \frac{\partial G_{pri}}{\partial n'} + \frac{\partial G_{refl}}{\partial x'}\frac{\partial y'}{\partial \theta'} - \frac{\partial G_{refl}}{\partial y'}\frac{\partial x'}{\partial \theta'}\end{aligned} \tag{4.20}$$

where $(x'(\theta'), y'(\theta'))$ describe the surface of the scatterer. The primary field term G_{pri} and its derivative are the same as (4.18) except k_d should be replaced by k_l, and

$$\begin{aligned}\frac{\partial G_{refl}}{\partial x'} &= \frac{1}{\pi}\int_0^\infty \left[\tilde{G}_{refl} - \tilde{G}_{refl}^{(0)}\right] k_x \sin k_x(x - x')dk_x \\ &\quad + g_1^{(0)}(x - x', y, y')\end{aligned} \tag{4.21}$$

$$\frac{\partial G_{refl}}{\partial y'} = \frac{1}{\pi}\int_0^{\infty}\left[\frac{\partial \tilde{G}_{refl}}{\partial y'} - \frac{\partial \tilde{G}^{(0)}_{refl}}{\partial y'}\right]\cos k_x(x-x')dk_x + g_2^{(0)}(x-x', y, y') \tag{4.22}$$

where

$$\frac{\partial \tilde{G}_{refl}}{\partial x'} = \frac{j\omega\varsigma_l}{2}A_{1,2,3,4} \tag{4.23}$$

$$\frac{\partial \tilde{G}^{(0)}_{refl}}{\partial x'} = \frac{j\omega\varsigma_l}{2}B_{1,2,3,4} \tag{4.24}$$

$$\frac{\partial \tilde{G}_{refl}}{\partial y'} = \frac{j\omega\varsigma_l}{2}\{A_{1,3} - A_{2,4}\} \tag{4.25}$$

$$\frac{\partial \tilde{G}^{(0)}_{refl}}{\partial y'} = \frac{j\omega\varsigma_l}{2}\{B_{1,3} - B_{2,4}\} \tag{4.26}$$

$$g_1^{(0)}(x-x', y, y') = \frac{k_l}{4j}\sum_{i=1}^{4} b_i H_1^{(2)}(k_l\rho_i)\frac{(x-x')}{\rho_i} \tag{4.27}$$

$$g_2^{(0)}(x-x', y, y') = \frac{k_l}{4j}\sum_{i=1}^{4} b_i H_1^{(2)}(k_l\rho_i)\frac{(-\alpha_i)^i}{\rho_i} \tag{4.28}$$

are the so-called "quasi-dynamic" terms. With such subtractions, the Sommerfeld integral can be calculated more rapidly.

With the above Green's functions and their derivatives, equation (5.2) can be rewritten in terms of a parameter θ along the boundary:

$$E_z^{inc}(\theta) = \frac{E_z(\theta)}{2} - \int_0^{2\pi}\frac{\partial E_z(\theta')}{\partial n'}G_l(\theta,\theta')\left|\frac{d\mathbf{r}'}{d\theta'}\right|d\theta' + \int_0^{2\pi}E_z(\theta')\frac{\partial G_l(\theta,\theta')}{\partial n'}\left|\frac{d\mathbf{r}'}{d\theta'}\right|d\theta' \tag{4.29}$$

where $|\frac{d\mathbf{r}'}{d\theta'}| = \frac{ds'}{d\theta'} = \sqrt{[r'(\theta')]^2 + (\frac{dr'}{d\theta'})^2}$. Since the scatterer has a smooth surface, and $E_z(\theta)$ and $\partial E_z(\theta)/\partial n$ are smooth and periodic functions of θ on the closed boundary, they can be approximated by truncated Fourier series as

$$E_z^N(\theta) = \sum_{n=-\frac{N}{2}}^{\frac{N}{2}-1} \phi_n e^{-jn\theta} \tag{4.30}$$

$$\frac{\partial E_z^N(\theta)}{\partial n'} = \sum_{n=-\frac{N}{2}}^{\frac{N}{2}-1} \psi_n e^{-jn\theta} \tag{4.31}$$

where ϕ_n and ψ_n are Fourier coefficients. By substituting them into (4.29), we have

$$\begin{aligned} E_z^{inc}(\theta) =& \frac{1}{2} \sum_{n=-\frac{N}{2}}^{\frac{N}{2}-1} \phi_n e^{-jn\theta} - \sum_{n=-\frac{N}{2}}^{\frac{N}{2}-1} \psi_n \int_0^{2\pi} e^{-jn\theta'} G_l(\theta, \theta') \left| \frac{d\mathbf{r}'}{d\theta'} \right| d\theta' \\ &+ \sum_{n=-\frac{N}{2}}^{\frac{N}{2}-1} \phi_n \int_0^{2\pi} e^{-jn\theta'} \frac{G_l(\theta, \theta')}{\partial n'} \left| \frac{d\mathbf{r}'}{d\theta'} \right| d\theta' \end{aligned} \tag{4.32}$$

The above integrals are simply Fourier transforms and can be calculated using FFT. However, to be able to obtain spectral accuracy, singular terms in the Green's functions and the non-smooth terms in their derivatives must be handled carefully. As described in [45], two infinitely smooth functions are defined as follows

$$\hat{G}_\gamma(\theta, \theta') \equiv G_\gamma(\theta, \theta') + \frac{1}{2\pi} \ln \left| 2 \sin\left(\frac{\theta - \theta'}{2}\right) \right| J_0(k_\gamma R) \tag{4.33}$$

$$\hat{H}_\gamma(\theta, \theta') \equiv \frac{\partial G_\gamma(\theta, \theta')}{\partial n'} - \frac{k_\gamma}{2\pi} \ln \left| 2 \sin\left(\frac{\theta - \theta'}{2}\right) \right| J_1(k_\gamma R) \frac{\mathbf{R} \cdot \mathbf{n}}{R} \tag{4.34}$$

In [42], the free space Green's functions are used. For our problem here, the layered-medium Green's functions must be used. Since the singularity occurs only for the primary field term when source and field points are in the same layer, one can add the layered-medium Green's function (without the primary field term) and its derivative directly to the smooth terms, $\hat{G}_\gamma(\theta,\theta')$ and $\hat{H}_\gamma(\theta,\theta')$, respectively. Uniformly sampled N points along the surface of the scatterer are used as testing points as in the point-matching (collocation) in MOM. After testing, (4.32) becomes

$$
\begin{aligned}
E_z^{inc}(\theta) = & \sum_{n=-\frac{N}{2}}^{\frac{N}{2}-1} \phi_n \left(2\pi h_{l,mn} - k_0 v_{l,mn}\right) \\
& - \sum_{n=-\frac{N}{2}}^{\frac{N}{2}-1} \psi_n \left(2\pi g_{l,mn} - u_{l,mn}\right) + \frac{1}{2} \sum_{n=-\frac{N}{2}}^{\frac{N}{2}-1} \phi_n E_{mn}
\end{aligned}
\tag{4.35}
$$

where $E_{mn} = e^{in\theta_m}$; m is the index of a testing point on the boundary, and n the index of the Fourier series; $g_{l,mn}$ and $h_{l,mn}$ are Fourier transforms of the smooth part of the $G_l(\theta_m,\theta'_n)$ and $H_l(\theta_m,\theta'_n) = \partial G_l(\theta_m,\theta'_n)/\partial n'$, respectively; $u_{l,mn}$ and $v_{l,mn}$ are Fourier transforms of the non-smooth term of the $G_l(\theta_m,\theta'_n)$ and $H_l(\theta_m,\theta'_n)$, respectively, and can be calculated via convolution of the logarithmic functions with the Bessel functions [45], [42].

Equation (5.3) can be discretized in the same way. Then (4.35) and the equation corresponding to (5.3) can be written in a matrix form as follows,

$$\mathbf{C}^l\mathbf{\Phi} + \mathbf{D}^l\mathbf{\Psi} = \mathbf{F} \tag{4.36}$$

$$\mathbf{C}^d\mathbf{\Phi} + \mathbf{D}^d\mathbf{\Psi} = 0 \tag{4.37}$$

where

$$C^\gamma_{mn} = 2\pi h^\gamma_{mn} + k_\gamma v^\gamma_{mn} + (-1)^j E_{mn}/2$$

$$D^\gamma_{mn} = -2\pi g^\gamma_{mn} + u^\gamma_{mn}$$

$$\mathbf{F} = \mathbf{E}\Psi^{inc}$$

and $\mathbf{\Phi}$ and $\mathbf{\Psi}$ are vectors of ϕ_n and ψ_n, respectively.

By using (4.36) and (4.37), ϕ_n and ψ_n can be obtained easily. Then the scalar field (E_z) and its normal derivative ($\partial E_z/\partial n'$) on the boundary of the scatter can be computed by using ϕ_n and ψ_n via FFT. Once the problem is solved on the boundary of the scatter, at any point (inside or outside the object), the scattered field and its normal derivative can be computed by using the left-hand sides of (5.2) and (5.3).

Similar to the free space case, since the above operations involve the FFT of smooth functions, the accuracy of E_z and $\partial E_z/\partial n'$ increases exponentially as the number of the discrete points increases, a basic property of the FFT algorithm. For the layered medium case, however, the accuracy also depends on the accuracy of the layered medium Green's functions. Here, they are calculated adaptively, hence error-controllable to high accuracy.

In this work, the biconjugate-gradient (BCG) method is used to solve the matrix equation which requires $O(KN^2)$ CPU time and $O(N^2)$ memory, where N is the number of unknowns and K is the number of iterations. Since the main purpose of this work is the reduction of the number of unknowns (N), we have not implemented any acceleration methods (such as the fast multipole method and adaptive integral method) to further reduce the computation time and storage requirements.

4.3 Numerical Results

4.3.1 A Circular Cylinder in Air

To show the accuracy and efficiency of the method, a circular dielectric object in free space is chosen as the first example as it has an analytical solution. An infinite dielectric circular cylinder with radius $r = 0.04$ m and $\epsilon_r = 16$ is excited with a TM_z plane wave at $f = 300$ MHz impinging at an angle $\theta^{inc} = 0°$ along the x-direction. The receiver points are chosen along the $y = 1$ m line, from $x = -1$ m to $x = 1$ m. Figure 4.3 shows the comparison between the SIM result and analytical solution for the scattered field. For this example, 64 points along the boundary of the object are used, and excellent agreement has been observed.

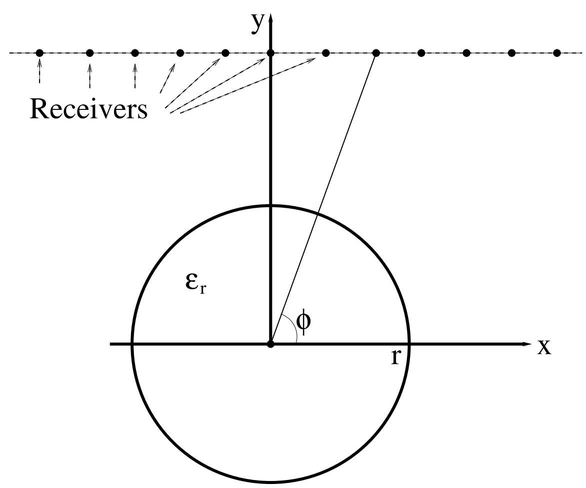

Figure 4.2: An infinite dielectric circular cylinder in free space.

Figure 4.4 shows the error convergence curve and the CPU time versus the number of discretization points per wavelength (PPW) on the dielectric object. The error decreases exponentially with the number of discretization points, confirming that the SIM has a spectral accuracy. The result shows that even with a small discretization number $N = 32$ (or at 2.7 PPW) on the boundary of the cylinder, the relative error is smaller than 1 %.

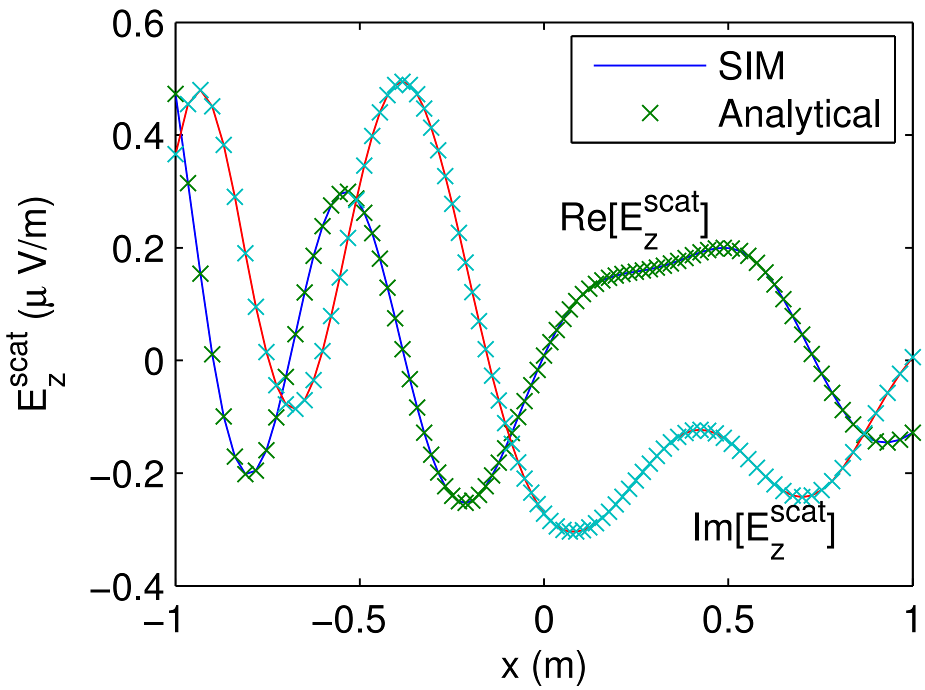

Figure 4.3: *Example A:* Comparison of the SIM and analytical results for the real and imaginary parts of the scattered field for the free space case.

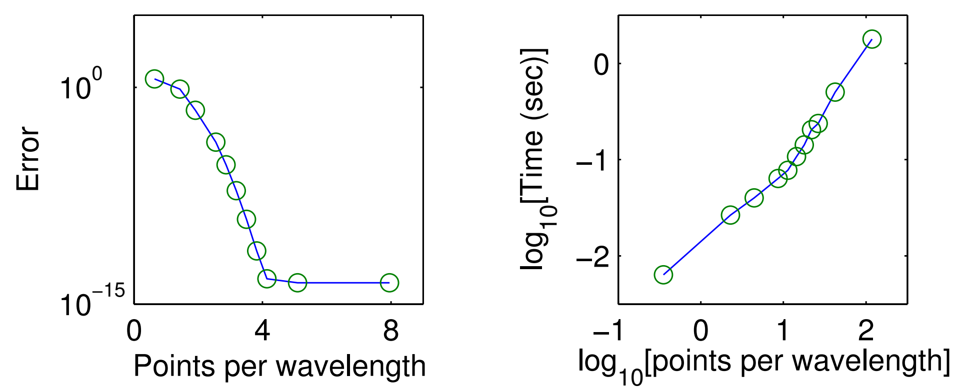

Figure 4.4: Error and execution time versus the number of discretization points per wavelength for the free space case (*Example A*).

4.3.2 A Circular Cylinder in a Five-Layer Medium

The second example is an infinite circular dielectric cylinder embedded in a 5-layer medium depicted in Figure 4.5. All layers have different permittivity values and thickness. A line source is located at $(-0.12, 0.12)$ m, and the object with $r = 0.04$, $\epsilon_r = 57.2$, and $\sigma = 0.25$ S/m is embedded in the third layer. Green's functions for the background have been calculated with a relative error tolerance of 10^{-8} relative. Figure 4.6 shows the comparison of the field inside the object calculated with SIM and

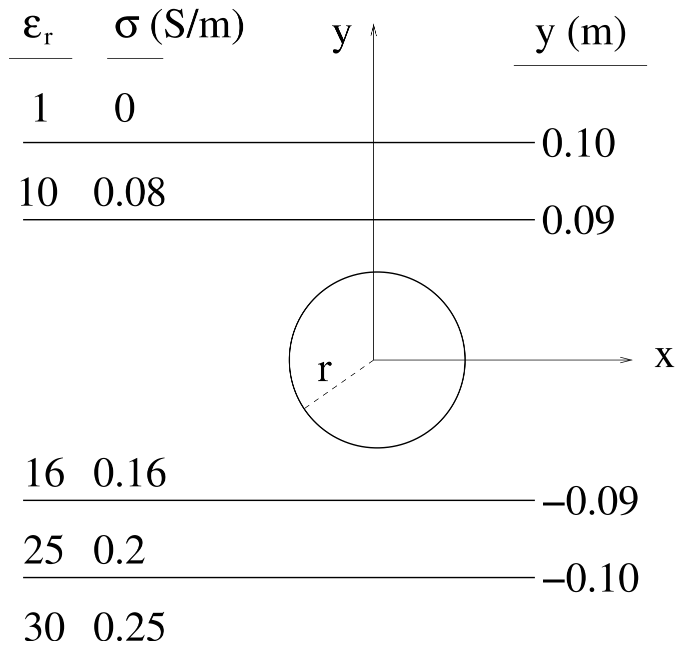

Figure 4.5: *Example B:* An infinite circular dielectric cylinder embedded in a 5-layer medium.

2D volume integral equation (VIE) approach [49], [51]. The test points are chosen along the $x = 0$ axis, from $y = -0.04$ m to $y = 0.04$ m. A very good agreement has been observed between the SIM and VIE results.

Figure 4.7 compares the scattered field E_z^{scat} outside the object calculated with SIM and 2D volume integral equation (VIE) approach [49], [51]. The test points are chosen along the $y = 0.12$ axis, from $x = -0.12$ m to $x = 0.12$ m. Excellent agreement is observed between the SIM and VIE results.

Another issue studied is the continuity of the scattered field across layer interfaces.

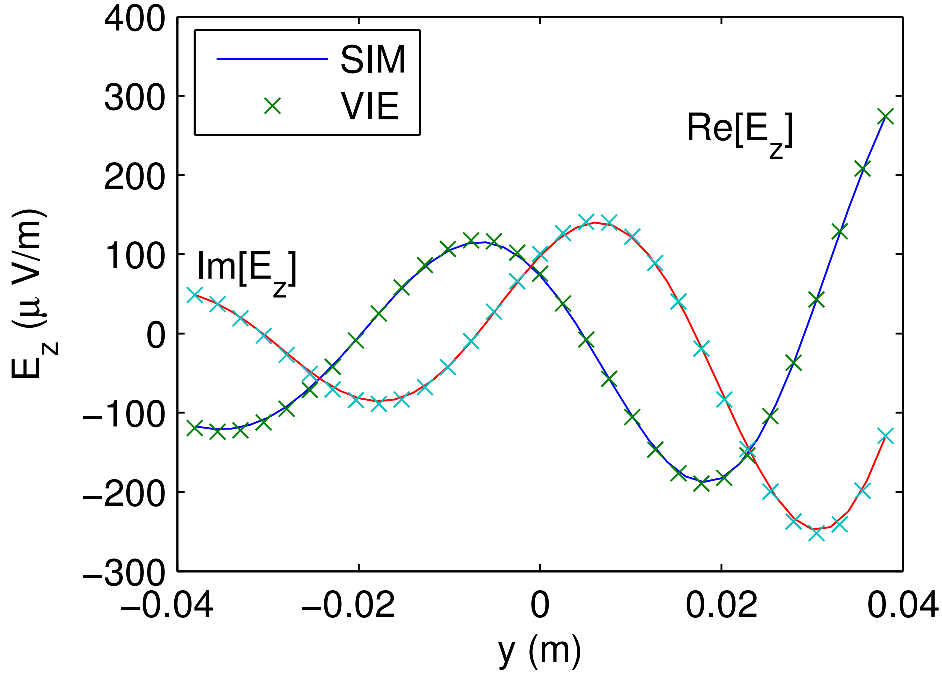

Figure 4.6: The field E_z inside the scatterer along the (0.0:-0.04,0.04) m, for the circular dielectric object in a 5-layer medium in Fig. 4.5 (*Example B*).

Figure 4.8 shows the comparison of scattered field along the $x = 0.06$ m axis, from $y = -0.12$ m to $y = 0.12$ m (from first layer to the last one). Both SIM and VIE results show expected continuity across layer interfaces.

The convergence of error with the number of discretization PPW is shown in Fig. 4.15. Since the Green's functions for the background have been calculated with 10^{-8} relative error tolerance, the minimum relative error that can be obtained is approximately in this level. Clearly, 2.7 PPW guarantees 1% accuracy.

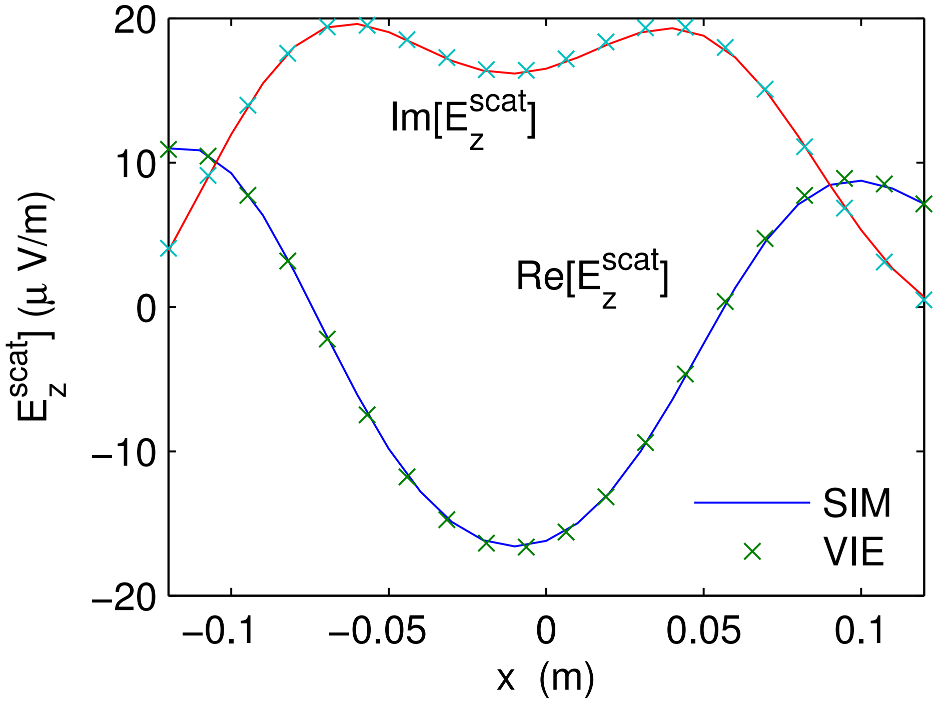

Figure 4.7: The scattered field along the (-0.12:0.12,0.12) m for the circular dielectric object in a 5 layer medium in Fig. 4.5 (*Example B*).

4.3.3 An Elliptical Dielectric Object in a Nine-Layer Medium

In the next example, an elliptical cylinder ($\epsilon_r = 57.2$ and $\sigma = 1.08$ S/m) is embedded in a 9-layer medium shown in Figure 4.9. The elliptical object is defined as

$$x(\theta) = r_1 \cos(\theta) \qquad y(\theta) = r_2 \sin(\theta)$$

where $r_1 = 0.08$ m, $r_2 = 0.04$ m, and $\theta \in (0, 2\pi)$.

A line source with $f = 400$ MHz is located at $(0, 0.3)$ m in the first layer. The receivers are located on $x = 0.12$ m axis from $y = 0.3$ m to $y = -0.3$ m (from top layer to the bottom layer). Figure 4.10 shows the comparison of the real and imaginary parts of the scattered field obtained by using 16 points (4.16 PPW) and 128 points (33.27 PPW) on the object.

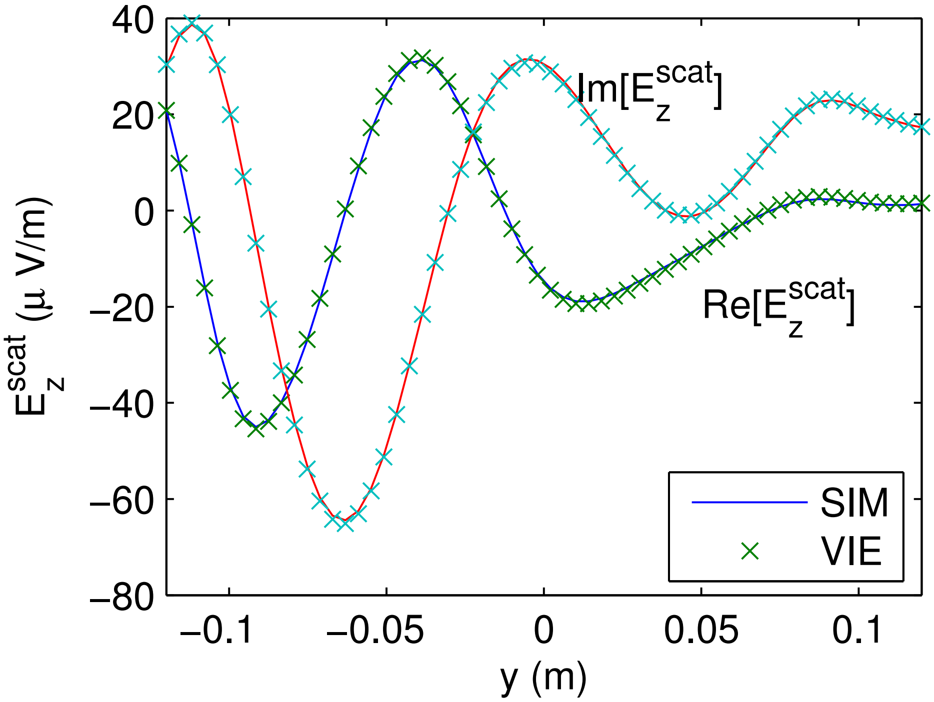

Figure 4.8: The scattered field along the (0.06,-0.12:0.12) m for the circular dielectric object in a 5-layer medium in Fig. 4.5 (*Example B*).

The convergence of error with the number of discretization PPW is obtained by using the case with 33.27 PPW as a reference and is shown in Fig. 4.15. Again, the minimum relative error that can be obtained is limited by the accuracy of the Green's functions for the background layered medium. Clearly, 4 PPW guarantees 1% accuracy.

4.3.4 An Elliptical PEC Object in a Nine-Layer Medium

The fourth example is similar to the ones presented in [52] to demonstrate the validity of the method for PEC objects. Since the tangential component of the electric field is zero on the boundary, the integrals in (5.2) and (5.3) only have the first terms. In this case, a PEC object with the same elliptical shape as in the previous example is

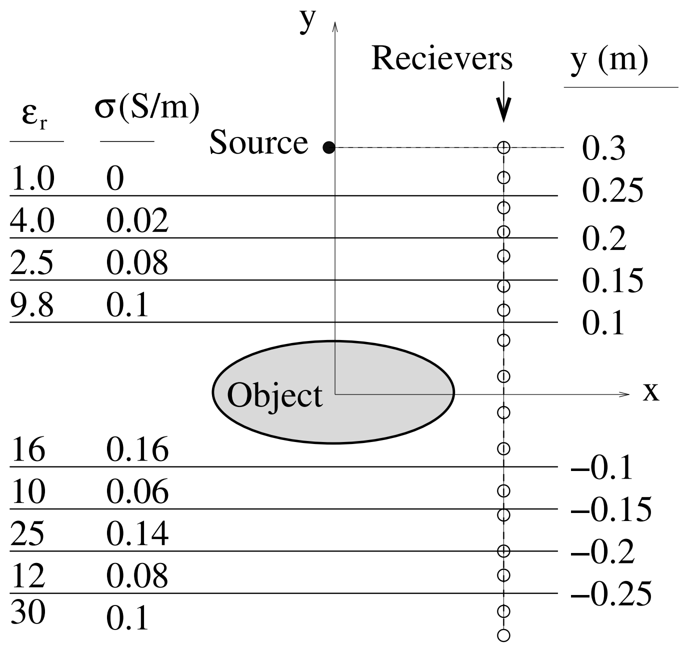

Figure 4.9: An elliptical cylinder embedded in a 9-layer medium for *Example C.*

embedded in the 9-layer medium depicted in Figure 4.9. All other properties are the same as in the previous case. Figure 4.11 compares the scattered field obtained by using 12 points (4.3 PPW) and 128 points (45.9 PPW) on the object. The convergence of error with the number of discretization PPW is obtained by using the case with 45.9 PPW as a reference and is plotted as *Example D* in Fig. 4.15. Note that 1% accuracy can be obtained with 2.7 PPW sampling.

4.3.5 A Complex Object in a Nine-Layer Medium

A complex cylinder ($\epsilon_r = 57.2$, $\sigma = 1.08$ S/m) shown in Figure 4.12 (left panel) is embedded at center of the 9-layer medium in Fig. 4.9. The object is defined as follows

$$x(\theta) = 0.04\cos(\theta) + 0.006\sin(2\theta) + 0.0032625\cos(4\theta)$$

$$y(\theta) = 0.04\sin(\theta) + 0.006\cos(2\theta) + 0.0032625\sin(4\theta)$$

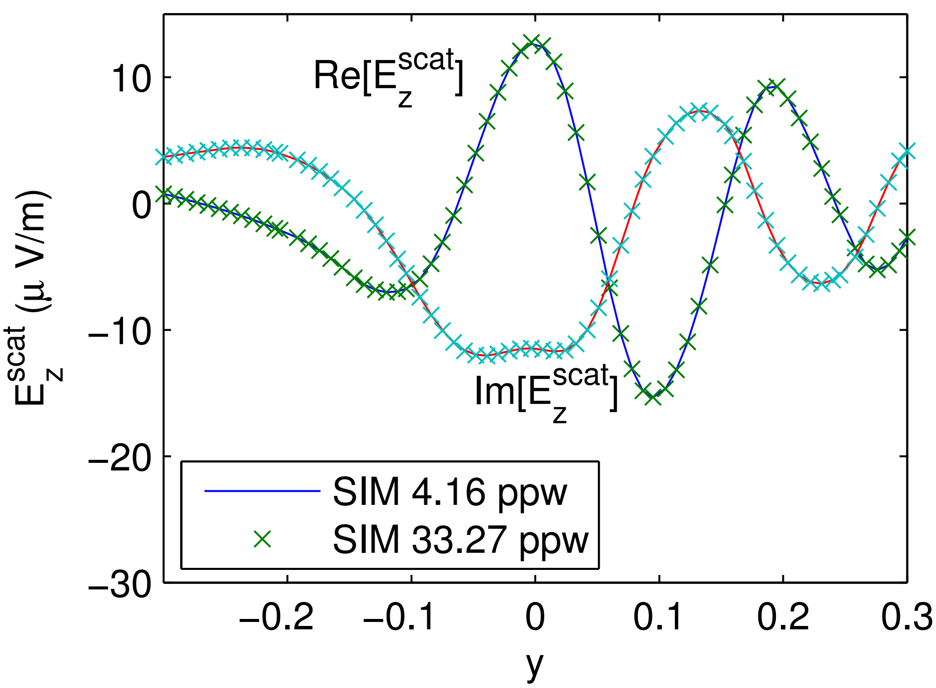

Figure 4.10: *Example C:* Real and imaginary parts of the scattered field from the elliptical dielectric object in the 9-layer medium in Fig. 4.9.

where $\theta \in \ (0, 2\pi)$. The frequency is 1 GHz and the circumference of the object is equal to $6.4\lambda_{object}$. A line source is located at $(0, 0.12)$ m. The receivers are located on $x = 0.2$ m axis from $y = 0.3$ m to $y = -0.3$ m (from top layer to the bottom layer). Figure 4.13 shows the comparison of the real and imaginary parts of the scattered field obtained by using 32 points (5.0 PPW) and 256 points (40.1 PPW) on the object.

The convergence of error with the number of discretization PPW is obtained by using the case with 40.1 PPW as a reference and is shown in Fig. 4.15. Again, 2.7 PPW guarantees 1% accuracy.

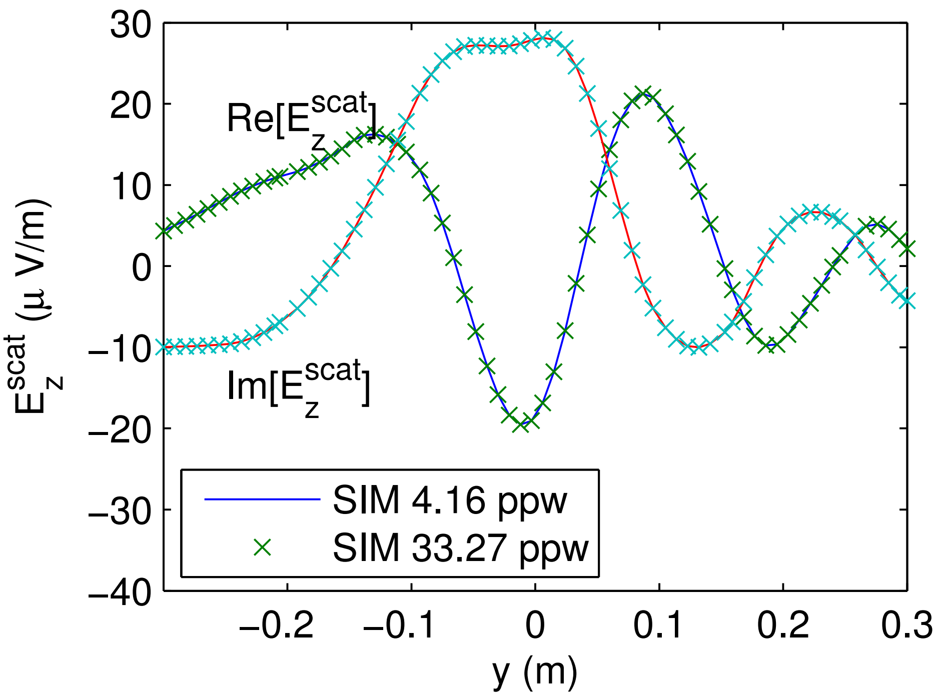

Figure 4.11: *Example D:* Real and imaginary parts of the scattered field from the elliptical PEC object in the 9-layer medium in Fig. 4.9.

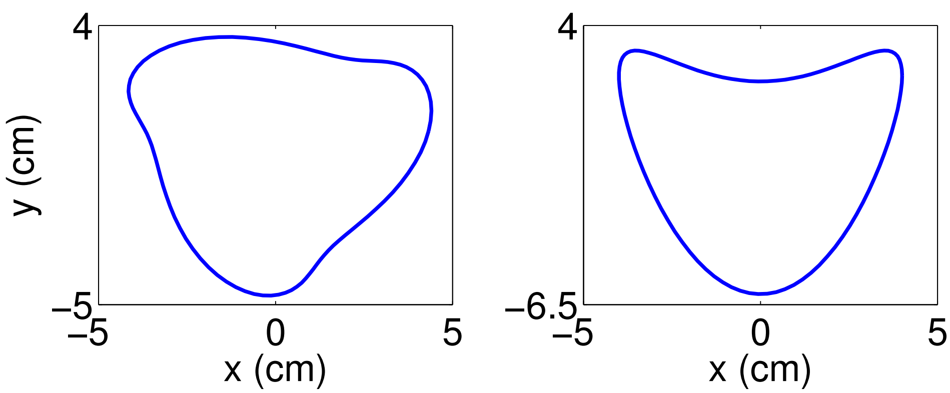

Figure 4.12: A complex convex cylinder (left panel) for *Example E*, and a concave cylinder (right panel) for *Example F*.

4.3.6 A Concave Object in a Five-Layer Medium

In order to study the performance of the SIM for concave objects, we replace the circular object in *Example B* with a concave cylinder defined by $x(\theta) = 0.04\cos(\theta)$

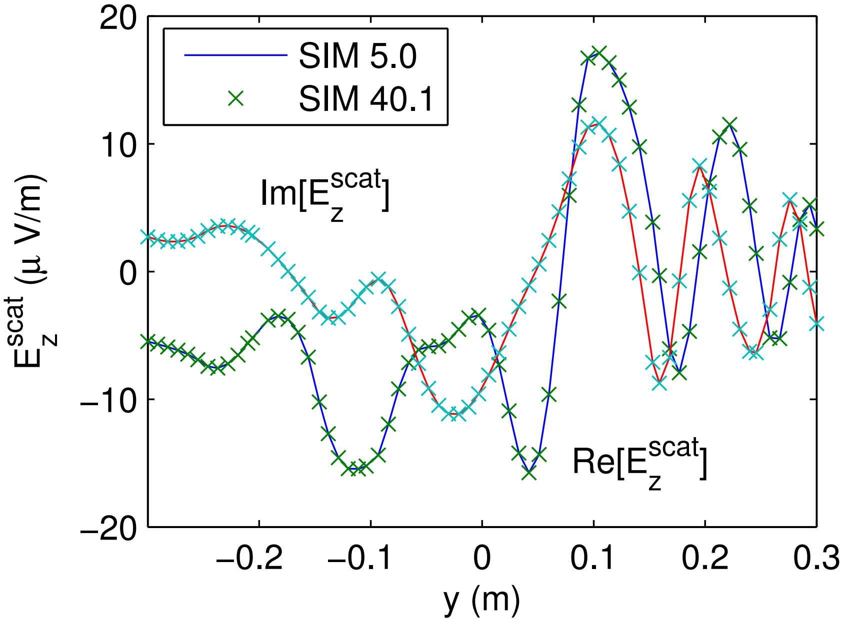

Figure 4.13: *Example E:* Real and Imaginary parts of the scattered field for Fig. 4.12 in the nine-layer medium in Fig. 4.9.

and $y(\theta) = 0.04\sin(\theta) + 0.02\cos(2\theta)$ and shown in the right panel of Fig. 4.12. All other parameters are the same as in *Example B*. Fig. 4.14 shows the comparison of the real and imaginary parts of the scattered electric field along the $(0.06, -0.12 : 0.12)$ m obtained by using 24 points (4.6 PPW) and 256 points (49.0 PPW) on the object. The convergence of error with the number of discretization PPW is obtained by using the case with 49.0 PPW as a reference and is shown in Fig. 4.15.

In this work, we have used θ for parameterization of the object surface; alternatively, one can directly use the arc length for parameterization.

All the above examples demonstrate that the method has spectral accuracy for smooth objects. For the objects with corners, the method will be still valid but the expected accuracy will decrease from the smooth objects. Future studies will investigate non-smooth objects.

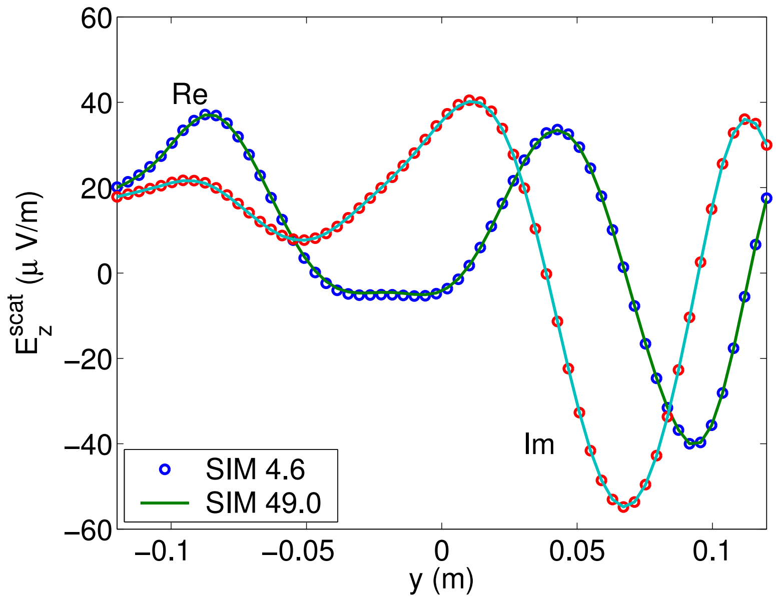

Figure 4.14: *Example F:* Real and Imaginary parts of the scattered electric field along $(0.06, -0.12 : 0.12)$ m for a concave object in the right panel of Fig. 4.12 in a 5-layer medium in Fig. 4.5.

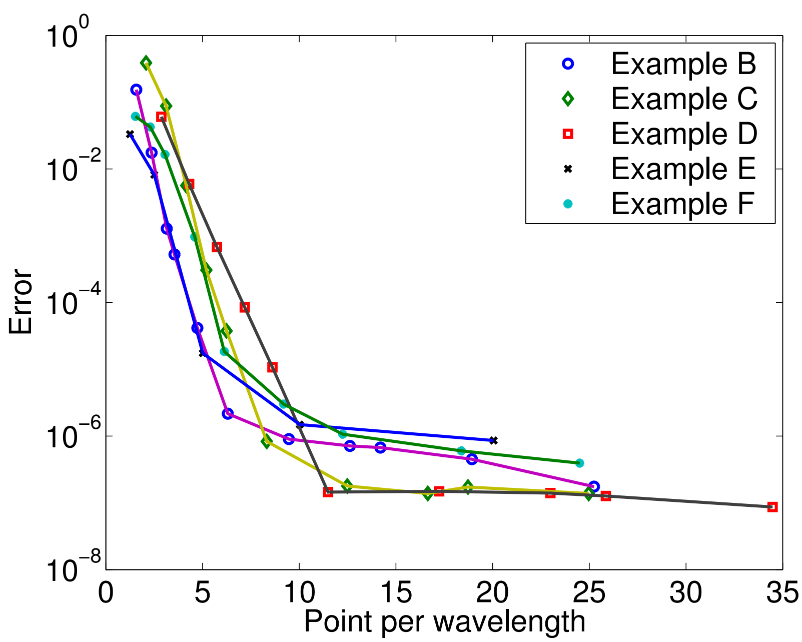

Figure 4.15: Convergence of error with the number of discretization points for examples B through F.

4.4 Conclusion

We develop a spectral integral method for homogeneous dielectric objects and perfect conductors with closed smooth boundary embedded in a layered medium. The high accuracy and the efficiency of the method has been demonstrated. 1% accuracy can be obtained with about three points per wavelength sampling. Numerical results also confirm that the SIM is applicable to concave objects. The method can be further extended to periodic structures and to three dimensions, as well as to objects traversing layer interfaces.

Chapter 5

2D Hybrid Spectral Integral/Finite Element Method for Layered Media

For homogeneous objects embedded in a layered medium, surface integral equations (SIEs) are more appropriate than volume integral equations (VIE). However, for inhomogeneous objects, the SIE must be combined with other methods such as the finite element method (FEM) in order to account for the inhomogeneity. In this approach, the computational domain can be truncated by using a radiation boundary condition (RBC). In the last three decades, several RBCs have been developed [53]-[77]. One of them is the hybrid finite element/boundary element method (FEM/BEM), which uses SIE as an RBC on the boundary surrounding the scatterer(s), and FEM in the bounded region [54]-[58], [63], [69]. In this method, the number of the required samples taken on the boundary can be decreased depending on the accuracy of SIE, hence the matrix size of the FEM problem can be reduced. Because of this lower memory requirement and geometrical and material adaptability, FEM/BEM is a very useful and powerful method for analysis of scattering by inhomogeneous objects in layered media.

The matrix size of the FEM problem depends on the accuracy of the basis functions used for both FEM and BEM. Most of the published results use zeroth and first order basis functions, thus requiring at least ten points per wavelength sampling density in the discretization. The usage of higher-order methods can reduce the minimum required sampling density.

A spectral integral method (SIM), which has been developed to solve the SIE for electromagnetic scattering by homogeneous objects with a smooth boundary in homogeneous background [42], and in layered media [79], is one of the most efficient higher-order methods. The usage of fast Fourier transform (FFT) algorithm provides exponentially accurate results and it has been shown that approximately three points per wavelength guarantees an error less than 1%. As a result, using this exponentially accurate method, SIM, as an RBC can reduce the minimum required sampling density on the radiation boundary.

Recently, Liu *et al.* propose that the spectral integral method can be utilized as an efficient RBC to truncate the computational domain in the FEM for a homogenous background medium [80]. The goal of this work is the extension of this method to layered media problems. Basically, there are two main steps.

The first step is the implementation of SIM for inhomogeneous background. In the previous chapter, we described the implementation of SIM for layered media problems, but only for objects completely embedded within one single layer in the multilayered medium. In this chapter, we improve SIM to handle the discontinuous behaviors of the fields and Green's function (i.e., the functions or their derivatives being discontinuous) across the layer interfaces so that SIM can be now applied to a scatterer straddling several layers. This step is a curicial improvement over [79], and makes SIM applicable for large number of layered medium problems.

The second step is utilization of SIM as an RBC for layered medium problems. For the implementation of radiation boundary condition, an artificial boundary $\partial\Gamma$ is applied to truncate the arbitrarily shaped inhomogenous scatterer(s) from the layered medium. The finite element method is applied in the interior region to calculate the field, while the spectral integral method is applied on the outer boundary $\partial\Gamma$ to relate the field and induced current. The field and current on the boundary for the FEM are obtained from the SIM results via highly accurate trigonometric interpolation through FFT. The singular terms in the Green's functions and the non-smooth terms in their derivatives are handled appropriately. The high-order accuracy of SIM provides the capability of low sampling density on the outer boundary $\partial\Gamma$, which significantly reduces the number of unknowns on $\partial\Gamma$.

Combining SIM with FEM has many advantages for both homogeneous and layered media problems beside reducing the matrix size. First, scattering problems can be solved for arbitrarily shaped inhomogeneous scatterers. Second, the number of the scatterers can be as many as needed. Third, the scatterers can reside in several layers. Finally, the freedom of using any type of smooth element, e.g. an ellipse, as an outher boundary helps to reduce the size of truncated domain.

5.1 Spectral Integral Method For A Scatterer Residing In Several Layers

Consider a general multilayer medium consisting of N layers separated by $N-1$ interfaces parallel to the x axis. Layer i ($i = 1, \cdots, N$) exists between $y = y_i$ and y_{i-1} ($y_0 \to -\infty$ and $y_N \to \infty$) and is characterized by relative complex permittivity $\tilde{\epsilon}_{r,i}$ and relative permeability $\mu_{r,i}$; the wavenumber inside the layer is given by $k_i = \omega\sqrt{\tilde{\epsilon}_i \mu_i}$. An incident TM_z wave is assumed and the time dependence of $e^{j\omega t}$ is implied.

For the TM_z case, the 2D Helmholtz equation for the scalar field E_z is

$$\nabla \cdot \mu_{r,\gamma}^{-1} \nabla E_z + k_0^2 \tilde{\epsilon}_{r,\gamma} E_z = -f_\gamma \tag{5.1}$$

where subscript γ indicates the region outside ($\gamma = l$) or inside ($\gamma = d$) the object, f_γ is the source excitation, $k_\gamma = \omega\sqrt{\mu_\gamma \tilde{\epsilon}_\gamma}$, and $k_0 = \omega\sqrt{\mu_0 \epsilon_0}$. .

For a smooth dielectric object embedded in a layered medium, the boundary integral equations on the surface of the scatterer D are

$$E_z^{inc}(\mathbf{r}) + \oint_D \left[\frac{\partial E_z(\mathbf{r}')}{\partial n'} G_l(\mathbf{r}, \mathbf{r}') \right. \\ \left. - E_z(\mathbf{r}') \frac{\partial G_l(\mathbf{r}, \mathbf{r}')}{\partial n'}\right] ds' = \frac{E_z(\mathbf{r})}{2} \tag{5.2}$$

$$- \oint_D \left[\frac{\partial E_z(\mathbf{r}')}{\partial n'} G_d(\mathbf{r}, \mathbf{r}') - E_z(\mathbf{r}') \frac{\partial G_d(\mathbf{r}, \mathbf{r}')}{\partial n'}\right] ds' \\ = \frac{E_z(\mathbf{r})}{2} \tag{5.3}$$

for $\mathbf{r} \in D$, where f_d is assumed zero, E_z^{inc} is the incident wave from outside the object (i.e., $f_l \neq 0$, $f_d = 0$). $\hat{\mathbf{n}}$ is the outward unit normal. Inside the dielectric object, the homogeneous space Green's function, $G_d(\mathbf{r}, \mathbf{r}')$, outside the object, the layered-medium Green's function, $G_l(\mathbf{r}, \mathbf{r}')$, are used. Singular terms' contributions are calculated by defining two infinitely smooth functions as described in Chapter 4.

In terms of a parameter θ (in this case the azimuthal angle $\theta \in [0, 2\pi]$), the boundary can be described as $r = r(\theta)$, or equivalently $[x = x(\theta), y = y(\theta)]$. Eqn. (5.2) can be written as

$$E_z^{inc}(\theta) = \frac{E_z(\theta)}{2} - \int_0^{2\pi} \frac{\partial E_z}{\partial n'} G_l(\theta, \theta') J_a(\theta') d\theta' \\ + \int_0^{2\pi} E_z(\theta') \frac{\partial G_l(\theta, \theta')}{\partial n'} J_a(\theta') d\theta' \tag{5.4}$$

where $J_a(\theta') = |\frac{ds'}{d\theta'}| = \sqrt{\left(\frac{\partial x'}{\partial \theta'}\right)^2 + \left(\frac{\partial y'}{\partial \theta'}\right)^2}$ is the Jacobian for the mapping between the arc length and θ.

$E_z(\theta)$ and $\partial E_z(\theta)/\partial n$ can be approximated by truncated Fourier series as

$$E_z(\theta') \approx \sum_{n=-N_s/2}^{N_s/2-1} \tilde{e}_{zn}^b e^{jn\theta'}, \quad \frac{\partial E_z(\theta')}{\partial n'} \approx \sum_{n=-N_s/2}^{N_s/2-1} \tilde{h}_{tn}^b e^{jn\theta'} \tag{5.5}$$

where $\tilde{e}_{zn}^b$ and $\tilde{h}_{tn}^b$ are the Fourier's coefficients of $E_z(\theta')$ and $\frac{\partial E_z(\theta')}{\partial n'}$, respectively, and N_s is the number of discretized Fourier transform points. Substituting these Fourier series into Eqn. (5.4) yields

$$\begin{aligned} E_z^{inc} =& \frac{1}{2} \sum_{n=-N_s/2}^{N_s/2-1} \tilde{e}_{zn}^b e^{jn\theta} \\ &- \sum_{n=-N_s/2}^{N_s/2-1} \tilde{h}_{tn}^b \int_0^{2\pi} e^{jn\theta'} G_l(\theta,\theta') J_a(\theta') d\theta' \\ &+ \sum_{n=-N_s/2}^{N_s/2-1} \tilde{e}_{zn}^b \int_0^{2\pi} e^{jn\theta'} \frac{\partial G_l(\theta,\theta')}{\partial n'} J_a(\theta') d\theta' \end{aligned} \tag{5.6}$$

Note that Equation (5.6) relates the Fourier coefficients of the unknown E_z and its normal derivative. Then the two integrations in Eqn. (5.6) can be calculated using FFT with high accuracy. After collocation at $\{\theta_m\}$ points, Eqn. (5.6) becomes

$$L\tilde{\mathbf{e}}_z^b + M\tilde{\mathbf{h}}_t^b = \mathbf{E}_z^{inc} \tag{5.7}$$

where $L_{mn} = e^{jn\theta_m}/2 + 2\pi h_{mn} + k_b v_{mn}$ and $M_{mn} = -2\pi g_{mn} + u_{mn}$ in which $m, n = 1, 2, \cdots, N_s$, are the indices of basis and testing points on the discrete boundary; g_{mn} and h_{mn} are Fourier transforms of the smooth parts, and u_{mn} and v_{mn} are Fourier transforms of the two non-smooth terms of the Green's function and its normal derivative. Because of the use of singularity subtraction and FFT, the calculations of these terms are convergent, fast, and have high accuracy.

Equation (5.3) can be discretized in the same way. The final form of the equations can be solved for scalar field (E_z) and its normal derivative ($\partial E_z/\partial n'$) on the boundary of the scatter [42], [79]. The validity and efficiency of the described method is shown with the following example.

A Numerical Example

A circular PEC cylinder with radius of $r = 12.5$ cm is partially buried in a 2-layer

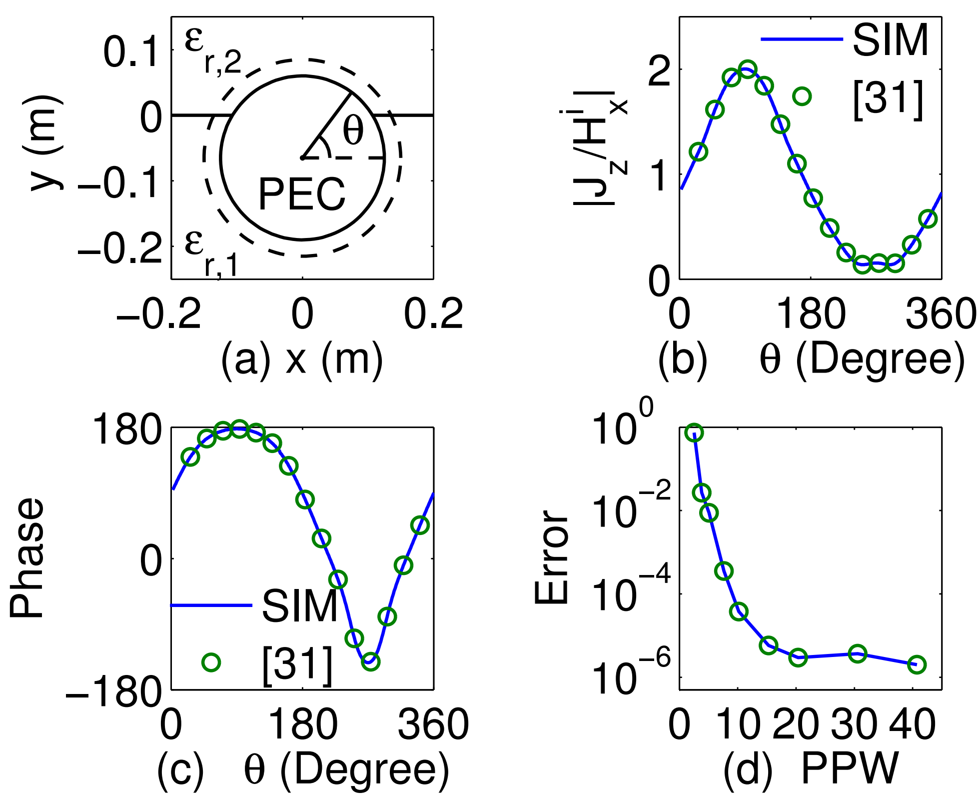

Figure 5.1: (a) A partially buried PEC cylinder of radius $r = 12.5$ cm, whose center is 6.5 cm below the interface. (b) Magnitude of current induced on the object. (c) Phase of current (in degree). (d) Convergence of error with the number of discretization points on the surface of the scatterer.

medium shown as Fig. 5.1 (a). The frequency of the normal TM_z incident wave is

300 MHz, $\mu_{r,2} = \epsilon_{r,2} = 1$, $\mu_{r,1} = 1$, $\epsilon_{r,1} = 4$. The center of the object is 6.5 cm below the interface.

Figure 5.1 (c) and (d) show the comparisons of magnitude and phase of the current induced on the scatterer obtained with this method and [81]. The convergence of error with the number of discretization points per wavelength (PPW) is obtained by using the case with 82 PPW as a reference and is plotted in Fig. 5.1 (d). The error decreases exponentially with the number of discretization points, confirming that the SIM has a spectral accuracy. The result shows that even with a small discretization number $N = 8$ (or at 5.0 PPW) on the boundary of the cylinder, the relative error is smaller than 1 %. Note that. the Green's functions for the background have been calculated with 10^{-7} relative error tolerance, and the minimum relative error that can be obtained is approximately in this level.

5.2 FEM/SIM for Layered Media

Consider an arbitrary two-dimensional inhomogeneous object in a layered medium as shown in Fig. 5.2. To solve the electromagnetic wave scattering problem using the finite element method, a radiation boundary condition is required to truncate the computational domain so that the FEM is used in the interior region (region I). With a correct radiation boundary condition on the surface $\partial\Gamma$, the field in the layered media, the exterior region (region II), can be calculated once the field in region I (including the boundary) is solved. In region I, the material is inhomogeneous with relative permeability $\mu_r(x, y)$ and relative permittivity $\epsilon_r(x, y)$. There may also exist metallic materials and electric/magnetic sources in region I. Region II is a layered medium described in Section 5.1. The goal is to solve for the electromagnetic fields scattered by the inhomogeneous object.

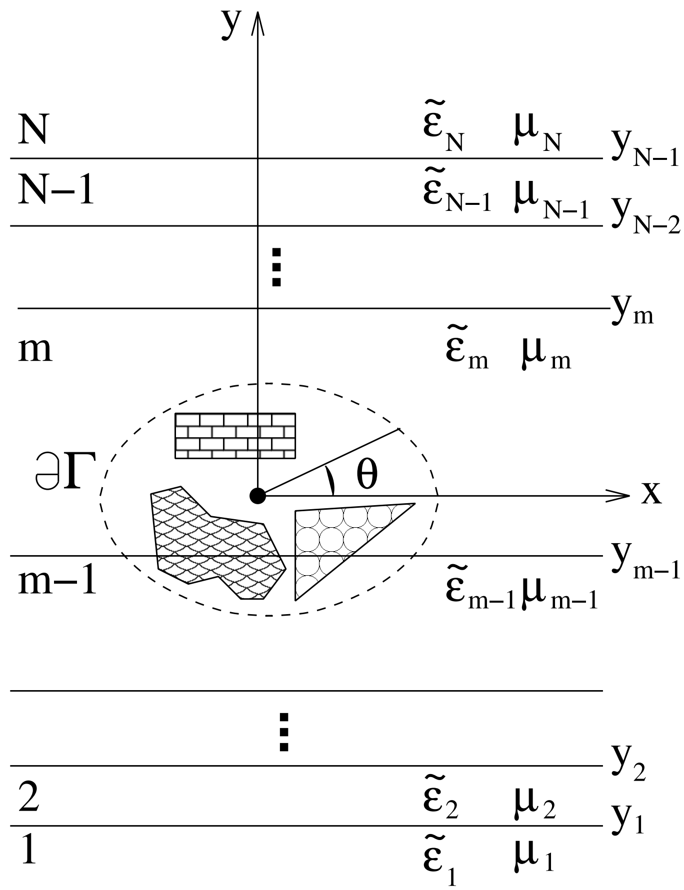

Figure 5.2: An N-layer medium scattering problem.

5.2.1 The Finite-Element Method

For TM_z waves, the total electric field $E_z(x, y)$ in region I (bounded by $\partial\Gamma$) can be determined from the solution of the scalar wave equation in (5.1). To discretize Eqn. (5.1), we multiply the equation by the testing function $W_m(x, y)$, where m is the index of the testing function, and integrate it over region I. Using vector identities and Gauss theorem, we obtain a weak-form equation as

$$\iint_{\Gamma} \left[\xi_1(x,y)E_z(x,y) - \xi_2(x,y)\cdot\nabla E_z(x,y)\right] dxdy$$

$$+\oint_{\partial\Gamma} \xi_3(x,y)\frac{\partial E_z(x,y)}{\partial n} ds = \iint_{\Gamma} \xi_4(x,y) dxdy \tag{5.8}$$

where $\hat{n}$ is the outward unit normal vector on the boundary $\partial\Gamma$ and

$$\xi_1(x,y) = k_0^2 \epsilon_r(x,y) W_m(x,y) \tag{5.9}$$

$$\xi_2(x,y) = \mu_r^{-1}(x,y)\nabla W_m(x,y) \tag{5.10}$$

$$\xi_3(x,y) = W_m(x,y)\mu_r^{-1}(x,y) \tag{5.11}$$

$$\xi_4(x,y) = -W_m(x,y) f_d \tag{5.12}$$

To solve Eqn. (5.8) using the FEM scheme, region I is discretized into triangular elements and linear pyramid basis function $P_n(x,y)$ is used to expand the electric field $E_z(x,y)$ in the interior region I and triangular basis function $T_n(x,y)$ is used to expand the boundary value $\frac{\partial E_z}{\partial n}$ on $\partial\Gamma$ (with nodal points collocated with the nodal points of the pyramid basis function on the boundary), as following equations

$$E_z(x,y) = \sum_{n=1}^{N_i} e_{zn}^i P_n(x,y) + \sum_{n=N_i+1}^{N_i+N_b} e_{zn}^b P_n(x,y) \tag{5.13}$$

$$\frac{\partial E_z}{\partial n} = \sum_{n=1}^{N_b} h_{tn}^b T_n(s) \tag{5.14}$$

where N_i and N_b are the numbers of nodes in region I and on the boundary $\partial\Gamma$, respectively, and s is the arc length on the boundary, e_{zn}^b and h_{tn}^b are equal to ϕ_n and ψ_n, respectively, given in Eq. (4.31).

Using pyramid testing functions

$$W_m(x,y) = P_m(x,y), \quad m = 1, \cdots, N_i + N_b \tag{5.15}$$

and substituting Eqns. (5.13) and (5.14) into Eqn. (5.8), the following linear equations are obtained

$$Z^{(1)} \begin{pmatrix} \mathbf{e}_z^i \\ \mathbf{e}_z^b \end{pmatrix} + Z^{(2)} \begin{pmatrix} \mathbf{e}_z^i \\ \mathbf{e}_z^b \end{pmatrix} + Z^{(3)} \mathbf{h}_t^b = \begin{pmatrix} \mathbf{S} \\ 0 \end{pmatrix} \tag{5.16}$$

where

$$Z_{mn}^{(1)} = \iint_\Gamma k_0^2 \epsilon_r(x,y) P_m(x,y) P_n(x,y) dxdy \tag{5.17}$$

$$Z_{mn}^{(2)} = -\iint_\Gamma \mu_r^{-1}(x,y) \nabla P_m(x,y) \cdot \nabla P_n(x,y) dxdy \tag{5.18}$$

$$Z_{mn}^{(3)} = \mu_{rb}^{-1} \int_{\partial\Gamma} P_m(x,y) T_n(x,y) ds \tag{5.19}$$

$$S_m = -\iint_\Gamma P_m(x,y) f_d dxdy \tag{5.20}$$

with $m = 1, 2, \cdots, N_b + N_i$ for $Z_{mn}^{(1)}$, $Z_{mn}^{(2)}$ and $Z_{mn}^{(3)}$, $m = 1, 2, \cdots, N_i$ for S_m, $n = 1, 2, \cdots, N_b + N_i$ for $Z_{mn}^{(1)}$, $Z_{mn}^{(2)}$ and $n = 1, 2, \cdots, N_b$ for $Z_{mn}^{(3)}$.

With the properties of $Z_{mn}^{(1)}$, $Z_{mn}^{(2)}$ and $Z_{mn}^{(3)}$, Eqn. (5.16) can be further written as

$$Z^i \mathbf{e}_z^i + X_b^T \mathbf{e}_z^b = \mathbf{S} \tag{5.21}$$

$$X_b \mathbf{e}_z^i + Z^b \mathbf{e}_z^b + K \mathbf{h}_t^b = 0 \tag{5.22}$$

where $Z_{mn}^i = Z_{mn}^{(1)} + Z_{mn}^{(2)}$ $(m, n = 1, 2, \cdots, N_i)$, $Z_{mn}^b = Z_{N_i+m,N_i+n}^{(1)} + Z_{N_i+m,N_i+n}^{(2)}$ $(m, n = 1, 2, ..., N_b)$, and $X_{bmn} = Z_{N_i+m,n}^{(1)} + Z_{N_i+m,n}^{(2)}$ $(m = 1, 2, \cdots, N_b, n = 1, 2, \cdots, N_i)$ are parts of the summation of $Z_{mn}^{(1)}$ and $Z_{mn}^{(2)}$; $K_{mn} = Z_{mn}^{(3)}$ $(m, n = 1, 2, \cdots, N_b)$, and X_b^T is the transpose of X_b.

There are more unknowns than the number of equations in (5.21) and (5.22), and additional conditions are provided by the radiation boundary condition which is the spectral integral method to obtain a unique solution of the system.

5.2.2 SIM as an RBC and Spectral Interpolation

In order to use the SIM as a radiation boundary condition in (4.36) for the FEM, we need to utilize this RBC to relate the electric field and its normal derivative. Since $\tilde{e}^b_{zn}$ and $\tilde{h}^b_{tn}$ are Fourier coefficients of electric field and its normal derivative on the boundary, the pyramid basis expansion coefficients e^b_{zm} and h^b_{tm} can be obtained by $\tilde{e}^b_{zn}$ and $\tilde{h}^b_{tn}$, which are obtained from Eq. (4.36), through trigonometric interpolation,

$$e^b_{zm} = \frac{1}{N_s} \sum_{n=-N_s/2}^{N_s/2-1} e^{jn(\theta^F_m - \theta_1)} \tilde{e}^b_{zn} \tag{5.23}$$

$$h^b_{tm} = \frac{1}{N_s} \sum_{n=-N_s/2}^{N_s/2-1} e^{jn(\theta^F_m - \theta_1)} \tilde{h}^b_{tn} \tag{5.24}$$

where $\{\theta^F_m\}$ are the positions of the FEM nodal points on the boundary in term of parameter θ, and θ_1 is the first discretization point for the SIM.

Substituting Eqns. (5.23) and (5.24) into (5.21) and (5.22), we obtain

$$Z^i \mathbf{e}^i_z + X^T_b T_r \tilde{\mathbf{e}}^b_z = \mathbf{S} \tag{5.25}$$

$$X_b \mathbf{e}^i_z + Z^b T_r \tilde{\mathbf{e}}^b_z + K T_r \tilde{\mathbf{h}}^b_t = 0 \tag{5.26}$$

where T_r is the trigonometric interpolation matrix with

$$T_{rmn} = \frac{1}{N_s} e^{jn(\theta^F_m - \theta_1)} \tag{5.27}$$

and $m = 1, 2, \cdots, N_b$, $n = 1, 2, \cdots, N_s$.

Combining Eqns. (5.25) and (5.26) with (4.36), one can solve the linear equations for $\tilde{e}^b_{zn}$, $\tilde{h}^b_{tn}$ and e^i_{zn}, thus obtaining the electric field in region I. Using the inverse FFT, electric field E_z and its normal derivative $\nabla E_z \cdot \hat{n}$ are obtained on the boundary $\partial\Gamma$. Because of high accuracy of SIM and trigonometric interpolation operations, even a small number of discretization point of about five points per wavelength (5 PPWs) can give an accuracy better than 1%. On the other hand, the FEM used for the interior region has a second-order accuracy; thus, the overall accuracy of the hybrid FEM/SIM will depend on the accuracy of the FEM part. In fact, in all the calculations, we choose N_s much smaller than N_b to accomplish SIM and trigonometric interpolation with the same accuracy as the FEM. The system in Eqns. (5.25), (5.26) and (4.36) is over-determined because we have $N_i+N_b+N_s$ equations and N_i+2N_s unknowns, therefore an iterative solver would be preferred to solve this system. Alternatively, multiplying Eqn. (5.26) by T_r^+, the conjugate transpose of the trigonometric interpolation matrix T_r, the system matrix becomes square and thus a direct solver can also be used.

The advantage of the hybrid FEM/SIM method is the highly accurate radiation boundary condition with very few discretization points on the boundary. Indeed, the number of unknowns in the original FEM is $N_i + 2N_b$ points ($N_i + N_b$) points for the electric field, and N_b points for the normal derivative of the electric field on the boundary), the FEM/SIM hybrid method has $N_i + 2N_s$ unknowns, where the ratio of $N_b/N_s > 2$ as the sampling density in FEM and SIM is approximately 10 (or more) and 5 points per wavelength for roughly 1% accuracy. Therefore, the number of unknowns in the FEM/SIM hybrid method is actually smaller than the FEM with a Neumann boundary condition. In the next section, we will show the numerical results of the hybrid FEM/SIM method.

5.3 Numerical Results

For all the examples presented here, the scatterer is excited with TM_z plane wave incident normally to the interface ($\theta^{inc} = 90°$).

5.3.1 A Circular Cylinder/Circular Boundary

First, a circular PEC object with radius of 0.5 m is centered on the interface of a 2-layer medium. The top layer is air ($\epsilon_{r,2} = \mu_{r,2} = 1$) and the bottom layer is soil ($\epsilon_{r,1} = 4$, $\mu_{r,1} = 1$). The frequency is 300 MHz and the radiation boundary is a circle with radius of 0.6 m. To apply the FEM in the interior region, the dielectric object is discretized into triangular elements using NETGEN (NETGEN/NGSolve V4.4, Developed at Johannes Kepler University Linz, Austria). The number of triangular elements is 2102, and the number of FEM nodes is 1257. Fig. 5.3 shows the scattered field along the radiation boundary obtained with two different ways. First, SIM (30 PPW) is used to solve the problem for $\frac{\partial E_z(\theta')}{\partial n'}$ on the surface of scatterer and then scattered field is calculated by using SIE. Second, SIM (30 PPW) is used as an RBC on the radiation boundary, and FEM is used for the interior region as explained. An excellent agreement has been observed between these results. In the same figure, the result which is obtained by using 5 PPW only is also depicted, which has very good agreement with others.

The convergence of FEM/SIM method is analyzed in two different ways. First, shown as Fig. 5.4 (a), the number of SIM points on the radiation boundary is changed for the fixed the frequency and sampling density for the interior region. Clearly, 5 PPW guarantees 1% accuracy. Second, the frequency of the problem is changed for the same mesh, the number of the SIM points is 36 (4.77 PPW for $f = 300$ MHz).

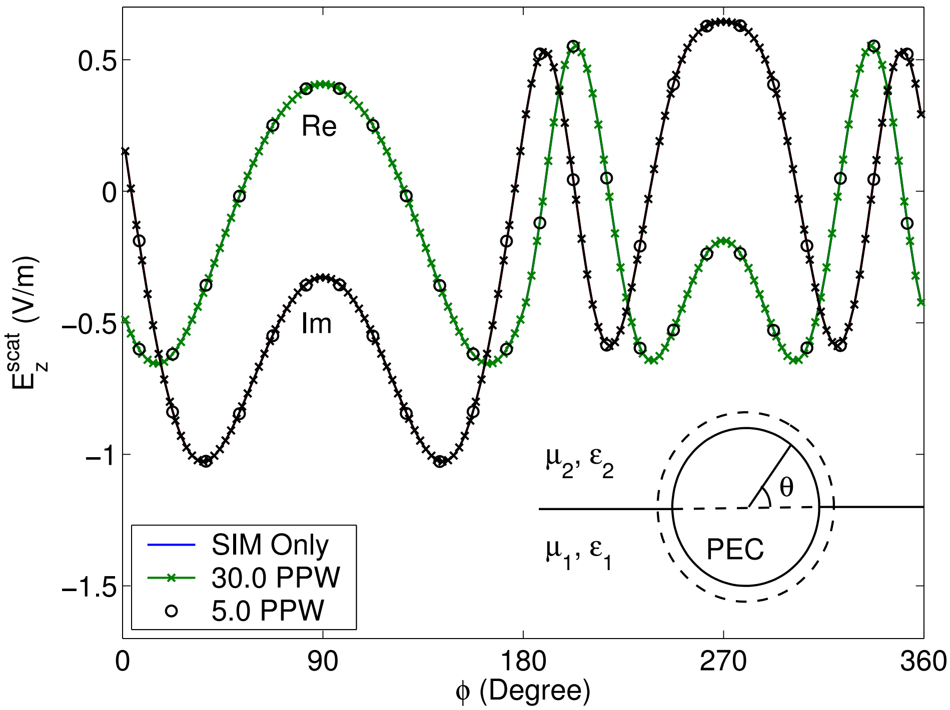

Figure 5.3: The scattered field along the radiation boundary for a circular PEC object in a 2-layer medium.

Fig. 5.4 (b) shows the convergence of error with decreasing frequency.

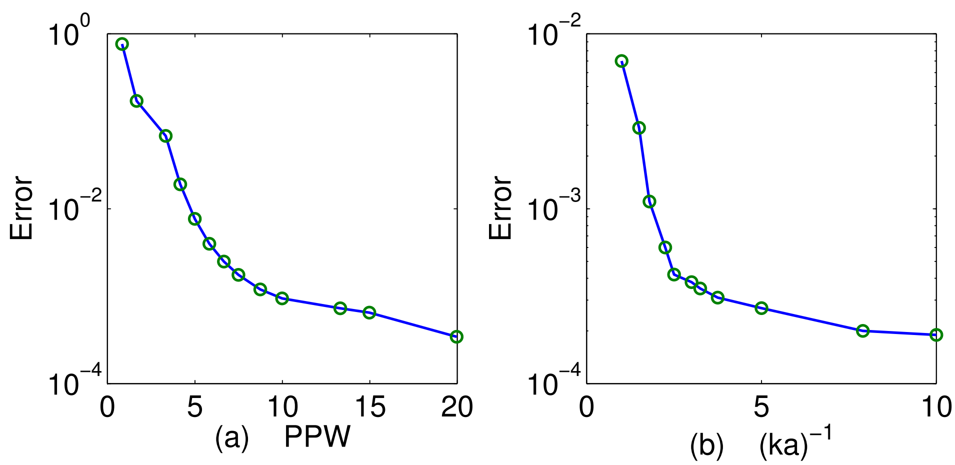

Figure 5.4: The convergence of error for *Example A* (a) with the number of discretization points along the radiation boundary (b) with decreasing frequency.

Note that, the number of boundary nodes in the FEM is 224, which is 6.2 times the number of SIM boundary nodes. Therefore, in the FEM/SIM method, the total number of unknowns is $N_i + 2N_s = 1105$; in contrast, for an FEM with a Neumann boundary condition, the number of unknowns would have been $N_i + N_b = 1257$, still greater than the number of unknowns in the FEM/SIM method. To further reduce the number of unknowns in the FEM/SIM method, ideally, in the future one can combine the SIM with higher-order FEM to further improve the efficiency of the overall scheme.

5.3.2 A Rectangular Cylinder/Elliptical Boundary

Second, the circular PEC object presented in the previous example, is replaced with a rectangular PEC object (12.5 cm $\times$ 5 cm). In this case, an elliptical radiation boundary is used with radii of 0.2 m and 0.1 m. The number of triangular elements is 2670, and the number of FEM nodes is 1525. Fig. 5.5 shows the scattered field along the radiation boundary obtained with FEM/SIM method, and SIM itself. Again, an excellent agreement has been observed. In the same figure, the result which is obtained by using 5 PPW is also shown, which agrees well with others, the error is less than 1%, using SIM solution as a reference.

5.3.3 Circular Scatterer with Coating

In the first two examples, it is shown that FEM/SIM method works well for homogeneous objects. In this example, the scatterer, shown as Fig. 5.6 (a), is an inhomogeneous scatterer. The frequency is 300 MHz; $r_{bound} = 0.6$ m, $r_{coat} = 0.55$ m, $r_{pec} = 0.5$ m; $\epsilon_{r,l1} = 4$, $\epsilon_{r,l2} = 1$. The number of triangular elements is 2462, and the number of FEM nodes is 1437. In this example we used 4 different sets of ($\epsilon_{r,c1}$,$\epsilon_{r,c2}$)

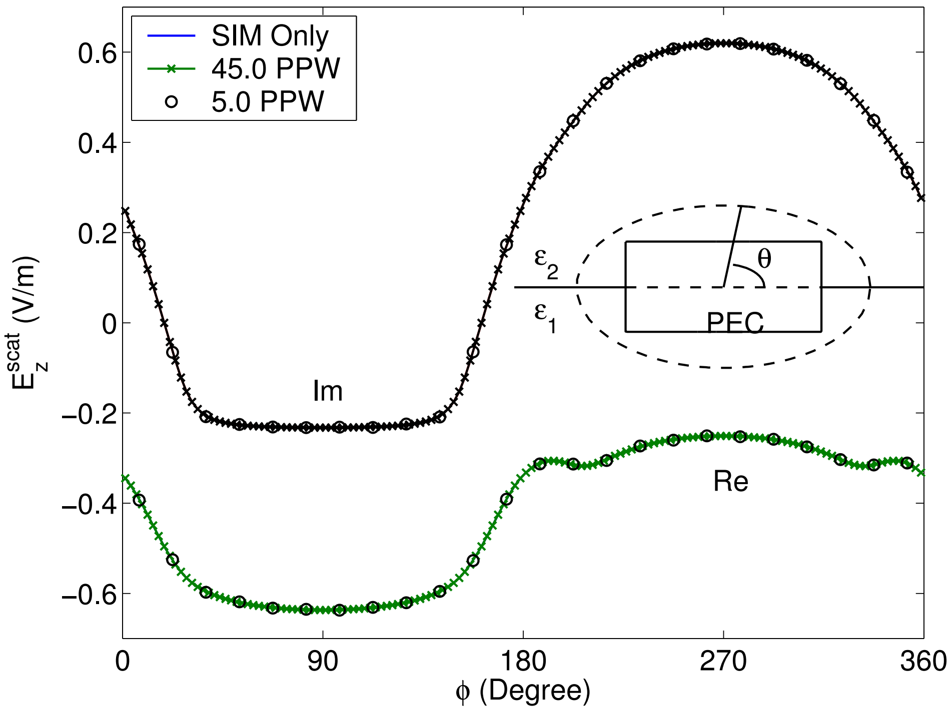

Figure 5.5: The scattered field along the radiation boundary for a rectangular PEC object in a 2-layer medium.

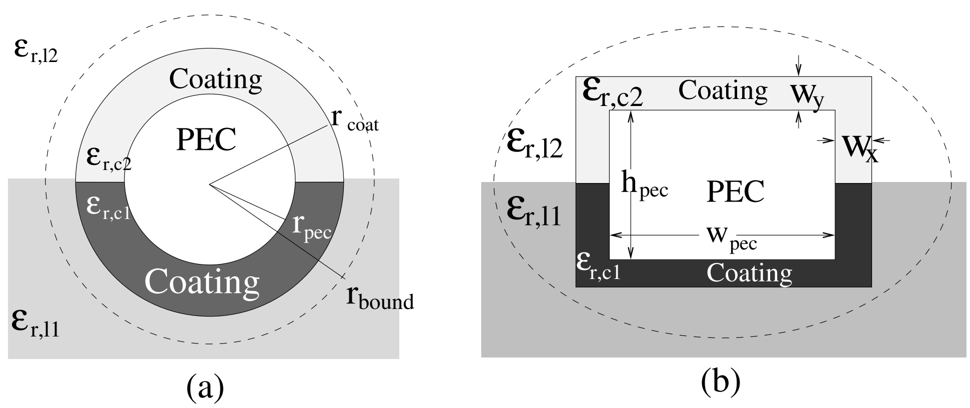

Figure 5.6: Inhomogeneous scatterers: (a) a circular (b) a rectangular PEC cylinder surrounded with coating in a 2-layered medium.

values, which are given in Table I. Note that, case (d) is the same as *Example A*. Figures 5.7 shows the magnitude and phase of the scattered fields for the four different cases, respectively. The transformation from (a) through (d) depicts the affect of

Table 5.1: Circular Coating Models

	(a)	(b)	(c)	(d)
$\epsilon_{r,c1}$	16	9	4	4
$\epsilon_{r,c2}$	16	9	4	1

coating, clearly.

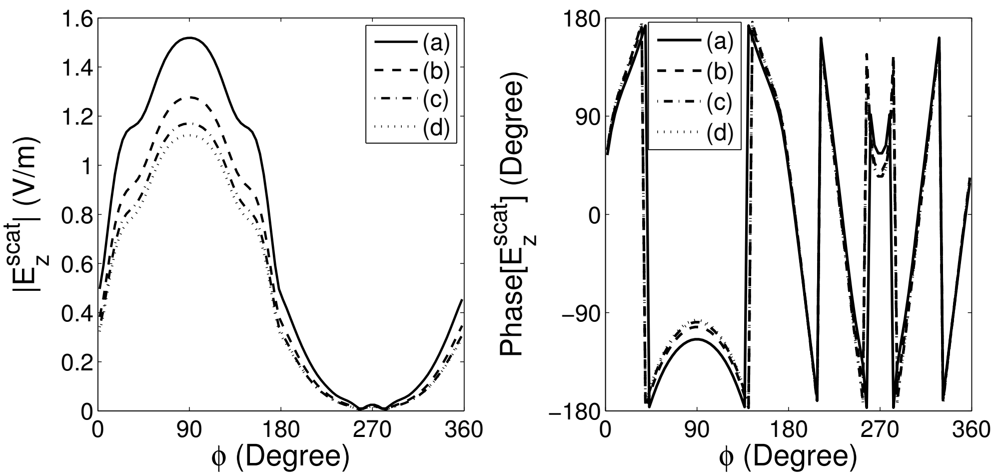

Figure 5.7: The magnitude and phase of the scattered fields along the radiation boundary for a circular PEC object surrounded with coating in a 2-layer medium.

5.3.4 Rectangular Scatterer with Coating

Similar to *Example C*, in this example, a rectangular PEC object used in *Example B* is coated with different materials, shown as Fig. 5.6 (b). Again $f = 300$ MHz, $r_{bound} = (20, 10)$ cm for the elliptical outer boundary, $w_{pec} = 12.5$ cm, $h_{pec} = 5.0$ cm; $w_x = 1.0$ cm, $w_y = 1.5$ cm; $\epsilon_{r,l1} = 4$, and $\epsilon_{r,l2} = 1$. The center of the object is on the interface. The number of triangular elements is 3376, and the number of FEM nodes is 1878. 4 different sets of ($\epsilon_{r,c1}$,$\epsilon_{r,c2}$,σ_1,σ_2) values are used, which are given in Table II. Note that, case (d) is the same as *Example B*. Figures 5.8 shows the magnitude

Table 5.2: Rectangular Coating Models

	(a)	(b)	(c)	(d)
$\epsilon_{r,c1}$	64	9	4	4
$\epsilon_{r,c2}$	64	9	4	1
σ_1 (S/m)	8	3	2	0
σ_2 (S/m)	8	3	2	0

and phase of the scattered fields for the four different cases, respectively.

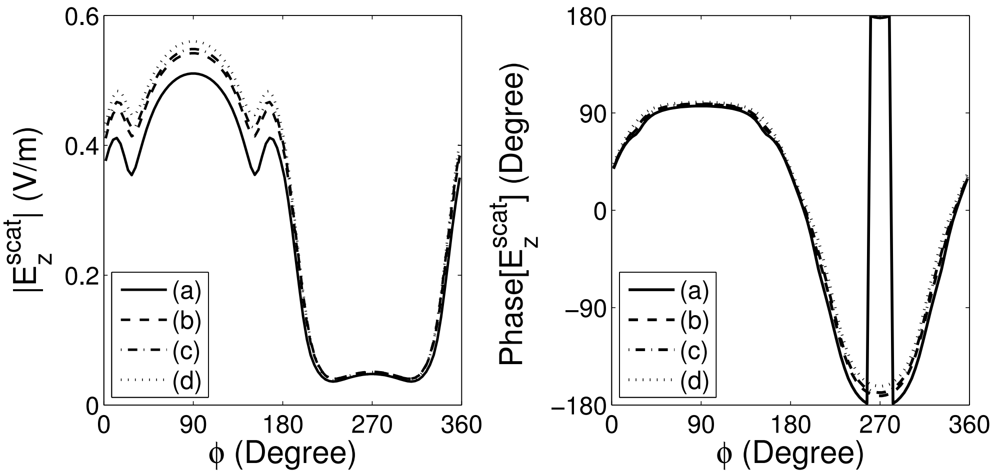

Figure 5.8: The magnitude and phase of the scattered fields along the radiation boundary for a coated rectangular PEC object in a 2-layer medium.

5.3.5 A Complex Scatterer

In the last example, a scatterer, which is similar to a MOSFET, shown as Fig. 5.9, is analyzed. The problem is assumed as a 3-layer medium: air, silicon, and PEC (like the ground of a MOSFET). The frequency of the incident field is 300 THz. The relative permittivity of silicon and oxide are 11.7 and 3.9, respectively. The conductivity of p-Si and n-Si are 0 and 2 S/m, respectively. The dimensions are depicted in Fig. 5.9. An elliptical boundary with radii of (2.0,1.0) μm is used as a radiation boundary which has a circumference of $27.4\lambda_{Si}$. This example is approximately 10 times bigger than the previous ones, so the number of triangular elements and nodes are approximately 10 times bigger: 57678 triangular elements, and 30507 FEM nodes.

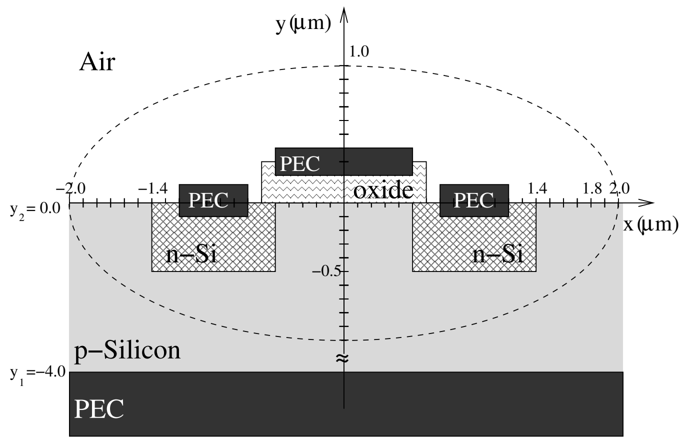

Figure 5.9: A MOSFET like scatterer.

Fig. 5.10 shows the scattered field along the radiation boundary by using 4.67 PPW (128 points) and 37.35 PPW (1024 points). A very good agreement has been observed between these two results. Note that the number of boundary nodes in the FEM is 2168, 16.9 times bigger than 128, which indicates the efficiency of this hybrid FEM/SIM method clearly.

5.4 Conclusion

In this chapter, we extend SIM to the problems having a scatterer residing in several layers of a multilayer medium. Based on this improvement, we use the SIM as a novel radiation boundary condition, to truncate the computational domain of the finite-element method. This radiation boundary condition is easy to implement comparing to PML and other traditional RBCs. It needs less extra memory and reduces computational complexity compared to using the method of moments (MOM). Moreover,

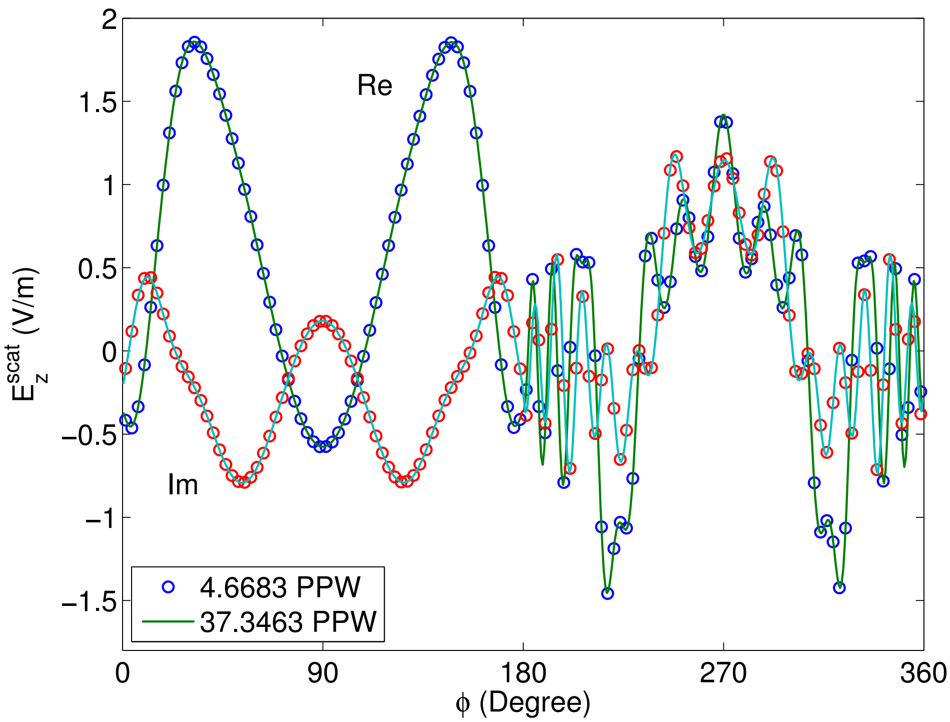

Figure 5.10: The scattered field along the radiation boundary for a MOSFET like scatterer.

once we calculate the layered media Green's function for RBC, we can use it for several times, for any kind of object inside the artificial boundary. This hybrid FEM/SIM method is suitable for objects with arbitrary boundaries and structures. Numerical results show an overall 2nd-order convergence because of using linear basis and testing functions for the FEM part. The number of points on the radiation boundary is only around 5 points per wavelength, thus giving substantial saving in memory and CPU time requirements. Applications are also demonstrated for inhomogeneous and composite structures.

Chapter 6

3D Surface Integral Equation and its Method of Moments Solution for Layered Media

Method of Moments (MoM) is a very well known technique to solve linear complex problems and it has been successfully implemented in different areas of science for decades. From the very general point of view, MoM can be viewed as a translation of an integral equation problem to a system of simultaneous linear equations by defining the unknown quantities in terms of a set of basis functions and testing the integral equation. In this direction, the spectral integral method, which is presented in Chapter 3, can be thought as a very high order MoM. Even though, this method is quite old, it is still very popular and widely used in electromagnetics. The main reason of this popularity comes from MoM's applicability to unbounded geometries. In other words, it does not require discretizing the exterior and/or inner domains; only the boundary of a homogeneous scatterer needs to be discretized. However, this approach is only valid for homogeneous case and the impedance matrix, which needs to be inverted to obtain the solution, is a dense matrix.

In the last decade, many researchers have been focused on the modeling of microstrip antennas and printed circuits. They try to analyze integrated circuit designs from the electromagnetic point of view. Many of them used the layered medium Green's functions and MoM, mostly only for metallic patches and wires embedded in a layered medium. When we assume that the printed circuit elements are all perfectly electrical conductors (PEC), this approach is valid and effective. In some other applications, scattering from dielectric materials is of interest. However, as it is explained in the following chapter, our primary target is the development of a 3D hybrid finite element/boundary element method which can handle inhomogeneity in a layered medium. In order to achieve this goal, we need a 3D surface integral equation (SIE) solver for layered media. Even though we are only interested in the exterior part of the surface integral equation formulation for the hybrid method, it is helpful to have an SIE solver for layered media, hence we can check the accuracy of the formulation and implementation and later we can compare our hybrid method's results with the SIE solver's solution for homogeneous scatterers.

In this chapter, first, the surface equivalence principle is presented. Based on this principle, the surface integral equations for both homogeneous and multilayered background are given. Then, some implementation details, such as singularity treatment, meshing, and interpolation, are discussed. Finally, the validity of the implementation is supported with numerical examples.

The presented Method of Moment solution of the surface integral equation is valid for both 3D dielectric and PEC materials embedded in homogeneous space or in a layered medium. In terms of the formulation and the used basis functions, different than previous chapters, there is nothing new in this chapter. All the formulas and other details can be found in the referenced sources. The materials are presented here as a background of the next chapter.

6.1 Surface Equivalence Principle

According to the *Uniqueness Theorem*, a field in a lossy region is uniquely specified by the sources within the region plus the tangential components of the electric or magnetic field or the combination of them over the boundary by sharing different parts of the total boundary. In other words, if the tangential electric and magnetic fields are completely known over a closed surface, the fields can be determined in the source-free region. In this direction, one can choose the equivalent sources which makes fields inside (outside) the closed surface vanish and fields outside (inside) equal to the total fields produced by the actual sources.

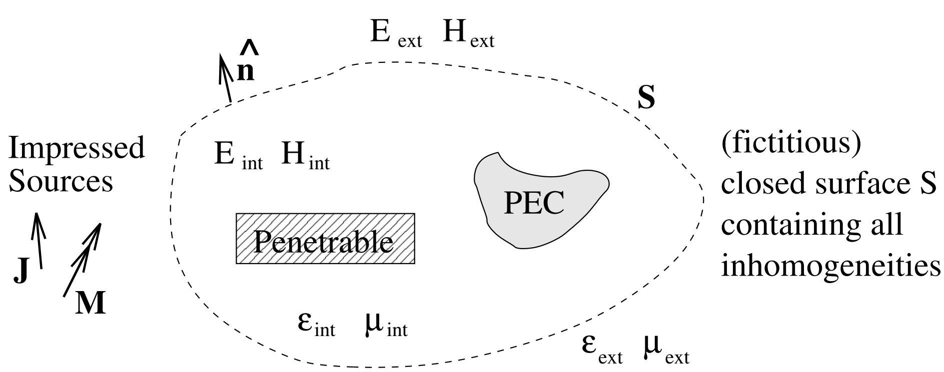

Figure 6.1: Description of Huygen's surface equivalence theorem. A fictitious closed surface S, containing all the inhomogeneities, divide the problem domain into two: *exterior* and *interior*.

The primary task is to replace the original problem in Fig. 6.1 with an equivalent that yields the same fields $\mathbf{E}_{ext}$ and $\mathbf{H}_{ext}$ exterior to the scatterer (equivalent exterior problem). Since interior fields are of no interest for the equivalent exterior problem, an obvious (but not the only possible) choice is to set them to zero (i.e., $\mathbf{E}_{int}$=$\mathbf{H}_{int}$=0 inside the surface S). For vanishing interior fields, the material properties can be selected arbitrarily, but the fields must satisfy the boundary conditions. Thus on the imaginary surface there must exist the equivalent surface current densities, $\mathbf{J}_s^{ext,eqv}$

and $\mathbf{M}_s^{ext,eqv}$, such that

$$\mathbf{J}_s^{ext,eqv} = \hat{\mathbf{n}} \times \mathbf{H}_{ext} = \hat{\mathbf{n}} \times \mathbf{H}^+ = \hat{\mathbf{n}} \times \mathbf{H}, \qquad (\mathbf{x} \in S^+) \tag{6.1a}$$

$$\mathbf{M}_s^{ext,eqv} = -\hat{\mathbf{n}} \times \mathbf{E}_{ext} = -\hat{\mathbf{n}} \times \mathbf{E}^+ = -\hat{\mathbf{n}} \times \mathbf{E}, \qquad (\mathbf{x} \in S^+) \tag{6.1b}$$

where $\hat{\mathbf{n}}$ is the unit normal to the surface S. The equivalent exterior problem defined this way is illustrated in Fig. 6.2. (It should be emphasized again that the equivalent problem is not unique since the interior fields and material properties could be selected arbitrarily).

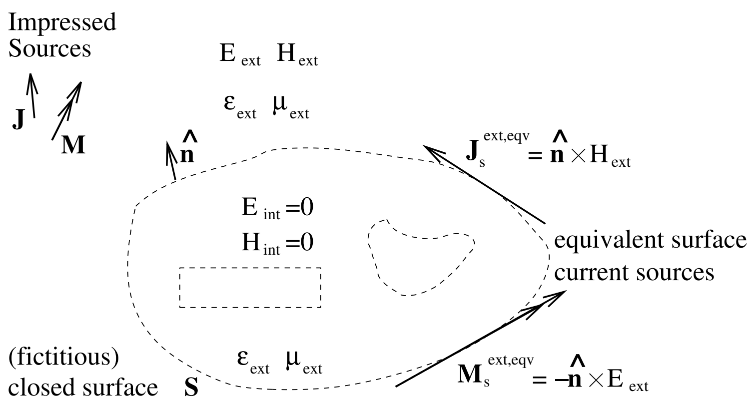

Figure 6.2: Equivalent exterior problem of Fig. 6.1. The interior fields are of no interest, $\mathbf{E}_{int}$ and $\mathbf{H}_{int}$ are set to zero inside the surface S.

The combination of the original (impressed) sources and the equivalent sources produces the exterior fields, $\mathbf{E} = \mathbf{E}_{ext}$ and $\mathbf{H} = \mathbf{H}_{ext}$, which are identical to those of the original problem in Fig. 6.1. The equivalent sources completely account for the effects of the scatterer (i.e., the effects due to the inhomogeneities with respect to the background). Therefore, the fields produced by the equivalent sources are denoted as scattered fields. The interior fields are not identical to those of the original problem; in fact, null fields are produced throughout the interior by the combination of original and equivalent sources. This result is sometimes called extinction theorem since the equivalent sources produce fields $\mathbf{E}_{int}$ and $\mathbf{H}_{int}$ compensating for the interior fields due to the impressed sources.

Similarly, for interior equivalent problem, one can set the exterior fields to zero, and can define the equivalent surface current densities as follow

$$\mathbf{J}_s^{int,eqv} = (-\hat{\mathbf{n}}) \times \mathbf{H}_{ext} = -\hat{\mathbf{n}} \times \mathbf{H}^- = -\hat{\mathbf{n}} \times \mathbf{H}, \qquad (\mathbf{x} \in S^-), \tag{6.2a}$$

$$\mathbf{M}_s^{int,eqv} = -(-\hat{\mathbf{n}}) \times \mathbf{E}_{ext} = \hat{\mathbf{n}} \times \mathbf{E}^- = \hat{\mathbf{n}} \times \mathbf{E}, \qquad (\mathbf{x} \in S^-). \tag{6.2b}$$

Note that $\mathbf{J}_s^{ext,eqv} = -\mathbf{J}_s^{int,eqv}$ and $\mathbf{M}_s^{ext,eqv} = -\mathbf{M}_s^{int,eqv}$. These equivalent electric and magnetic surface currents are the unknowns to be determined by using surface integral equations.

6.2 3D Surface Integral Equation: Free Space

Assume that there is an arbitrarily shaped homogeneous object with the surface S, electrical permittivity ϵ_2, and permeability μ_2 in a homogeneous background described with ϵ_1 and μ_1, depicted as Fig. 6.3. Assume that the object is illuminated with the incident electric and magnetic fields, $\mathbf{E}^{inc}$ and $\mathbf{H}^{inc}$ respectively, which create the induced electric and magnetic surface currents, $\mathbf{J}_s$ and $\mathbf{M}_s$.

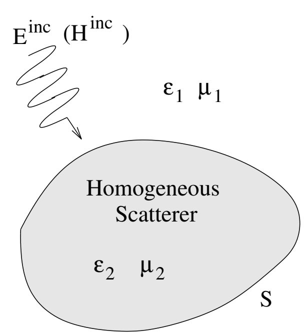

Figure 6.3: Arbitrarily shaped homogeneous dielectric object in homogeneous background.

When we use the continuity of the tangential component of the electric field along the boundary S and $\mathbf{J}_s = \mathbf{J}_s^{ext,eqv} = -\mathbf{J}_s^{int,eqv}$ and $\mathbf{M}_s = \mathbf{M}_s^{ext,eqv} = -\mathbf{M}_s^{int,eqv}$, we obtain a set of integral equations for the unknown electric and magnetic currents, which is known as PMCHW formulation derived by Poggio, Miller, Chang, Harrington, and Wu [93, 94, 95], as follows

$$\begin{aligned} \hat{n} \times \mathbf{E}^{inc}(\mathbf{r}) =& \hat{n} \times \{ j\omega \left[\mathbf{A}_1(\mathbf{r}) + \mathbf{A}_2(\mathbf{r}) \right] + \left[\nabla \Phi_1(\mathbf{r}) + \nabla \Phi_2(\mathbf{r}) \right] \\ &+ \nabla \times \left[\mathbf{F}_1(\mathbf{r})/\epsilon_1 + \mathbf{F}_2(\mathbf{r})/\epsilon_2 \right] \} \quad \text{on } S, \end{aligned} \tag{6.3}$$

$$\begin{aligned} \hat{n} \times \mathbf{H}^{inc}(\mathbf{r}) =& \hat{n} \times \{ j\omega \left[\mathbf{F}_1(\mathbf{r}) + \mathbf{F}_2(\mathbf{r}) \right] + \left[\nabla U_1(\mathbf{r}) + \nabla U_2(\mathbf{r}) \right] \\ &- \nabla \times \left[\mathbf{A}_1(\mathbf{r})/\mu_1 + \mathbf{A}_2(\mathbf{r})/\mu_2 \right] \} \quad \text{on } S. \end{aligned} \tag{6.4}$$

where

$$\mathbf{A}_i(\mathbf{r}) = \frac{\mu_i}{4\pi} \int_S \mathbf{J}(\mathbf{r}') G_i(\mathbf{r}, \mathbf{r}') d\mathbf{S}', \tag{6.5}$$

$$\mathbf{F}_i(\mathbf{r}) = \frac{\epsilon_i}{4\pi} \int_S \mathbf{M}(\mathbf{r}') G_i(\mathbf{r}, \mathbf{r}') d\mathbf{S}', \tag{6.6}$$

$$\Phi_i(\mathbf{r}) = -\frac{1}{4\pi j\omega\epsilon_i} \int_S \nabla_s' \cdot \mathbf{J}(\mathbf{r}') G_i(\mathbf{r}, \mathbf{r}') d\mathbf{S}', \tag{6.7}$$

$$U_i(\mathbf{r}) = -\frac{1}{4\pi j\omega\mu_i} \int_S \nabla_s' \cdot \mathbf{M}(\mathbf{r}') G_i(\mathbf{r}, \mathbf{r}') d\mathbf{S}', \tag{6.8}$$

and free space Green's function for both homogeneous background ($i = 1$) and homogeneous object ($i = 2$)

$$G_i(\mathbf{r}) = \frac{e^{-jk_i|\mathbf{r}-\mathbf{r}'|}}{|\mathbf{r} - \mathbf{r}'|}. \tag{6.9}$$

Note that PMCHW formulation uses the superposition principle as well, given by

$$\mathbf{E}^{tot} = \mathbf{E}^{inc} + \mathbf{E}^{scat}, \qquad \mathbf{H}^{tot} = \mathbf{H}^{inc} + \mathbf{H}^{scat}. \tag{6.10}$$

In order to solve (6.3) and (6.4) numerically, the Method of Moments (MoM) is used which is also known in other fields as the method of projections or method of weighted residuals [96]. In this method, first, the unknown surface currents, $\mathbf{J}_s$ and $\mathbf{M}_s$, are expanded in terms of the basis functions $\mathbf{f}_n(\mathbf{r})$ on S, the surface of the homogeneous scatterer, as follows,

$$\mathbf{J}_s(\mathbf{r}') = \sum_{n=1}^{N_s} I_n \mathbf{f}_n(\mathbf{r}'), \qquad \mathbf{M}_s(\mathbf{r}') = \eta_0 \sum_{n=1}^{N_s} M_n \mathbf{f}_n(\mathbf{r}'), \qquad \mathbf{r}' \in S, \tag{6.11}$$

where N_s is the total number of edges on S, η_0 is characteristic impedance in free space. For Galerkin type MoM, the testing functions are chosen the same as the basis functions and we test (6.3) with $\mathbf{f}_m$ and (6.4) with $\eta_0 \mathbf{f}_m$, we obtain a $2N_s \times 2N_s$ matrix equation given by

$$\mathbf{ZI} = \mathbf{V}, \tag{6.12}$$

where

$$\mathbf{Z} = \begin{bmatrix} Z_{mn}^{JJ} & C_{mn}^{JM} \\ D_{mn}^{JJ} & Y_{mn}^{JM} \end{bmatrix}, \qquad \mathbf{I} = \begin{bmatrix} I_n \\ M_n \end{bmatrix}, \qquad \mathbf{V} = \begin{bmatrix} V_m \\ W_m \end{bmatrix}. \tag{6.13}$$

$$V_m = \int_{T_m} \mathbf{f}_m(\mathbf{r}) \cdot \mathbf{E}^{inc}(\mathbf{r}) d\mathbf{r}, \qquad W_m = \int_{T_m} \mathbf{f}_m(\mathbf{r}) \cdot \eta_0 \mathbf{H}^{inc}(\mathbf{r}) d\mathbf{r}. \tag{6.14}$$

$$Z_{mn}^{JJ} = j\omega \int_{T_m} \mathbf{f}_m(\mathbf{r}) \cdot \left[\mathbf{A}_{1mn} + \mathbf{A}_{2mn}\right] d\mathbf{r} - \int_{T_m} \nabla_s \cdot \mathbf{f}_m(\mathbf{r}) \left[\Phi_{1mn} + \Phi_{2mn}\right] d\mathbf{r} \tag{6.15}$$

$$Y_{mn}^{MM} = j\omega\eta_0^2 \int_{T_m} \mathbf{f}_m(\mathbf{r}) \cdot \left[\frac{\mathbf{A}_{1mn}}{\eta_1^2} + \frac{\mathbf{A}_{2mn}}{\eta_2^2}\right] d\mathbf{r} - \eta_0^2 \int_{T_m} \nabla_s \cdot \mathbf{f}_m(\mathbf{r}) \left[\frac{\Phi_{1mn}}{\eta_1^2} + \frac{\Phi_{2mn}}{\eta_2^2}\right] d\mathbf{r} \tag{6.16}$$

$$C_{mn}^{JM} = \eta_0 \int_{T_m} \mathbf{f}_m(\mathbf{r}) \cdot \nabla \times \left[\frac{\mathbf{A}_{1mn}}{\mu_1} + \frac{\mathbf{A}_{2mn}}{\mu_2}\right] d\mathbf{r} = -D_{mn}^{MJ} \tag{6.17}$$

$$\mathbf{A}_{imn} = \frac{\mu_i}{4\pi} \int_{T_n} \mathbf{f}_n(\mathbf{r}') G_i(\mathbf{r}_m, \mathbf{r}') d\mathbf{S}', \qquad i = 1, 2 \tag{6.18}$$

$$\Phi_{imn} = -\frac{1}{4\pi j\omega\epsilon_i}\int_{T_n} \nabla'_s \cdot \mathbf{f}_n(\mathbf{r}')G_i(\mathbf{r}_m, \mathbf{r}')d\mathbf{S}'. \tag{6.19}$$

where T_m and T_n are the supports of testing and basis functions, respectively.

The singularity of the above integrals is one of the most important part of the whole procedure. For the singularity existing in (6.15), (6.16), (6.18), and (6.19), the Duffy Transformation is used, as explained in the following section. However, before giving some details about Duffy Transformation, it should be noted that for (6.17), we can use the "Principal Value" integration as follows

$$\begin{aligned}\nabla \times \mathbf{A}_{1mn} &= \nabla \times \frac{\mu_1}{4\pi}\int_{T_n} \mathbf{f}_n(\mathbf{r}')G_1(\mathbf{r}_m, \mathbf{r}')d\mathbf{S}' \\ &= \frac{\mu_1}{4\pi}\left\{-\frac{1}{2}\hat{n} \times \mathbf{f}_n + \nabla \times \int_{PV,T_n} \mathbf{f}_n(\mathbf{r}')G_1(\mathbf{r}_m, \mathbf{r}')d\mathbf{S}'\right\},\end{aligned} \tag{6.20}$$

$$\begin{aligned}\nabla \times \mathbf{A}_{2mn} &= \nabla \times \frac{\mu_2}{4\pi}\int_{T_n} \mathbf{f}_n(\mathbf{r}')G_2(\mathbf{r}_m, \mathbf{r}')d\mathbf{S}' \\ &= \frac{\mu_2}{4\pi}\left\{\frac{1}{2}\hat{n} \times \mathbf{f}_n + \nabla \times \int_{PV,T_n} \mathbf{f}_n(\mathbf{r}')G_2(\mathbf{r}_m, \mathbf{r}')d\mathbf{S}'\right\},\end{aligned} \tag{6.21}$$

$$\begin{aligned}\nabla \times \left[\frac{\mathbf{A}_{1mn}}{\mu_1} + \frac{\mathbf{A}_{2mn}}{\mu_2}\right] =& \frac{1}{4\pi}\left\{\nabla \times \int_{PV,T_n} \mathbf{f}_n(\mathbf{r}')G_1(\mathbf{r}_m, \mathbf{r}')d\mathbf{S}'\right. \\ &\left. + \nabla \times \int_{PV,T_n} \mathbf{f}_n(\mathbf{r}')G_2(\mathbf{r}_m, \mathbf{r}')d\mathbf{S}'\right\}.\end{aligned} \tag{6.22}$$

6.3 3D Surface Integral Equation: Layered Media

The definition of the planarly layered medium is given in Chapter 2. Assume that an object embedded in a planar stratified medium is illuminated by primary (impressed) sources located outside the scatterer in the top layer of a stratified medium. It is known that the scatterer can be replaced by (equivalent) induced sources radiating into a predefined background medium (e.g., the planar stratified medium of interest here). Consider splitting the fields into two parts, one associated with the primary sources and another due to the equivalent surface current sources. The fields produced by the primary sources in the absence of the scatterer (i.e., the fields produced in the stratified medium for the scatterer not present) is denoted as the incident electric and magnetic fields, $\mathbf{E}^{inc}$ and $\mathbf{H}^{inc}$, respectively.

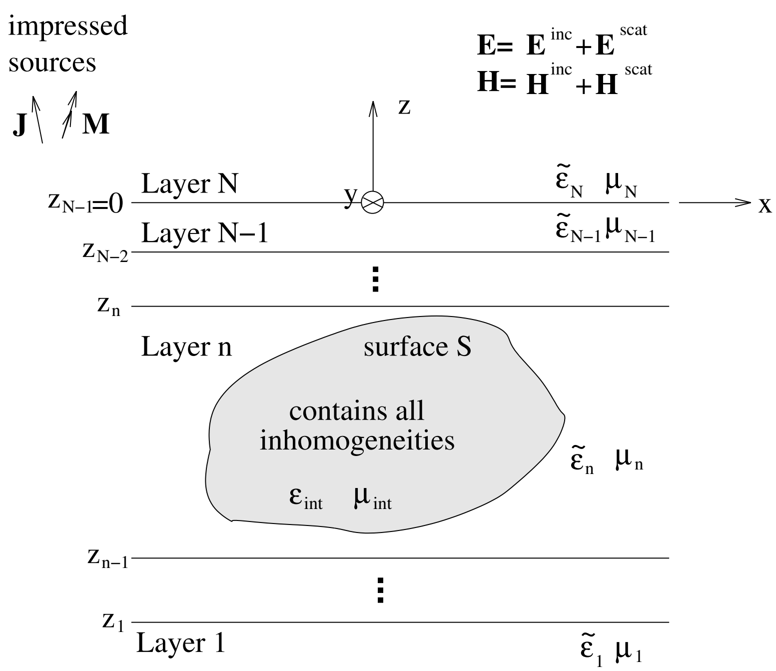

Figure 6.4: General scattering problem for an object buried in a layered media.

For the equivalent exterior problem, the secondary induced sources also radiate into the stratified background environment and produce the scattered fields $\mathbf{E}^{scat}$ and $\mathbf{H}^{scat}$. The superposition of incident and scattered fields

$$\mathbf{E}(\mathbf{r}) = \mathbf{E}^{inc}(\mathbf{r}) + \mathbf{E}^{scat}(\mathbf{r}) \tag{6.23a}$$

$$\mathbf{H}(\mathbf{r}) = \mathbf{H}^{inc}(\mathbf{r}) + \mathbf{H}^{scat}(\mathbf{r}) \tag{6.23b}$$

yields the total fields in the presence of the scatterer. At this step of our work, we deal with homogeneous scatterers only, since in the following step, the surface integral equation will be used as a radiation boundary condition.

6.3.1 Integral Equations for a PEC Scatterer in a Layered Medium

Assume that the arbitrarily shaped PEC object resides in the ith layer of the multi-layered medium. We know that the magnetic current cannot exist on the surface of a PEC scatterer, $\mathbf{M}_s^{ext,eqv} = 0$. Moreover, for $\mathbf{r} \in \mathbf{S}$,

$$\mathbf{J}_s^{ext,eqv}(\mathbf{r}) = (-\hat{\mathbf{n}}) \times \mathbf{H}_{ext}(\mathbf{r}), \tag{6.24}$$

$$\hat{\mathbf{n}} \times \mathbf{E}^{inc}(\mathbf{r}) = -\hat{\mathbf{n}} \times \mathbf{E}^{scat}(\mathbf{r}). \tag{6.25}$$

The relationship between the magnetic vector potential and electric current density can be written as

$$\mathbf{A}(\mathbf{r}) = \int_S \bar{\mathbf{G}}^A(\mathbf{r}|\mathbf{r}') \cdot \mathbf{J}(\mathbf{r}') dS', \tag{6.26}$$

where $\bar{\mathbf{G}}^A$ is the dyadic Green's function explained in Chapter 2. By using this definition, Eq. (6.25) can be written as

$$\hat{\mathbf{n}} \times \mathbf{E}^{inc}(\mathbf{r}) = \hat{\mathbf{n}} \times j\omega \sum_i \mu_i \int_{S_i} \left(\bar{\mathbf{I}} + \frac{\nabla\nabla}{k_i^2} \right) \cdot \bar{\mathbf{G}}^A(\mathbf{r}|\mathbf{r}') \cdot \mathbf{J}(\mathbf{r}') dS', \ \mathbf{r} \in S. \tag{6.27}$$

This equation is called the vector-potential Electric-Field Integral Equation.

By using the corresponding scalar potential the Mixed-Potential EFIE can be written as

$$\begin{aligned} \hat{\mathbf{n}} \times \mathbf{E}^{inc}(\mathbf{r}) =& \hat{\mathbf{n}} \times \Big[j\omega \sum_i \mu_i \int_{S_i} \bar{\mathbf{K}}^A(\mathbf{r}|\mathbf{r}') \cdot \mathbf{J_s}(\mathbf{r}') dS' \\ & - \sum_i \frac{\nabla}{j\omega\epsilon_i} \int_{S_i} \bar{\mathbf{K}}^\Phi(\mathbf{r}|\mathbf{r}') \nabla_s' \cdot \mathbf{J_s}(\mathbf{r}') dS' \Big], \ \mathbf{r} \in S. \end{aligned} \tag{6.28}$$

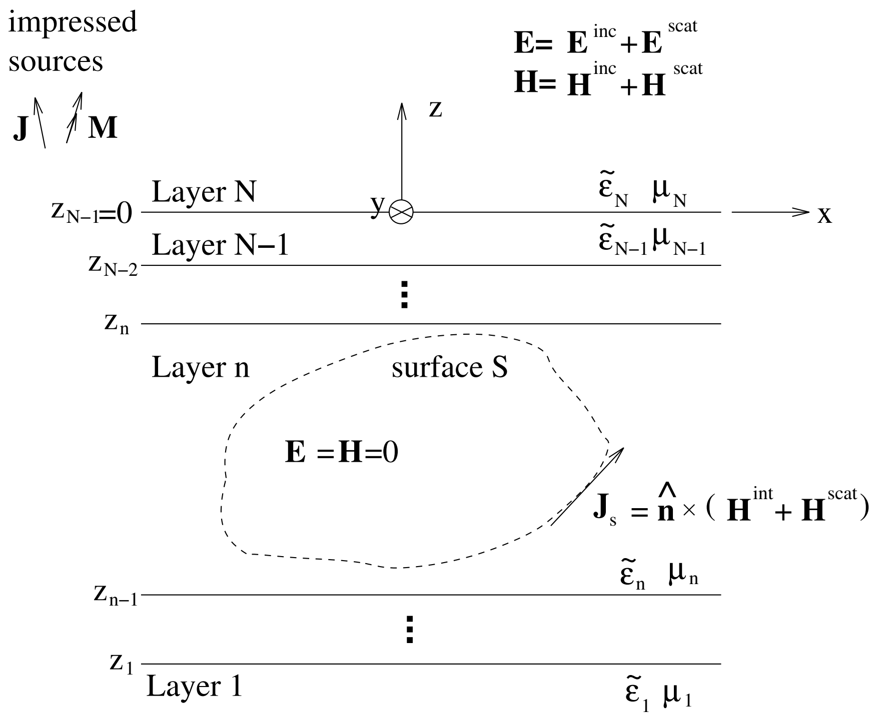

Figure 6.5: Equivalent exterior problem for a PEC object.

Note that the definitions of $\bar{\mathbf{K}}^A$ and $\bar{\mathbf{K}}^\Phi$ are presented in Chapter 2.

Similarly, the magnetic field integral equation can be derived from the boundary conditions as follows

$$\begin{aligned}\hat{\mathbf{n}} \times \mathbf{H}^{inc}(\mathbf{r}) =& \mathbf{J_s}(\mathbf{r}') - \hat{\mathbf{n}} \times \mathbf{H}^{scat}(\mathbf{r}) \\ =& \mathbf{J_s}(\mathbf{r}') - \hat{\mathbf{n}} \times \int_S \bar{\mathbf{G}}^A(\mathbf{r}|\mathbf{r}') \cdot \mathbf{J}(\mathbf{r}')dS', \mathbf{r} \in S^+.\end{aligned} \tag{6.29}$$

On the other hand, since $\hat{\mathbf{n}} \times \mathbf{E}^{inc}$ gives the tangential component of the field on the surface, one can write the following equation by using an arbitrary unit vector $\hat{\mathbf{t}}$

tangential to the surface

$$\hat{\mathbf{t}} \cdot \mathbf{E}^{inc}(\mathbf{r}) = -\hat{\mathbf{t}} \cdot \mathbf{E}^{scat}(\mathbf{r}) = \hat{\mathbf{t}} \cdot j\omega\Big(\bar{\mathbf{I}} + \frac{\nabla\nabla}{k_i^2}\Big) \cdot \mathbf{A}$$

$$= \hat{\mathbf{t}} \cdot \Big[j\omega \sum_i \mu_i \int_{S_i} \bar{\mathbf{K}}^A(\mathbf{r}|\mathbf{r}') \cdot \mathbf{J}_\mathbf{s}(\mathbf{r}')dS' - \sum_i \frac{\nabla}{j\omega\epsilon_i} \int_{S_i} \bar{\mathbf{K}}^\Phi(\mathbf{r}|\mathbf{r}')\nabla_s' \cdot \mathbf{J}_\mathbf{s}(\mathbf{r}')dS'\Big], \mathbf{r} \in S. \tag{6.30}$$

The given EFIE and MFIE equations are derived from the boundary conditions for Maxwell's equations. Note that the MFIE cannot be used for open surfaces and both EFIE and MFIE have interior resonance problem, which means the solution is not unique at certain frequencies corresponding to the resonant frequencies of the cavity inside the PEC scatterer surface. There are several techniques to overcome this problem, and one of them is the combined field integral equation (CFIE), which is given by

$$\hat{\mathbf{t}} \cdot \Big\{\alpha\mathbf{E}^{inc} + \eta_i(1-\alpha)\hat{\mathbf{n}} \times \mathbf{H}^{inc}\Big\} = \hat{\mathbf{t}} \cdot \Big\{-\alpha\mathbf{E}^{scat} + \eta_i(1-\alpha)\Big[\mathbf{J}_s - \hat{\mathbf{n}} \times \mathbf{H}^{inc}(\mathbf{r} \in S^+)\Big]\Big\}, \tag{6.31}$$

where $0 \leq \alpha \leq 1$.

6.3.2 Integral Equations for Homogeneous Penetrable Scatterer in a Layered Medium

In order to simplify the problem, first let us define new operators for the equivalent exterior problem which is depicted in Fig. 6.6.

$$\begin{aligned} \mathcal{L}_{EJ}^{ext}\{\mathbf{J}_s\} &= -j\omega\mu_i \int_S \Big(\bar{\mathbf{I}} + \frac{\nabla\nabla}{k_i^2}\Big) \cdot \bar{\mathbf{G}}^A(\mathbf{r}|\mathbf{r}') \cdot \mathbf{J}_\mathbf{s}(\mathbf{r}')dS' \\ &= -j\omega\mu_i \int_S \bar{\mathbf{K}}^A(\mathbf{r}|\mathbf{r}') \cdot \mathbf{J}_\mathbf{s}(\mathbf{r}')dS' + \frac{\nabla}{j\omega\epsilon_i} \int_S K^{\Phi e}(\mathbf{r}|\mathbf{r}')\nabla_s' \cdot \mathbf{J}_\mathbf{s}(\mathbf{r}')dS' \end{aligned} \tag{6.32}$$

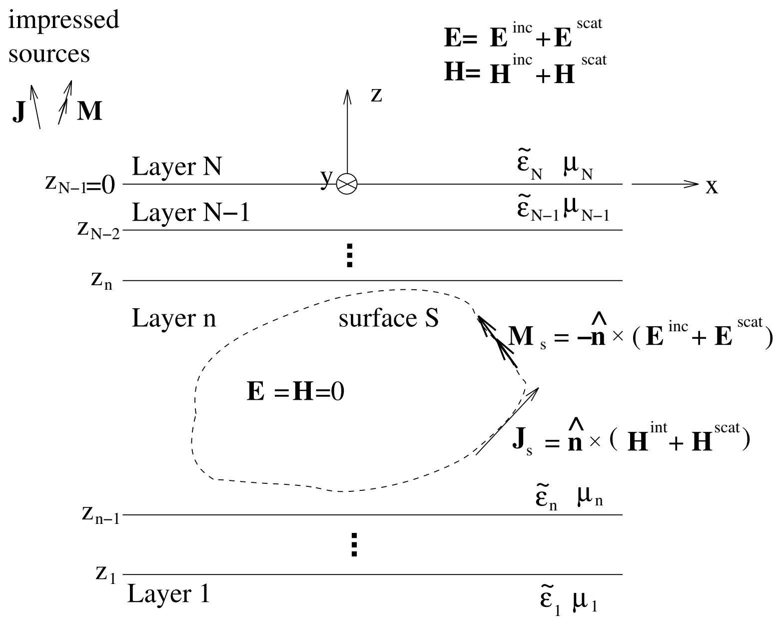

Figure 6.6: The equivalent exterior problem for a homogeneous penetrable object. The interior fields are of no interest, $\mathbf{E}_{int}$ and $\mathbf{H}_{int}$ are set to zero inside the surface S

$$\mathcal{L}_{HJ}^{ext}\{\mathbf{J}_s\} = \nabla \times \int_S \bar{\mathbf{G}}^A(\mathbf{r}|\mathbf{r}') \cdot \mathbf{J_s}(\mathbf{r}')dS' = \int_S \nabla \times \bar{\mathbf{G}}^A(\mathbf{r}|\mathbf{r}') \cdot \mathbf{J_s}(\mathbf{r}')dS' \tag{6.33}$$

$$\mathcal{L}_{EM}^{ext}\{\mathbf{M}_s\} = -\nabla \times \int_S \bar{\mathbf{G}}^F(\mathbf{r}|\mathbf{r}') \cdot \mathbf{M_s}(\mathbf{r}')dS' = -\int_S \nabla \times \bar{\mathbf{G}}^A(\mathbf{r}|\mathbf{r}') \cdot \mathbf{M_s}(\mathbf{r}')dS' \tag{6.34}$$

$$\begin{aligned}\mathcal{L}_{HM}^{ext}\{\mathbf{M}_s\} &= -j\omega\epsilon_i \int_S \left(\bar{\mathbf{I}} + \frac{\nabla\nabla}{k_i^2}\right) \cdot \bar{\mathbf{G}}^F(\mathbf{r}|\mathbf{r}') \cdot \mathbf{M_s}(\mathbf{r}')dS' \\ &= -j\omega\epsilon_i \int_S \bar{\mathbf{K}}^F(\mathbf{r}|\mathbf{r}') \cdot \mathbf{M_s}(\mathbf{r}')dS' + \frac{\nabla}{j\omega\mu_i}\int_S K^{\Phi m}(\mathbf{r}|\mathbf{r}')\nabla_s' \cdot \mathbf{M_s}(\mathbf{r}')dS'\end{aligned} \tag{6.35}$$

where operator $\mathcal{L}_{PQ}$ will be used to calculate P type field (P is either E or M) due to Q type current source (Q is either J or M). The operators for the equivalent interior problem depicted in Fig. 6.7 are

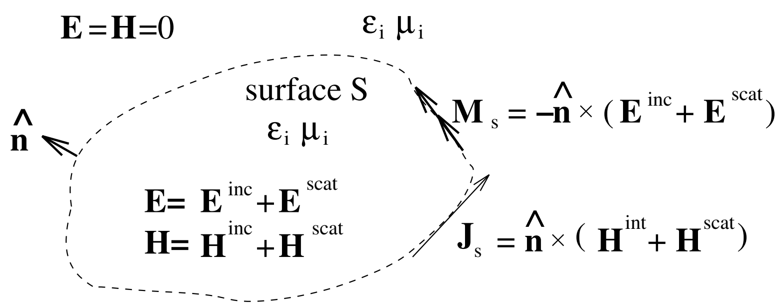

Figure 6.7: The equivalent interior problem for a homogeneous penetrable object. The exterior fields are of no interest, $\mathbf{E}_{ext}$ and $\mathbf{H}_{ext}$ are set to zero outside the surface S.

$$\begin{aligned}\mathcal{L}_{EJ}^{int}\{-\mathbf{J}_s\} &= j\omega\mu_i \int_S \Big(\bar{\mathbf{I}} + \frac{\nabla\nabla}{k_i^2}\Big) g(\mathbf{r}|\mathbf{r}') \cdot \mathbf{J_s}(\mathbf{r}')dS' \\ &= j\omega\mu_i \int_S g(\mathbf{r}|\mathbf{r}')\mathbf{J_s}(\mathbf{r}')dS' - \frac{\nabla}{j\omega\epsilon_i}\int_S g(\mathbf{r}|\mathbf{r}')\nabla_s' \cdot \mathbf{J_s}(\mathbf{r}')dS'\end{aligned} \tag{6.36}$$

$$\mathcal{L}_{HJ}^{int}\{-\mathbf{J}_s\} = -\nabla \times \int_S g(\mathbf{r}|\mathbf{r}')\mathbf{J_s}(\mathbf{r}')dS' = -\int_S \nabla g(\mathbf{r}|\mathbf{r}') \times \mathbf{J_s}(\mathbf{r}')dS' \tag{6.37}$$

$$\mathcal{L}_{EM}^{int}\{-\mathbf{M}_s\} = \nabla \times \int_S h(\mathbf{r}|\mathbf{r}')\mathbf{M_s}(\mathbf{r}')dS' = \int_S \nabla g(\mathbf{r}|\mathbf{r}') \times \mathbf{M_s}(\mathbf{r}')dS' \tag{6.38}$$

$$\begin{aligned}\mathcal{L}_{HM}^{int}\{-\mathbf{M}_s\} &= j\omega\epsilon_i \int_S \Big(\bar{\mathbf{I}} + \frac{\nabla\nabla}{k_i^2}\Big) g(\mathbf{r}|\mathbf{r}') \cdot \mathbf{M_s}(\mathbf{r}')dS' \\ &= j\omega\epsilon_i \int_S g(\mathbf{r}|\mathbf{r}')\mathbf{M_s}(\mathbf{r}')dS' - \frac{\nabla}{j\omega\mu_i}\int_S g(\mathbf{r}|\mathbf{r}')\nabla_s' \cdot \mathbf{M_s}(\mathbf{r}')dS'\end{aligned} \tag{6.39}$$

By using these operators, for penetrable scatterers the EFIE can be written as

$$\hat{\mathbf{n}} \times \mathbf{E}^{inc}(\mathbf{r}) \mid_{\mathbf{r}\in S} = -\mathbf{M}_s(\mathbf{r}) \mid_{\mathbf{r}\in S} - \hat{\mathbf{n}} \times \Big[\mathcal{L}_{EJ}^{ext}\{\mathbf{J}_s\} + \mathcal{L}_{EM}^{ext}\{\mathbf{M}_s\}\Big]_{\mathbf{r}\in S_+} \tag{6.40}$$

$$0 = \mathbf{M}_s(\mathbf{r}) \mid_{\mathbf{r}\in S} + \hat{\mathbf{n}} \times \Big[\mathcal{L}_{EJ}^{int}\{-\mathbf{J}_s\} + \mathcal{L}_{EM}^{int}\{-\mathbf{M}_s\}\Big]_{\mathbf{r}\in S_-} \tag{6.41}$$

Similarly, the MFIE can be written as

$$\hat{\mathbf{n}} \times \mathbf{H}^{inc}(\mathbf{r}) \mid_{\mathbf{r}\in S} = \mathbf{J}_s(\mathbf{r}) \mid_{\mathbf{r}\in S} - \hat{\mathbf{n}} \times \Big[\mathcal{L}_{HJ}^{ext}\{\mathbf{J}_s\} + \mathcal{L}_{HM}^{ext}\{\mathbf{M}_s\}\Big]_{\mathbf{r}\in S_+} \tag{6.42}$$

$$0 = -\mathbf{J}_s(\mathbf{r}) \mid_{\mathbf{r}\in S} + \hat{\mathbf{n}} \times \left[\mathcal{L}_{HJ}^{int}\{-\mathbf{J}_s\} + \mathcal{L}_{HM}^{int}\{-\mathbf{M}_s\} \right]_{\mathbf{r}\in S_-} \tag{6.43}$$

In this case, the CFIE can be written as follow

$$\begin{aligned} \hat{\mathbf{n}} \times \mathbf{E}^{inc}(\mathbf{r}) \mid_{\mathbf{r}\in S} = &- \hat{\mathbf{n}} \times \left[\mathcal{L}_{EJ}^{int}\{\mathbf{J}_s\} + \mathcal{L}_{EM}^{int}\{\mathbf{M}_s\} \right]_{\mathbf{r}\in S_-} \\ &- \hat{\mathbf{n}} \times \left[\mathcal{L}_{EJ}^{ext}\{\mathbf{J}_s\} + \mathcal{L}_{EM}^{ext}\{\mathbf{M}_s\} \right]_{\mathbf{r}\in S_+} \end{aligned} \tag{6.44}$$

$$\begin{aligned} \hat{\mathbf{n}} \times \mathbf{H}^{inc}(\mathbf{r}) \mid_{\mathbf{r}\in S} = &- \hat{\mathbf{n}} \times \left[\mathcal{L}_{HJ}^{int}\{\mathbf{J}_s\} + \mathcal{L}_{HM}^{int}\{\mathbf{M}_s\} \right]_{\mathbf{r}\in S_-} \\ &- \hat{\mathbf{n}} \times \left[\mathcal{L}_{HJ}^{ext}\{\mathbf{J}_s\} + \mathcal{L}_{HM}^{ext}\{\mathbf{M}_s\} \right]_{\mathbf{r}\in S_+} \end{aligned} \tag{6.45}$$

6.4 Some Implementation Issues

6.4.1 Duffy Transformation

As mentioned before, we have some integrals consisting of Green's functions and current elements. For example, the vector magnetic potential is given by

$$\mathbf{A}(\mathbf{r}) = \int_S \bar{\mathbf{G}}^A(\mathbf{r}|\mathbf{r}').\mathbf{J}(\mathbf{r}')dS'. \tag{6.46}$$

However, $\bar{\mathbf{G}}^A$ brings the singularity problem at ($\mathbf{r}$ = ($\mathbf{r}'$. To understand the situation, let us focus on the following example on the $\hat{xy}$ plane.

Assume that we want to calculate the vector magnetic potential at the origin as follows

$$h(0,0,0) = \int_S \frac{f(x,y)}{\sqrt{x^2+y^2}} dS = \int_0^1 \int_0^1 \frac{f(x,y)}{\sqrt{x^2+y^2}} dydx. \tag{6.47}$$

Clearly, the denumerator has the singularity at $(0,0)$. To overcome this problem, Duffy transformation [89] can be used. First, we need to divide the square into two

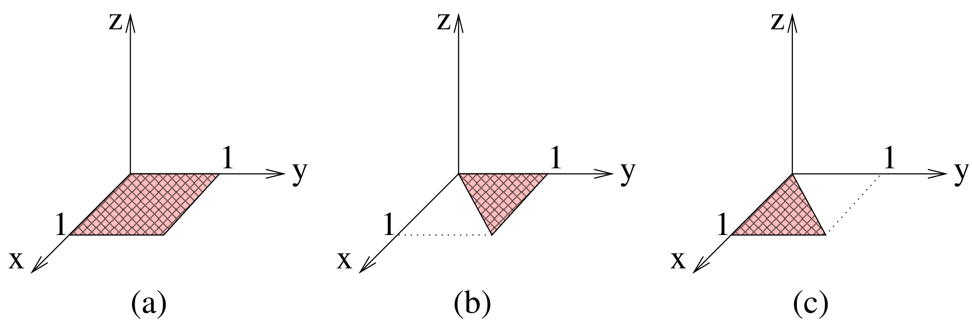

Figure 6.8: Duffy Transform example: singularity exists at the corner of a rectangular integration area.

triangles.

$$h(0,0,0) = \int_0^1 \int_0^x \frac{f(x,y)}{\sqrt{x^2+y^2}} dydx + \int_0^1 \int_0^y \frac{f(x,y)}{\sqrt{x^2+y^2}} dxdy \tag{6.48}$$

For the first term, let us change y element with $y = ux$ ($dy = xdu$), and for the second term change x element with $x = vy$ ($dx = ydv$)

$$\begin{aligned} h(0,0,0) &= \int_0^1 \int_0^1 x \frac{f(x,ux)}{\sqrt{x^2(1+u^2)}} dudx + \int_0^1 \int_0^1 y \frac{f(vy,y)}{\sqrt{y^2(1+v^2)}} dvdy \\ &= \int_0^1 \int_0^1 \frac{f(x,ux)}{\sqrt{1+u^2}} dudx + \int_0^1 \int_0^1 \frac{f(vy,y)}{\sqrt{1+v^2}} dvdy. \end{aligned} \tag{6.49}$$

Clearly, there is no more singularity problem.

6.4.2 Basis Functions and Numerical Integration

In this work, the surfaces of objects are modeled using planar triangular or rectangular patches and the RWG (Rao, Wilton, Glisson) basis functions [97] are used to approximate the surface currents.

Fig. 6.9 (a) shows two adjacent triangle patches forming one RWG basis, triangle T_n^+ and triangle T_n^- correspond to nth edge of a triangulated surface. The vector

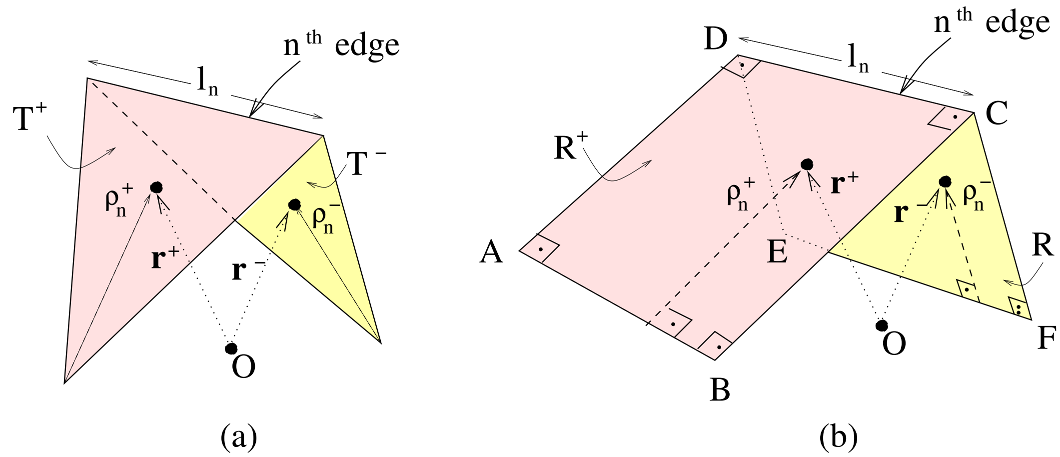

Figure 6.9: (a) Triangle pair and geometrical parameters. (b) Rectangle pair and geometrical parameters.

basis function associated with the nth edge is given by

$$\mathbf{f}_n(\mathbf{r}) = \begin{cases} \frac{l_n}{2A_n^+}\boldsymbol{\rho}_n^+, & \mathbf{r} \in T_n^+ \\ \frac{l_n}{2A_n^-}\boldsymbol{\rho}_n^-, & \mathbf{r} \in T_n^- \\ 0 & \text{otherwise,} \end{cases} \tag{6.50}$$

where l_n is the length of the edge and $A_n^{\pm}$ is the area of the triangle $T_n^{\pm}$, $\boldsymbol{\rho}_n^{\pm}$ is the position vector with respect to the free vertex of $T_n^{\pm}$. This set of basis functions is widely used by researchers in various fields of science. When we have a uniformly rectangulated planar surface, these RWG basis functions look like rooftops and this is why sometimes they are called rooftop basis functions.

There are several advantages of working with RWG basis functions; one of them is that the surface divergence of $\mathbf{f_n}$ is proportional to the surface charge density associated with the basis element as follows,

$$\nabla_s \cdot \mathbf{f}_n(\mathbf{r}) = \begin{cases} \frac{l_n}{A_n^+}, & \mathbf{r} \in T_n^+ \\ -\frac{l_n}{A_n^-}, & \mathbf{r} \in T_n^- \\ 0 & \text{otherwise,} \end{cases} \tag{6.51}$$

which means that the charge density is constant in each triangle pair, and the total charge is zero.

For the numerical integration, the Gaussian quadrature rule is followed as explained next. It is very well known that a quadrature rule is an approximation of the definite integral of a function, usually stated as a weighted sum of function values at specified points within the domain of integration. For example, assume that we want to integrate the function f over a rectangle ($\mathrm{x} \in [-1,1], \mathrm{y} \in [-1,1]$)

$$\int_{-1}^{1}\int_{-1}^{1} f(r,s)dr\ ds = \sum_{i=1}^{n} f(r_i, s_i)W_i \tag{6.52}$$

We can approximate the exact integral by a weighted sum of function values at specified points as it is given in the right hand side of (6.52). The higher is the number of specified points n, the higher is the accuracy.

The following tables [70, 71] provide Gaussian quadrature points and weights on a triangle and a quadrilateral, respectively.

6.4.3 Meshing

In order to discretize the surface of a scatterer into triangular elements, NETGEN (NETGEN/NGSolve V4.4, developed at Johannes Kepler University Linz, Austria), which can be obtained for free for academic purposes, can be used. However, one of our future targets is the implementation of the fast Fourier transform algorithm which requires a uniformly rectangulated mesh. Due to this reason, a simple mesh generator code is written in Fortran 77. Fig. 6.10 shows a simple example of this mesh generator code.

Table 6.1: Gaussian quadrature on a triangle.

n	W_i	ζ_1	ζ_2, ζ_3	M	p
1	1.000000000000000	0.333333333333333	0.333333333333333		1
			0.333333333333333	1	
3	0.333333333333333	0.666666666666667	0.166666666666667		2
			0.166666666666667	3	
4	-0.562500000000000	0.333333333333333	0.333333333333333		3
			0.333333333333333	1	
	0.520833333333333	0.600000000000000	0.200000000000000		
			0.200000000000000	3	
6	0.109951743655322	0.816847572980459	0.091576213509771		4
			0.091576213509771	3	
	0.223381589678011	0.108103018168070	0.445948490915965		
			0.445948490915965	3	
7	0.225000000000000	0.333333333333333	0.333333333333333		5
			0.333333333333333	1	
	0.125939180544827	0.797426985353087	0.101286507323456		
			0.101286507323456	3	
	0.132394152788506	0.059715871789770	0.470142064105115		
			0.470142064105115	3	
12	0.050844906370207	0.873821971016996	0.063089014491502		6
			0.063089014491502	3	
	0.116786275726379	0.501426509658179	0.249286745170910		
			0.249286745170910	3	
	0.082851075618374	0.636502499121399	0.310352451033785		
			0.053145049844816	6	

6.4.4 Interpolation for Layered Medium Implementation

Assume that we have a simple cuboid surface with N_x elements along the $\hat{\mathbf{x}}$-direction, N_y elements along the $\hat{\mathbf{y}}$-direction, and N_z elements along the $\hat{\mathbf{z}}$-direction. The total number of rectangular elements, N_{reg}, can be given as

$$N_{reg} = 2\left(N_x N_y + N_y N_z + N_z N_x\right).$$

If we use the first order rooftop basis functions, we need to calculate $N_{reg} \times$

Table 6.2: Gaussian quadrature on a quadrilateral for $n = 1, 4, 9$.

n	i	r_i	s_i	W_i
1	1	0	0	4
4	1	$-1/\sqrt{3}$	$-1/\sqrt{3}$	1
	2	$+1/\sqrt{3}$	$-1/\sqrt{3}$	1
	3	$-1/\sqrt{3}$	$+1/\sqrt{3}$	1
	4	$+1/\sqrt{3}$	$+1/\sqrt{3}$	1
9	1	$-\sqrt{3/5}$	$-\sqrt{3/5}$	25/81
	2	0	$-\sqrt{3/5}$	40/81
	3	$+\sqrt{3/5}$	$-\sqrt{3/5}$	25/81
	4	$-\sqrt{3/5}$	$-\sqrt{3/5}$	40/81
	5	0	0	64/81
	6	$+\sqrt{3/5}$	0	40/81
	7	$-\sqrt{3/5}$	$+\sqrt{3/5}$	25/81
	8	0	$+\sqrt{3/5}$	40/81
	9	$+\sqrt{3/5}$	$+\sqrt{3/5}$	25/81

N_{reg} sets of Green's functions for the impedance matrix. However, if we use *the interpolation* [49, 50], this number can be reduced dramatically. A uniformly meshed surface makes *the interpolation* technique very useful. The Sommerfeld integral sets can be precalculated for the required $(z|z')$ couples for a fixed range of ρ. Assume that we take N_ρ samples along the $\hat{\rho}$ direction, the Green's function sets is only

$$N_{intpol} = (N_z + 2)^2 \times N_{rho}.$$

if $N_x = N_y = N_z = 10 \rightarrow$	Regular Approach	Interpolation	Ratio
Number of GF Sets	90000 $(= 300^2)$	2160 $(= 12^2 \times 15)$	42

Note that for the selection of N_ρ, we follow the rule of "having at least 10 points per wavelength sampling density".

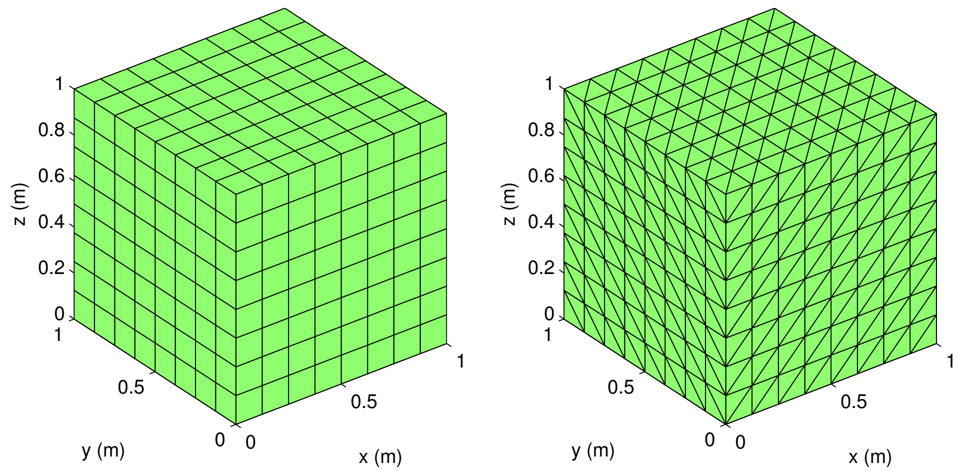

Figure 6.10: (a) $8 \times 8 \times 8$ squares are used to mesh the surface of a cube. (b) When we divide each square into two pieces, we obtain a simple uniform triangular surface mesh.

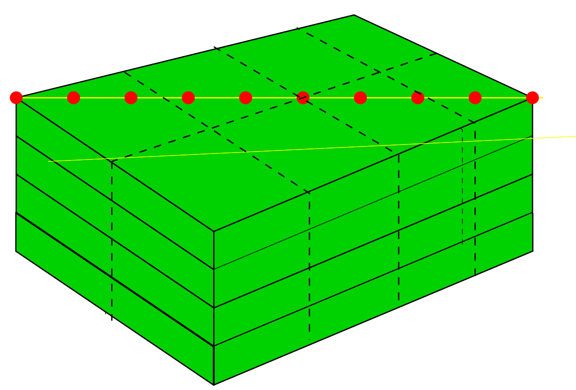

Figure 6.11: A uniformly meshed surface makes *the interpolation* technique very useful. The Sommerfeld integral sets can be precalculated for the required $(z|z')$ couples for a fixed range of ρ.

6.4.5 Required Green's Function Sets

As it is mentioned before, we can write the integral equations to link the electric and magnetic fields to electric and magnetic currents by using the Green's functions as

$$\mathbf{E}(\mathbf{r}) = \frac{1}{j\omega\epsilon}(\nabla\nabla \cdot +k^2)\langle \bar{\mathbf{G}}^{J}(\mathbf{r}, \mathbf{r}'); \mathbf{J}(\mathbf{r}')\rangle + \nabla \times \langle \bar{\mathbf{G}}^{M}(\mathbf{r}, \mathbf{r}'); \mathbf{M}(\mathbf{r}')\rangle, \tag{6.53}$$

$$\mathbf{H}(\mathbf{r}) = \frac{1}{j\omega\mu}(\nabla\nabla\cdot + k^2)\langle \bar{\mathbf{G}}^{\,M}(\mathbf{r},\mathbf{r}\,'); \mathbf{M}(\mathbf{r}')\rangle + \nabla\times\langle\bar{\mathbf{G}}^{\,J}(\mathbf{r},\mathbf{r}\,'); \mathbf{J}(\mathbf{r}')\rangle. \tag{6.54}$$

We can also define a new set dyadic Green's functions. For example,

$$\bar{\mathbf{G}}^{\,EM}(\mathbf{r},\mathbf{r}\,') = \nabla\times\bar{\mathbf{G}}^{\,M}(\mathbf{r},\mathbf{r}\,'), \tag{6.55}$$

$$\bar{\mathbf{G}}^{\,HJ}(\mathbf{r},\mathbf{r}\,') = \nabla\times\bar{\mathbf{G}}^{\,J}(\mathbf{r},\mathbf{r}\,'), \tag{6.56}$$

$$\bar{\mathbf{G}}^{\,EJ}(\mathbf{r},\mathbf{r}\,') = -j\omega\mu\left[\bar{\mathbf{I}} + \frac{\nabla\nabla}{k^2}\right]\cdot\bar{\mathbf{G}}^{\,J}(\mathbf{r},\mathbf{r}\,'), \tag{6.57}$$

$$\bar{\mathbf{G}}^{\,HM}(\mathbf{r},\mathbf{r}\,') = -j\omega\epsilon\left[\bar{\mathbf{I}} + \frac{\nabla\nabla}{k^2}\right]\cdot\bar{\mathbf{G}}^{\,M}(\mathbf{r},\mathbf{r}\,'). \tag{6.58}$$

where $\bar{\mathbf{G}}^{PQ}(\mathbf{r},\mathbf{r}\,')$ is the Dyadic Green's Function (DGF) relating P-type fields at $\mathbf{r}$ due to Q-type currents at $\mathbf{r}\,'$ [26]. Then, Eq.s (6.53) and (6.54) becomes

$$\mathbf{E}(\mathbf{r}) = \langle\bar{\mathbf{G}}^{\,EJ}(\mathbf{r},\mathbf{r}\,'); \mathbf{J}(\mathbf{r}')\rangle + \langle\bar{\mathbf{G}}^{\,EM}(\mathbf{r},\mathbf{r}\,'); \mathbf{M}(\mathbf{r}')\rangle, \tag{6.59}$$

$$\mathbf{H}(\mathbf{r}) = \langle\bar{\mathbf{G}}^{\,HJ}(\mathbf{r},\mathbf{r}\,'); \mathbf{J}(\mathbf{r}')\rangle + \langle\bar{\mathbf{G}}^{\,HM}(\mathbf{r},\mathbf{r}\,'); \mathbf{M}(\mathbf{r}')\rangle \tag{6.60}$$

By using the TLGF's defined in Chapter 3, the explicit forms of these 4 set of dyadic layered medium Green's functions can be written as follows

$$\tilde{G}^{EJ} = \begin{bmatrix} \frac{k_x^2}{k_\rho^2}\tilde{G}_{mi}^{TM,VI} + \frac{k_y^2}{k_\rho^2}\tilde{G}_{mi}^{TE,VI} & \frac{k_xk_y}{k_\rho^2}\left(\tilde{G}_{mi}^{TM,VI} - \tilde{G}_{mi}^{TE,VI}\right) & \frac{k_x}{\omega\epsilon_s}\tilde{G}_{mi}^{TM,VV} \\ \frac{k_xk_y}{k_\rho^2}\left(\tilde{G}_{mi}^{TM,VI} - \tilde{G}_{mi}^{TE,VI}\right) & \frac{k_x^2}{k_\rho^2}\tilde{G}_{mi}^{TE,VI} + \frac{k_y^2}{k_\rho^2}\tilde{G}_{mi}^{TM,VI} & \frac{k_y}{\omega\epsilon_s}\tilde{G}_{mi}^{TM,VV} \\ -\frac{k_x}{\omega\epsilon_m}\tilde{G}_{mi}^{TM,II} & -\frac{k_y}{\omega\epsilon_m}\tilde{G}_{mi}^{TM,II} & \frac{k_\rho^2}{\omega^2\epsilon_s\epsilon_m}\tilde{G}_{mi}^{TM,IV} \end{bmatrix} \tag{6.61}$$

$$\tilde{G}^{HJ} = \begin{bmatrix} \frac{k_xk_y}{k_\rho^2}\left(\tilde{G}_{mi}^{TM,II} - \tilde{G}_{mi}^{TE,II}\right) & \frac{k_x^2}{k_\rho^2}\tilde{G}_{mi}^{TE,II} + \frac{k_y^2}{k_\rho^2}\tilde{G}_{mi}^{TM,II} & \frac{k_y}{\omega\epsilon_s}\tilde{G}_{mi}^{TM,IV} \\ -\frac{k_x^2}{k_\rho^2}\tilde{G}_{mi}^{TM,II} - \frac{k_y^2}{k_\rho^2}\tilde{G}_{mi}^{TE,II} & \frac{k_xk_y}{k_\rho^2}\left(\tilde{G}_{mi}^{TE,II} - \tilde{G}_{mi}^{TM,II}\right) & -\frac{k_x}{\omega\epsilon_s}\tilde{G}_{mi}^{TM,IV} \\ \frac{k_y}{\omega\mu_m}\tilde{G}_{mi}^{TE,VI} & -\frac{k_x}{\omega\mu_m}\tilde{G}_{mi}^{TE,VI} & 0 \end{bmatrix} \tag{6.62}$$

$$\tilde{G}^{EM} = \begin{bmatrix} \frac{k_x k_y}{k_\rho^2}\left(\tilde{G}_{mi}^{TM,VV} - \tilde{G}_{mi}^{TE,VV}\right) & -\frac{k_x^2}{k_\rho^2}\tilde{G}_{mi}^{TM,VV} - \frac{k_y^2}{k_\rho^2}\tilde{G}_{mi}^{TE,VV} & -\frac{k_y}{\omega\mu_s}\tilde{G}_{mi}^{TE,VI} \\ \frac{k_x^2}{k_\rho^2}\tilde{G}_{mi}^{TE,VV} + \frac{k_y^2}{k_\rho^2}\tilde{G}_{mi}^{TM,VV} & \frac{k_x k_y}{k_\rho^2}\left(\tilde{G}_{mi}^{TE,VV} - \tilde{G}_{mi}^{TM,VV}\right) & \frac{k_x}{\omega\mu_s}\tilde{G}_{mi}^{TE,VI} \\ -\frac{k_y}{\omega\epsilon_m}\tilde{G}_{mi}^{TM,IV} & \frac{k_x}{\omega\epsilon_m}\tilde{G}_{mi}^{TM,IV} & 0 \end{bmatrix} \tag{6.63}$$

$$\tilde{G}^{HM} = \begin{bmatrix} -\frac{k_x^2}{k_\rho^2}\tilde{G}_{mi}^{TE,IV} - \frac{k_y^2}{k_\rho^2}\tilde{G}_{mi}^{TM,IV} & \frac{k_x k_y}{k_\rho^2}\left(\tilde{G}_{mi}^{TM,IV} - \tilde{G}_{mi}^{TE,IV}\right) & -\frac{k_x}{\omega\mu_s}\tilde{G}_{mi}^{TE,II} \\ \frac{k_x k_y}{k_\rho^2}\left(\tilde{G}_{mi}^{TM,IV} - \tilde{G}_{mi}^{TE,IV}\right) & -\frac{k_x^2}{k_\rho^2}\tilde{G}_{mi}^{TM,IV} - \frac{k_y^2}{k_\rho^2}\tilde{G}_{mi}^{TE,IV} & -\frac{k_y}{\omega\mu_s}\tilde{G}_{mi}^{TE,II} \\ \frac{k_x}{\omega\mu_m}\tilde{G}_{mi}^{TE,VV} & \frac{k_y}{\omega\mu_m}\tilde{G}_{mi}^{TE,VV} & -\frac{k_\rho^2}{\omega^2\mu_s\mu_m}\tilde{G}_{mi}^{TE,VI} \end{bmatrix} \tag{6.64}$$

in the spectral domain. We can define several sets of dyadic layered medium Green's functions. In this work, we follow the Michalski's Formulation-C. In this formulation, some components can be simplified as follows,

$$\tilde{G}^{EJ} = \begin{bmatrix} \frac{1}{j\omega\mu_s}\tilde{G}_{mi}^{TE,VI} & 0 & 0 \\ 0 & \frac{1}{j\omega\mu_s}\tilde{G}_{mi}^{TE,VI} & 0 \\ \frac{k_x}{jk_\rho^2}(\tilde{G}_{mi}^{TE,II} - \tilde{G}_{mi}^{TM,II}) & \frac{k_y}{jk_\rho^2}(\tilde{G}_{mi}^{TE,II} - \tilde{G}_{mi}^{TM,II}) & \frac{1}{j\omega\epsilon_s}\tilde{G}_{mi}^{TM,IV} \end{bmatrix} \tag{6.65}$$

$$\bar{G}^{\,HM} = \begin{bmatrix} \frac{1}{j\omega\epsilon_m}\tilde{G}_{mi}^{TM,IV} & 0 & 0 \\ 0 & \frac{1}{j\omega\epsilon_m}\tilde{G}_{mi}^{TM,IV} & 0 \\ \frac{k_x}{jk_\rho^2}(\tilde{G}_{mi}^{TM,VV} - \tilde{G}_{mi}^{TE,VV}) & \frac{k_y}{jk_\rho^2}(\tilde{G}_{mi}^{TM,VV} - \tilde{G}_{mi}^{TE,VV}) & \frac{1}{j\omega\mu_i}\tilde{G}_{mi}^{TE,VI} \end{bmatrix} \tag{6.66}$$

However, $\nabla\nabla\cdot$ operator has a hyper singular behavior which leads us to mixed potential Green's function formulation. We want to find such a scalar function $G_\Phi^{EJ/HM}$ which satisfies

$$\nabla \cdot \langle \bar{\mathbf{G}}^{\,EJ/HM}; \mathbf{X}\rangle = -\langle \nabla' G_\Phi^{EJ/HM}; \mathbf{X}\rangle = \langle G_\Phi^{EJ/HM}; \nabla' \cdot \mathbf{X}\rangle. \tag{6.67}$$

If the scalar potential GF is continuous on the interfaces, the contour integrals on the interfaces disappear. Because of this reason we define a *Correction Term* $\mathbf{C}^{\,EJ/HM}$

[26] as follows,

$$\nabla \cdot \bar{\mathbf{G}}^{EJ/HM} = -\nabla' G_{\Phi}^{EJ/HM} + \mathbf{C}^{EJ/HM} \tag{6.68}$$

This new term's contribution can be seen from the following equation by defining two new DGFs, $\bar{\mathbf{K}}^{J}$ and $\bar{\mathbf{K}}^{M}$,

$$\begin{aligned}\mathbf{E} =& - j\omega\mu_0 \langle \bar{\mathbf{G}}^{EJ}; \mathbf{J} \rangle + \frac{1}{j\omega\epsilon_0} \nabla \left\{ \langle G_{\Phi}^{EJ}, \nabla' \cdot \mathbf{J} \rangle + \langle \mathbf{C}^{EJ}; \mathbf{J} \rangle \right\} + \langle \bar{\mathbf{G}}^{EM}; \mathbf{M} \rangle \\ =& - j\omega\mu_0 \langle \bar{\mathbf{K}}^{J}; \mathbf{J} \rangle + \frac{1}{j\omega\epsilon_0} \nabla \langle G_{\Phi}^{EJ}, \nabla' \cdot \mathbf{J} \rangle + \langle \bar{\mathbf{G}}^{EM}; \mathbf{M} \rangle\end{aligned} \tag{6.69}$$

$$\begin{aligned}\mathbf{H} =& - j\omega\epsilon_0 \langle \bar{\mathbf{G}}^{HM}; \mathbf{M} \rangle + \frac{1}{j\omega\mu_0} \nabla \left\{ \langle G_{\Phi}^{HM}, \nabla' \cdot \mathbf{M} \rangle + \langle \mathbf{C}^{HM}; \mathbf{M} \rangle \right\} + \langle \bar{\mathbf{G}}^{HJ}; \mathbf{J} \rangle \\ =& - j\omega\epsilon_0 \langle \bar{\mathbf{K}}^{M}; \mathbf{M} \rangle + \frac{1}{j\omega\mu_0} \nabla \langle G_{\Phi}^{HM}, \nabla' \cdot \mathbf{M} \rangle + \langle \bar{\mathbf{G}}^{HJ}; \mathbf{J} \rangle\end{aligned} \tag{6.70}$$

where

$$\bar{\mathbf{K}}^{J} = \begin{bmatrix} \frac{1}{j\omega\mu_s} \tilde{G}_{mi}^{TE,VI} & 0 & \partial C_z^J / \partial x' \\ 0 & \frac{1}{j\omega\mu_s} \tilde{G}_{mi}^{TE,VI} & \partial C_z^J / \partial y' \\ \frac{k_x}{jk_\rho^2} (\tilde{G}_{mi}^{TE,II} - \tilde{G}_{mi}^{TM,II}) & \frac{k_y}{jk_\rho^2} (\tilde{G}_{mi}^{TE,II} - \tilde{G}_{mi}^{TM,II}) & \frac{1}{j\omega\epsilon_s} \tilde{G}_{mi}^{TM,IV} + \partial C_z^J / \partial z' \end{bmatrix} \tag{6.71}$$

$$\tilde{G}_{\Phi}^{EJ} = \frac{j\omega\epsilon_m}{4\pi^2 k_\rho^2} (\tilde{G}_{mi}^{TM,VI} - \tilde{G}_{mi}^{TE,VI}) \tag{6.72}$$

$$\bar{\mathbf{K}}^{M} = \begin{bmatrix} \frac{1}{j\omega\epsilon_m} \tilde{G}_{mi}^{TM,IV} & 0 & \partial C_z^M / \partial x' \\ 0 & \frac{1}{j\omega\epsilon_m} \tilde{G}_{mi}^{TM,IV} & \partial C_z^M / \partial y' \\ \frac{k_x}{jk_\rho^2} (\tilde{G}_{mi}^{TM,VV} - \tilde{G}_{mi}^{TE,VV}) & \frac{k_y}{jk_\rho^2} (\tilde{G}_{mi}^{TM,VV} - \tilde{G}_{mi}^{TE,VV}) & \frac{1}{j\omega\mu_i} \tilde{G}_{mi}^{TE,VI} + \partial C_z^M / \partial z' \end{bmatrix} \tag{6.73}$$

$$\tilde{G}_{\Phi}^{HM} = \frac{j\omega\mu_m}{4\pi^2 k_\rho^2} (\tilde{G}_{mi}^{TE,IV} - \tilde{G}_{mi}^{TM,IV}) \tag{6.74}$$

From the above formulation we can conclude that the following type of Green's functions are required: (i) $\bar{\mathbf{K}}^{J}$, (ii) G_{Φ}^{EJ}, (iii) $\bar{\mathbf{G}}^{EM}$, (iv) $\bar{\mathbf{K}}^{M}$, (v) G_{Φ}^{HM}, (vi) $\bar{\mathbf{G}}^{HJ}$.

However, we do not need to write 6 different subroutines in our code to produce these GF sets. Once we have the subroutines for $\bar{\mathbf{K}}^J$, G_Φ^J, and $\bar{\mathbf{G}}^{HJ}$, we can obtain the other components easily by using duality. In fact, in near field, GF pairs, e.g. $\bar{\mathbf{K}}^J$ and $\bar{\mathbf{K}}^M$, show very similar behaviors. The difference occurs at the far field. For example, Fig. 6.12 shows the magnitude of the 4 different components of $\bar{\mathbf{K}}^J$ and $\bar{\mathbf{K}}^M$ when $z = 1.4$ mm and $z' = 0.4$ mm (first row), and $z = z' = 0.4$ mm (second row) and for the 6-layer medium given in Figure 3.4 in Chapter 3; whereas Fig. 6.13 shows the magnitude of the 4 different components of $\bar{\mathbf{G}}^{EJ}$ and $\bar{\mathbf{G}}^{HM}$ for the same problem. Clearly, GF pair have very similar characteristics in the near field, but not in the far field. In order to obtain the MoM solution of the surface integral equation

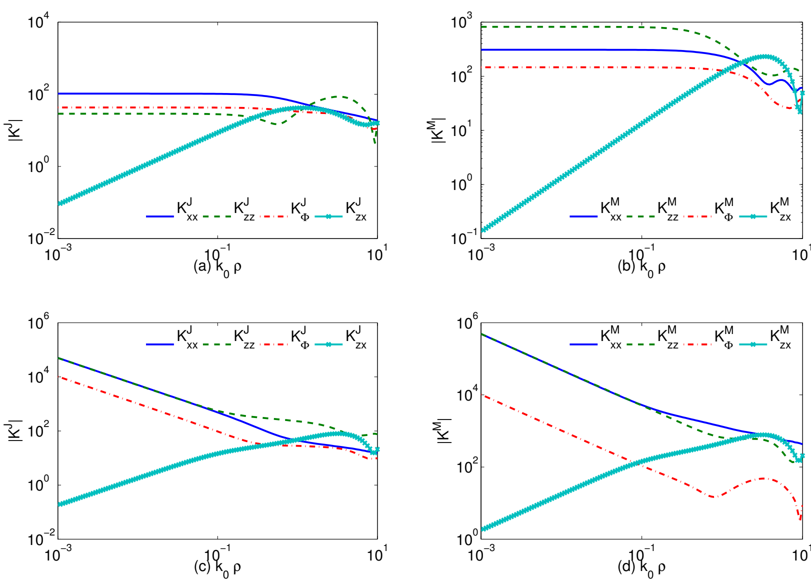

Figure 6.12: The magnitude of the 4 different components of $\bar{\mathbf{K}}^J$ and $\bar{\mathbf{K}}^M$ when $z = 1.4$ mm and $z' = 0.4$ mm (first row), and $z = z' = 0.4$ mm (second row) and for the 6-layer medium given in Figure 3.4 in Chapter 3.

for a layered medium, again we first expand the unknown currents in terms of the basis functions $\mathbf{f}_n(\mathbf{r})$ and $\mathbf{b}_n(\mathbf{r})$, which both are vector basis functions defined on the

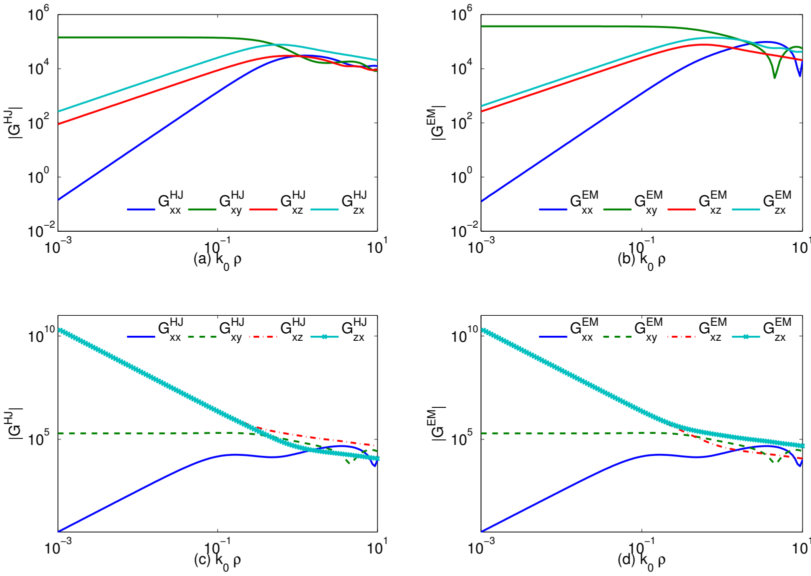

Figure 6.13: The magnitude of the 4 different components of $\bar{\mathbf{G}}^{EM}$ and $\bar{\mathbf{G}}^{HJ}$ when $z = 1.4$ mm and $z' = 0.4$ mm (first row), and $z = z' = 0.4$ mm (second row) and for the 6-layer medium given in Figure 3.4 in Chapter 3.

adjacent triangles or rectangles associated with nth edge, as

$$\mathbf{J}(\mathbf{r}) = \sum_{n=1}^{N} I_n \mathbf{f}_n(\mathbf{r}), \quad \text{and} \quad \mathbf{M}(\mathbf{r}) = \sum_{n=1}^{N} P_n \mathbf{b}_n(\mathbf{r}),$$

where N is the number of interior edges. When we apply the Galerkin type MoM, with the same type of functions for the testing, we obtain

$$\begin{aligned} \int_S \mathbf{f}_i \cdot \mathbf{E}\, dS = \sum_{n=1}^{N} I_n \Big\{ & -j\omega\mu_0 \int_S \int_{S'} \mathbf{f}_i \cdot \bar{\mathbf{K}}^J \cdot \mathbf{f}_n dS' dS \\ & + \frac{1}{j\omega\epsilon_0} \int_S \int_{S'} \nabla \cdot \mathbf{f}_i G_\Phi^{EJ} \nabla' \cdot \mathbf{f}_n dS' dS \Big\} \\ & + \sum_{n=1}^{N} P_n \int_S \int_{S'} \mathbf{f}_i \cdot \bar{\mathbf{G}}^{EM} \cdot \mathbf{b}_n dS' dS \end{aligned} \qquad (6.75)$$

$$
\begin{aligned}
\int_S \mathbf{b}_i \cdot \mathbf{H}\, dS = \sum_{n=1}^{N} P_n \Big\{ & -j\omega\epsilon_0 \int_S \int_{S'} \mathbf{b}_i \cdot \bar{\mathbf{K}}^M \cdot \mathbf{b}_n dS' dS \\
& + \frac{1}{j\omega\mu_0} \int_S \int_{S'} \nabla \cdot \mathbf{b}_i G_\Phi^{HM} \nabla' \cdot \mathbf{b}_n dS' dS \Big\} \\
& + \sum_{n=1}^{N} I_n \int_S \int_{S'} \mathbf{b}_i \cdot \bar{\mathbf{G}}^{HJ} \cdot \mathbf{f}_n dS' dS
\end{aligned} \tag{6.76}
$$

6.5 Numerical Examples

In order to validate the accuracy of our MoM implementation, the stabilized biconjugate gradient-fast Fourier Transform (BCGS-FFT) is used which has been developed by Dr. Liu's current and former students and post-docs such as Dr. Xuemin Millard and Dr. Lin-Ping Song. Even though BCGS-FFT is a volume integral equation solver, the usage of an iterative solver and the fast Fourier Transform algorithm make it a very fast solver.

Even though the objective of the following numerical experiments is the control of the accuracy of the developed MoM solver, the comparison of the surface elements, *triangular* or *rectangular*, is also of interest because of our future projects. Basically, we compare three different solution sets obtained by using MoM with triangular surface elements, MoM with rectangular surface elements, and BCGS-FFT. The following table shows their abbreviations.

Table 6.3: Abbreviations

Abbreviation	Method
MoM-T	Method of Moments by using a triangulated surface mesh.
MoM-R	Method of Moments by using a rectangulated surface mesh.
BCGS-FFT	Stabilized biconjugate gradient-fast Fourier Transform.

In order to verify our MoM results for a layered medium, we locate a dielectric homogeneous cuboid in the top layer of a 3-layer background as shown in Fig. 6.14.

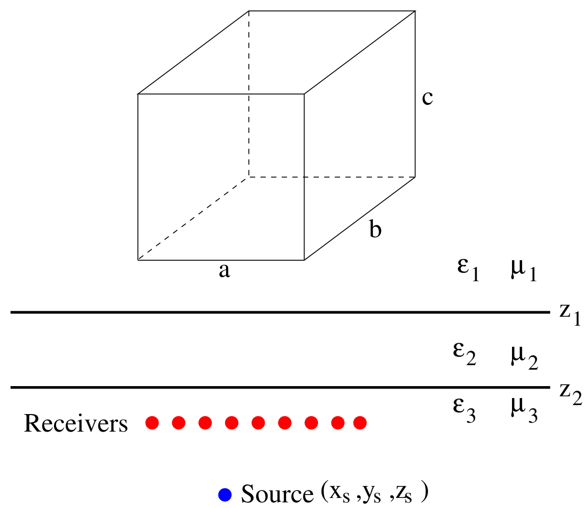

Figure 6.14: A homogeneous cuboid in the top layer of a 3-layer medium. The source and receivers are in the bottom layer.

Setup 1:

A point source is located at $(2.1, 2.1, 3.675)$ m. The frequency of the problem is $f = 25$ MHz. There are 16 receivers located uniformly along the line $(0.9 : 3.2, 1.9, 3.425)$ m. The dimensions of the cuboid are $(a, b, c) = (1.6, 1.6, 1.15)$ m, and the electrical parameters are $\epsilon_{r,c} = 16$, $\sigma_c = 0.01$ S/m. The center of the cuboid is at $(2.05, 2.05, 1.825)$ m. The 3-layer background can be defined as $\epsilon_{r,l1} = 1.44$, $\epsilon_{r,l2} = 1.21$, $\epsilon_{r,l3} = 1.0$; $z_1 = 2.75$ m, $z_2 = 3.25$ m. In order to compare our MoM results, the BCGS-FFT solver is used where $32 \times 32 \times 23$ voxels are used for the volumetric discretization. For the rectangulated surface mesh (for MOM-R) $8 \times 8 \times 6$ rectangular surface patches are used. The MoM-T solver uses the triangle mesh modified from the rectangle mesh in MoM-R.

Fig. 6.15 shows three different set of results obtained by using MoM-R, MoM-T, and BCGS-FFT. The left, middle, and right columns show the real, imaginary parts and the magnitude of the E_x^{scat} (top row), E_y^{scat} (middle row), E_z^{scat} (bottom row) components of the scattered field at the receiver points. There is a good agreement between MoM and BCGS-FFT solutions.

Setup 2:

A point source is located at $(2.1, 2.1, 3.675)$ m. The frequency of the problem is $f = 10$ MHz. There are 16 receivers located uniformly along the line $(0.9 : 3.2, 1.9, 3.425)$ m. The dimensions of the cuboid are $(a, b, c) = (1.6, 1.6, 1.15)$ m, and the electrical parameters are $\epsilon_{r,c} = 16$, $\sigma_c = 0.01$ S/m. The center of the cube is at $(2.05, 2.05, 1.825)$ m. The 3-layer background can be defined as $\epsilon_{r,l1} = 4$, $\epsilon_{r,l2} = 12$, $\epsilon_{r,l3} = 1.0$; $z_1 = 2.75$ m, $z_2 = 3.25$ m. In order to compare our MoM results, BCGS-FFT solver is used where $32 \times 32 \times 23$ voxels are used for the volumetric discretization. For the rectangulated surface mesh (for MOM-R) $8 \times 8 \times 6$ rectangular surface patches are used. The MoM-T solver uses the triangle mesh modified from the rectangle mesh in MoM-R.

Fig. 6.16 shows three different sets of results obtained by using MoM-R, MoM-T, and BCGS-FFT. The left, middle, and right columns show the real, imaginary parts and the magnitude of the E_x^{scat} (top row), E_y^{scat} (middle row), E_z^{scat} (bottom row) components of the scattered field at the receiver points. Again, there is a good agreement between MoM and BCGS-FFT solutions.

For both cases, the difference between MoM-R and MoM-T solutions is less than 1% which means that the written code is capable of using both rectangular and triangular elements. Moreover, MoM-R and MoM-T solutions agree well with the BCGS-FFT solution, the difference is around 5%. We made this experiment with and without interpolation. In terms of the accuracy, the difference between two sets of solution is less than 1 %. However in terms of the CPU time, there is a huge different between two solutions. For regular approach, the one without any interpolation, requires 8022.3 seconds to solve the problem, whereas the one with interpolation only takes 175 seconds (the preparation of Sommerfeld integral Tables is 90.1 sec, the preparation of Impedance matrix: 84.3 sec).

Several other experiments have been done to check the accuracy of the method. Since there are several different examples in the next chapter, we provide only two examples here.

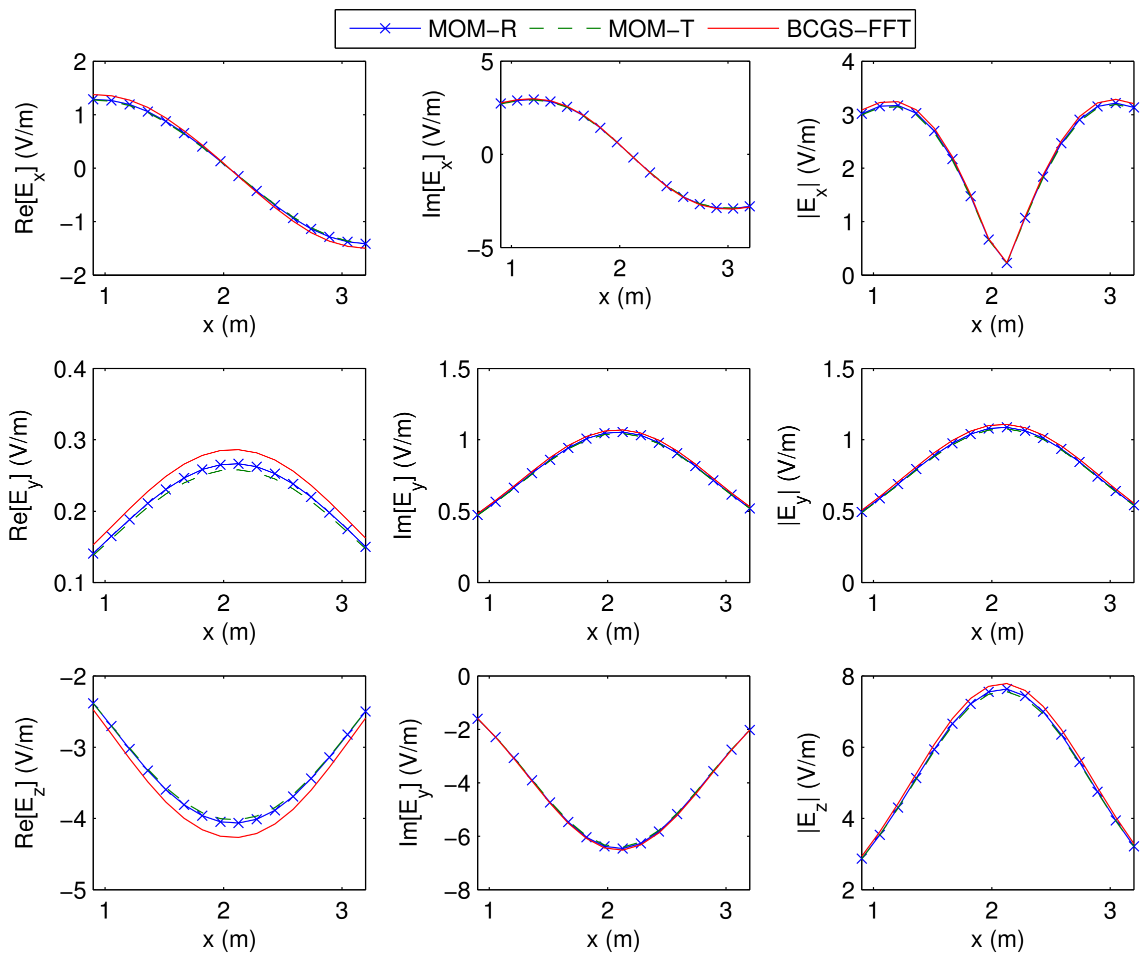

Figure 6.15: Three different solution sets obtained by using MoM-R, MoM-T, and BCGS-FFT: the left, middle, and right columns show the real, imaginary parts and the magnitude of the x (top row), y (middle row), z (bottom row) components of the scattered field at the receiver points for Setup-1.

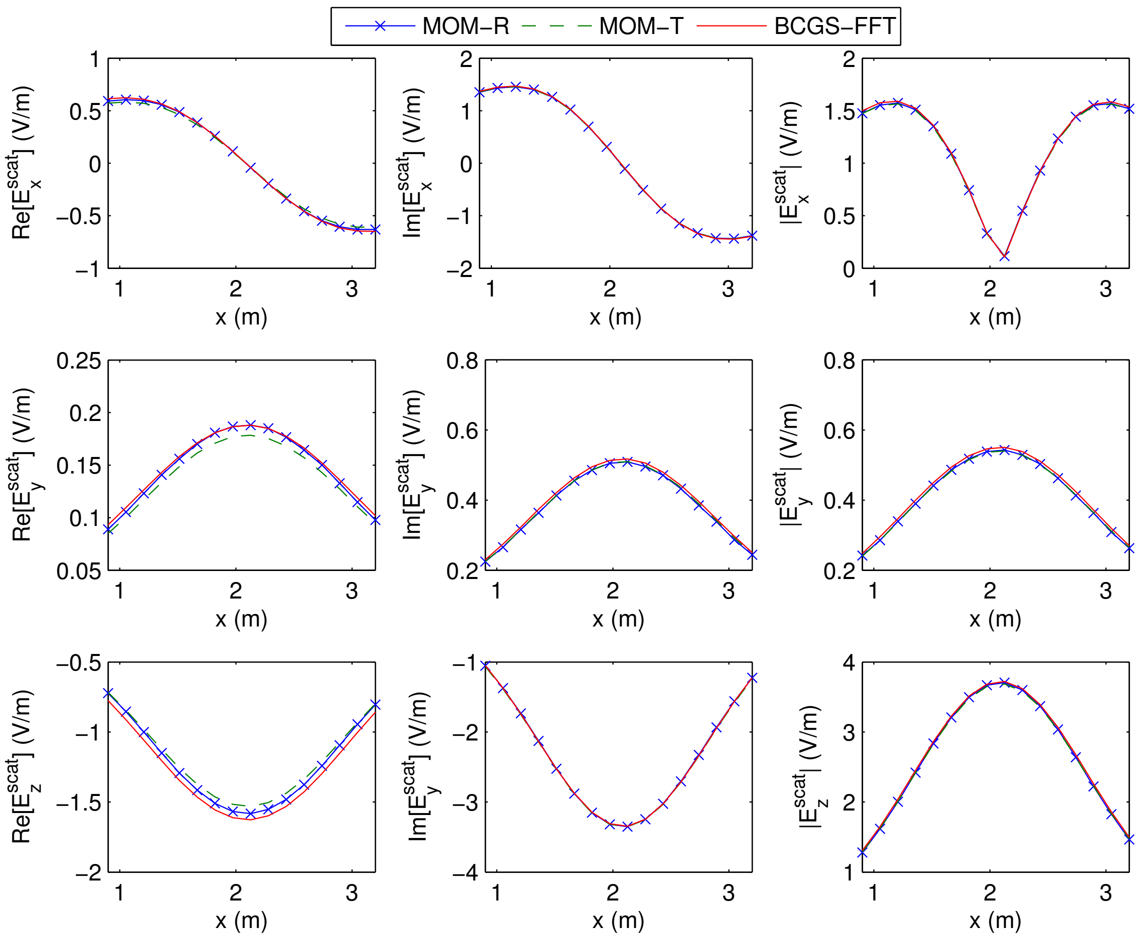

Figure 6.16: Three different solution sets obtained by using MoM-R, MoM-T, and BCGS-FFT: the left, middle, and right columns show the real, imaginary parts and the magnitude of the x (top row), y (middle row), z (bottom row) components of the scattered field at the receiver points for Setup-2.

6.6 Conclusion

In this chapter, a Method of Moment solution of the surface integral equation is presented for layered medium applications. The formulation and implementation can handle 3D dielectric and PEC objects either in free space or a layered medium. For the singular terms, the Duffy transformation is utilized. The surface of the scatterer can be discretized with rectangular or triangular patches. A simple interpolation technique has been used to accelerate the layered medium Green's function calculation. The effect of this step is shown to be less than 1% in terms of the accuracy, whereas in terms of the computation time there is a big improvement. The accuracy of the overall method is validated with several examples. As long as the sampling density is bigger than 10 PPW, the implemented MoM can produce very accurate results.

Chapter 7

3D Hybrid Finite-Element/Method of Moment for Layered Media

Today's circuits, chips and interconnects are all very complicated designs. Most of the time, there is no exact closed-form solution. Thus it is very important to develop numerical methods to model thse complex problems.

The finite element method (FEM), which was first developed in 1943 by R. Courant to analyze vibration systems, is a numerical analysis method to model and analyze the complex engineering and science problems. Since 1943, FEM has been very popular due to its capability of analyzing inhomogeneous structures, and it has been implemented in very different areas of engineering and science. From the mathematical point of view, FEM can be used to solve partial differential equations and integral equations. FEM does not require a uniform mesh, which is one of the major advantages of this method; however the whole problem domain has to be discretized unless it is truncated via an absorbing or radiation boundary. However, little progress has been made in absorbing or radiation boundary conditions for layered medium. Let us assume that we have a simple micostrip patch antenna shown in Figure 7.1, and the frequency of the problem is high so that the structure can be approximated as a planar multilayered geometry. Even though the patch is a PEC, we need to discretize the whole structure if we want to analyze this geometry by using the FEM. As it is presented in the previous chapter, we only need to discretize the metallic patch, if we use the layered medium Green's functions and MoM. However, MoM cannot handle

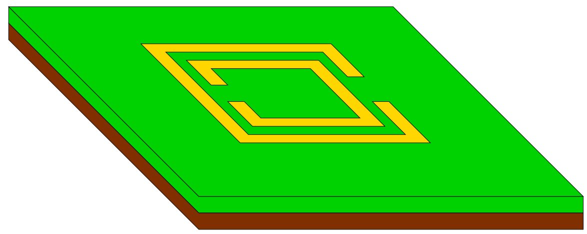

Figure 7.1: A microstip antenna: a metallic patch on a substrate. The bottom layer is ground (PEC).

inhomogeneity effectively. In order to solve this kind of complex (inhomogeneous) problems in a very efficient way, we need to combine these two methods.

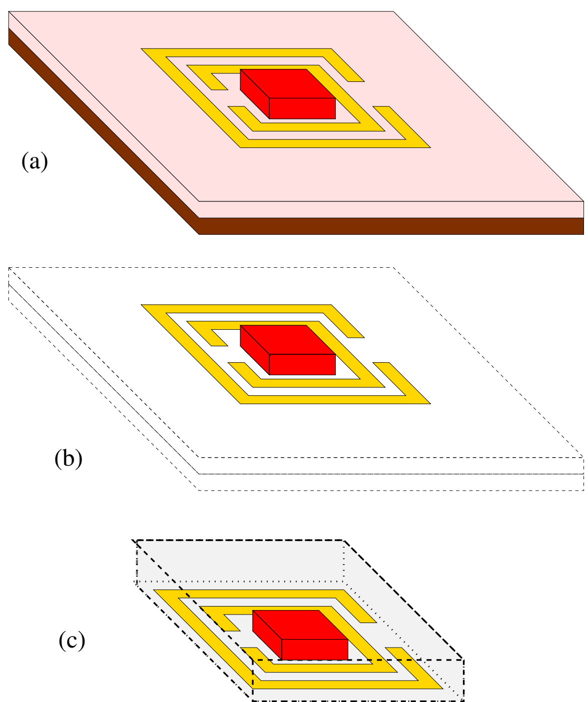

Figure 7.2: (a) An inhomoneous structure. (b) Usage of layered medium Green's functions removes the requirement of multilayered structure's discretization. (c) Using MoM as a radiation boundary makes it possible to use FEM for the inhomogeneous part. From top to the bottom, the size of the problem decreases.

Figure 7.2 (a) shows an inhomogeneous structure which has an additional inhomogeneous dielectric cuboid with respect to the geometry in Figure 7.1. Since the

problem is inhomogeneous, a combination of surface and volume integral equations can be used. The MoM is very inefficient in this particular case. We can solve this problem by using the FEM, however we have to discretize the whole domain, not only the metallic patch and the dielectric cuboid but also the background. From previous chapters, we know that we can reduce the size of the problem domain by using
(i) layered medium Green's Functions (LMGF), and
(ii) a radiation boundary.
It is true that the evaluation of the LMGFs is a time consuming procedure. However LMGFs have $(\rho, z|z')$ dependency instead of $(\mathbf{r}, \mathbf{r}')$ dependency, hence very simple interpolation techniques can decrease required CPU time. Furthermore, when LMGFs are used, we no longer need to discretize the multilayered background, so there is a dramatic reduction in the matrix size. It should be noted that, in most cases, such as circuit design, we only need to produce the layered medium Green's functions once. Then the interior design can be changed freely for the optimization.

The usage of LMGFs changes problem domain (a) to (b) in Figure 7.2. However, we need to bound the problem domain by using an artificial boundary in order to use FEM. As it is shown in Chapter-4 for 2D objects, we can use the exterior surface integral equation as a radiation boundary to truncate the problem domain.

For the implementation of 3D radiation boundary condition, an artificial boundary $\partial\Gamma$ is applied to truncate the arbitrarily 3D shaped inhomogenous scatterer(s) from the layered medium. The finite element method is applied in the interior region to calculate the field, while the method of moments is applied on the outer boundary $\partial\Gamma$ to relate the field and induced current. Due to the form of the chosen basis functions and meshing, the fields and currents on the boundary for the FEM are obtained from the solution of the final matrix equation without using any interpolation.

The detailed information about the MoM part can be found in the previous chapter. For the FEM part, we adopt the code EMAP (ElectroMagnetic Analysis Program), a three-dimensional finite element modeling code developed by several researchers at University of Missouri [99], in this work. This code is written in C to analyze simple 3-dimensional geometries and distributed in source code form. The EMAP code is not intended to compete with commercial finite element modeling codes. It does not have a sophisticated mesh generator, graphical output, or unlimited technical support. Its primary strength is ease-of-use, modest resource requirements, and accurate modeling of simple three-dimensional configurations over a wide range of frequencies.

In this chapter, first, 3D FEM formulation is briefly presented. Second, some details about the evaluation of FEM matrices are given. Then the coupling of FEM and MoM methods is described. Finally, the validity of the proposed method is demonstrated with several numerical examples.

7.1 The Finite Element Method (FEM)

7.1.1 Formulation

The second order Maxwell's wave equation in strong form with imposed electric current density $\mathbf{S}$ is given by

$$\nabla \times (\mu_r^{-1} \nabla \times \mathbf{E}) - \epsilon_r k_0^2 \mathbf{E} = -jk_0 \eta_0 \mathbf{S}. \tag{7.1}$$

We can also write this equation as a residual function as follows

$$\mathbf{R} \equiv \nabla \times (\mu_r^{-1} \nabla \times \mathbf{E}) - \epsilon_r k_0^2 \mathbf{E} + jk_0 \eta_0 \mathbf{S}. \tag{7.2}$$

The order of Eq. (7.2) can be reduced by multiplying it by a set of weighting functions $\mathbf{\Phi}_i(\mathbf{r})$, and integrating over the finite-element domain as follows,

$$
\begin{aligned}
R_i^e &= \int_v \mathbf{\Phi}_i(\mathbf{r}) \cdot \mathbf{R} dv = 0, \\
&= \int_v \mathbf{\Phi}_i(\mathbf{r}) \cdot \left[\nabla \times (\mu_r^{-1} \nabla \times \mathbf{E}) - \epsilon_r k_0^2 \mathbf{E} + j k_0 \eta_0 \mathbf{S}\right] dv, \\
&= \int_v \left[(\mu_r^{-1} \nabla \times \mathbf{E}) \cdot (\nabla \times \mathbf{\Phi}_i(\mathbf{r})) - \epsilon_r k_0^2 \mathbf{\Phi}_i(\mathbf{r}) \cdot \mathbf{E} + j k_0 \eta_0 \mathbf{\Phi}_i(\mathbf{r}) \cdot \mathbf{S}\right] dv \\
&\quad + \oint_s \hat{\mathbf{n}} \cdot (\mu_r^{-1} \nabla \times \mathbf{E} \times \mathbf{\Phi}_i(\mathbf{r}) ds. \qquad (7.3)
\end{aligned}
$$

Furthermore, by using

$$
\nabla \times \mathbf{E} = j\omega\mu\mathbf{H} \;\; \Rightarrow \;\; \mu_r^{-1} \nabla \times \mathbf{E} \times \mathbf{\Phi}_i(\mathbf{r}) = j\omega\mu_0 \mathbf{H} \times \mathbf{\Phi}_i(\mathbf{r}), \qquad (7.4)
$$

$$
\mathbf{A} \cdot \mathbf{B} \times \mathbf{C} = \mathbf{C} \cdot \mathbf{A} \times \mathbf{B} \;\; \Rightarrow \;\; \hat{\mathbf{n}} \cdot (j\omega\mu_0 \mathbf{H} \times \mathbf{\Phi}_i(\mathbf{r})) = jw\mu_0 \mathbf{\Phi}_i(\mathbf{r}) \cdot \hat{\mathbf{n}} \times \mathbf{H}, \qquad (7.5)
$$

the weak form equation can be written as

$$
\begin{aligned}
&\int_v \left[(\mu_r^{-1} \nabla \times \mathbf{E}) \cdot (\nabla \times \mathbf{\Phi}_i(\mathbf{r})) - \epsilon_r k_0^2 \mathbf{\Phi}_i(\mathbf{r}) \cdot \mathbf{E}\right] dv + j\omega\mu_0 \oint_s \mathbf{\Phi}_i(\mathbf{r}) \cdot (\hat{\mathbf{n}} \times \mathbf{H})\, ds \\
&= -j k_0 \eta_0 \int_v \mathbf{\Phi}_i(\mathbf{r}) \cdot \mathbf{S} dv \qquad (7.6)
\end{aligned}
$$

Eq. (7.6) basically gives the relationship betweeen the electric field inside the finite-element domain and the tangential magnetic field surrounding that domain.

In order to discretize the finite element domain, we use tetrahedral elements and volume basis functions $\mathbf{\Phi}_n(\mathbf{r})$ to expand the unknowns. Assume that the numbers of inner and boundary edges are N_i and N_b, respectively, where $N = N_i + N_b$. Then, we can expand the unknown electric field and current as

$$
\mathbf{E} = \sum_{n=1}^{N} E_n \mathbf{\Phi}_n(\mathbf{r}) = \sum_{n=1}^{N_i} E_n^i \mathbf{\Phi}_n(\mathbf{r}) + \sum_{n=1}^{N_b} E_n^b \mathbf{\Phi}_n(\mathbf{r}),
$$

$$\hat{\mathbf{n}} \times \mathbf{H} = \sum_{n=1}^{N_b} J_n \mathbf{f}_n(\mathbf{r}) \tag{7.7}$$

The weak form equation (7.6) becomes,

$$\sum_{n=1}^{N} E_n \int_v \left[(\mu_r^{-1} \nabla \times \boldsymbol{\Phi}_n(\mathbf{r})) \cdot (\nabla \times \boldsymbol{\Phi}_i(\mathbf{r})) - \epsilon_r k_0^2 \boldsymbol{\Phi}_n(\mathbf{r}) \cdot \boldsymbol{\Phi}_i(\mathbf{r}) \right] dv$$

$$+ jw\mu_0 \sum_{n=1}^{N_b} J_n \oint_s \boldsymbol{\Phi}_n(\mathbf{r}) \cdot \mathbf{f}_i(\mathbf{r}) ds = S_i \tag{7.8}$$

Eq. (7.8) can be written in matrix form,

$$[\mathbf{A}' + \mathbf{B}']\mathbf{E} + \mathbf{G}\mathbf{J} = \mathbf{S}^{\mathbf{i}} \tag{7.9}$$

where E_n, J_n are unknown coefficients, $\hat{S}$ is the source vector and $\mathbf{A}', \mathbf{B}', \mathbf{G}$ are stiffness mass matrices defined as,

$$\begin{aligned}
S_i &= -jk_0\eta_0 \int_v \boldsymbol{\Phi}_i(\mathbf{r}) \cdot \mathbf{S} dv \\
A'_{i,n} &= \int_v (\mu_r^{-1} \nabla \times \boldsymbol{\Phi}_n(\mathbf{r})) \cdot (\nabla \times \boldsymbol{\Phi}_i(\mathbf{r})) dv \\
B'_{i,n} &= -\epsilon_r k_0^2 \int_v \boldsymbol{\Phi}_n(\mathbf{r}) \cdot \boldsymbol{\Phi}_i(\mathbf{r}) dv \\
G_{i,n} &= jw\mu_0 \oint_s \mathbf{f}_n(\mathbf{r}) \times \boldsymbol{\Phi}_i(\mathbf{r}) ds
\end{aligned} \tag{7.10}$$

Furthermore, the matrix form can be written as,

$$\mathbf{A}\mathbf{E}^{\mathbf{i}} + \mathbf{B}\mathbf{E}^{\mathbf{b}} \qquad = \mathbf{S}^{\mathbf{i}} \tag{7.11}$$

$$\mathbf{B}^{\mathbf{T}}\mathbf{E}^{\mathbf{i}} + \mathbf{C}\mathbf{E}^{\mathbf{b}} + \mathbf{G}\mathbf{J} = \mathbf{0} \tag{7.12}$$

where matrices $\mathbf{A}, \mathbf{B}, \mathbf{C}$ are submatrices of matrix $\{\mathbf{A}' + \mathbf{B}'\}$ which are explained later in this chapter.

7.1.2 Basis Functions

For the above discretization, we chose the vector basis functions proposed in [98]. in order to satisfy the continuity of the tangential components of the fields automatically. Each edge of a tetrahedron shown in Figure 7.3 can be defined by using two vertices

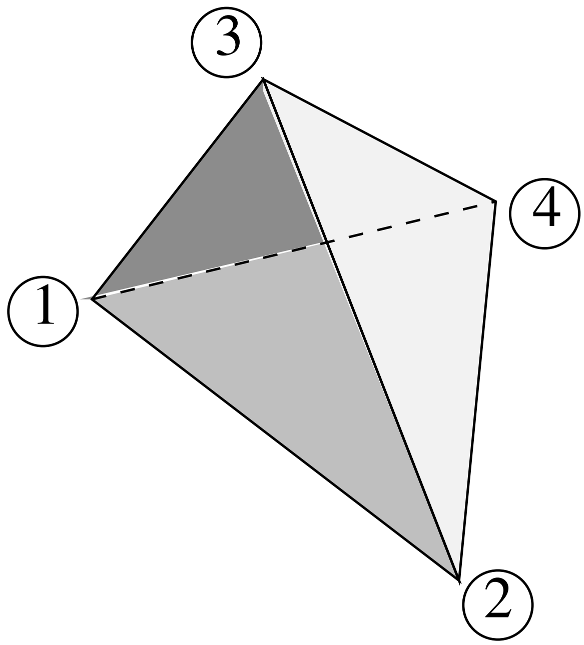

Figure 7.3: A tetrahedron element with four corners.

as shown in the following table.

Edge Number k	Vertex Number k_1	Vertex Number k_2
1	1	2
2	1	3
3	1	4
4	2	3
5	4	2
6	3	4

Now let us define three new variables

$$b_k = x_{k2} - x_{k1}\ ,\ c_k = y_{k2} - y_{k1}\ ,\ d_k = z_{k2} - z_{k1}. \tag{7.13}$$

where $k = 1, 2, \cdots, 6$, and (x_j, y_j, z_j) is the jth edge, $j = 1, 2, 3, 4$. By using (7.13), we can define the vector at the kth edge, $\mathbf{e}_k$, as follows,

$$\mathbf{e}_k = b_k\hat{\mathbf{x}} + c_k\hat{\mathbf{y}} + d_k\hat{\mathbf{z}} \tag{7.14}$$

where $\hat{\eta}$ is the unit vector in η direction, $\eta = x, y, z$. The magnitude of $\mathbf{e}_k$ is the length of the kth edge.

Now, we can form our basis function as,

$$\mathbf{\Phi}_k(\mathbf{r}) = \begin{cases} \mathbf{f}_k + \mathbf{g}_k \times \mathbf{r} & \mathbf{r} \text{ in the tetrahedron} \\ 0 & \text{otherwise} \end{cases} \tag{7.15}$$

where V_e is the volume of the tetrahedron and

$$\mathbf{f}_k = \frac{|\mathbf{e}_k|}{6V_e}\left[\mathbf{r}_{(7-k)_1} \times \mathbf{r}_{(7-k)_2}\right], \tag{7.16}$$

$$\mathbf{g}_k = \frac{|\mathbf{e}_{7-k}|}{6V_e}\left[\mathbf{r}_{(7-k)_1} - \mathbf{r}_{(7-k)_2}\right]. \tag{7.17}$$

There are two important properties of this type of basis functions:

(i) $\nabla \cdot \mathbf{\Phi}_k(\mathbf{r}) = 0$ (divergence free),

(ii) $\nabla \times \mathbf{\Phi}_k(\mathbf{r}) = \mathbf{g}_k$ (constant curl).

For more details, the reader is referred to [98] and [99]. One important remark is that the above $\mathbf{f}_k$ terms are the same as the one given in Chapter 6, Eq. (57) and more importantly, on the boundary surface S, $\mathbf{f}_k$ and $\mathbf{\Phi}_k$ are related by

$$\mathbf{\Phi}_k(\mathbf{r}) = \hat{\mathbf{n}} \times \mathbf{f}_k(\mathbf{r})|_{\mathbf{r} \text{ on the surface } S}. \tag{7.18}$$

Eq. (7.18) is crucial for the MoM-FEM coupling.

7.1.3 Evaluation of FEM Matrices

For the FEM part, mainly we have three integral forms.

Matrix A

In order to evaluate matrix $\mathbf{A}$, we need to evaluate the following integral analytically

$$A''_{i,n} = \int_v (\nabla \times \mathbf{\Phi}_n(\mathbf{r})) \cdot (\nabla \times \mathbf{\Phi}_i(\mathbf{r})) dv \tag{7.19}$$

Since $\nabla \times \mathbf{\Phi}_k(\mathbf{r}) = \mathbf{g}_k$, simply

$$A''_{i,n} = 4\mathbf{g}_i \cdot \mathbf{g}_n V_e, \tag{7.20}$$

which can be also written as,

$$\begin{aligned} A''_{i,n} = \frac{l_i l_n V_e}{(6V_e)^4} & [(c_{i1}d_{i2}\ (c)_{i2}d_{i1})(c_{n1}d_{n2}\ (c)_{n2}d_{n1}) \\ & + (d_{i1}b_{i2} - d_{i2}b_{i1})(d_{n1}b_{n2} - d_{n2}b_{n1}) \\ & + (b_{i1}c_{i2}\ (b)_{i2}c_{i1})(b_{n1}c_{n2}\ (b)_{n2}c_{n1})] \end{aligned} \tag{7.21}$$

where $l_k = |\mathbf{e}_k|$, the length of the kth edge.

Matrix B

In order to evaluate matrix $\mathbf{B}$, we need to evaluate the following integral analytically

$$B''_{i,n} = \int_v \mathbf{\Phi}_n(\mathbf{r}) \cdot \mathbf{\Phi}_i(\mathbf{r}) dv. \tag{7.22}$$

Assume that we write

$$\mathbf{\Phi}_k(x, y, z) = \alpha_1 + \alpha_2 x + \alpha_3 y + \alpha_z \tag{7.23}$$

and obtain the coefficients $\alpha_1, \alpha_2, \alpha_3, \alpha_4$ by enforcing at the four nodes of the tetrahedron element. In [70], it is stated that $B''_{i,n}$ can be written in more compact form by using $\alpha_{i,n} = (\alpha_2)_i (\alpha_2)_n + (\alpha_3)_i (\alpha_3)_n + (\alpha_4)_i (\alpha_4)_n$ as follows.

$$B''_{1,1} = \frac{(l_1)^2}{720V_e} (\alpha_{2,2} - \alpha_{1,2} + \alpha_{1,1}) \tag{7.24}$$

$$B''_{1,2} = \frac{l_1 l_2}{720V_e} (2\alpha_{2,3} - \alpha_{2,1} - \alpha_{1,3} + \alpha_{1,1}) \tag{7.25}$$

$$B''_{1,3} = \frac{l_1 l_3}{720V_e} (2\alpha_{2,4} - \alpha_{2,1} - \alpha_{1,4} + \alpha_{1,1}) \tag{7.26}$$

$$B''_{1,4} = \frac{l_1 l_4}{720V_e} (\alpha_{2,3} - \alpha_{2,2} - 2\alpha_{1,3} + \alpha_{1,2}) \tag{7.27}$$

$$B''_{1,5} = \frac{l_1 l_5}{720V_e} (\alpha_{2,2} - \alpha_{2,4} - \alpha_{1,2} + \alpha_{1,4}) \tag{7.28}$$

$$B''_{1,6} = \frac{l_1 l_6}{720V_e} (\alpha_{2,4} - \alpha_{2,3} - \alpha_{1,4} + \alpha_{1,3}) \tag{7.29}$$

$$B''_{2,2} = \frac{(l_2)^2}{360V_e} (\alpha_{3,3} - \alpha_{1,3} + \alpha_{1,1}) \tag{7.30}$$

$$B''_{2,3} = \frac{l_2 l_3}{720V_e} (2\alpha_{3,4} - \alpha_{1,3} - \alpha_{1,4} + \alpha_{1,1}) \tag{7.31}$$

$$B''_{2,4} = \frac{l_2 l_4}{720V_e} (\alpha_{3,3} - \alpha_{2,3} - \alpha_{1,3} + 2\alpha_{1,2}) \tag{7.32}$$

$$B''_{2,5} = \frac{l_2 l_5}{720V_e} (\alpha_{2,3} - \alpha_{3,4} - \alpha_{1,2} + \alpha_{1,4}) \tag{7.33}$$

$$B''_{2,6} = \frac{l_2 l_6}{720V_e} (\alpha_{3,4} - \alpha_{3,3} - 2\alpha_{1,4} + \alpha_{3,4}) \tag{7.34}$$

$$B''_{3,3} = \frac{(l_3)^2}{360V_e} \left(\alpha_{4,4} - \alpha_{1,4} + \alpha_{1,1}\right) \quad (7.35)$$

$$B''_{3,4} = \frac{l_3 l_4}{720V_e} \left(\alpha_{3,4} - \alpha_{2,4} - \alpha_{1,3} + \alpha_{1,2}\right) \quad (7.36)$$

$$B''_{3,5} = \frac{l_3 l_5}{720V_e} \left(\alpha_{2,4} - \alpha_{4,4} - 2\alpha_{1,2} + \alpha_{1,4}\right) \quad (7.37)$$

$$B''_{3,6} = \frac{l_3 l_6}{720V_e} \left(\alpha_{4,4} - \alpha_{3,4} - \alpha_{1,4} + 2\alpha_{1,3}\right) \quad (7.38)$$

$$B''_{4,4} = \frac{(l_4)^2}{360V_e} \left(\alpha_{3,3} - \alpha_{2,3} + \alpha_{2,2}\right) \quad (7.39)$$

$$B''_{4,5} = \frac{l_4 l_5}{720V_e} \left(\alpha_{2,3} - 2\alpha_{3,4} - \alpha_{2,2} + \alpha_{2,4}\right) \quad (7.40)$$

$$B''_{4,6} = \frac{l_4 l_6}{720V_e} \left(\alpha_{3,4} - \alpha_{3,3} - 2\alpha_{2,4} + \alpha_{2,3}\right) \quad (7.41)$$

$$B''_{5,5} = \frac{(l_5)^2}{360V_e} \left(\alpha_{2,2} - \alpha_{2,4} + \alpha_{4,4}\right) \quad (7.42)$$

$$B''_{5,6} = \frac{l_5 l_6}{720V_e} \left(\alpha_{2,4} - 2\alpha_{2,3} - \alpha_{4,4} + \alpha_{3,4}\right) \quad (7.43)$$

$$B''_{6,6} = \frac{(l_6)^2}{360V_e} \left(\alpha_{4,4} - \alpha_{3,4} + \alpha_{3,3}\right) \quad (7.44)$$

Matrix G

In order to evaluate matrix $\mathbf{G}$, we need to evaluate the following integral analytically

$$G''_{i,n} = \int_S \mathbf{\Phi}_n(\mathbf{r}) \cdot \mathbf{f}_i(\mathbf{r}) dS. \quad (7.45)$$

We know that $\mathbf{\Phi}_n(\mathbf{r}) = \hat{\mathbf{n}} \times \mathbf{f}_n(\mathbf{r})$. So, when $i = n$, $G''_{i,n} = 0$. Furthermore, when ith and nth edges do not lie on a comman triangle, $G''_{i,n}$ has to be zero also. As a result, we have nonzero $G''_{i,n}$ elements when ith and nth edges do not lie on a common triangle but $i \neq n$. For that case, we can evaluate $G''_{i,n}$ as follows.

$$
\begin{aligned}
G''_{i,n} =& \int_S \mathbf{\Phi}_n(\mathbf{r}) \cdot \mathbf{f}_i(\mathbf{r}) dS, \\
=& \int_S [\hat{\mathbf{n}} \times \mathbf{f}_n(\mathbf{r})] \cdot \mathbf{f}_i(\mathbf{r}) dS, \\
=& \hat{\mathbf{n}} \cdot \int_S [\mathbf{f}_n(\mathbf{r}) \times \mathbf{f}_i(\mathbf{r})] \, dS, \\
=& \left(\frac{\pm l_n}{2A}\right)\left(\frac{\pm l_i}{2A}\right) \ \hat{\mathbf{n}} \cdot \int_S [(\mathbf{r} - \mathbf{r}_i) \times (\mathbf{r} - \mathbf{r}_n)] \, dS, \\
=& \left(\frac{\pm l_n}{2A}\right)\left(\frac{\pm l_i}{2A}\right) \ \hat{\mathbf{n}} \cdot \int_S [\mathbf{r}_i \times \mathbf{r}_n + (\mathbf{r}_n - \mathbf{r}_i) \times \mathbf{r}] \, dS,
\end{aligned}
\tag{7.46}
$$

where A is the area of the common triangle, and the sign (either $+$ or $-$) depends on the edge direction. The final form of Eq. (7.46) can be evaluated by using the Gaussian quadrature method.

7.1.4 Coupling of FEM and MoM Matrices

The exterior electric field integral given by ch6finalext can be written in a compact form,

$$
S_m = \sum_{n=1}^{N_s} j_n \left[Z^{(1)}_{mn} + Z^{(2)}_{mn} \right] + \sum_{n=1}^{N_s} m_n Z^{(3)}_{mn} \tag{7.47}
$$

where vector and matrices are defined as

$$
S_m = \int_s \mathbf{f}_m(\mathbf{r}) \cdot E^{inc}(\mathbf{r}) ds(\mathbf{r}),
$$

$$
\begin{aligned}
Z_{mn}^{(1)} = &\; jk_0\eta_0 \int_s \int_s \mathbf{f}_m(\mathbf{r}) \cdot \mathbf{K}^J(\mathbf{r},\mathbf{r}')\mathbf{f}_n(\mathbf{r}')ds(\mathbf{r}')ds(\mathbf{r}), \\
Z_{mn}^{(2)} = &\; \frac{j\eta_0}{k_0} \int_s \int_s \nabla \cdot \mathbf{f}_m(\mathbf{r}) \cdot G_\Phi^{EJ}(\mathbf{r},\mathbf{r}')\nabla' \cdot \mathbf{f}_n(\mathbf{r}')ds(\mathbf{r}')ds(\mathbf{r}), \\
Z_{mn}^{(3)} = &\; P.V. \int_s \int_s \mathbf{f}_m(\mathbf{r}) \cdot \nabla'\mathbf{G}^{EM}(\mathbf{r},\mathbf{r}') \cdot \mathbf{f}_n(\mathbf{r}')ds(\mathbf{r}')ds(\mathbf{r})(\mathbf{r}), \\
&-\frac{1}{2}\int_s \mathbf{f}_m(\mathbf{r}) \cdot \mathbf{f}_n(\mathbf{r})ds(\mathbf{r}).
\end{aligned}
\tag{7.48}
$$

We know the relationship between the magnetic current and the tangential electric on the surface. By using $\mathbf{M}(\mathbf{r}) = -\hat{\mathbf{n}} \times \mathbf{E}|_s$, we can couple FEM and MoM equations, (7.12) and (7.47), as

$$
\left[\begin{array}{ccc} \mathbf{A} & \mathbf{B} & \\ \mathbf{B}^T & \mathbf{C} & \mathbf{G} \\ & \mathbf{Z^{(3)}} & \mathbf{Z^{(1)}} + \mathbf{Z^{(2)}} \end{array}\right]
\left[\begin{array}{c} \mathbf{E^i} \\ \mathbf{E^b} \\ \mathbf{J} \end{array}\right]
=
\left[\begin{array}{c} \mathbf{S^i} \\ \mathbf{0} \\ \mathbf{S^e} \end{array}\right].
\tag{7.49}
$$

However, the above formulation is valid only if the FEM mesh matches MoM mesh on the boundary. In order to couple arbitrary meshes, some additional interpolation functions are required.

The matrix equation (7.49) is a straight-forward solution but not a very efficient one. The advantage of having a sparse and symmetric FEM matrix should be utilized in a clever way. In this manner, let us reformulate the matrix equation. We can re-write Eq.s (7.12) and (7.51) as follows

$$
\left[\begin{array}{cc} \mathbf{A} & \mathbf{B} \\ \mathbf{B}^T & \mathbf{C} \end{array}\right]
\left[\begin{array}{c} \mathbf{E}^i \\ \mathbf{E}^b \end{array}\right]
=
\left[\begin{array}{cc} 0 & 0 \\ 0 & \mathbf{G} \end{array}\right]
\left[\begin{array}{c} 0 \\ \mathbf{J} \end{array}\right]
+
\left[\begin{array}{c} \mathbf{S}^i \\ 0 \end{array}\right],
\tag{7.50}
$$

and

$$
\mathbf{D}\ \mathbf{J} + \mathbf{F}\ \mathbf{E^b} = \mathbf{S^e},
\tag{7.51}
$$

respectively, where $\mathbf{D} = \left[\mathbf{Z^{(1)}} + \mathbf{Z^{(2)}}\right]$ and $\mathbf{F} = \mathbf{Z^{(3)}}$. In Eq. (7.51), we can leave the electric current alone on the left hand side as

$$\mathbf{J} = -\mathbf{D^{-1}}\ \mathbf{F}\ \mathbf{E^b} + \mathbf{D^{-1}}\ \mathbf{S^e}. \tag{7.52}$$

Let us substitute (7.52) into (7.50) to obtain

$$\begin{bmatrix} \mathbf{A} & \mathbf{B} \\ \mathbf{B}^T & \mathbf{C} - \mathbf{GD^{-1}F} \end{bmatrix} \begin{bmatrix} \mathbf{E}^i \\ \mathbf{E}^b \end{bmatrix} = \begin{bmatrix} \mathbf{S}^i \\ \mathbf{D^{-1}S^e} \end{bmatrix}. \tag{7.53}$$

Clearly, Eq. (7.53) is more compact than Eq. (7.49) but this does not mean that the solving (7.53) is the most efficient way. Since the FEM matrix is symmetric, the Hermitian of this matrix is simply its complex conjugate. Moreover, the FEM matrix is sparse. By using a row-indexed scheme [100], we can easily and efficiently reach the non-zero elements of the FEM matrix, which is a very important property for the solvers constructed on the biconjugate-gradient (BCG) method . As a result of these, it is more efficient to store the FEM and MoM matrices seperately as follows,

$$\left(\begin{bmatrix} \mathbf{A} & \mathbf{B} \\ \mathbf{B}^T & \mathbf{C} \end{bmatrix} + \begin{bmatrix} 0 & 0 \\ 0 & -\mathbf{GD^{-1}F} \end{bmatrix} \right) \begin{bmatrix} \mathbf{E}^i \\ \mathbf{E}^b \end{bmatrix} = \begin{bmatrix} \mathbf{S}^i \\ \mathbf{D^{-1}S^e} \end{bmatrix}. \tag{7.54}$$

In this work, the biconjugate-gradient (BCG) method is used to solve the matrix equation which requires $O(KN^2)$ CPU time and $O(N^2)$ memory, where N is the number of unknowns and K is the number of iterations. Since the main purpose of this work is the reduction of the number of unknowns (N), we have not implemented any acceleration methods (such as the fast multipole method and adaptive integral method) to further reduce the computation time and storage requirements.

7.2 Numerical results

The hybrid FEM/MoM for layered media has been implemented with a combination of FORTRAN 77 and C programs. All the programs were compiled on a Dell Optiplex GX260 desktop with Intel P4 2.4 GHz processor and 1024M RAM. For all the examples presented below, the tolerance value used for the BCG solver is 10^{-4}. The scatterers are illuminated with a $\hat{\mathbf{z}}$-directed electric dipole located at $(2.1, 2.1, 3.675)$ m, with a frequency of $f = 10$ MHz. There are 16 receivers located uniformly along the line $(0.9 : 3.2, 1.9, 3.425)$ m. The dimensions of the cuboid are $(a, b, c) = (1.6, 1.6, 1.15)$ m, and the center of the cuboid is at $(2.05, 2.05, 1.825)$ m.

7.2.1 A homogeneous scatterer in a layered medium

For the following four examples, the FEM volume is discretized with 540 inner edges and 625 tetrahedrons; the MoM surface is discretized with 300 triangles and 450 boundary edges. 6.58 MBytes of memory is required to solve the matrix equation. In order to compare our FEM/MoM results, the BCGS-FFT solver is used where $32 \times 32 \times 23$ voxels are used for the volumetric discretization.

Example 1: First, similar to the setup used in the previous chaper, here we have a dielectric cuboid embedded in the top layer of a 3-layer medium shown as Figure 7.4 (a). Electrical parameters of the dielectric cuboid are $\epsilon_{r,c} = 16$, $\sigma_c = 0.01$ S/m. Having 300 triangles for the surface of the cuboid results in a sampling of density 22 points per wavelength (PPW). The 3-layer background is defined by $\epsilon_{r,1} = 1$, $\epsilon_{r,2} = 12$, $\epsilon_{r,3} = 4$; $z_2 = 2.75$ m, $z_1 = 3.25$ m. The source and receivers are located in the bottom layer. Some details of the implementation is given in Figure 7.4 (b).

Figure 7.4 (c) shows the comparison of the hybrid FEM/MoM and BCGS-FFT results for the magnitude and phase of the scattered field at the receiver points. Clearly, two results agree very well. The difference between two results is less than 2%.

Example 2: In the hybrid FEM/MoM method, the number of the layers and the location of the source, receivers, and scatterer can be arbitrary. In order to investigate this statement, we add one more layer between $z = 3.25$ m and $z = 3.75$ m for this case. The relative permittivity of this additional layer is 8. All other parameters are same the as the previous example, except the conductivity of the homogeneous cuboid 0.001 S/m here. Note that additional layer makes the source, the receivers and the scatterer all locate in different layers of the multilayered background. Figure 7.5 (c) is the comparison of the hybrid FEM/MoM and BCGS-FFT results for the magnitude and phase of the scattered field at the receiver points. Clearly, there is a very good agreement between two results. One important observation is that the number of iterations used for the BCG solver is less than the previous case. When we increase the conductivity of the problem, we also increase the number of iterations used for the iterative solver to obtain the desired level of accuracy. Since in this example, the conductivity of the scatterer is less than the previous case, it requires less iterations.

Example 3: In the first two examples of this chapter, the homogeneous scatterer is embedded in the top layer of the multilayered medium, which is similar to a half-space as we only observe the transmission effect instead of having both transmission and reflection effects. In order to observe both effects, now we place the scatterer in the middle layer of a 3-layer medium shown as Figure 7.6 (a). Note that $\epsilon_{r,2} = 4$,

$\epsilon_{r,3} = 12$. Figure 7.6 (c) shows the comparison of the hybrid FEM/MoM and BCGS-FFT results for the magnitude and phase of the scattered field at the receiver points. Again, there is a very good agreement between two results. The difference is less than 2%. It should be noted that the scattered field is stronger than all the previous cases.

Example 4: Very similar to Example 3, here we have a homogeneous cuboid in the middle layer of a 3-layer medium, however, here the relative permittivity of the scatterer is 32. Figure 7.7 (c) shows the good agreement between the hybrid FEM/MoM and BCGS-FFT results for the magnitude and phase of the scattered field at the receiver points. The difference is less than 2%. We can reach the same conclusion about dependence of the iteration number on the conductivity. The scatterer's relative permittivity is higher than the scatterer in Example 3, so this one is less conductive, hence the BCG solver uses less iterations (133 iterations in this case, whereas it is 141 for Example 3).

For all the above examples, homogeneous cuboids are used to validate the method. The examples with inhomogeneous scatterers are given next. Before focusing on inhomogeneous examples, there are some computational details to be mentioned. The number of iterations depends on the tolerance used for the BCG solver. As mentioned above, we set the tolerance to 10^{-4}. When the number of the unknowns is around 1000, we can safely use this tolerance because in the worst case scenario, we will have a round off error for single precision data around $1000 \times 1.2\ 10^{-7} = 1.2\ 10^{-4}$ which is still larger than our tolerance. When we look at the number of iterations used for the BCG solver in the above examples, it is almost one third of the number of boundary edges, or less. Since the MoM matrix is a dense matrix of dimension

N_b, using only $N_b/3$ iterations, where the total number of the unknowns is $N_i + N_b$, menas the iterative solver works very efficiently. Furthermore, when we look at the time usage reports, we can see that we are capable of solving matrices with 950 unknowns in less than a minute.

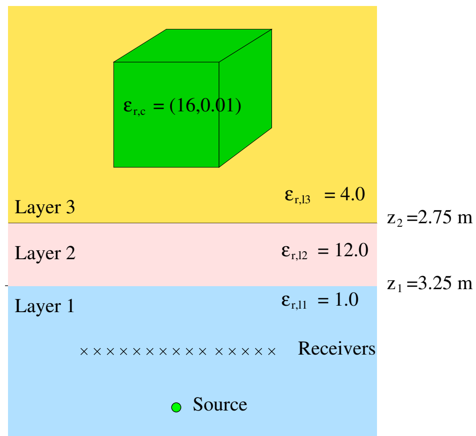

(a)

FEM Volume: 540 inner edges, 625 tetrahedrons
MoM Region: 300 triangles, 450 boundary edges Sampling density: 23.4 PPW
Used Memory : 6.58 M Bytes
Time Usage Report: LMGF Tables: 24 seconds FEM/MoM Matrices: 116 seconds Solving the hybrid matrix equation: 23 seconds
Bi-Conjugate Gradient Solver Report: tolerence: 1.00e-04 the least residue: 6.61e-05 total iteration number: 121

(b)

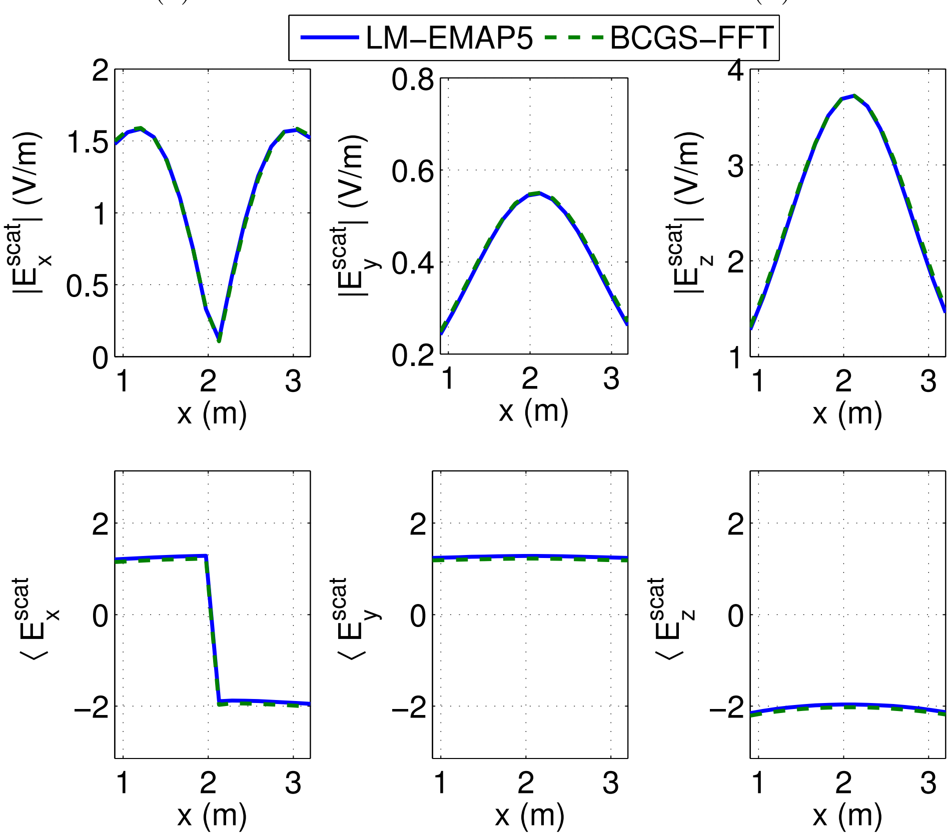

(c)

Figure 7.4: (a) A homogeneous cuboid in the top layer of a 3-layer medium. The source and receivers are located in the bottom layer. (b) Numerical details of the implementation. (c) The comparison of FEM/MoM and BCGS-FFT results for the magnitude and phase of the scattered field at the receiver points for Example 1.

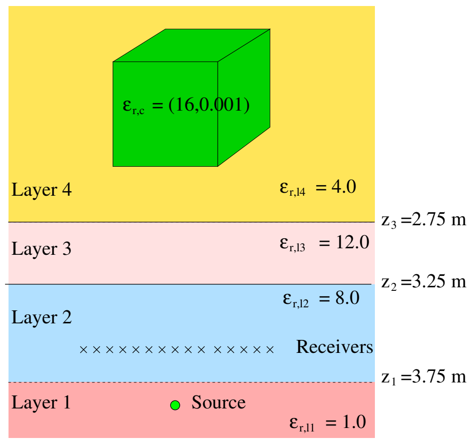

(a)

FEM Volume: 540 inner edges, 625 tetrahedrons
MoM Region: 300 triangles, 450 boundary edges Sampling density: 23.4 PPW
Used Memory : 6.58 M Bytes
Time Usage Report: LMGF Tables: 25 seconds FEM/MoM Matrices: 288 seconds Solving the hybrid matrix equation: 62 seconds
Bi-Conjugate Gradient Solver Report: the least residue: 7.03e-05 total iteration number: 168

(b)

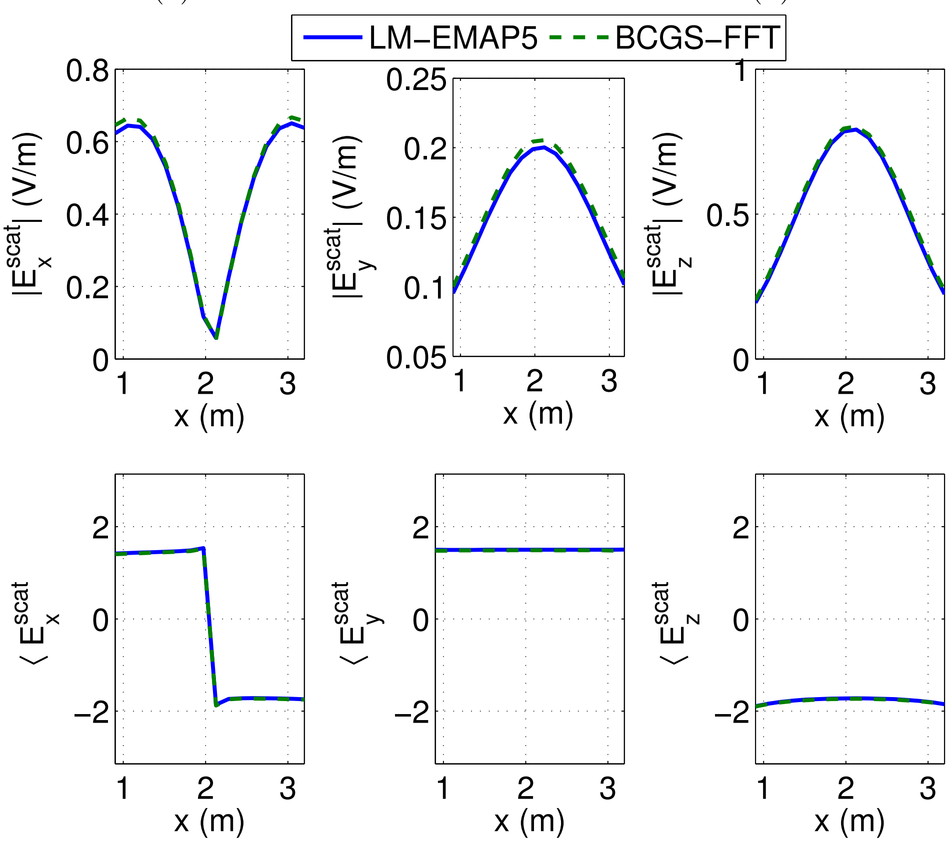

(c)

Figure 7.5: (a) A homogeneous cuboid in the top layer of a 4-layer medium. The source is in the bottom layer, and the receivers are located in the second layer. (b) Numerical details of the implementation. (c) The comparison of FEM/MoM and BCGS-FFT results for the magnitude and phase of the scattered field at the receiver points for Example 2.

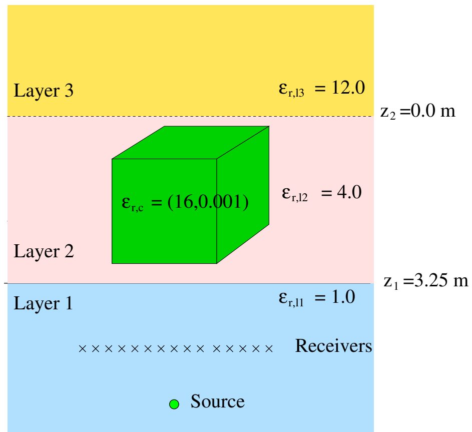

(a)

FEM Volume: 540 inner edges, 625 tetrahedrons
MoM Region: 300 triangles, 450 boundary edges Sampling density: 23.4 PPW
Used Memory : 6.58 M Bytes
Time Usage Report: LMGF Tables: 25 seconds FEM/MoM Matrices: 286 seconds Solving the hybrid matrix equation: 53 seconds
Bi-Conjugate Gradient Solver Report: the least residue: 8.57e-05 total iteration number: 141

(b)

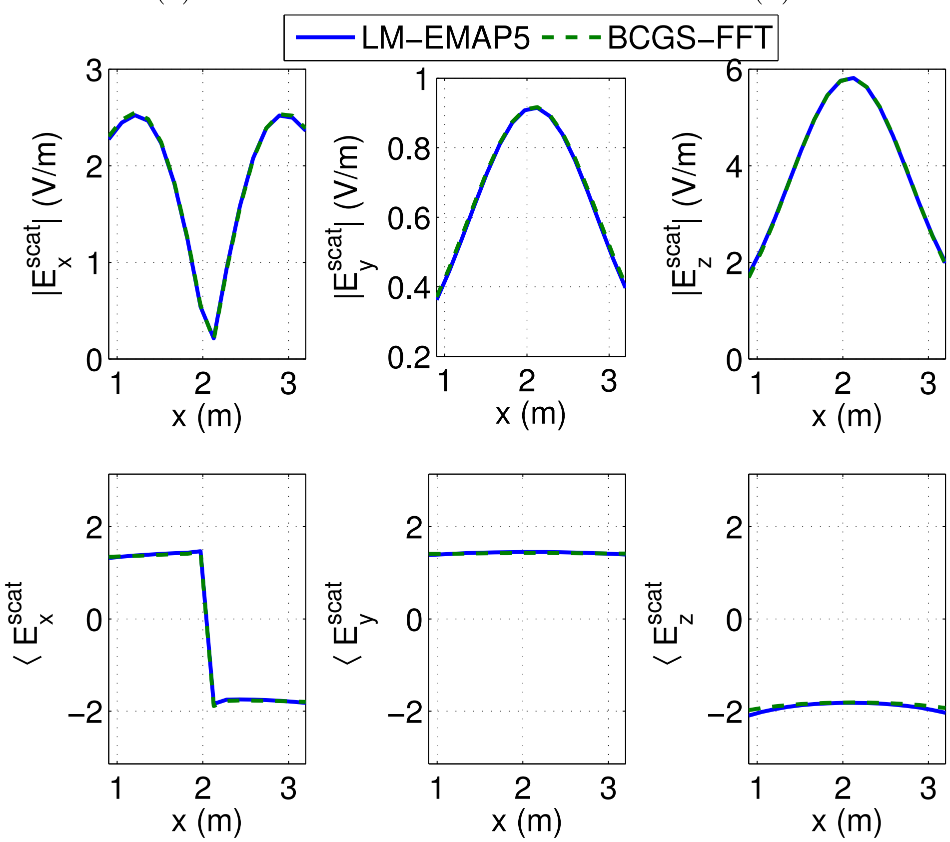

(c)

Figure 7.6: (a) A homogeneous cuboid in the middle layer of a 3-layer medium. The source and receivers are located in the bottom layer. (b) Numerical details of the implementation. (c) The comparison of FEM/MoM and BCGS-FFT results for the magnitude and phase of the scattered field at the receiver points for Example 3.

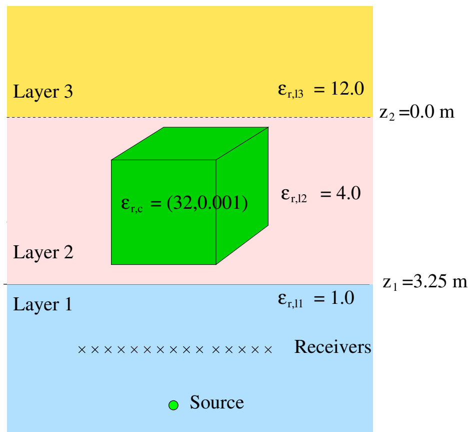

(a)

FEM Volume: 540 inner edges, 625 tetrahedrons
MoM Region: 300 triangles, 450 boundary edges Sampling density: 16.5 PPW
Used Memory : 6.58 M Bytes
Time Usage Report: LMGF Tables: 24 seconds FEM/MoM Matrices: 117 seconds Solving the hybrid matrix equation: 25 seconds
Bi-Conjugate Gradient Solver Report: tolerence: 1.00e-04 the least residue: 8.19e-05 total iteration number: 133

(b)

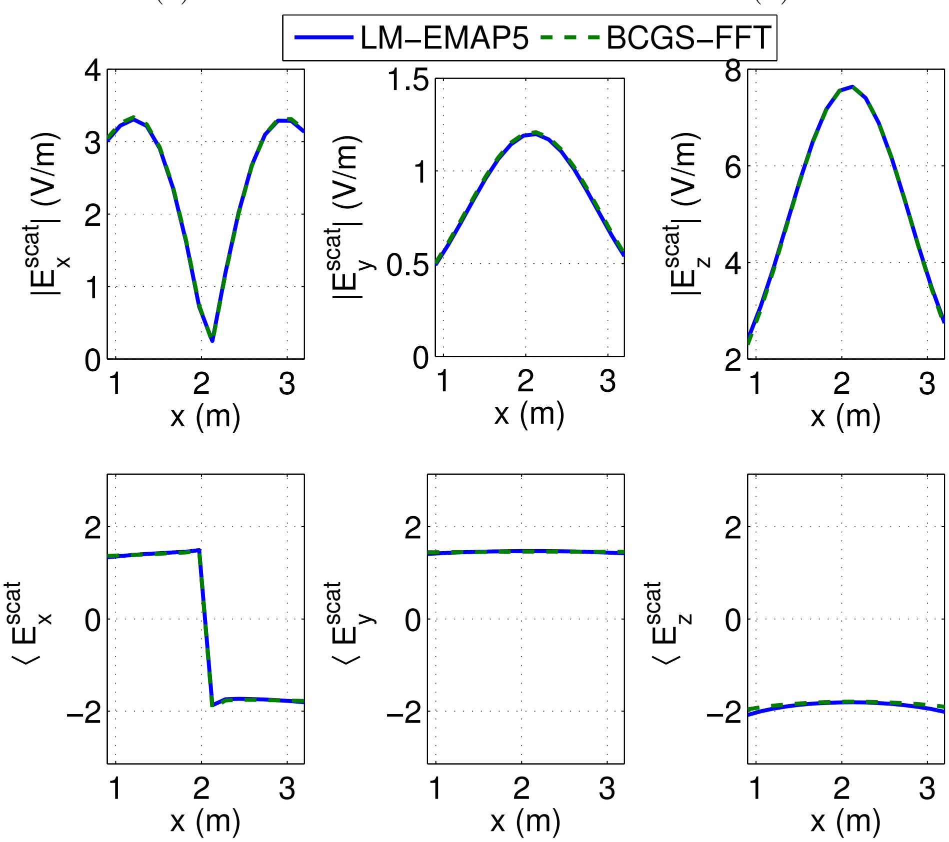

(c)

Figure 7.7: (a) A homogeneous cuboid in the top layer of a 3-layer medium. The source and receivers are located in the bottom layer. (b) Numerical details of the implementation. (c) The comparison of FEM/MoM and BCGS-FFT results for the magnitude and phase of the scattered field at the receiver points for Example 4.

7.2.2 An inhomogeneous scatterer in a layered medium

In the previous subsection, homogeneous scatterers are used to validate the accuracy of the hybrid FEM/MoM implentation. Now, we can focus on some inhomogeneous examples. For the following four examples, the FEM volume is disrecretized with 903 inner edges and 1000 tetrahedrons; the MoM surface is discretized with 420 triangles and 630 boundary edges. 12.86 MBytes of memory is required to solve the matrix equation.

Example 5: Assume that right half of the scatterer used in Example 1 is replaced with another material, having a relative permittivity of 8 which results an inhomogeneous cuboid, shown as Figure 7.9 (a). All the other parameters are the same as Example 2. Again, we solve this problem by using the hybrid method and the BCGS-FFT method. Figure 7.9 (c) shows the good agreement between two different sets of results for the magnitude and phase of the scattered field at the receiver points. Even though it is not very easy to see, the plotted field lines are no longer symmetric. The number of samples used for the discretization in the $\hat{\mathbf{x}}$-direction is more than the previous cases, thus more unknowns, memory and CPU times are required, see Figure 7.9 (b) for the details.

Example 6: We repeat Example 5 with a minor modification: the relative permittivity of the left half is 32. Figure 7.10 (c) shows the very good agreement between FEM/MoM and BCGS-FFT results for the magnitude and phase of the scattered field at the receiver points. Note that the number of iterations is larger than the previous case due to more complex (unsymmetric) behaviour of the FEM matrix.

Examples 7 and 8: For the following two examples, we put the inhomogeneous scatterer in the middle layer. Figures 7.11 (a) and 7.12 (a) show the problem geometries and Figures 7.11 (c) and 7.12 (c) depict the FEM/MoM and BCGS-FFT results for the magnitude and phase of the scattered field at the receiver points. Note that the number of iterations used for Example 8 is larger than Example 7 due to the more complex (unsymmetric) behaviour of the FEM matrix.

It is mentioned that the FEM is capable of working with a non-uniform mesh. Figure 7.8 shows the same inhomogeneous cuboid discretized in two different ways: (a) two cuboids having 4 units in the $\hat{\mathbf{x}}$-direction, (b) one cuboid still has 4 units in the $\hat{\mathbf{x}}$-direction, but the other one has only 2 units. When we think about the sampling density requirements, in order to have enough samples for the region with the highest permittivity, we might oversample other regions with smaller permittivities unless we use a non-uniform mesh. For the last example presented in this chapter, the relative permittivities of the left and right cuboids are 32 and 8, respectively. Since the wavelength in the cuboid-1 is only the half of the one in cuboid-2, if we use n units in the $\hat{\mathbf{x}}$-direction for cuboid-1, we need to use only $n/2$ units for the second cuboid in order to have the same sampling density in each region. For this specific example, the memory requirement is reduced from 12.86 MBytes to 8.44 MBytes by using the non-uniform mesh depicted in Figure 7.8 (b).

For all the presented examples, it can be said that the number of iterations used for the BCG solver is almost half of the boundary edges, or less. As mentioned before, when we compare the iteration number to the matrix dimension, N_b, using only $N_b/2$ iterations means the iterative method works very efficiently. When we look at the time usage reports, we can see that we are capable of solving for 1533 unknowns in less than 100 seconds.

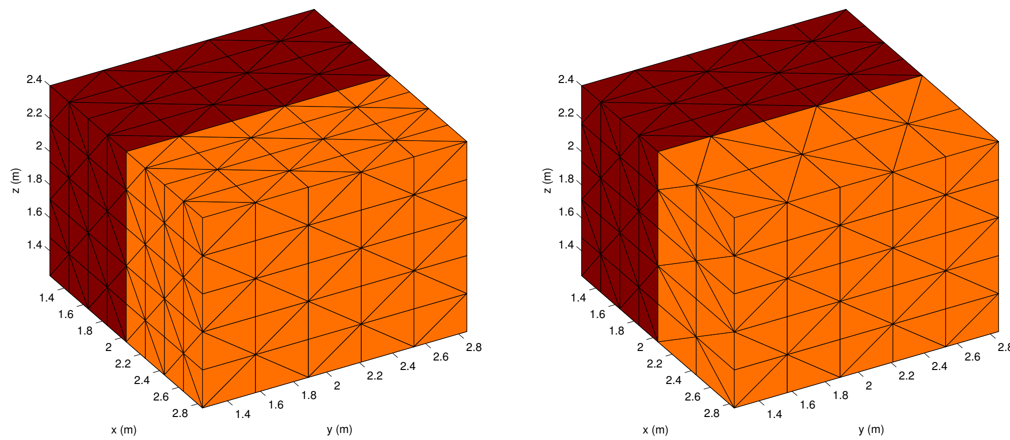

(a) (b)

Figure 7.8: (a) Both cuboids have 4 units in the $\hat{\mathbf{x}}$-direction. The FEM volume is disrecretized with 903 inner edges and 1000 tetrahedrons; the MoM surface is discretized with 420 triangles and 630 boundary edges. 12.86 MBytes of memory is required to solve the matrix equation. (b) While one cuboid still has 4 units in the $\hat{\mathbf{x}}$-direction, the other one has only 2. the FEM volume is disrecretized with 661 inner edges and 750 tetrahedrons; the MoM surface is discretized with 340 triangles and 510 boundary edges. 8.44 MBytes of memory is required to solve the matrix equation.

All the results presented in Chapters 8 and 9 support the validity of the formulation and implementation of the surface integral equation solution for layered media. The complexity of the problems can be increased freely as long as we satisfy the minimum sampling density requirements and as long as we consider our computers' limitations. The presented examples have very simple geometries in order to keep the memory and CPU time requirements low. We can simply formulate the memory requirement as follows

$$\text{Required Memory} = \frac{4 \times N_b^2 + 22 \times N_i}{10^6} \text{ (MBytes)}.$$

Finally, it should be noted that when we change the scatteter's electrical parameters, we do not need to calculate the layered medium Green's functions again. For example, we use the same Green's functions for Examples 7 and 8.

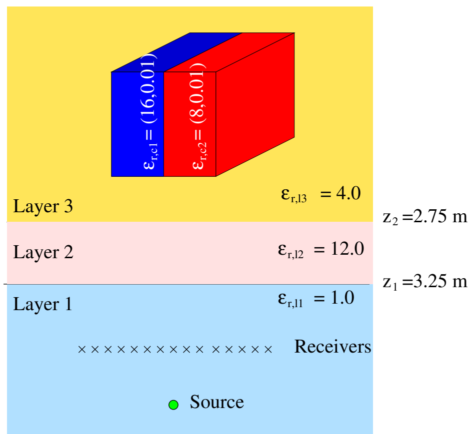

(a)

FEM Volume: 903 inner edges, 1000 tetrahedrons
MoM Region: 420 triangles, 630 boundary edges Sampling density: 23.4 PPW
Used Memory : 12.86 M Bytes
Time Usage Report: LMGF Tables: 30 seconds FEM/MoM Matrices: 281 seconds Solving the hybrid matrix equation: 65 seconds
Bi-Conjugate Gradient Solver Report: the least residue: 8.47e-05 total iteration number: 180

(b)

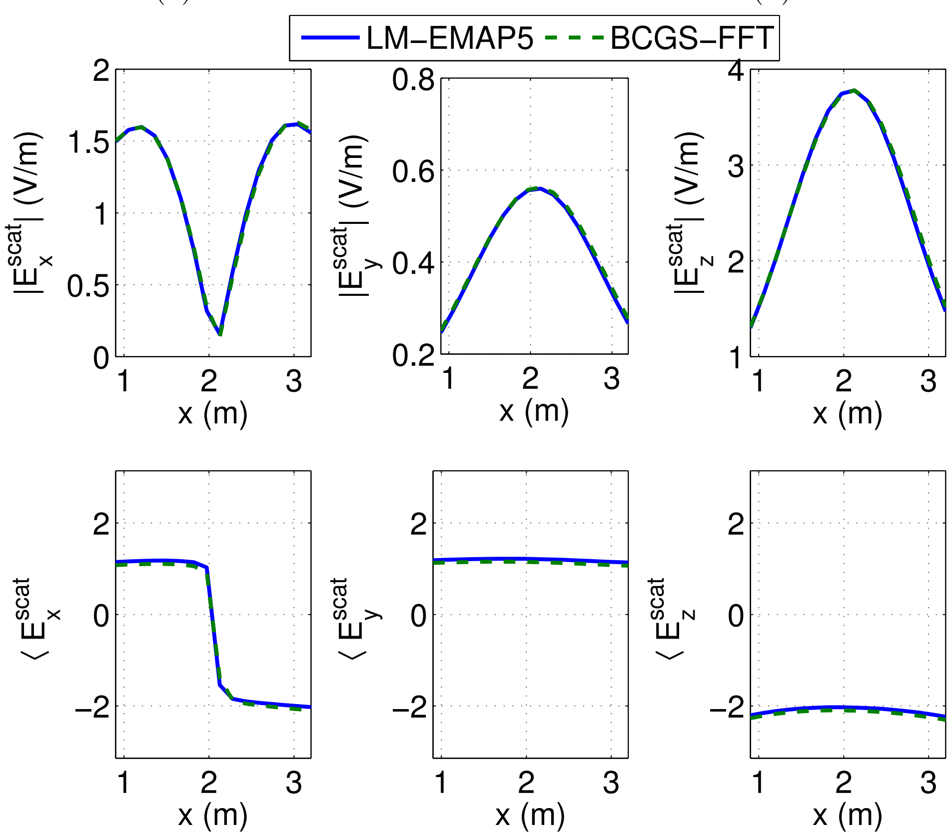

(c)

Figure 7.9: (a) An inhomogeneous cuboid in the top layer of a 3-layer medium. The source and receivers are located in the bottom layer. (b) Numerical details of the implementation. (c) The comparison of FEM/MoM and BCGS-FFT results for the magnitude and phase of the scattered field at the receiver points for Example 5.

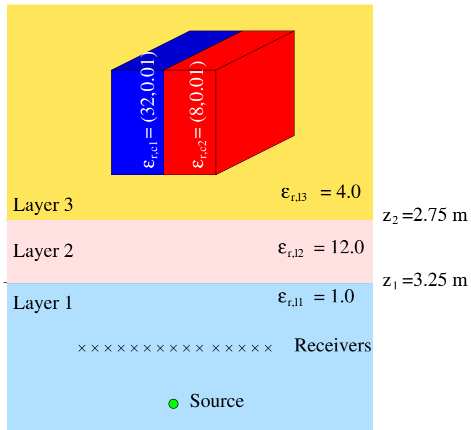

(a)

FEM Volume: 903 inner edges, 1000 tetrahedrons
MoM Region: 420 triangles, 630 boundary edges Sampling density: 16.5 PPW
Used Memory : 12.86 M Bytes
Time Usage Report: LMGF Tables: 32 seconds FEM/MoM Matrices: 283 seconds Solving the hybrid matrix equation: 82 seconds
Bi-Conjugate Gradient Solver Report: the least residue: 6.88e-05 total iteration number: 225

(b)

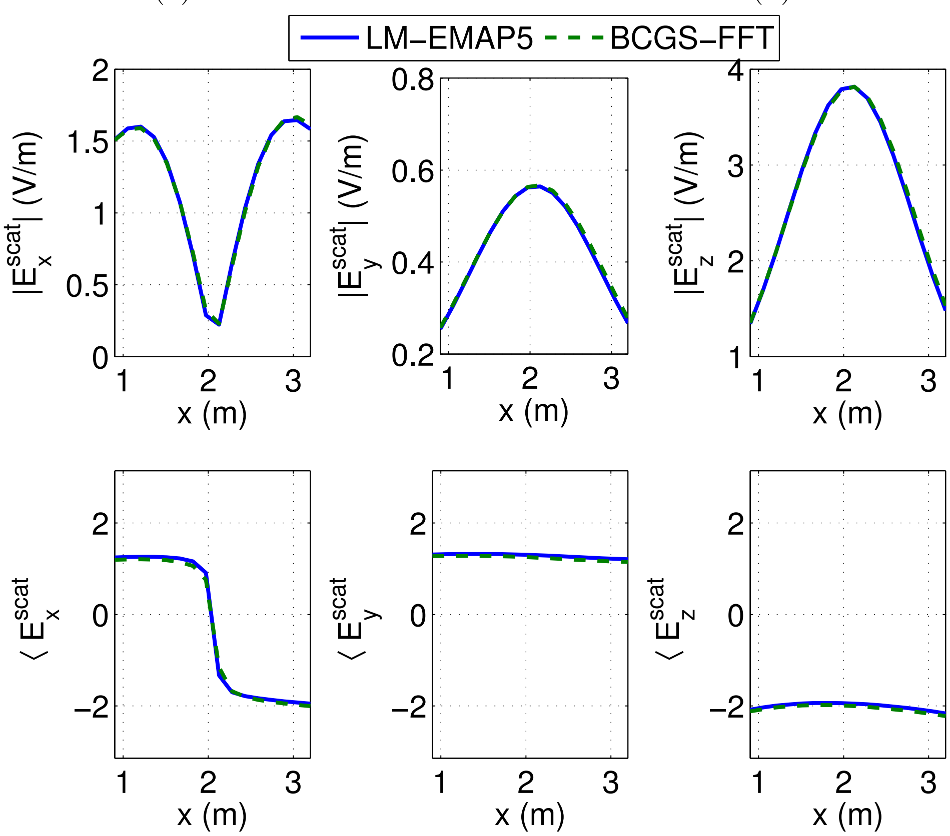

(c)

Figure 7.10: (a) An inhomogeneous cuboid in the top layer of a 3-layer medium. The source and receivers are located in the bottom layer. (b) Numerical details of the implementation. (c) The comparison of FEM/MoM and BCGS-FFT results for the magnitude and phase of the scattered field at the receiver points for Example 6.

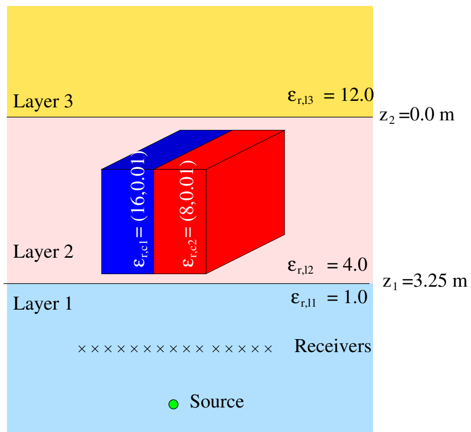

(a)

FEM Volume: 903 inner edges, 1000 tetrahedrons
MoM Region: 420 triangles, 630 boundary edges Sampling density: 23.4 PPW
Used Memory : 12.86 M Bytes
Time Usage Report: LMGF Tables: 32 seconds FEM/MoM Matrices: 281 seconds Solving the hybrid matrix equation: 82 seconds
Bi-Conjugate Gradient Solver Report: the least residue: 9.18e-05 total iteration number: 225

(b)

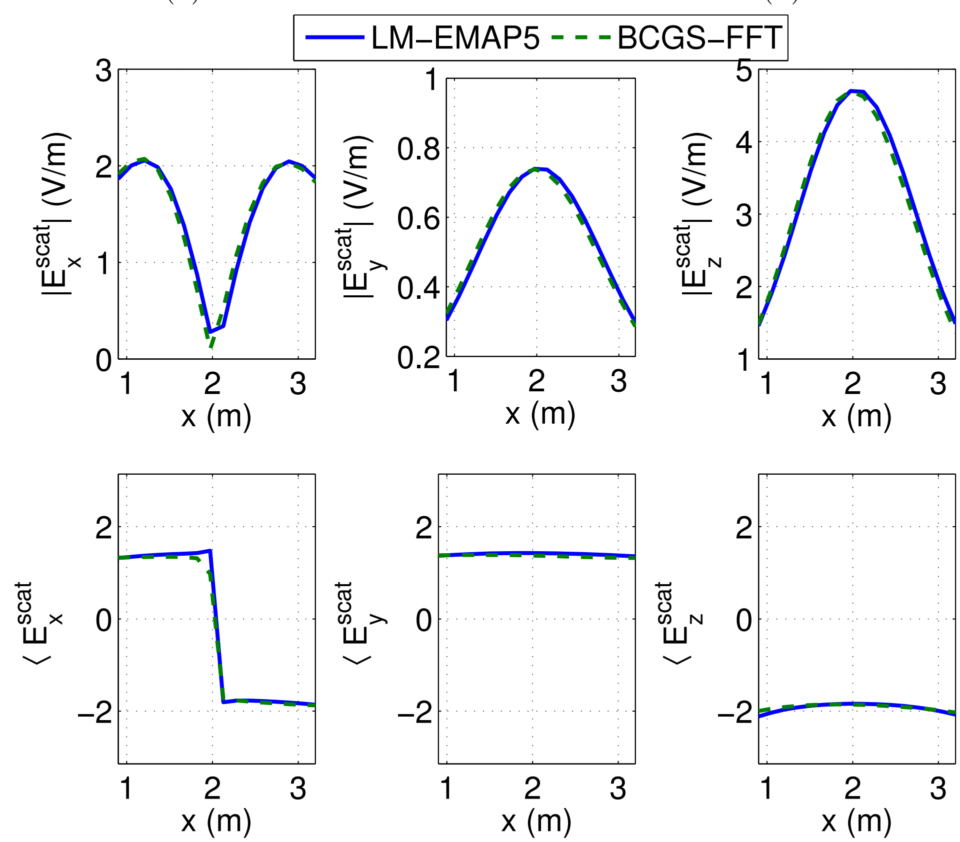

(c)

Figure 7.11: (a) An inhomogeneous cuboid in the middle layer of a 3-layer medium. The source and receivers are located in the bottom layer. (b) Numerical details of the implementation. (c) The comparison of FEM/MoM and BCGS-FFT results for the magnitude and phase of the scattered field at the receiver points for Example 7.

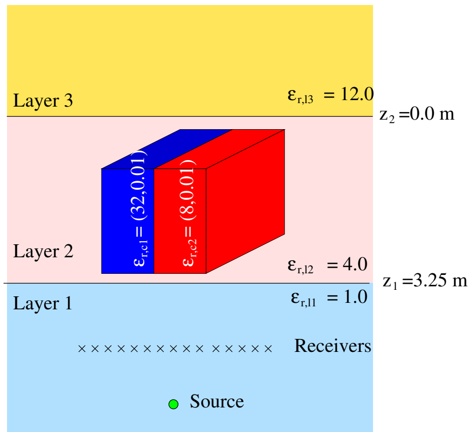

(a)

FEM Volume: 903 inner edges, 1000 tetrahedrons
MoM Region: 420 triangles, 630 boundary edges Sampling density: 16.5 PPW
Used Memory : 12.86 M Bytes
Time Usage Report: LMGF Tables: 33 seconds FEM/MoM Matrices: 284 seconds Solving the hybrid matrix equation: 96 seconds
Bi-Conjugate Gradient Solver Report: the least residue: 8.38e-05 total iteration number: 256

(b)

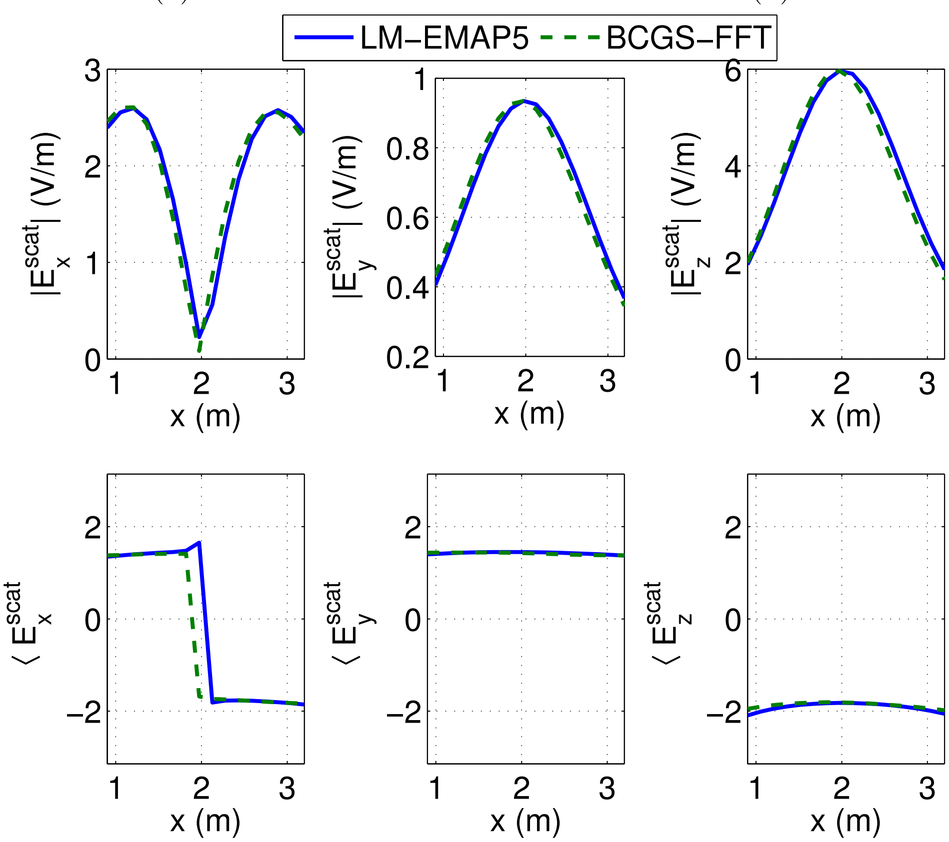

(c)

Figure 7.12: (a) An inhomogeneous cuboid in the middle layer of a 3-layer medium. The source and receivers are located in the bottom layer. (b) Numerical details of the implementation. (c) The comparison of FEM/MoM and BCGS-FFT results for the magnitude and phase of the scattered field at the receiver points for Example 8.

7.3 Conclusion

In this chapter, a hybrid FEM/MoM solver is presented that can handle both homogeneous and inhomogeneous scatterers both in free space and in a layered medium. The layered medium Green's funtions are evaluated efficiently by using an interpolation technique and then utilized in the exterior surface integral formulation, which actually is used as a radiation boundary condition, to truncate the computational domain of the finite-element method. The FEM is utilized for the inhomogeneous interior problem, which is discretized with tetrahedrons. In order to increase the efficiency of the overall method, the symmetric and sparse FEM matrix is stored with a row-indexed scheme, and the bi-conjugate gradient solver is used. The validity of the hybrid method is supported with several examples by using homogeneous and inhomogeneous scatterers.

Chapter 8

Future Work

Table 8 summarizes the numerical methods developed by myself and the other members of Dr. Liu's research group in order to solve layered medium scattering problems. As indicated in the table, each method has different capabilities. When we

Table 8.1: Developed Methods for Layered Media and Their Capabilities

	Surface Integral	Volume Integral	Hybrid
2D	SIM *Homogeneous* *PEC or DIE*	BCGS-FFT *Inhomogeneous* *DIE only*	SIM/FEM *Inhomogeneous* *DIE-PEC comb.*
3D	MoM *Homogeneous* *PEC or DIE*	BCGS-FFT *Inhomogeneous* *DIE only*	MoM/FEM *Inhomogeneous* *DIE-PEC comb.*

think about the advantages and disadvantages of each method, we should not try to use just one single method for all different configurations. For example, using a hybrid method for a homogeneous target is not an appropriate choice. On the other hand, currently each method has its own input/output file style, even though they are very similar to each other, there are some major differences. As a result of these, an ultimate goal of my future work would be combining of these different methods to create a *Layered Medium Toolbox* in such a way that the code would be able to choose the solution method by itself by using a general input file. However, before creating this toolbox, there are some other important steps to go.

(a) Special Treatment for Objects Straddling Multiple Layers

Our current 3D FEM/MoM implementation is not capable of solving for objects straddling multiple layers. We have experienced this problem for 2D case too, however by applying our subtraction technique appropriately, we could add that capability to our 2D SIM/FEM solver. We need to follow the same procedure here. In terms of the theory, we have everything we need: the dyadic layered medium Green's functions with singularity subtraction and the hybrid FEM/MoM code. The only remaining step is the utilization of these two elements. This feature is *a must* for the completeness of the work and will be completed in the following months.

(b) Mesh Generator

SIFT5, which is designed to generate input files for the field solver EMAP5, can produce cuboid meshes with metallic patches only. In order to generate more complicated and sophisticated geometries, we need a better mesh generator. As a result, we need to utilize a more sophisticated mesh generator, such as NETGEN (NETGEN/NGSolve V4.4, developed at Johannes Kepler University Linz, Austria) for our FEM/MoM solver.

(c) Acceleration via FFT

For the developed surface integral equation solvers and hybrid algorithms, the solution of the matrix equation can be accelerated by using the fast Fourier transform (FFT) for the objects having a surface partially parallel to the xy plane (assuming planar layers are all parallel to the xy plane). For example, assume that we have a cuboid (RBC), with the dimensions of $(2L_x \times 2L_y \times 2L_z)$, centered at the origin $(0, 0, 0)$. First, only consider the first basis functions are on the $\{z = L_z\}$ plane. Using the first testing functions on the $\{z = \pm L_z\}$ plane, the impedance matrix will be written as

$$Z_{mn}^{(1)} = jk_b\eta_b \int_{y_{m_y-1}}^{y_{m_y}} \int_{x_{m_x-1}}^{x_{m_x+1}} \int_{y_{n_y-1}}^{y_{n_y}} \int_{x_{n_x-1}}^{x_{n_x+1}} \mathbf{f}_{m_x,1}(\mathbf{r})\cdot\bar{\mathbf{K}}^J(\mathbf{r},\mathbf{r}')\mathbf{f}_{n_x,1}(\mathbf{r}')dx'dy'dxdy. \quad (8.1)$$

We can transform the integration variables into local variables, ξ and η, and obtain

$$R = |\mathbf{r}-\mathbf{r}'| = \sqrt{(x_{m_x}+\xi-x_{n_x}-\xi')^2+(y_{m_y}+\eta-y_{n_y}-\eta')^2+(L_z \mp L_z)^2}, \quad (8.2)$$

$$Z_{mn}^{(1)} = jk_b\eta_b \int_{-h_y}^{0} \int_{-h_x}^{h_x} \int_{-h_y}^{0} \int_{-h_x}^{h_x} (1-\frac{|\xi|}{h_x})\bar{\mathbf{K}}^J(k_bR)(1-\frac{|\xi'|}{h_x})d\xi'd\eta'd\xi d\eta, \quad (8.3)$$

where we can utilize Gaussian quadratures in order to evaluate the integrals numerically. Suppose we use only one point in each element, and quadrature points in local domain are $(-\xi_g,-\eta_g)$,$(\xi_g,-\eta_g)$,$(-\xi_g',-\eta_g')$ and $(\xi_g',-\eta_g')$. Therefore, the distances from testing points to basis points are

$$\begin{aligned} R =& \sqrt{(x_{m_x}\mp\xi_g-x_{n_x}\mp\xi_g')^2+(y_{m_y}-\eta_g-y_{n_y}+\eta_g')^2+(L_z\mp L_z)^2} \\ =& \sqrt{(x_{m_x}-x_{n_x}\mp(\xi_g\mp\xi_g'))^2+(y_{m_y}-y_{n_y})^2+(L_z\mp L_z)^2}. \end{aligned} \quad (8.4)$$

The impedance matrix (8.1) becomes

$$\begin{aligned} Z_{mn}^{(1)} =& jk_b\eta_b \int_{-h_y}^{0} \int_{-h_x}^{h_x} \int_{-h_y}^{0} \int_{-h_x}^{h_x} (1-\frac{|\xi|}{h_x})\bar{\mathbf{K}}^J(k_bR)(1-\frac{|\xi'|}{h_x})d\xi'd\eta'd\xi d\eta \\ =& jk_b\eta_b \Big\{ w_g(1-\frac{\xi_g}{h_x})\bar{\mathbf{K}}^J(k_bR_1)(1-\frac{\xi_g'}{h_x}) + w_g(1-\frac{\xi_g}{h_x})\bar{\mathbf{K}}^J(k_bR_2)(1-\frac{\xi_g'}{h_x}) \\ & + w_g(1-\frac{\xi_g}{h_x})\bar{\mathbf{K}}^J(k_bR_3)(1-\frac{\xi_g'}{h_x}) + w_g(1-\frac{\xi_g}{h_x})\bar{\mathbf{K}}^J(k_bR_4)(1-\frac{\xi_g'}{h_x}) \Big\}. \end{aligned} \quad (8.5)$$

For the special case, we have $\xi = \xi' = h_x/2$ and $\eta = \eta' = h_y/2$. Hence (8.5) can be written as

$$Z_{mn}^{(1)} = \frac{jk_b\eta_b w_g}{4}\left\{\bar{\mathbf{K}}^J(k_bR_1)+\bar{\mathbf{K}}^J(k_bR_2)+\bar{\mathbf{K}}^J(k_bR_3)+\bar{\mathbf{K}}^J(k_bR_4)\right\}, \quad (8.6)$$

where

$$R_1 = R_4 = \sqrt{(x_{m_x} - x_{n_x})^2 + (y_{m_y} - y_{n_y})^2 + (L_z \mp L_z)^2}, \tag{8.7}$$

$$R_2 = \sqrt{(x_{m_x} - x_{n_x} - h_x)^2 + (y_{m_y} - y_{n_y})^2 + (L_z \mp L_z)^2}, \tag{8.8}$$

$$R_3 = \sqrt{(x_{m_x} - x_{n_x} + h_x)^2 + (y_{m_y} - y_{n_y})^2 + (L_z \mp L_z)^2}. \tag{8.9}$$

When we look at the Eq. (8.5) carefully, we can see that

$$Z^{(1)}_{mn} = Z^{(1)}_{mn}(x_{m_x} - x_{n_x}, y_{m_y} - y_{n_y}) = Z^{(1)}_{m_x - n_x; m_y - n_y} = Z^{(1)}_{m-n}, \tag{8.10}$$

which shows that the impedance matrix partially allow us to use the convolution property. In other words, for the calculation of these the impedance matrix blocks, the fast Fourier transform can be applied which not only accelerates the whole process but also increases the accuracy using the singularity subtraction technique described in Chapter 3. Even though we have not implemented the FFT into our method, we can project the computational cost by using our BCGS-FFT method. Note that BCGS-FFT is a volume integral equation solver, but it can treated as surface integral equation solver if we use one element in the $\hat{\mathbf{z}}$-direction. Figure 8 (a) shows the example mesh, where we have one element in the $\hat{\mathbf{z}}$-direction. Figure 8 (b) shows the used CPU times in order to solve the problem by using different number of elements, N, where $N = N_x \times N_y$, and N_x and N_y are the number of elements in the $\hat{\mathbf{x}}$ and $\hat{\mathbf{y}}$ directions, respectively. The dashed line is $O\left(N \log N\right)$ line, which is included in order to improve the visualization. Clearly, CPU time is $O\left(N \log N\right)$ as expected. For the current finite element/boundary element implementation, we utilized the Method of moments, which requires $O(N^2)$ memory usage and $O(N^3)$ CPU time. As a result, when we add this FFT capability, we will accelerate the method dramatically.

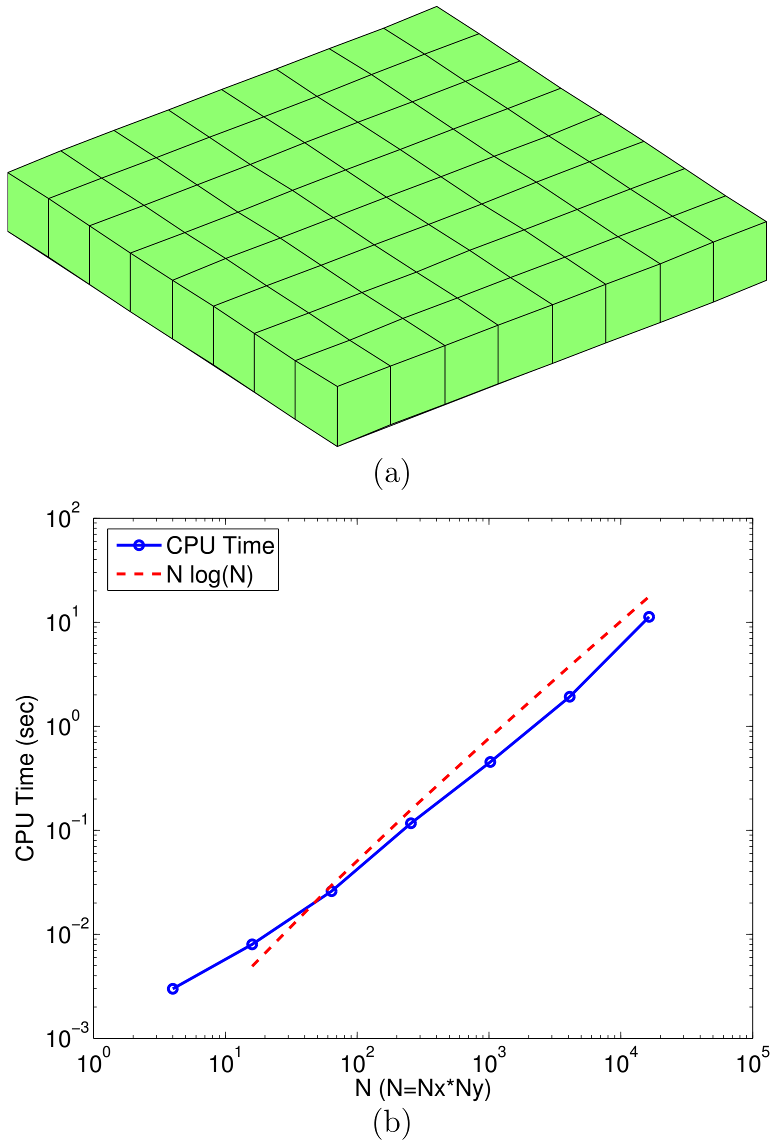

Figure 8.1: (a) A cuboid mesh with one element in the $\hat{\mathbf{z}}$-direction. (b) CPU time for different discretizations.

(d) Replacing FEM with SEM

Another future project possibility would be the replacement of FEM with spectral element method (SEM) in the hybrid implementations. SEM is developed by our lab members in order to obtain spectral accuracy with the orders of the basis functions. The SEM can be considered as a special class of the general FEM, with the choice of nodal points and quadrature integration points based on Gauss-Lobatto-Legendre GLL polynomials. This modification would allow us to obtain same accuracy by using 5 PPW sampling density, whereas we have to have at least 10 PPW for our current MoM/FEM implementation.

(e) Periodic Layered Medium Green's functions and SIM

Periodic structures are frequently used in photonic applications. Efficient and accurate evaluation of periodic layered medium Green's functions is one of the major steps for integral equation solvers. As a result, we can enhance our LMGF codes to the periodic case and we can extend our SIM to periodic problems.

Appendix A

Singularity Subtraction

The time dependency of e^{jwt} is implied. The primary field term's contribution is not included, only the reflection terms are considered. The substcript l is the layer number of the field point, and the substcript m is the layer number of the source point. There are $n+1$ layers, where $l, m = 0, 1, \cdots, n$.

A.1 The Spectral Domain Green's Functions

For the spectral domain Green's functions, the typical equation is in the form of

$$\mathbf{A}_{2n,2n}\mathbf{X}_{2n} = \mathbf{S}_{2n}, \tag{A.1}$$

which is explained next.

For a transversely magnetic wave due to a vertical electric dipole, VED^{TM}, the formulation is as follows,

$$
\begin{aligned}
&A_{11}=\frac{1}{u_0},\ A_{12}=-\frac{1}{u_1}e^{-u_1h_1},\ A_{13}=-\frac{1}{u_1},\\
&A_{21}=\frac{1}{\epsilon_0},\ A_{22}=-\frac{1}{\epsilon_1}e^{-u_1h_1},\ A_{23}=\frac{1}{\epsilon_1},\\
&A_{2n-1,2n-2}=\frac{1}{u_{n-1}},\ A_{2n-1,2n-1}=\frac{1}{u_{n-1}}e^{-u_{n-1}h_{n-1}},\ A_{2n-1,2n}=-\frac{1}{u_n},\\
&A_{2n,2n-2}=\frac{1}{\epsilon_{n-1}},\ A_{2n,2n-1}=-\frac{1}{\epsilon_{n-1}}e^{-u_{n-1}h_{n-1}},\ A_{2n,2n}=\frac{1}{\epsilon_n},\\
&A_{2i-1,2i-2}=\frac{1}{u_{i-1}},\ A_{2i-1,2i-1}=\frac{1}{u_{i-1}}e^{-u_{i-1}h_{i-1}},\\
&A_{2i-1,2i}=-\frac{1}{u_i}e^{-u_ih_i},\ A_{2i-1,2i+1}=-\frac{1}{u_i},\\
&A_{2i,2i-2}=\frac{1}{\epsilon_{i-1}},\ A_{2i,2i-1}=-\frac{1}{\epsilon_{i-1}}e^{-u_{i-1}h_{i-1}},\\
&A_{2i,2i}=-\frac{1}{\epsilon_i}e^{-u_ih_i},\ A_{2i,2i+1}=\frac{1}{\epsilon_i}.
\end{aligned}
\tag{A.2}
$$

where $u_i = jk_{z,i}$, h_i is the ith layer width, and $i = 2, \cdots, n-1$.

$$x_1 = A_0,\ x_{2n} = B_n,\ x_{2i} = A_i,\ x_{2i+1} = B_i. \tag{A.3}$$

$$
\begin{aligned}
&S_{2m-1}=\frac{1}{u_m}e^{-u_m|z_{m-1}-z'|},\ S_{2m}=\frac{1}{\epsilon_m}e^{-u_m|z_{m-1}-z'|},\\
&S_{2m+1}=-\frac{1}{u_m}e^{-u_m|z_m-z'|},\ S_{2m+2}=\frac{1}{\epsilon_m}e^{-u_m|z_m-z'|}.
\end{aligned}
\tag{A.4}
$$

Note that, if $m = 0$, only S_{2m+1} and S_{2m+2} are non-zero; if $m = n$, only S_{2m-1} and S_{2m} are nonzero.

Similarly, for a HED^{TM} wave,

$$\begin{aligned}
&A_{11} = 1,\ A_{12} = -e^{-u_1 h_1},\ A_{13} = -1,\\
&A_{21} = \frac{u_0}{\epsilon_0},\ A_{22} = -\frac{u_1}{\epsilon_1} e^{-u_1 h_1},\ A_{23} = \frac{u_1}{\epsilon_1},\\
&A_{2n-1,2n-2} = 1,\ A_{2n-1,2n-1} = e^{-u_{n-1} h_{n-1}},\ A_{2n-1,2n} = -1,\\
&A_{2n,2n-2} = \frac{u_{n-1}}{\epsilon_{n-1}},\ A_{2n,2n-1} = -\frac{u_{n-1}}{\epsilon_{n-1}} e^{-u_{n-1} h_{n-1}},\ A_{2n,2n} = \frac{u_n}{\epsilon_n},\\
&A_{2i-1,2i-2} = 1,\ A_{2i-1,2i-1} = e^{-u_{i-1} h_{i-1}},\\
&A_{2i-1,2i} = -e^{-u_i h_i},\ A_{2i-1,2i+1} = -1,\\
&A_{2i,2i-2} = \frac{u_{i-1}}{\epsilon_{i-1}},\ A_{2i,2i-1} = -\frac{u_{i-1}}{\epsilon_{i-1}} e^{-u_{i-1} h_{i-1}},\\
&A_{2i,2i} = -\frac{u_i}{\epsilon_i} e^{-u_i h_i},\ A_{2i,2i+1} = \frac{u_i}{\epsilon_i}.
\end{aligned} \tag{A.5}$$

$$x_1 = C_0,\ x_{2n} = D_n,\ x_{2i} = C_i,\ x_{2i+1} = D_i \tag{A.6}$$

$$\begin{aligned}
&S_{2m-1} = -e^{-u_m |z_{m-1} - z'|},\ S_{2m} = -\frac{u_m}{\epsilon_m} e^{-u_m |z_{m-1} - z'|},\\
&S_{2m+1} = -e^{-u_m |z_m - z'|},\ S_{2m+2} = \frac{u_m}{\epsilon_m} e^{-u_m |z_m - z'|}.
\end{aligned} \tag{A.7}$$

Finally, for a HED^{TE} wave,

$$
\begin{aligned}
&A_{11} = \frac{\mu_0}{u_0},\ A_{12} = -\frac{\mu_1}{u_1}e^{-u_1 h_1},\ A_{13} = -\frac{\mu_1}{u_1},\\
&A_{21} = 1,\ A_{22} = -e^{-u_1 h_1},\ A_{23} = 1,\\
&A_{2n-1,2n-2} = \frac{\mu_{n-1}}{u_{n-1}},\ A_{2n-1,2n-1} = \frac{\mu_{n-1}}{u_{n-1}}e^{-u_{n-1}h_{n-1}},\ A_{2n-1,2n} = -\frac{\mu_n}{u_n},\\
&A_{2n,2n-2} = 1,\ A_{2n,2n-1} = -e^{-u_{n-1}h_{n-1}},\ A_{2n,2n} = 1,\\
&A_{2i-1,2i-2} = \frac{\mu_{i-1}}{u_{i-1}},\ A_{2i-1,2i-1} = \frac{\mu_{i-1}}{u_{i-1}}e^{-u_{i-1}h_{i-1}},\\
&A_{2i-1,2i} = -\frac{\mu_i}{u_i}e^{-u_i h_i},\ A_{2i-1,2i+1} = -\frac{\mu_i}{u_i},\\
&A_{2i,2i-2} = 1,\ A_{2i,2i-1} = -e^{-u_{i-1}h_{i-1}},\\
&A_{2i,2i} = -e^{-u_i h_i},\ A_{2i,2i+1} = 1.
\end{aligned}
\tag{A.8}
$$

$$x_1 = E_0,\ x_{2n} = F_n,\ x_{2i} = E_i,\ x_{2i+1} = F_i \tag{A.9}$$

$$
\begin{aligned}
S_{2m-1} &= \frac{\mu_m}{u_m}e^{-u_m|z_{m-1}-z'|},\ S_{2m} = e^{-u_m|z_{m-1}-z'|},\\
S_{2m+1} &= -\frac{\mu_m}{u_m}e^{-u_m|z_m-z'|},\ S_{2m+2} = e^{-u_m|z_m-z'|}.
\end{aligned}
\tag{A.10}
$$

A.2 Some Useful Identities

For the subtraction of the singularities, the following identities are very useful,

$$\int_0^\infty e^{-k_\rho\alpha}J_0(k_\rho\rho)dk_\rho = \frac{1}{\sqrt{\alpha^2+\rho^2}}, \tag{A.11}$$

$$\int_0^\infty e^{-k_\rho\alpha}J_1(k_\rho\rho)dk_\rho = \frac{1}{\rho}\left(1 - \frac{\alpha}{\sqrt{\alpha^2+\rho^2}}\right), \tag{A.12}$$

$$\int_0^\infty e^{-k_\rho\gamma}k_\rho J_0(k_\rho\rho)dk_\rho = \frac{\gamma}{(\gamma^2+\rho^2)^{3/2}}, \tag{A.13}$$

$$\int_0^\infty e^{-k_\rho \gamma} k_\rho^2 J_0(k_\rho \rho) dk_\rho = \frac{2\gamma^2 - \rho^2}{(\gamma^2+\rho^2)^{5/2}}, \tag{A.14}$$

$$\int_0^\infty e^{-k_\rho \gamma} k_\rho J_1(k_\rho \rho) dk_\rho = \frac{\rho}{(\gamma^2+\rho^2)^{3/2}}, \tag{A.15}$$

$$\int_0^\infty e^{-k_\rho \gamma} k_\rho^2 J_1(k_\rho \rho) dk_\rho = \frac{3\gamma\rho}{(\gamma^2+\rho^2)^{5/2}}. \tag{A.16}$$

A.3 The Singularity Treatment for $\mathbf{G}^{HJ}$

$$G_{xx(l)}^{HJ} = \frac{(x-x')(y-y')}{4\pi\rho^2}\left[-\frac{2}{\rho}S_{H1} + S_{H2}\right], \tag{A.17}$$

$$G_{yx(l)}^{HJ} = \frac{1}{4\pi}\left[-\frac{(x-x')^2}{\rho^2}S_{H2} + S_{H3} - \left(\frac{1}{\rho} - \frac{2(x-x')^2}{\rho^3}\right)S_{H1}\right], \tag{A.18}$$

$$G_{zx(l)}^{HJ} = \frac{1}{4\pi}\frac{(y-y')}{\rho}S_{H4}, \tag{A.19}$$

$$G_{xy(l)}^{HJ} = -\frac{1}{4\pi}\left[-\frac{(y-y')^2}{\rho^2}S_{H2} + S_{H3} - \left(\frac{1}{\rho} - \frac{2(y-y')^2}{\rho^3}\right)S_{H1}\right], \tag{A.20}$$

$$G_{yy(l)}^{HJ} = -G_{xx(l)}^{HJ}, \tag{A.21}$$

$$G_{zy}^{HJ} = -\frac{1}{4\pi}\frac{(x-x')}{\rho}S_{H4}, \tag{A.22}$$

$$G_{xz(l)}^{HJ} = -\frac{1}{4\pi}\frac{(y-y')}{\rho}S_{H5}, \tag{A.23}$$

$$G_{yz(l)}^{HJ} = \frac{1}{4\pi}\frac{(x-x')}{\rho}S_{H5}, \tag{A.24}$$

$$G_{zz(l)}^{HJ} = 0. \tag{A.25}$$

where

$$S_{H1} = \int_0^\infty \left[(C_l+E_l)e^{-u_l(z_l-z)} + (D_l-F_l)e^{-u_l(z-z_{l-1})}\right] J_1(k_\rho\rho)dk_\rho, \tag{A.26}$$

$$S_{H2} = \int_0^\infty k_\rho \left[(C_l+E_l)e^{-u_l(z_l-z)} + (D_l-F_l)e^{-u_l(z-z_{l-1})}\right] J_0(k_\rho\rho)dk_\rho, \tag{A.27}$$

$$S_{H3} = \int_0^\infty k_\rho \left[E_l e^{-u_l(z_l - z)} - F_l e^{-u_l(z - z_{l-1})} \right] J_0(k_\rho \rho) dk_\rho, \tag{A.28}$$

$$S_{H4} = \int_0^\infty \frac{k_\rho^2}{u_l} \left[E_l e^{-u_l(z_l - z)} + F_l e^{-u_l(z - z_{l-1})} \right] J_1(k_\rho \rho) dk_\rho, \tag{A.29}$$

$$S_{H5} = \int_0^\infty \frac{k_\rho^2}{u_l} \left[A_l e^{-u_l(z_l - z)} + B_l e^{-u_l(z - z_{l-1})} \right] J_1(k_\rho \rho) dk_\rho, \tag{A.30}$$

We can obtain the asymptotes $\tilde{A}_l$, $\tilde{B}_l$, $\tilde{C}_l$, $\tilde{D}_l$, $\tilde{E}_l$, and $\tilde{F}_l$ simply by calculating $A_l(k_\rho \to \infty)$, $B_l(k_\rho \to \infty)$, $C_l(k_\rho \to \infty)$, $D_l(k_\rho \to \infty)$, $E_l(k_\rho \to \infty)$, and $F_l(k_\rho \to \infty)$, respectively.

- First Integral:

$$\begin{aligned} \tilde{S}_{H1} = \int_0^\infty & \left\{ \left[(C_l + E_l) e^{-u_l(z_l - z)} + (D_l - F_l) e^{-u_l(z - z_{l-1})} \right] \right. \\ & - \left. \left[(\tilde{C}_l + \tilde{E}_l) e^{-k_\rho(z_l - z)} + (\tilde{D}_l - \tilde{F}_l) e^{-k_\rho(z - z_{l-1})} \right] \right\} J_1(k_\rho \rho) dk_\rho, \end{aligned} \tag{A.31}$$

  where we use Eq. (A.12) and the counterpart of the subtracted term in spatial domain is

$$S_{H1}^{add} = (\tilde{C}_l + \tilde{E}_l) \frac{1}{\rho} \left(1 - \frac{\gamma_1}{\sqrt{\gamma_1^2 + \rho^2}} \right) + (\tilde{D}_l - \tilde{F}_l) \frac{1}{\rho} \left(1 - \frac{\gamma_2}{\sqrt{\gamma_2^2 + \rho^2}} \right), \tag{A.32}$$

  where $\gamma_1 = z - z_l$ and $\gamma_2 = z_{l-1} - z$. By following the same procedure, we can formulate the singularity subtraction procedure as follows.

- Second Integral:

$$\begin{aligned} \tilde{S}_{H2} = \int_0^\infty & k_\rho \left\{ \left[(C_l + E_l) e^{-u_l(z_l - z)} + (D_l - F_l) e^{-u_l(z - z_{l-1})} \right] \right. \\ & - \left. \left[(\tilde{C}_l + \tilde{E}_l) e^{-k_\rho(z_l - z)} + (\tilde{D}_l - \tilde{F}_l) e^{-k_\rho(z - z_{l-1})} \right] \right\} J_0(k_\rho \rho) dk_\rho, \end{aligned} \tag{A.33}$$

where we use Eq. (A.13) and the counterpart of the subtracted term in spatial domain is

$$S_{H2}^{add} = (\tilde{C}_l + \tilde{E}_l)\frac{\gamma_1}{(\gamma_1^2+\rho^2)^{3/2}} + (\tilde{D}_l - \tilde{F}_l)\frac{\gamma_2}{(\gamma_2^2+\rho^2)^{3/2}}. \tag{A.34}$$

- Third Integral:

$$\begin{aligned}\tilde{S}_{H3} = \int_0^\infty & k_\rho \left\{ \left[E_l e^{-u_l(z_l-z)} - F_l e^{-u_l(z-z_{l-1})}\right] \right.\\ & \left. - \left[\tilde{E}_l e^{-k_\rho(z_l-z)} - \tilde{F}_l e^{-k_\rho(z-z_{l-1})}\right]\right\} J_0(k_\rho\rho)dk_\rho,\end{aligned} \tag{A.35}$$

where we use Eq. (A.13) and the spatial domain counterpart of the subtracted term is

$$S_{H3}^{add} = \tilde{E}_l\frac{\gamma_1}{(\gamma_1^2+\rho^2)^{3/2}} - \tilde{F}_l\frac{\gamma_2}{(\gamma_2^2+\rho^2)^{3/2}} \tag{A.36}$$

- Fourth Integral:

$$\begin{aligned}\tilde{S}_{H4} = \int_0^\infty & \left\{ \frac{k_\rho^2}{u_l}\left[E_l e^{-u_l(z_l-z)} + F_l e^{-u_l(z-z_{l-1})}\right] \right.\\ & \left. - k_\rho\left[\tilde{E}_l e^{-k_\rho(z_l-z)} + \tilde{F}_l e^{-k_\rho(z-z_{l-1})}\right]\right\} J_1(k_\rho\rho)dk_\rho,\end{aligned} \tag{A.37}$$

where we use Eq. (A.15) and the spatial domain counterpart of the subtracted term is

$$S_{H4}^{add} = \tilde{E}_l\frac{\rho}{(\gamma_1^2+\rho^2)^{3/2}} + \tilde{F}_l\frac{\rho}{(\gamma_2^2+\rho^2)^{3/2}} \tag{A.38}$$

- Fifth Integral:

$$\begin{aligned}\tilde{S}_{H5} = \int_0^\infty & \left\{ \frac{k_\rho^2}{u_l}\left[A_l e^{-u_l(z_l-z)} + B_l e^{-u_l(z-z_{l-1})}\right] \right.\\ & \left. - k_\rho\left[\tilde{A}_l e^{-k_\rho(z_l-z)} + \tilde{B}_l e^{-k_\rho(z-z_{l-1})}\right]\right\} J_1(k_\rho\rho)dk_\rho,\end{aligned} \tag{A.39}$$

where we use Eq. (A.15) and the spatial domain counterpart of the subtracted term is

$$S_{H5}^{add} = \tilde{A}_l \frac{\rho}{(\gamma_1^2 + \rho^2)^{3/2}} + \tilde{B}_l \frac{\rho}{(\gamma_2^2 + \rho^2)^{3/2}} \tag{A.40}$$

A.4 The Singularity Treatment for $\mathbf{G}^{EJ}$

$$G_{xx(l)}^{EJ} = \frac{1}{4\pi j\omega\epsilon_l}\left[\left(\frac{1}{\rho} - \frac{2(x-x')^2}{\rho^3}\right)S_{E1} + \frac{(x-x')^2}{\rho^2}S_{E2} + k_l^2 S_{E3}\right], \tag{A.41}$$

$$G_{yx(l)}^{EJ} = \frac{1}{4\pi j\omega\epsilon_l}\left[-\frac{2(x-x')(y-y')}{\rho^3}S_{E1} + \frac{(x-x')(y-y')}{\rho^2}S_{E2}\right], \tag{A.42}$$

$$G_{zx(l)}^{EJ} = \frac{1}{4\pi j\omega\epsilon_l}\frac{(x-x')}{\rho}S_{E4}, \tag{A.43}$$

$$G_{xy(l)}^{EJ} = G_{yx(l)}^{EJ}, \tag{A.44}$$

$$G_{yy(l)}^{EJ} = \frac{1}{4\pi j\omega\epsilon_l}\left[\left(\frac{1}{\rho} - \frac{2(y-y')^2}{\rho^3}\right)S_{E1} + \frac{(y-y')^2}{\rho^2}S_{E2} + k_l^2 S_{E3}\right], \tag{A.45}$$

$$G_{zy(l)}^{EJ} = \frac{1}{4\pi j\omega\epsilon_l}\frac{(y-y')}{\rho}S_{E4}, \tag{A.46}$$

$$G_{xz(l)}^{EJ} = -\frac{1}{4\pi j\omega\epsilon_l}\frac{(x-x')}{\rho}S_{E6}, \tag{A.47}$$

$$G_{yz(l)}^{EJ} = -\frac{1}{4\pi j\omega\epsilon_l}\frac{(y-y')}{\rho}S_{E6}, \tag{A.48}$$

$$G_{zz(l)}^{EJ} = \frac{1}{4\pi j\omega\epsilon_l}S_{E5} \tag{A.49}$$

where

$$S_{E1} = \int_0^\infty \left[(u_l C_l - \frac{k_l^2}{u_l}E_l)e^{-u_l(z_l - z)} - (u_l D_l + \frac{k_l^2}{u_l}F_l)e^{-u_l(z-z_{l-1})}\right] J_1(k_\rho \rho)dk_\rho, \tag{A.50}$$

$$S_{E2} = \int_0^\infty k_\rho \left[(u_l C_l - \frac{k_l^2}{u_l}E_l)e^{-u_l(z_l - z)} - (u_l D_l + \frac{k_l^2}{u_l}F_l)e^{-u_l(z-z_{l-1})}\right] J_0(k_\rho \rho)dk_\rho, \tag{A.51}$$

$$S_{E3} = \int_0^\infty k_\rho \left[\frac{1}{u_l} E_l e^{-u_l(z_l - z)} + \frac{1}{u_l} F_l e^{-u_l(z - z_{l-1})} \right] J_0(k_\rho \rho) dk_\rho, \tag{A.52}$$

$$S_{E4} = \int_0^\infty k_\rho^2 \left[C_l e^{-u_l(z_l - z)} + D_l e^{-u_l(z - z_{l-1})} \right] J_1(k_\rho \rho) dk_\rho, \tag{A.53}$$

$$S_{E5} = \int_0^\infty \frac{k_\rho^3}{u_l} \left[A_l e^{-u_l(z_l - z)} + B_l e^{-u_l(z - z_{l-1})} \right] J_0(k_\rho \rho) dk_\rho, \tag{A.54}$$

$$S_{E6} = \int_0^\infty k_\rho^2 \left[A_l e^{-u_l(z_l - z)} - B_l e^{-u_l(z - z_{l-1})} \right] J_1(k_\rho \rho) dk_\rho. \tag{A.55}$$

- First Integral:

$$\begin{aligned} \tilde{S}_{E1} = \int_0^\infty \Bigg\{ &\left[(u_l C_l - \frac{k_l^2}{u_l} E_l) e^{-u_l(z_l - z)} - (u_l D_l + \frac{k_l^2}{u_l} F_l) e^{-u_l(z - z_{l-1})} \right] \\ -k_\rho &\left[\tilde{C}_l e^{-k_\rho(z_l - z)} - \tilde{D}_l e^{-k_\rho(z - z_{l-1})} \right] \Bigg\} J_1(k_\rho \rho) dk_\rho, \end{aligned} \tag{A.56}$$

where the terms with $1/u_l$ have zero asymptote. We use Eq. (A.15), and the spatial domain counterpart of the subtracted term is

$$S_{E1}^{add} = \tilde{C}_l \frac{\rho}{(\gamma_1^2 + \rho^2)^{3/2}} - \tilde{D}_l \frac{\rho}{(\gamma_2^2 + \rho^2)^{3/2}}. \tag{A.57}$$

- Second Integral:

$$\begin{aligned} \tilde{S}_{E2} = \int_0^\infty \Bigg\{ &k_\rho \left[(u_l C_l - \frac{k_l^2}{u_l} E_l) e^{-u_l(z_l - z)} - (u_l D_l + \frac{k_l^2}{u_l} F_l) e^{-u_l(z - z_{l-1})} \right] \\ - k_\rho^2 &\left[\tilde{C}_l e^{-k_\rho(z_l - z)} - \tilde{D}_l e^{-k_\rho(z - z_{l-1})} \right] \Bigg\} J_0(k_\rho \rho) dk_\rho. \end{aligned} \tag{A.58}$$

Different than the previous case, we can use Eq. (A.11) for $1/u_l$ terms, since k_ρ/u_l ratio goes to 1. However, these terms' magnitudes are very small with respect to the other two, we can neglect them. We use Eq. (A.14), and the spatial domain counterpart of the subtracted term is

$$S_{E2}^{add} = \tilde{C}_l \frac{2\gamma_1^2 - \rho^2}{(\gamma_1^2 + \rho^2)^{5/2}} - \tilde{D}_l \frac{2\gamma_2^2 - \rho^2}{(\gamma_2^2 + \rho^2)^{5/2}}. \tag{A.59}$$

- Third Integral

$$\tilde{S}_{E3} = \int_0^\infty \left\{ k_\rho \left[\frac{1}{u_l} E_l e^{-u_l(z_l - z)} + \frac{1}{u_l} F_l e^{-u_l(z - z_{l-1})} \right] \right.$$
$$\left. - \left[\tilde{E}_l e^{-k_\rho(z_l - z)} + \tilde{F}_l e^{-k_\rho(z - z_{l-1})} \right] \right\} J_0(k_\rho \rho) dk_\rho, \tag{A.60}$$

By using Eq. (A.11),

$$S_{E3}^{add} = \frac{\tilde{E}_l}{(\gamma_1^2 + \rho^2)^{1/2}} + \frac{\tilde{F}_l}{(\gamma_2^2 + \rho^2)^{1/2}}. \tag{A.61}$$

- Fourth Integral

$$\tilde{S}_{E4} = \int_0^\infty k_\rho^2 \left[C_l e^{-u_l(z_l - z)} + D_l e^{-u_l(z - z_{l-1})} \right.$$
$$\left. - \tilde{C}_l e^{-k_\rho(z_l - z)} - \tilde{D}_l e^{-k_\rho(z - z_{l-1})} \right] J_1(k_\rho \rho) dk_\rho, \tag{A.62}$$

We use Eq. (A.16), and the spatial domain counterpart of the subtracted term is

$$S_{E4}^{add} = \tilde{C}_l \frac{3\gamma_1 \rho}{(\gamma_1^2 + \rho^2)^{5/2}} + \tilde{D}_l \frac{3\gamma_2 \rho}{(\gamma_2^2 + \rho^2)^{5/2}}. \tag{A.63}$$

- Fifth Integral

$$\tilde{S}_{E5} = \int_0^\infty k_\rho^2 \left[\frac{k_\rho}{u_l} A_l e^{-u_l(z_l - z)} + \frac{k_\rho}{u_l} B_l e^{-u_l(z - z_{l-1})} \right.$$
$$\left. - \tilde{A}_l e^{-k_\rho(z_l - z)} - \tilde{B}_l e^{-k_\rho(z - z_{l-1})} \right] J_0(k_\rho \rho) dk_\rho, \tag{A.64}$$

$$S_{E5}^{add} = \tilde{A}_l \frac{2\gamma_1^2 - \rho^2}{(3\gamma_1 \rho)^{5/2}} + \tilde{B}_l \frac{2\gamma_2^2 - \rho^2}{(3\gamma_2 \rho)^{5/2}}. \tag{A.65}$$

- Sixth Integral

$$\tilde{S}_{E6} = \int_0^\infty k_\rho^2 \left[A_l e^{-u_l(z_l-z)} - B_l e^{-u_l(z-z_{l-1})} \right.$$
$$\left. -\tilde{A}_l e^{-k_\rho(z_l-z)} + \tilde{B}_l e^{-k_\rho(z-z_{l-1})}\right] J_1(k_\rho\rho)dk_\rho. \tag{A.66}$$

$$S_{E6}^{add} = \tilde{A}_l \frac{2\gamma_1^2 - \rho^2}{(3\gamma_1\rho)^{5/2}} - \tilde{B}_l \frac{3\gamma_2\rho}{(\gamma_2^2+\rho^2)^{5/2}}. \tag{A.67}$$

A.5 The Singularity Treatment for $\mathbf{K}^{AJ}$ and K_ϕ

$$K_{xx(l)}^{AJ} = \frac{1}{4\pi} S_{I2}, \tag{A.68}$$

$$K_{yy(l)}^{AJ} = K_{xx(l)}^{AJ}, \tag{A.69}$$

$$K_{xy(l)}^{AJ} = K_{yx(l)}^{AJ} = 0, \tag{A.70}$$

$$K_{zx(l)}^{AJ} = \frac{x-x'}{4\pi\rho} S_{I3}, \tag{A.71}$$

$$K_{zy(l)}^{AJ} = \frac{y-y'}{4\pi\rho} S_{I3}, \tag{A.72}$$

$$K_{xz(l)}^{AJ} = \frac{1}{k_l^2}\frac{x-x'}{4\pi\rho}(-S_{I4} - S_{I5} + S_{I6}), \tag{A.73}$$

$$K_{yz(l)}^{AJ} = \frac{1}{k_l^2}\frac{y-y'}{4\pi\rho}(-S_{I4} - S_{I5} + S_{I6}), \tag{A.74}$$

$$K_{zz(l)}^{AJ} = G_{zz(l)}^{AJ} + G_{zz(l)}^{PJ} = \frac{1}{4\pi} S_{I1} + \frac{1}{k_l^2}\frac{1}{4\pi}(S_{I7} + S_{I8} - S_{I9}), \tag{A.75}$$

$$K_\phi = \frac{1}{4\pi\mu_l\epsilon_l}(SI_2 - SI_0), \tag{A.76}$$

where

$$S_{I1} = \int_0^\infty \frac{k_\rho}{u_l}[A_l e^{u_l(z-z_l)} + B_l e^{-u_l(z-z_{l-1})}] J_0(k_\rho\rho)dk_\rho, \tag{A.77}$$

$$S_{I2} = \int_0^\infty \frac{k_\rho}{u_l}[E_l e^{u_l(z-z_l)} + F_l e^{-u_l(z-z_{l-1})}] J_0(k_\rho \rho) dk_\rho, \tag{A.78}$$

$$S_{I3} = \int_0^\infty [(C_l + E_l) e^{u_l(z-z_l)} + (D_l - F_l) e^{-u_l(z-z_{l-1})}] J_1(k_\rho \rho) dk_\rho, \tag{A.79}$$

$$S_{I4} = \int_0^\infty k_\rho^2 [A_l e^{u_l(z-z_l)} - B_l e^{-u_l(z-z_{l-1})}] J_1(k_\rho \rho) dk_\rho, \tag{A.80}$$

$$S_{I5} = \int_0^\infty \frac{k_\rho^2}{u_l}[E_l' e^{u_l(z-z_l)} - F_l' e^{-u_l(z-z_{l-1})}] J_1(k_\rho \rho) dk_\rho, \tag{A.81}$$

$$S_{I6} = \int_0^\infty u_l [(C_l' + E_l') e^{u_l(z-z_l)} - (D_l' - F_l') e^{-u_l(z-z_{l-1})}] J_1(k_\rho \rho) dk_\rho, \tag{A.82}$$

$$S_{I7} = \int_0^\infty k_\rho u_l [A_l e^{u_l(z-z_l)} + B_l e^{-u_l(z-z_{l-1})}] J_0(k_\rho \rho) dk_\rho, \tag{A.83}$$

$$S_{I8} = \int_0^\infty k_\rho [E_l' e^{u_l(z-z_l)} - F_l' e^{-u_l(z-z_{l-1})}] J_0(k_\rho \rho) dk_\rho, \tag{A.84}$$

$$S_{I9} = \int_0^\infty \frac{u_l^2}{k_\rho}[(C_l' + E_l') e^{u_l(z-z_l)} + (D_l' - F_l') e^{-u_l(z-z_{l-1})}] J_0(k_\rho \rho) dk_\rho, \tag{A.85}$$

$$S_{I0} = \int_0^\infty \frac{u_l}{k_\rho}[(C_l + E_l) e^{u_l(z-z_l)} - (D_l - F_l) e^{-u_l(z-z_{l-1})}] J_0(k_\rho \rho) dk_\rho, \tag{A.86}$$

and

$$C_l' = \frac{dC_l}{dz'}, D_l' = \frac{dD_l}{dz'}, E_l' = \frac{dE_l}{dz'}, F_l' = \frac{dF_l}{dz'}. \tag{A.87}$$

- First Integral:

$$\begin{aligned} \tilde{S}_{I1} = \int_0^\infty & \left\{ \frac{k_\rho}{u_l}[A_l e^{-u_l(z_l-z)} + B_l e^{-u_l(z-z_{l-1})}] \right. \\ & \left. - [\tilde{A}_l e^{-u_l(z_l-z)} + \tilde{B}_l e^{-u_l(z-z_{l-1})}] \right\} J_0(k_\rho \rho) dk_\rho, \end{aligned} \tag{A.88}$$

  where we use Eq. (A.11) and the spatial domain counterpart of the subtracted term is

$$S_{I1}^{add} = \tilde{A}_l \frac{1}{\sqrt{\gamma_1^2 + \rho^2}} + \tilde{B}_l \frac{1}{\sqrt{\gamma_2^2 + \rho^2}} \tag{A.89}$$

- Second Integral:

$$\begin{aligned}\tilde{S}_{I2} = \int_0^\infty &\Big\{ \frac{k_\rho}{u_l}[E_l e^{-u_l(z_l-z)} + F_l e^{-u_l(z-z_{l-1})}] \\ &- [\tilde{E}_l e^{-u_l(z_l-z)} + \tilde{F}_l e^{-u_l(z-z_{l-1})}]\Big\} J_0(k_\rho \rho) dk_\rho,\end{aligned} \tag{A.90}$$

where we use Eq. (A.11) and the spatial domain counterpart of the subtracted term is

$$S_{I2}^{add} = \tilde{E}_l \frac{1}{\sqrt{\gamma_1^2+\rho^2}} + \tilde{F}_l \frac{1}{\sqrt{\gamma_2^2+\rho^2}} \tag{A.91}$$

- Third Integral:

$$\begin{aligned}\tilde{S}_{I3} = \int_0^\infty &\Big\{ [(C_l + E_l) e^{-u_l(z_l-z)} + (D_l - F_l) e^{-u_l(z-z_{l-1})}] \\ &- [(\tilde{C}_l + \tilde{E}_l) e^{-u_l(z_l-z)} + (\tilde{D}_l - \tilde{F}_l) e^{-u_l(z-z_{l-1})}]\Big\} J_1(k_\rho \rho) dk_\rho,\end{aligned} \tag{A.92}$$

where we use Eq. (A.12) and the spatial domain counterpart of the subtracted term is

$$S_{I3}^{add} = (\tilde{C}_l + \tilde{E}_l)\frac{1}{\rho}\left(1 - \frac{\gamma_1}{\sqrt{\gamma_1^2+\rho^2}}\right) + (\tilde{D}_l - \tilde{F}_l)\frac{1}{\rho}\left(1 - \frac{\gamma_2}{\sqrt{\gamma_2^2+\rho^2}}\right) \tag{A.93}$$

- Fourth Integral:

$$\begin{aligned}\tilde{S}_{I4} = \int_0^\infty &\Big\{ k_\rho^2[A_l e^{-u_l(z_l-z)} - B_l e^{-u_l(z-z_{l-1})}] \\ &- k_\rho^2[\tilde{A}_l e^{-u_l(z_l-z)} - \tilde{B}_l e^{-u_l(z-z_{l-1})}]\Big\} J_1(k_\rho \rho) dk_\rho,\end{aligned} \tag{A.94}$$

where we use Eq. (A.16) and the spatial domain counterpart of the subtracted term is

$$S_{I4}^{add} = \tilde{A}_l \frac{3\gamma_1\rho}{(\gamma_1^2+\rho^2)^{5/2}} - \tilde{B}_l \frac{3\gamma_2\rho}{(\gamma_2^2+\rho^2)^{5/2}} \tag{A.95}$$

- Fifth Integral:

$$\tilde{S}_{I5} = \int_0^\infty \left\{ \frac{k_\rho^2}{u_l}[E_l' e^{-u_l(z_l - z)} - F_l' e^{-u_l(z - z_{l-1})}] \right.$$
$$\left. - k_\rho[\tilde{E}_l' e^{-u_l(z_l - z)} - \tilde{F}_l' e^{-u_l(z - z_{l-1})}] \right\} J_1(k_\rho \rho) dk_\rho, \tag{A.96}$$

where we use Eq. (A.15) and the spatial domain counterpart of the subtracted term is

$$S_{I5}^{add} = \tilde{E}_l' \frac{\rho}{(\gamma_1^2 + \rho^2)^{3/2}} - \tilde{F}_l' \frac{\rho}{(\gamma_2^2 + \rho^2)^{3/2}} \tag{A.97}$$

- Sixth Integral:

$$\tilde{S}_{I6} = \int_0^\infty \left\{ u_l[(C_l' + E_l')e^{-u_l(z_l - z)} - (D_l' - F_l')e^{-u_l(z - z_{l-1})}] \right.$$
$$\left. - k_\rho[(\tilde{C}_l' + \tilde{E}_l')e^{-u_l(z_l - z)} - (\tilde{D}_l' - \tilde{F}_l')e^{-u_l(z - z_{l-1})}] \right\} J_1(k_\rho \rho) dk_\rho, \tag{A.98}$$

where we use Eq. (A.15) and the spatial domain counterpart of the subtracted term is

$$S_{I6}^{add} = (\tilde{C}_l' + \tilde{E}_l') \frac{\rho}{(\gamma_1^2 + \rho^2)^{3/2}} - (\tilde{D}_l' - \tilde{F}_l') \frac{\rho}{(\gamma_2^2 + \rho^2)^{3/2}} \tag{A.99}$$

- Seventh Integral:

$$\tilde{S}_{I7} = \int_0^\infty \left\{ k_\rho u_l[A_l e^{-u_l(z_l - z)} + B_l e^{-u_l(z - z_{l-1})}] \right.$$
$$\left. - k_\rho^2[\tilde{A}_l e^{-u_l(z_l - z)} + \tilde{B}_l e^{-u_l(z - z_{l-1})}] \right\} J_0(k_\rho \rho) dk_\rho, \tag{A.100}$$

where we use Eq. (A.14) and the spatial domain counterpart of the subtracted term is

$$S_{I7}^{add} = \tilde{A}_l \frac{2\gamma_1^2 - \rho^2}{(\gamma_1^2 + \rho^2)^{5/2}} + \tilde{B}_l \frac{2\gamma_2^2 - \rho^2}{(\gamma_2^2 + \rho^2)^{5/2}} \tag{A.101}$$

- Eight Integral:

$$\begin{aligned}\tilde{S}_{I8} = \int_0^\infty & \Big\{ k_\rho [E_l^{'} e^{-u_l(z_l - z)} - F_l^{'} e^{-u_l(z - z_{l-1})}] \\ & - k_\rho [\tilde{E}_l^{'} e^{-u_l(z_l - z)} - \tilde{F}_l^{'} e^{-u_l(z - z_{l-1})}] \Big\} J_0(k_\rho \rho) dk_\rho,\end{aligned} \tag{A.102}$$

where we use Eq. (A.15) and the spatial domain counterpart of the subtracted term is

$$S_{I8}^{add} = \tilde{E}_l^{'} \frac{\gamma_1}{(\gamma_1^2 + \rho^2)^{3/2}} - \tilde{F}_l^{'} \frac{\gamma_2}{(\gamma_2^2 + \rho^2)^{3/2}} \tag{A.103}$$

- Nineth Integral:

$$\begin{aligned}\tilde{S}_{I9} = \int_0^\infty & \Big\{ \frac{u_l^2}{k_\rho} [(C_l^{'} + E_l^{'}) e^{-u_l(z_l - z)} + (D_l^{'} - F_l^{'}) e^{-u_l(z - z_{l-1})}] \\ & - k_\rho [(\tilde{C}_l^{'} + \tilde{E}_l^{'}) e^{-u_l(z_l - z)} + (\tilde{D}_l^{'} - \tilde{F}_l^{'}) e^{-u_l(z - z_{l-1})}] \Big\} J_0(k_\rho \rho) dk_\rho,\end{aligned} \tag{A.104}$$

where we use Eq. (A.15) and the spatial domain counterpart of the subtracted term is

$$S_{I9}^{add} = (\tilde{C}_l^{'} + \tilde{E}_l^{'}) \frac{\gamma_1}{(\gamma_1^2 + \rho^2)^{3/2}} + (\tilde{D}_l^{'} - \tilde{F}_l^{'}) \frac{\gamma_2}{(\gamma_2^2 + \rho^2)^{3/2}} \tag{A.105}$$

- Zeroth Integral:

$$\begin{aligned}\tilde{S}_{I0} = \int_0^\infty & \Big\{ \frac{u_l}{k_\rho} [(C_l + E_l) e^{-u_l(z_l - z)} - (D_l - F_l) e^{-u_l(z - z_{l-1})}] \\ & - [(\tilde{C}_l + \tilde{E}_l) e^{-u_l(z_l - z)} - (\tilde{D}_l - \tilde{F}_l) e^{-u_l(z - z_{l-1})}] \Big\} J_0(k_\rho \rho) dk_\rho,\end{aligned} \tag{A.106}$$

where we use Eq. (A.11) and the spatial domain counterpart of the subtracted term is

$$S_{I0}^{add} = (\tilde{C}_l + \tilde{E}_l) \frac{1}{\sqrt{\gamma_1^2 + \rho^2}} - (\tilde{D}_l - \tilde{F}_l) \frac{1}{\sqrt{\gamma_2^2 + \rho^2}} \tag{A.107}$$

Appendix B

George Green

George Green (14 July 1793-31 May 1841), was a British mathematician and physicist who wrote An Essay on the Applications of Mathematical Analysis to the Theories of Electricity and Magnetism (Green, 1828). The essay introduced several important concepts, among them a theorem similar to modern Green's theorem, the idea of potential functions as currently used in physics, and the concept of what are now called Green's functions.

Green's life story is remarkable in that he was almost entirely self-taught. He was born and lived for most of his life in the English town of Sneinton, Nottinghamshire, nowadays part of the city of Nottingham. His father (also named George) was a baker who had built and owned a brick windmill used to grind grain. The younger Green only had about one year of formal schooling as a child, between the ages of 8 and 9.

In his adult life, Green worked in his father's mill, taking ownership upon his father's death in 1829. At some point, he began to study mathematics. As Nottingham had little in the way of intellectual resources, it is unclear to historians exactly where Green obtained information on current developments in mathematics. Only one person educated in mathematics, John Toplis, is known to have lived in Nottingham at the time. When Green published his Essay in 1828, it was sold on a subscription basis to 51 people, most of whom were friends and probably could not understand it. Mathematician Edward Bromhead bought a copy and encouraged Green to do further work in mathematics. Not believing the offer was sincere, Green did not contact

Bromhead for two years.

Finally, Green contacted Bromhead, who enabled Green to enter Cambridge University. Green entered as an undergraduate in 1833 at age 40. His academic career was excellent, and after his graduation in 1837 he stayed on the faculty at Gonville and Caius College. He wrote on optics, acoustics, and hydrodynamics. However, in 1840 he became ill and returned to Nottingham, where he died the next year.

Green's work was not well-known in the mathematical community during his lifetime. In 1846, Green's work was rediscovered by Lord Kelvin, who popularised it for future mathematicians.

The George Green Library at the University of Nottingham is named after him, and houses the majority of the University's Science and Engineering Collection. In 1986, Green's mill was restored to working order. It now serves both as a working example of a 19th century mill and as a museum and science centre dedicated to George Green.

`Source: http://en.wikipedia.org/wiki/George_Green`

Bibliography

[1] A. Sommerfeld, *Partial Differential Equations in Physics.* New York: Academic Press, 1949.

[2] J. R. Mosig and F. E. Gardiol, "Analytic and numerical techniques in the Green's function treatment of microstrip antennas and scatterers," *Inst. Elect. Eng. Proc.*, vol. 130, pt. H, pp. 175-182, Mar. 1983.

[3] J. R. Mosig and F. E. Gardiol, "General integral equation formulation for microstrip antennas and scatterers," *Inst. Elect. Eng. Proc.*, vol. 132, pt. H, pp. 424-432, Dec. 1985.

[4] N. K. Das and D. M. Pozar, "A generalized spectral-domain Green.s function for the multilayer dielectric substrates with application to multilayer transmission lines," *IEEE Trans. Microwave Theory tech.*, vol. MTT-35, no.3, pp.326-335, Mar. 1987.

[5] J. Zhao, S. Kapur, D. E. Long, and W. W. M. Dai, "Efficient three-dimensional extraction based on static and full wave layered Green's functions," *Proceedings of the* 35^{th} *Design Automation Conference*, June 1998.

[6] L. Tsang, C. Ong, C.C. Huang and V. Jandhyala, "Evaluation of the Green's function for the mixed potential integral equation (MPIE) method in the time domain for layered media," *IEEE Trans. Antennas and Propagat.*, vol. 51, no. 7, pp. 1559-1571, July , 2003.

[7] W. Cai and T. Yu, "Fast calculations of Dyadic Green's functions for electromagnetic scattering in a multilayer medium," *J. Comput. Phys.*, 165, pp. 1-21, 2000.

[8] I. V. Lindell and E. Alanen, "Exact image theory for the Sommerfeld half space problem-Part 1: Vertical magnetic dipole," *IEEE Trans. Antennas and Propagat.*, pp. 126-132, Feb. 1984.

[9] I. V. Lindell and E. Alanen, "Exact image theory for the Sommerfeld half space problem-Part 2: Vertical electric dipole," *IEEE Trans. Antennas and Propagat.*, pp. 841-849, Oct. 1984.

[10] D. G. Fang, J. J. Yang, and G. Y. Delisle, "Discrete image theory for horizontal electric dipoles in a multilayered medium," *Inst. Elect. Eng. Proc.*, vol. 135, pt. H, pp. 297-303, Oct. 1988.

[11] Y. L. Chow, J. J. Yang, D. G. Fang, and G. E. Howard, "A closed-form spatial Green's function for the thick substrate," *IEEE Trans. Microwave Theory Tech.*, vol. 39, pp. 588-592, Mar. 1991.

[12] M. I. Aksun and R. Mittra, "Derivation of closed-form Green's functions for a general microstrip geometry," *IEEE Trans. Microwave Theory Tech.*, vol. 40, pp. 2055-2062, Nov. 1992.

[13] R. A. Kipp, C. H. Chan, A. T. Yang, and J. T. Yao, "Simulation of high frequency integrated circuits incorporating full wave analysis of microstrip discontinuities," *IEEE Trans. Microwave Theory Tech.*, vol. 41, pp. 848-854, May 1993.

[14] R. A. Kipp and C. H. Chan, "Complex image method for sources in bounded regions of multilayer structures," *IEEE Trans. Microwave Theory Tech.*, vol. 42, pp. 860-865, May 1994.

[15] G. Dural and M. I. Aksun, "Closed-form Green's functions for general sources in stratified media," *IEEE Trans. Microwave Theory Tech.*, vol. 43, pp. 1545-1552, July 1995.

[16] N. Hojjat, S. Safavi-Naeini, and Y. L. Chow, "Numerical computation of complex image Green's functions for multilayer dielectric media: near field zone and the interface region," *IEE Proc.-Microw. Antennas Propagat.*, vol. 145, no. 6, pp. 449-454, Dec. 1998.

[17] N. Hojjat, S. Safavi-Naeini, R. F. Dana, and Y. L. Chow, "Fast computation of the nonsymmetrical components of the Green's functions for multilayer dielectric media using complex images," *IEE Proc.-Microw. Antennas Propagat.*, vol. 145, no. 6, pp. 285-289, Aug. 1998.

[18] F. Ling, *Fast electromagnetic modeling of multilayer microstrip antennas and circuits*. Ph.D. Dissertation, University of Illinois at Urbana-Champaign, 2000.

[19] A. A. K. Mohsen, A. K. Abdelmageed, "An efficient evaluation of the nonsymmetrical components of the Green's function for multilayered media," *Microwave and Optical Technology Letters*, vol. 28, no. 3, pp. 199-202, 2001.

[20] Y. Liu, L.W. Li, T. Yeo and M.S. Leong. "Application of DCIM to MPIE-MoM analysis of 3D PEC objects in multilayered media," *IEEE Trans. Antennas Propagat.*, vol. 50, No. 2, pp. 157-162, Feb. 2002.

[21] K. P. Eselle and Y. Ge, "New closed-form Green's functions for microstrip structures-theory and results," *IEEE Trans. Microwave Theory Tech.*, vol. 50, no. 6, pp. 1556-1560, June 2002.

[22] P. Ylä-Oijala, M. Taskinen, and J. Sarvas, "Multilayered media Green's Functions for MPIE with general electric and magnetic sources by the Hertz potential approach," *Progress In Electromagnetics Research*, vol. 33, pp. 141-165, 2001.

[23] W. C. Chew, *Waves and Fields in Inhomogeneous Media.* Piscataway, NJ: IEEE Press, 1995.

[24] J. M. Jin and W.C. Chew, "Green's function methods," in *Encyclopedia of Electrical and Electronics Engineering,* J. Webster Ed., vol. 8, New York: Wiley, 1998, pp. 462-476.

[25] L. B. Felsen, and A. H. Kamel, "Hybrid ray-mode formulation of parallel plane waveguide Green's functions," *IEEE Trans. on Antennas and Propagat.*, vol. AP-29, July 1981, p. 637-649.

[26] K. A. Michalski and J. R. Mosig, "Multilayered media Green's functions in integral equation formulations," *IEEE Trans. Antennas Propagat.*" vol. 45, pp. 508-519, Mar. 1997.

[27] K. A. Michalski and D. Zheng, "Electromagnetic scattering and radiation by surfaces of arbitrary shape in layered media: Part-I: Theory," *IEEE Trans. Antennas Propagat.*, vol. 38, pp. 335-344, Mar. 1990.

[28] K. A. Michalski and D. Zheng, "Electromagnetic scattering and radiation by surfaces of arbitrary shape in layered media: Part-II: Implementation and results for contiguous half-spaces," *IEEE Trans. Antennas Propagat.*, vol. 38, pp. 355-352, Mar. 1990.

[29] N. Geng, L. Carin, "Wide-band electromagnetic scattering from a dielectric BOR buried in a layered lossy dispersive medium," *IEEE Trans. Antennas Propagat.*, vol. 47, pp. 610-619, Apr. 1999.

[30] E. Jørgensen, O. S. Kim, P. Meincke, and O. Breinbjerg, "Higher order hierarchical discretization scheme for surface integral equations for layered media," *IEEE Trans. Geosci. Remote Sensing*, vol. 42, No. 4, pp. 764-772, Apr. 2004.

[31] Y. H. Chen, W. C. Chew, S. Zeroug, "Fast multipole method as an efficient solver for 2D elastic wave surface integral equations," *Computational Mechanics*, vol. 20, no. 6, pp. 495-506, Nov. 1997

[32] B. Hu, and W. C. Chew, "Fast inhomogeneous plane wave algorithm for electromagnetic solutions in layered medium structures: 2D case," *Radio Science*, vol. 35, No. 1, pp. 31-43, 2000.

[33] B. Hu, and W. C. Chew, "Fast inhomogeneous plane wave algorithm for scattering from objects above the multilayered medium.", *IEEE Trans. Geosci. Remote Sens.*, vol. 39, No. 5, pp. 1028-1038, 2001.

[34] N. Geng, A. Sullivan, and L. Carin, "Multilevel fast-multipole algorithm for scattering from conducting targets above or embedded in a lossy half space," *IEEE Trans. Geosci. Remote Sensing*, vol. 38, pp. 1561-1573, July 2000.

[35] N. Geng, A. Sullivan, and L. Carin, "Fast multipole method for scattering from an arbitrary PEC target above or buried in a lossy half space," *IEEE Trans. Antennas Propagat.*, vol. 49, pp. 740-748, May 2001.

[36] E. Bleszynski, M. Bleszynski, and T. Jaroszewicz, "A fast integral equation solver for electromagnetic scattering problems," *IEEE AP-S Int. Symp. Dig.*, pp. 416-419, Seattle, WA, June 1994.

[37] E. Bleszynski, M. Bleszynski, and T. Jaroszewicz, "AIM: Adaptive integral method for solving large-scale electromagnetic scattering and radiation problems," *Radio Sci.*, vol. 31, No. 5, pp. 1225-1252, 1996.

[38] F. Ling, C.F. Wang, and J.M. Jin, "Application of adaptive integral method to scattering and radiation analysis of arbitrarily shaped planar structures," *IEEE Antennas and Propagat. Soc. Int. Symp.*, vol. 3, pp. 1778-1781, Jun. 1998.

[39] S.S. Bindiganavale, J.L. Volakis, H. Anastassiu, "Scattering from planar structures containing small features using the adaptive integral method (AIM)", *IEEE Trans. Antennas Propag.* vol. 46, No. 12, pp. 1867-1878, 1998.

[40] E. Topsakal, M. Carr, J.L. Volakis, M. Bleszynski, "Scattering from 3-D multilayered surfaces using adaptive integral method" *IEEE Antennas and Propag. Soc. Int. Symp.*, vol. 4, pp. 1868-1871, Jul. 2000.

[41] A. E. Yilmaz, J.M. Jin, and E. Michielssen, "Time domain adaptive integral method for surface integral equations," *IEEE Trans. Antennas and Propagation*, vol. 52 , No. 10, pp. 2692-2708, Oct. 2004.

[42] J. Liu and Q. H. Liu, "A Spectral Integral Method (SIM) for Periodic and Nonperiodic Structures," *IEEE Microwave and Wire. Comp. Lett.*, vol. 13, pp. 97-99, Mar. 2004.

[43] N. N. Bojarski, "Scattering by a cylinder: A fast exact numerical solution," *J. Acoust. Soc. Amer.*, vol. 75, no. 2, pp. 320-323, 1984.

[44] G. T. Schuster, "A fast exact numerical solution for the acoustic response of concentric cylinders with penetrable interfaces," *J. Acoust. Soc. Amer.*, vol. 87, no. 2, pp. 495-502, 1990.

[45] F. Q. Hu, "A spectral boundary integral equation method for the 2D Helmholtz equation," *J. Comp. Phys.*, vol. 120, pp. 340-347, 1995.

[46] M. Paulus, P. Gay-Balmaz, and O. J. F. Martin, "Accurate and efficient computation of the Green's tensor for stratified media, " *Physical Review*, vol. 62, np. 4, pp. 5797-5807, Oct 2000.

[47] M. I. Aksun, "A robust approach for the derivation of closed-form Green's functions," *IEEE Trans. Microwave Theory Tech.*, Vol. MTT-44, pp. 651-658, May 1996.

[48] E. Simsek, Q. H. Liu, and B. Wei, "Singularity subtraction for evaluation of Green's functions for multilayer media," *IEEE Trans. Microwave Theory Tech.*, vol. 54, no. 1,pp. 216-225, Jan. 2006..

[49] X. Millard, and Q. H. Liu, "A fast volume integral equation solver for electromagnetic scattering from large inhomogeneous objects in planarly layered media," *IEEE Trans. Antennas Propagat.*, vol. 51, no. 9, pp. 2393-2401, 2003.

[50] X. Millard, and Q. H. Liu, "Simulations of near-surface detection of objects in layered media by the BCGS-FFT method," *IEEE Trans. Geosci. Remote Sensing,* vol. 42 pp. 327Ű334, 2004.

[51] L. P. Song, E. Simsek, and Q.H. Liu, "A fast 2-D volume integral equation solver for scattering from inhomogeneous objects in layered media," *Microwave Opt. Technol. Lett.*, to appear in Oct. 2005.

[52] E. Simsek and Q.H. Liu, "Fast computation of dyadic Green's function for layered media and its application in interconnect simulations," *2004 USNC/URSI National Radio Science Meeting,* vol. 3, p. 2783, Monterey, CA, June 20-25, 2004.

[53] B. Engquist and A. Majda, "Absorbing boundary conditions for the numerical simulation of waves," *Math. Comput.*, vol. 31, pp. 629-651, 1977.

[54] J. M. Jin and V. V. Liepa, "Application of hybrid finite element method to electromagnetic scattering from coated cylinders," *IEEE Trans. Antennas Propag.*, vol. AP-36, no. 1, pp. 50-54, Jan. 1988.

[55] J. M. Jin and V. V. Liepa, "A note on the hybrid finite element method for solving scattering problems," *IEEE Trans. Antennas Propag.*, vol. AP-36, no. 10, pp. 1486-1490, Oct. 1988.

[56] J. D. Collins, J. M. Jin, and J. L. Volakis, "A combined finite element - boundary element formulation for solution of two-dimensional problems via CGFFT," *Electromagn.*, vol. 10, no. 4, pp. 423-437, 1990.

[57] J. M. Jin, J. L. Volakis, and J. D. Collins, "A finite element - boundary integral method for scattering and radiation by two- and three-dimensional structures," *IEEE Antennas Propag. Mag.*, vol. 33, no. 3, pp. 22-32, Jun. 1991.

[58] J. M. Jin and J. L. Volakis, "A hybrid finite element method for scattering and radiation by microstrip patch antennas and arrays residing in a cavity," *IEEE Trans. Antennas Propag.*, vol. AP-39, no. 11, pp. 1598-1604, Nov. 1991.

[59] J. P. Berenger, "A perfectly matched layer for the absorption of electromagnetic waves," *J. Comp. Phy.*, vol. 114, pp. 185-200, Oct. 1994.

[60] Z. S. Sachs, D. M. Kingsland, R. Lee, and J-F. Lee, "Performance of an anisotropic artificial absorber for truncating finite element meshes," *IEEE Trans. Antennas Propag.*, vol. 43, no. 12, pp. 1460-1463, Dec. 1995.

[61] W. C. Chew, and W. H. Weedon, "A 3D perfectly matched medium from modified Maxwell's equations with stretched coordinates," *Microwave Opt. Tech. Lett.*, vol. 7, pp. 599-604, 1994.

[62] S. D. Gedney, "An anistropic perfectly matched layer - Absorbing medium for trunction of FDTD lattices," *IEEE Trans. Antennas Propag.*, vol. 44, no. 12, pp. 1630-1639, 1996.

[63] M. D. Deshpande, C. R. Cockrell, and C. J. Reddy, "Electromagnetic scattering analysis of arbitrarily shaped material cylinder by FEM-BEM method," *NASA technical report*, Jul. 1996.

[64] Q. H. Liu, "An FDTD algorithm with perfectly matched layers for conductive media," *Micro. Opt. Tech. Lett.*, vol. 14, no. 2, pp. 134-137, 1997.

[65] T. F. Eibert, V. Hansen, "Calculation of unbounded field problems in free space by a 3D FEM/BEM - hybrid approach," *J. Electromag. Waves and Appl.,* vol. 10, no. 1, pp. 61-78, 1996.

[66] T. F. Eibert, V. Hansen, "3D FEM/BEM-hybrid approach for planar layered media," *Electromagnetics,* vol. 16, no. 3, pp. 253-272, 1996.

[67] T. F. Eibert, V. Hansen, "3-D FEM/BEM-hybrid approach based on a general formulation of Huygens' principle for planar layered media," *IEEE Trans. Microwave Theory Tech.,* vol. 45, no. 7, pp. 1005-1112, Jul. 1997

[68] T. F. Eibert, V. Hansen, "3-D FEM/BEM-hybrid modeling of surface mounted devices withinplanar circuits," *IEEE Trans. Microwave Theory Tech.,* vol. 46, no. 9, pp. 1334-1336, Sept. 1998.

[69] M. W. Ali, T. H. Hubing, and J. L. Drewniak, "A Hybrid FEM/MoM Technique for Electromagnetic Scattering and Radiation from Dielectric Objects with Attached Wires," *IEEE Trans. on Electromagn. Compat.*, vol. 39, no. 4, Nov.1997.

[70] J. Jin, *The Finite Element Method in Electromagnetics*, John Wiley & Sons, New York, 1993.

[71] D.A. Dunavant, "High degree ecient symmetrical Gaussian quadrature rules for the triangle,"*International Journal of Numerical Methods in Engineering,* vol. 21, pp. 1129-1148, 1985.

[72] J. L. Volakis, A. Chatterjee, and L. C. Kempel, *Finite Element Method for Electromagnetics*, IEEE Press, 1998.

[73] A. F. Peterson, A. L. Ray, and R. Mittra, *Computational Methods for Electromagnetics*, pp. 43, IEEE press, 1998.

[74] A. Musolino and M. Raugi, "A hybrid FEM/MOM formulation for nonlinear electromagnetic analysis," *IEEE Trans. Magn.* , vol. 34, no. 5, pp. 3292-3295, Sept. 1998.

[75] F. L. Teixeira, and W. C. Chew, "A general approach to extend Berenger's absorbing boundary condition to anisotropic and dispersive media," *IEEE Trans. Antennas Propag.*, vol. 46, no. 9, pp. 1386–1387, Sept. 1998.

[76] J. A. Roden, and S. D. Gedney, "Convolution PML (CPML): An efficient FDTD implementation of the CFS-PML for arbitrary media," *Microwave Opt. Technol. Lett.*, vol. 27, no. 5, pp. 334-339, 2000.

[77] G. X. Fan, and Q. H. Liu, "A strongly well-posed PML in lossy media," *IEEE Antennas Wireless Propag. Lett.*, vol. 2, no. 7, pp. 97-100, 2003.

[78] A. Musolino, "Finite-element method/method of moments formulation for the analysis of current distribution in rail launchers," *IEEE Trans. on Magnetics*, vol. 41, no. 1, pp. 387-392, Jan. 2005.

[79] E. Simsek, J. Liu, and Q. H. Liu, "A Spectral Integral Method (SIM) for Layered Media," *IEEE Transactions on Antennas and Propagation,* vol. 54, issue 6, pp. 1742-1749, June 2006.

[80] J. Liu, and Q. H. Liu, "A novel radiation boundary condition for finite-element method,"

[81] X.-B. Xu, C. M. Butler, "Scattering of TM excitation by coupled and partially buried cylinders at the interface between two media," *IEEE Trans. Antennas Propag.*, vol. AP-35, no. 5, pp. 529-538, May 1987.

[82] T.J. Cui, and W. C. Chew, "Fast evaluation of Sommerfeld integrals for EM scattering and radiation by three-dimensional buried objects," *IEEE Trans. Geoscience Remote Sensing*, vol. 37, pp. 887-900, March 1999.

[83] Mosig, J. R., "Arbitrarily shaped microstrip structures and their analysis with a mixed potential integral equation," *IEEE Trans. Microwave Theory Tech.*, vol. 36, pp. 314-323, Feb. 1988.

[84] D. Zheng, and K. A. Michalski, "Analysis of coaxially fed microstrip antennas of arbitrary shape with thick substrates," *Journal of Electromagnetic Waves and Applications*, vol. 5, no. 12, pp. 1303-1327, 1991.

[85] J. M. Jin, J. Liu, and F. Ling, "Efficient electromagnetic modeling of 3D multilayer microstrip antennas and circuits," *IEEE Trans. Microwave Theory Tech.*, vol. 50, no. 6, pp. 1628-1635, June 2002.

[86] I. S. Gradshteyn, and I. M. Ryzhik, *Table of Integrals, Series, and Products*, Academic Press, Inc., Florida, 1965.

[87] F. Li, Q. H. Liu, and L.-P. Song, "Three-dimensional reconstruction of objects buried in layered media using Born and distorted Born iterative methods," *IEEE Geosci. Remote Sensing Lett.*, vol. 1, no. 2, pp. 107–111, 2004.

[88] C. T. Tai, *Generalized Vector and Dyadic Analysis (2nd edition).* Piscataway, NJ: IEEE Press, 1997.

[89] M.G. Duffy, "Quadrature over a pyramid or cube of integrands with a singularity at a vertex," *SIAM J. Numer. Anal.*, vol.19, No. 6, Dec 1982.

[90] P.P. Silvester and R.L. Ferrari, *Finite Elements for Electrical Engineers*, Cambridge: Cambridge University Press, 1990.

[91] G. Szego, *Orthogonal Polynomials (4th edition).* Providence, RI: Amer. Math. Soc., 1975.

[92] M. Abramowitz, and I.A. Stegun, *Handbook of Mathematical Functions with Formulas, Graphs, and Mathematical Tables (9th printing).* New York: Dover, pp. 771-802, 1972.

[93] J. R. Mautz and R. F. Harrington, "H-field, E-field, and combined field solutions for conducting bodies of revolutions," *Arch. Elek. Ubertrag.* vol. 32, pp. 157-164, 1978.

[94] K. Umashankar, A. Taflove, and S.A. Rao, "Electromagnetic scattering by arbitrary shaped three-dimensional homogeneous lossy dielectric objects," *IEEE Trans Antennas Propagat.,* AP-34, pp. 758-766, 1986.

[95] P. L. Huddleston, L. N. Medgyesi-Mitschang, and J.M. Putnam, "Combined field integral equation formulation for scattering from dielectrically coated conducting bodies," *IEEE Trans. Antennas Propag.,* AP-34, pp. 510-520, 1986.

[96] R. F. Harrington, *Field Computation by Moment Methods,* 2nd ed. Malabar, Fla.:Krieger, 1982.

[97] S. Rao, D. Wilton, A. Glisson, "Electromagnetic scattering by surfaces of arbitrary shape," *IEEE Trans. Antennas Propag.,* vol. 30, no. 3, pp. 409-418, May 1982

[98] M. L. Barton and Z.J. Cendes, "New vector finite elements for three dimensional magnetic field computation," *J. Appl. Phys.,* vol. 61, pp. 3919-3921, Apr. 1982.

[99] M.W. Ali, "Development of a hybrid 3D numerical technique for analyzing printed circuit models with attaced wires," Ph.D. dissertation, Univ. Missouri, Rolla, 1996.

[100] W. H. Press, S. A. Teukolsky, W. T. Vettering, and B. P. Flannery, *Numerical Recipes in C: The Art of Scientific Computing, 2nd edition, New York: Cambridge University Press, 1992.*

Biography

Ergün Şimşek was born in 1979 in Yalova, Turkey. He received his B.S. degree in electrical engineering from Bilkent University, Ankara, Turkey, in 2001 and M.S. degree in electrical and computer engineering from University of Massachusetts Dartmouth, in 2003.

He worked as a research assistant for Prof. Qing H. Liu at Duke University between July 2003 and November 2006. His research interests include computational and applied electromagnetics, forward and inverse scattering problems, fast solvers, and simulation and design of nano and photonic devices. The below is a list of his publications.

Peer-reviewed Journal Publications

[P1] E. Simsek, Q. H. Liu, and B. Wei, "Singularity subtraction for evaluation of Green's functions for multilayer media," *IEEE Transactions on Microwave Theory and Techniques,* vol. 54, no. 1, pp. 216-225, Jan. 2006.

[P2] E. Simsek, J. Liu, and Q. H. Liu, "A Spectral Integral Method (SIM) for Layered Media," *IEEE Transactions on Antennas and Propagation,* vol. 54, issue 6, pp. 1742-1749, June 2006.

[P3] E. Simsek, J. Liu, and Q. H. Liu, "A Spectral Integral Method and Hybrid SIM/FEM for Layered Media,". *IEEE Transactions on Microwave Theory and Techniques*, vol. 54, no. 11, pp. 3878-3884, Nov. 2006.

[P4] L. P. Song, E. Simsek, and Q. H. Liu, "A Fast 2-D Volume Integral Equation Solver for Scattering from Inhomogeneous Objects in Layered Media," *Microwave and Optical Technology Letters,* vol. 47, No. 2 , pp. 128-134, Oct. 2005.

[P5] B. Wei, E. Simsek, and Q. H. Liu, "Improved diagonal tensor approximation (DTA) and hybrid DTA/BCGS-FFT method for accurate simulation of 3-D inhomogeneous objects in layered media," to appear on *Waves in Random and Complex Media.*

[P6] B. Wei, E. Simsek, C. Yu, and Q. H. Liu, "Three-Dimensional Electromagnetic Nonlinear Inversion in Layered Media by a Hybrid Diagonal Tensor Approximation - Stabilized Biconjugate Gradient Fast Fourier Transform Method," to appear on *Waves in Random and Complex Media.*

[P7] B. K. Sinha, E. Simsek, and Q. H. Liu, "Elastic wave propagation in deviated wells in anisotropic formations," *Geophysics,* vol. 71, no. 6, pp. 191-202, Nov. 2006.

Conference Papers and Abstracts

[C1] E. Simsek, Q. H. Liu, and J. Liu, "Fast computation of dyadic Green's function for layered media and its application in interconnect simulations," *IEEE Antennas and Propagation Society International Symposium and URSI,* Abstract, Monterey, CA, June 2004.

[C2] E. Simsek, J. Liu, and Q. H. Liu, "Fast Simulation of Periodic Structures in a Layered Medium", *IEEE Antennas and Propagation Society International Symposium and URSI*, Abstract, Washington, DC, July 2005.

[C3] E. Simsek, J. Liu, Q. H. Liu, "A 2D Hybrid Spectral-Integral/Finite-Element Method for Layered," *IEEE Antennas and Propagation Society International Symposium and URSI,* Albuquerque, NM, July, 2006.

[C4] E. Simsek, J. Liu, and Q. H. Liu, "A Spectral Integral Method (SIM) for Layered Media," *IEEE Antennas and Propagation Society International Symposium and URSI*, Abstract, Washington, DC, July 2005.

[C5] C. Yu, E. Simsek, and Q. H. Liu, "Accurate Simulation of Electromagnetic Waves Scattered by 3D Objects in a Multilayered Medium by a Surface Integral Equation Method," *IEEE Antennas and Propagation Society International Symposium and URSI, Albuquerque, NM,* July, 2006.

[C6] E. Simsek, J. Liu, Q. H. Liu, "A 3D Spectral Integral Method for Layered Media," *IEEE Antennas and Propagation Society International Symposium and URSI,* Albuquerque, NM, July, 2006.

[C7] J. Liu, J. H. Lee, E. Simsek, and Q. H. Liu, "A Hybrid Spectral Integral Method/Spectral Element Method for Electromagnetic Wave Scattering," *IEEE Antennas and Propagation Society International Symposium and URSI, Albuquerque, NM, July,* 2006.

[C8] J. Liu, E. Simsek, and Q. H. Liu, "A 3-dimensional Spectral Integral Method for Acoustic and Electromagnetic Wave Scattering," *IEEE Antennas and Propagation Society International Symposium and URSI,* Albuquerque, NM, July, 2006.

[C9] B. K. Sinha, E. Simsek, and Qing-Huo Liu, "Elastic wave propagation in deviated wells in anisotropic formations," *76th Annual International Meeting, Society of Exploration Geophysicists,* New Orleans, LA, Oct. 2006.